OSCILLATORY FLOW PAST CYLINDERS AT LOW KC NUMBERS

By

KUN YANG

B.Eng.

This thesis is presented for the degree of
Doctor of Philosophy

At

THE UNIVERSITY OF WESTERN AUSTRALIA
Achieving International Excellence

School of Civil and Resource Engineering
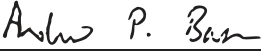
September 2013

DECLARATION

This thesis contains published work and/or work prepared for publication, which has been co-authored. The bibliographical details of the work and where it appears in the thesis are outlined below

Yang, K., Cheng, L., An, H., Bassom, A. and Zhao, M. (2013). "The effect of a piggyback cylinder on the flow characteristics in oscillatory flow". *Ocean Engineering*. Volume 62, P45-55. (Chapter 6)

Yang, K., Cheng, L., An, H., Bassom, A. and Zhao, M. (2014). "Effects of an axial flow component on the Honji instability". *Journal of Fluids and Structures*. (Accepted).

The estimated percentage contribution of the candidate is 75%.

KUN YANG		17/06/2014
PRINT NAME	SIGNATURE	DATE

LIANG CHENG		17/6/14
PRINT NAME	SIGNATURE	DATE

ANDREW BASSOM		17/6/14
PRINT NAME	SIGNATURE	DATE

HONGWEI AN		17/06/14
PRINT NAME	SIGNATURE	DATE

MING ZHAO		17/06/2014
PRINT NAME	SIGNATURE	DATE

I hereby declare that, except where specific reference is made to the work of others, the contents of this dissertation are original and have not been submitted in whole or in part for consideration for any other degree of qualification at this, or any other, university.

Kun YANG

June 2014

To my family.

ABSTRACT

Offshore pipelines are an indispensable element of the oil and gas industry. Understanding the interactions between the pipelines and their surrounding fluids is of paramount importance to the whole industry.

This thesis is concerned with oscillatory flow over cylindrical structures (representing pipelines) at low governing parameters. The two flow regimes considered are the Honji instability regime and the vortex shedding regime. Honji instability is the hydrodynamic instability responsible for causing a two-dimensional laminar flow to transit into a three-dimensional flow. Modifications in the resultant flow field under the Honji instability and the vortex shedding regimes have great engineering relevance as the flow characteristics often closely relate to the hydrodynamic forces on the immersed pipeline structures. However, our current knowledge of the resultant flow behaviours regarding the Honji instability and the vortex shedding phenomena remains quite limited. It is thus the aim of the present thesis to shed more light on our understanding of the two flow regimes under certain circumstances that are closely related to real engineering problems.

Previous studies on Honji instability are only limited to the situation when the approaching inflow is perpendicular to the cylinder, while in practice, pipelines and the incoming flow are not always orthogonal. Therefore, the first concern of the thesis is to consider the effects of an oblique angle of the inflow on the Honji instability. Through three-dimensional numerical simulations, the flow evolution as well as the instantaneous flow structures under the instability regime under different oblique angles are obtained and discussed.

The oblique free stream sees an elliptic cross-section of the cylinder, which indicates a geometrical analogy between the oblique inflow around a circular cylinder and the perpendicular flow around a cylinder with elliptic cross-sectional shape. In fact, many pipelines bear an elliptic cross-sectional shape in practice. A natural curiosity then arises regarding resultant flow behaviours of the Honji instability under the influences of different elliptic cross-sections. This thesis presents discussions on alterations of the typical Honji vortical structures formed at different elliptic shapes of the cylinder.

In addition, the thesis also presents an investigation on a dual-cylinder system with unequal diameters in the vortex shedding regime. This type of configuration represents as the so-called "piggyback cylinders" commonly encountered in industry. Through two-dimensional numerical simulations, the flow structures and associated hydrodynamic forces around the main cylinder are discussed under different vortex shedding modes, and the effects of the neighbouring smaller cylinder placed at various locations with respect to the primary cylinder are evaluated. Through examining the connection between the symmetricity of the resultant flow field and the hydrodynamic forces, this study proposes an estimating method that is easy to apply and is of great value for practical engineering applications.

All results presented in this thesis have been obtained through direct numerical simulations using a Petrov-Galerkin finite element method, for which details are given. Three-dimensional calculations are performed to study the Honji instability problem under the effects of oblique inflow as well as of different elliptic shapes of the cylinder, while two-dimensional simulations are conducted for the piggyback cylinders in the vortex shedding regime. In summary, this thesis has advanced our knowledge of oscillatory flow around cylindrical structures at low governing parameters under different scenarios commonly encountered in practice, so that more light is shed on the overall understanding of fluid-structure interactions that is of significant relevance to the oil and gas industry.

ACKNOWLEDGEMENTS

First and foremost, I would sincerely like to express my great gratitude to my supervisor, Winthrop Professor Liang Cheng, for giving me this opportunity to pursue my PhD study at UWA. During my four years' research work, his guidance and support have been of inestimable importance to me. His approach of rigours attitude with data, determined in seeking the truth and always providing encouragement has a continuous influence on my work as a scientist.

I owe a special debt to Dr Ming Zhao, whom I respect deeply for his broad knowledge and dedicated mind in research. His generous help and guidance have paved my way to the finishing of my PhD. Special thanks also go to Dr Hongwei An, who has always been there to provide help on the various research problems that I encountered whenever I knock on his office door. I am very grateful to Winthrop Professor Andrew Bassom for revising my papers and pushing me to revise the draft as soon as possible so that I have one paper presented in this thesis being published and another being under review at the present stage. My gratitude is also extended to Professor Chengwang Lei, who generously helped with my research and shared his life experience during his visit at UWA.

In addition, I would like to thank Patrick Morgan for providing me with an idea that finally grows into one of the main chapters in this thesis. I consider it a truly privilege to have worked alongside my colleagues from Liang's group. There have been so many who have influenced my thoughts that it is difficult to mention them all. However, I would like to single out Wei He, Feifei, Mehran, Zhihui, Wei Sun, Xu, who are all very intelligent while such a joy to befriend with.

I particular want to thank Dr Xianhua Liu for introducing UWA to me, without which I might not start my PhD studies here. I regard Dr. Liu as my family in Australia, and I am very grateful for his continuous support and care ever since my first days in Perth. His being unselfish, warm-hearted and pure-minded always serves as a good model for me to follow.

Although he had also been kept busy pursuing his own PhD during the same period, he had spent much time assisting me from all aspects of life. He has always been a wonderful companion and changed my life in UWA in the most positive way.

Last but not the least, my deepest gratitude goes to my dear mother (Mingzhen zhao) and father (Shengqi Yang), and all family for their endlessly spiritual support, love and concern. To all of you, I dedicate this dissertation.

LIST OF PUBLICATIONS

Journal

1. Yang, K., Cheng, L., An, H., Bassom, A. and Zhao, M. (2013). "The effect of a piggyback cylinder on the flow characteristics in oscillatory flow". *Ocean Engineering*. Volume 62, P45-55, ISSN 0029-8018, http://dx.doi.org/10.1016/j.oceaneng.2013.01.017.

2. Yang, K., Cheng, L., An, H., Bassom, A. and Zhao, M. (2014). "Effects of an axial flow component on the Honji instability". *Journal of Fluids and Structures*. (Accepted)

Conference

1. Yang, K., Cheng, L., An, H., and Zhao, M. (2011). "Direct numerical simulation of effects of small angle of incidence on Honji instability." *The ASME 2011 30th International Conference on Ocean, Offshore and Arctic Engineering: OMAE 2011,* Rotterdam, The Netherlands.

2. Yang, K., An, H., Cheng, L., and Zhao, M. (2011). "Oscillatory flow around a pair of cylinders of different diameters." *The Sixth International Conference on Asian and Pacific Coasts: APAC 2011,* Hong Kong, China.

3. Yang, K., Cheng, L., An, H., Bassom, A. and Zhao, M. (2012). "Effects of axial flow on 3D steady streaming at low *KC* number." *18th Australian Fluid Mechanics Conference,* Launceston, Australia.

TABLE OF CONTENTS

LIST OF FIGURES

LIST OF TABLES

NOMENCLATURE

2-D and 3-D: two-dimensional and three-dimensional.

A: amplitude of oscillation for fluid particles.

C_D and C_M: dimensionless drag and inertial coefficients, defined by Morison's formula.

C_F: dimensionless in-line force coefficient.

CFD: computational fluid dynamics.

C_{Fint}: interference coefficient for the in-line force, defined as $C_{Fint} = C_{Frms}/C_{F\infty}$.

C_{Frms}: root-mean-square value of C_F.

C_L: dimensionless lift force coefficient.

$C_{L\infty}$: root-mean-square value of the lift force coefficient acting on an isolated circular cylinder.

C_{Lint}: interference coefficient for the lift force, defined as $C_{Lint} = C_{Lrms}/C_{L\infty}$.

C_{Lrms}: root-mean-square value of C_L.

C_p: dimensionless mean pressure coefficient.

D: diameter of the cylinder.

DNS: direct numerical simulation.

f: frequency of the oscillatory flow.

FDM: finite difference method.

FEM: finite element method.

FFT: Fast Fourier Transform.

FVM: finite volume method.

g/D: gap distance between the secondary cylinder and the main cylinder, defined in Figure 6.1.

K: shape factor for the cross-section of the cylinder, defined as the ratio of minor axis to the major axis of the elliptic cross section of the cylinder. K = 1 represents a circular cylinder.

KC: Keulegan-Carpenter number, defined in Equation 1.2.

KC_{cr} and β_{cr}: critical KC and β for the onset of Honji instability predicted by the experimental study of Sarpkaya [18].

KC_h and β_h: critical KC and β for the onset of Honji instability predicted by the theoretical study of Hall [17].

$L_{px,y}$: pressure coefficient with regards to two measurement lines $x/D = 0$ and $y/D = 0$.

N: number of oscillation periods, $N_i = 1, 2, 3, \ldots 200$.

N_{cy2D}: number of elements on the cylinder circumference in the cross section of the domain.

N_{cy3D}: number of 2-D mesh layers.

N_{p2D} and N_{e2D}: total number of nodal points and elements respectively in the cross section of the domain.

N_{p3D} and N_{e3D}: total number of nodal points and elements respectively in the 3-D domain.

PG-FEM: Petrov-Galerkin Finite Element Method.

P_s: reference pressure taken from the far field.

R(z): correlation coefficient, defined in Equation 2.24.

Re: Reynolds number, defined as $Re = UD/v$, where U is the mean velocity, D is the characteristic length of the cylinder and v is the kinematic viscosity.

SP: perturbation as a source term, defined as $SP = A*\text{Random}[0,1]*\sin(2\pi ft)$, where A is the amplitude to be specified.

t^*: $t^* = t/T - 200$.

t/T: normalised flow oscillation period, where t is the actual time, and T is the flow oscillation period.

$\bar{T}$: critical overall non-local Taylor number.

T_c: critical Taylor number for the onset of Honji instability.

u'_{zstn}: standard deviation of the non-dimensionalized axial velocity component u_z/U_{mx} at the recorded points along the cylinder span.

U_{mx}: normalised amplitude of the flow velocity in x- direction, in this work, $U_{mx} = 1$.

u_x, u_y, u_z: normalised flow velocity component, in x-, y- and z- directions respectively.

v: kinematic viscosity.

x, y, z: Cartesian coordinates.

Δd_r: radial extent of one typical Honji vortical structure.

Δd_z: axial extent one typical Honji vortical structure.

$\Delta e/D$: distance between the first nodal point and the cylinder diameter in the radial direction of the cylinder.

$\Delta z/D$: axial density along the cylinder.

α: angle of attack in plane parallel to the flow oscillation, defined as $\tan\alpha = u_z/u_x$.

α_0: angle of attack in the cross-sectional plane of the cylinder, defined as $\tan\alpha = u_y/u_x$.

α_c: critical value of α at which Honji instability is suppressed.

β: frequency number, or Stokes number, defined in Equation 1.3.

θ: angle defined to represent the circumferential locations on the cylinder.

λ: spacing between the vortex pairs formed under Honji instability.

ω_x, ω_y and ω_z: non-dimensional vorticity components with respect to x-axis, y-axis and z-axis, respectively.

CHAPTER 1

INTRODUCTION

1.1 Overview

The oil and gas industry has been a chief energy provider all over the world. This situation continues despite the efforts to develop alternative and renewable sources of energy (such as solar energy) to meet the increasing energy demand of human population. In the oil and gas industry, ever since the construction of the first offshore structure in the Gulf of Mexico in 1947, offshore production has increased tremendously and continued to expand. In offshore extractions, the problem relating to delivery of the petroleum resources is always most challenging and troubling. As a transporting channel, pipelines serve as the link between offshore production structures and onshore post-processing facilities. According to a worldwide survey by Pipeline & Gas Journal [1], a total of approximately 188,030 km of pipelines were planned or under construction up to January 2013. As pipelines are a major element to the oil and gas industry, the design, construction and maintenance of pipelines account for a large portion of the total cost of the whole industry.

Pipelines exposed to marine environments are subject to hydrodynamic influences that are quite often blamed for causing damage to the structures. Therefore, obtaining confidently quantified hydrodynamic forces and a good understanding of flow structures around pipelines are of vital importance to the entire oil and gas industry. In addition, with an increasing number of challenges arising from the fact that the extraction processes are extending to increasingly complex ocean environments and deeper seas, our needs to understand the fluid-structure interactions (especially fluids around pipelines) remain continuously unfulfilled.

The topic of fluid-structure interactions, closely related to the real industrial world of oil and gas extraction, goes to the classical and fundamental problems of flow behaviours around blunt bodies under various flow conditions. In relevant research, the practical

problem of pipelines under water is often represented by a physical model of cylindrical structures immersed in fluids. In practice, the environments that a pipeline is exposed to can be quite diverse. For research purposes, it is a common practice to divide the types of flow into a steady flow and an unsteady flow depending on the motion of fluid particles. If the flow remains constant with time it is steady, otherwise the flow is regarded as unsteady. In particular, if unsteady fluid motion shows periodic reversal it is terminologically referred to as an oscillatory flow.

Different flow regimes for either a steady flow or oscillatory flow can be predicted by studying the dimensionless characteristic governing parameters based on observations from previous experimental studies. The governing parameter applied for a steady flow around a cylindrical structure is the Reynolds number (Re), commonly but not uniquely defined as

$$Re = UD/v$$

1.1

in which U is the mean velocity, D is the characteristic length of the cylinder and v is the kinematic viscosity. The parameter Re shows the measure of the ratio of inertial forces to viscous forces of the fluid particles near the blunt body.

Since steady flows are not a major concern of the present thesis, here the resultant flow regimes for a steady flow with the increase of Re is mentioned only briefly. In general, the reported characteristics in different regimes for steady flow are the same, although the critical Re number marking the division between these regimes differ slightly in different studies [2-9]. For $Re < 40$ [7] or $Re < 49$ [6, 9], the flow remains two-dimensional (2-D) laminar. For a slightly larger Re, 2-D vortex shedding is first observed before the wake transits into a three-dimensional (3-D) flow. The critical Re leading to the 2-D to 3-D transition is disputable [2-9], but is generally regarded to be approximately 200. When Re is over 300, the flow is regarded as in the subcritical regime, where laminar boundary layer separation is observed while the wake becomes completely turbulent. The subcritical regime spans over a large range of Re from 300 to roughly 3×10^5 [7] (or from 300 to 2×10^5 [9]). Further increasing Re results in the critical regime (for Re in the range from 3×10^5 to 3.5×10^5 [7] or from 2×10^5 to 5×10^5

[9]), where the transition from laminar separation to turbulent separation is observed. Then the flow enters a supercritical regime where the boundary layer has partially become turbulent as Re falls between 3.5×10^5 and 1.5×10^6 [7], followed by an upper transition regime where the boundary layer is completely turbulent at one side for values of Re in the range $1.5 \times 10^6 < Re < 4 \times 10^6$ [7]. The supercritical regime and upper transition regime proposed by Sumer and Fredøe [7] were combined into a supercritical regime by Lei [9], who defined it as a regime which marks a turbulent separation for $5 \times 10^5 < Re < 3.5 \times 10^6$. A fully turbulent boundary layer is obtained on both sides of the cylinder in the final regime, namely, the transcritical [7] or post-critical [9] regime for Re over a value of about 4×10^6 [7] or 3.5×10^6 [9].

For an oscillatory flow, an additional governing parameter associated with the oscillation period arises. Although it was first derived by Schlichting [10], this parameter is referred to as the Keulegan-Carpenter number (KC) [11], with a general definition given as

$$KC = U_{m}T/D$$

<div align="right">1.2a</div>

where U_{m} is the maximum velocity of the oscillatory flow and T is the oscillation period. In particular, if the oscillation is sinusoidal, then

$$KC = U_{m}T/D = 2\pi A/D$$

<div align="right">1.2b</div>

where A is the amplitude of excursion of the fluid particles during one oscillation period. The expression given in Equation 1.2b explicitly shows the physical meaning of the KC number, which can be regarded as a length ratio of the relative orbital motion of fluid particles with respect to the width of the cylinder. In many studies on oscillatory flows, a frequency parameter (also known as the Stokes parameter or the Sarpkaya parameter, denoted by β) is adapted to replace the Re number. The definition for β is

$$\beta = Re/KC = D^2/\ vT.$$

<div align="right">1.3</div>

which was first introduced by Sarpkaya [12] and fully evaluated in Sarpkaya [13]. Behaviors of an oscillatory flow around a cylinder can then be determined by the two governing parameters, namely, KC and β. According to Equation 1.3, for given values of KC and β, one can easily recover the Re number from $Re = \beta \times KC$.

The flow behaviors under different combinations of KC and β (denoted as (KC, β)) have been documented to some extent. The resultant different flow regimes with variation of (KC, β) bear some similarities to that of the steady flow, in the sense that as the flow becomes more unstable, the flow transits from being 2-D laminar to chaotic turbulence; however, discrepancies in the flow behaviors under oscillation apply due to the effects of the reversing nature of the fluid particles in an oscillatory flow. In the following the resultant flow regimes obtained for an oscillatory flow with increasing values of (KC, β) are described briefly. At low values of (KC, β), the flow is laminar without generation of vortical structures. As the governing parameters increase, separation near the cylinder occurs, before the flow enters a turbulent regime where the flow particles are in chaotic movement. Between a purely laminar regime and a totally turbulent regime, flow experiences a 2-D to 3-D transition through a hydrodynamic instability in the flow near the cylinder surface, a phenomenon conventionally referred to as the Honji instability [14, 15]. As given in Sumer and Fredøe [7], the Honji instability regime is found in the interval of $1.1 < KC < 1.6$. With a further increase of KC, a pair of symmetric vortices attached to the cylinder can be observed (for $1.6 < KC < 4$). Higher KC ($4 < KC < 7$) than that breaks the symmetry of the attached vortices, and finally causes the onset of vortex shedding when KC is greater than 7. All the KC ranges given above are based on a constant Re of 10^3 [7].

Based on the intrinsically distinct flow regimes obtained at different combinations of (KC, β), relevant research has an extensive scope. Among these studies, two topics arising from heated discussions on oscillatory flow around cylindrical structures at low values of (KC, β) are the hydrodynamic instability causing the 2-D to 3-D transition and the vortex shedding regime. These two topics serve as the primary research interests of

the present thesis. In the following, a literature review is given regarding previous relevant studies on these two aspects.

1.2 Review of relevant literature

1.2.1 Hydrodynamic instability causing 2-D to 3-D transition

A summary of the various possibilities for the behaviours of near-cylinder flow at low values of (KC, β) is found in Tatsuno and Bearman [16]. Through experiments on a circular cylinder oscillating in a fluid at rest, they identified eight flow regimes including an associated 3-D flow instability along the cylinder in a KC-β plane for the range of 1.6 < KC < 15 and 5 < β < 160. An interesting phenomenon to be noted here is the onset of 3-D flow features, which occur during a 2-D to 3-D transition under the effects of the so-called "Honji instability", a phenomena first reported by Honji [14].

Honji [14] conducted a series of laboratory experiments on a circular cylinder immersed and transversely oscillated in quiescent water at relatively small values of KC (1.3 < KC < 3.9) and β (70 < β < 700). He found that the intrinsically 2-D flow field broke into 3-D when KC increased to over 1.2 to 2.4 (depending on β). The instability mechanism that gives rise to the 3-D flow manifests itself as a series of mushroom-shaped vortical structures distributed along the cylinder span. The mushroom-shaped vortical structures, forming two axial rows of counter-rotating vortex pairs, locate near the cylinder crown at planes normal to the direction of cylinder oscillation. The vortical structures originate from detachment of the water particles from the surface of the cylinder and rolling-up of the boundary layer during each oscillation period. Honji mentioned that the 3-D structures seemed to form under a centrifugal-type instability. The typical mushroom-shaped vortices can only be observed at a narrow range of small KC and β with further increasing of KC leading to the appearance of separation and turbulence. The critical boundary in the KC-β plane marking the onset of the instability was identified by Honji for 70 < β < 700.

Ever since its first introduction by Honji [14], the instability causing the 2-D to 3-D flow transition in the form of mushroom-shaped vortices has received extensive

academic attention which motivated further relevant studies through analytical development [17], physical experiments [15, 18] and numerical simulations [19-23]. One common concern of studies on the instability problem is obtaining the dependence of flow regimes on the governing parameters. Hall [17] conducted a linear stability analysis of the 2-D to 3-D transition problem under the assumption of sufficiently small *KC* and large *β*. Hall derived a formula for the threshold of the inception of the Honji instability, which is known as the "Hall line" (H-Line). Following Sarpkaya's [15] notation, the H-Line is given by

$$KC\beta^{\frac{1}{4}} = 5.778(1 + \frac{0.205}{\beta^{\frac{1}{4}}} + \cdots).$$

1.4

At (*KC*, *β*) values above the H-Line the instability mechanism is operative and flow becomes unstable; below the Hall line the flow pattern assumes a featureless 2-D laminar form. Hall showed that the prediction given by Equation 1.4 for the onset of the instability was in good accord with the available experimental results [14, 15] and attributed the instability to be a Taylor-Görtler type.

In due course, Sarpkaya [15] suggested the now universally accepted terminology "Honji instability" for the instability mode first reported by Honji [14], based on the observations of its significant differences from the Taylor-Görtler instability. Sarpkaya conducted extensive experiments to further extend the parameter range to higher *β* values (roughly $5.5 \times 10^3 < \beta < 1.35 \times 10^6$). In addition to providing flow visualizations for demonstrating the flow structures, Sarpkaya also studied the possible effects of the Honji instability, separation and turbulence on the resultant in-line force coefficients obtained under the Stokes-Wang (S-W) theory. He found that the S-W theory only holds true for a 2-D laminar flow (when *KC* < 2 and *β* > 1000). When 2-D flow transits to 3-D under the effects of the Honji instability, the measured drag coefficient deviates from the S-W theory abruptly. It was also found that effects of the Honji instability on the resultant drag coefficient are stronger than the effects of transition to turbulence. Based on his observations, Sarpkaya divided the *KC*-*β* plane to present four flow regimes and discussed the coefficients and the associated flow structures in each regime.

A much more elaborate demonstration of flow structures under the Honji instability is given in a follow-up study by Sarpkaya [18], which covered a governing parameter range of $0.02 < KC < 1$ and $10^3 < \beta < 1.4 \times 10^6$. Through extensive flow visualizations from the experiments, Sarpkaya reported that the H-Line only stands for the instability with the typical mushroom-shaped vortical structures that could be sustained throughout the whole flow period. He observed the occurrence of other forms of early 3-D structures at lower KC than required by the H-Line. The threshold for the onset of this type of early 3-D structures based on Sarpkaya's experimental results follows a relation of

$$KC\beta^{\frac{2}{5}} = 12.5$$

1.5

which represents a "Sarpkaya Line" (S-Line). The refined KC-β map with both the H-Line and the S-Line to the first order accuracy is plotted in Figure 1.1 for the range of $0 < KC < 0.8$ and $10^3 < \beta < 10^6$. Sarpkaya reported that the S-Line (KC_{cr} and β_{cr}) stands for the inception of an instability that causes a 2-D flow to transit to 3-D; while the H-Line (KC_h and β_h) marks the points where the mushroom-shaped vortical structures persist with their most developed forms throughout each oscillation period. According to Figure 1.1, the two lines divide the whole KC-β map into three sections, representing three distinct flow regimes. Firstly, on the left and below the S-Line, the flow falls in a stable regime with either no 3-D features observed, or those generated (most likely at high-velocity moments during each oscillation period) being too weak to survive the low-velocity moments. Secondly, on the right and above the H-Line, the flow is in a strong unstable regime, where chaotic behaviours of vortices eventually lead to separation and turbulence. The structures of separation were studied by Sarpkaya [24] for KC varying between 0.6 to 5 at a constant β value of 6815; positions of the separation points and separation angles were recorded. Thirdly, in the area between the H-Line and the S-Line, the flow is in an "unstable transition region", where quasi-coherent structures (QCS) are observed with various shapes and changing sizes. Based on the identification of the QCS, Sarpkaya then proposed a correction for the nomenclature for the regular mushroom-shaped vortical structures by referring to them as the "coherent structures (CS)" (instead of the "Honji instability"), in comparison to

the QCS observed between the S-Line and H-Line. In the present thesis, it is regarded that the terminology "Honji instability" can be reasonably used for a general indication of the instability mechanism causing the transition from a 2-D flow to a 3-D flow.
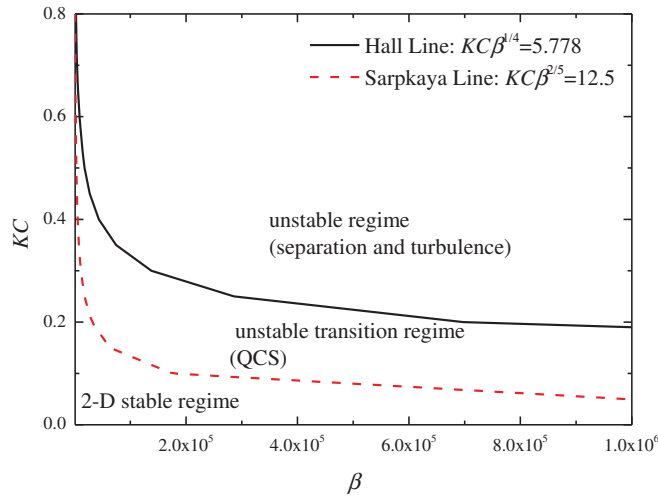
Figure 1.1 Dependence of KC and β for Hall's formula and Sarpkaya's formula in the range of $0 < KC < 0.8$ and $10^3 < \beta < 10^6$.

Sarpkaya has proposed repeatedly [18, 25] a necessity to further investigate the coherent and quasi-coherent structures (CS and QCS) formed at any possible point on the KC-β map through physical experiments or numerical simulations for a better understanding of the evolving turbulence. It is known that conducting precise physical experiments on hydrodynamic instability problems (e.g. the Honji instability) is not straightforward and can encounter various practical challenges. Fortunately, the advent of modern computational tools makes numerical simulation an increasingly preferable choice for investigators due to its accuracy, economic efficiency and convenience. In particular, direct numerical simulation has become a very useful tool for investigations of hydrodynamic instability problems that are often difficult to model in the laboratory. In the following discussions, several numerical simulations regarding the Honji instability will be mentioned.

Zhang and Dalton [19] studied oscillatory flow past a fixed cylinder using a combined finite-difference/spectral-method [26, 27]. They kept the frequency number at $\beta = 196$ and observed 2-D laminar flow at $KC = 1$ and appearance of the 3-D structures at $KC =$

2. Further increasing *KC* results in separation and chaotic behaviours of flow at *KC* numbers of 3.4 and 4, respectively. Using computational visualization techniques, Zhang and Dalton demonstrated plots of typical Honji vortices distributing along the cylinder's span represented by vorticity iso-surfaces. Their findings agree well in accordance with the previously mentioned *KC-β* map and their flow visualization pictures showing the vortical structures are very similar to that experimentally observed by Honji [14]. Although the study of Zhang and Dalton only considered a few (*KC*, *β*) points, it provides us with early results on Honji instability obtained by numerical models.

Another example of computer-visualized Honji structures is given by Lu and Ling [28]. The governing parameter they covered was *KC* = 2 and *β* varying from 100 to 600. They demonstrated the instantaneous vortical structures through vorticity contour plots, and were also able to obtain the typical Honji vortices in the form of mushroom-shape counter-rotating vortices distributing along the cylinder span alternatively. In addition, they also studied the non-dimensionalized force coefficient for the in-line force obtained through the Morison [29] equation for varying *KC* number at a constant *β* of 200.

At the same governing parameter range as that of Lu and Ling [28], i.e. *KC* = 2 and *β* = 100 ~ 600, more detailed flow structures of the Honji instability were presented by An et al. [21], through direct numerical simulations using the Petrov-Galerkin finite element method. In their study, An et al. captured the three distinct flow regimes depending on *β*: 2-D laminar flow at *β* = 100, typical mushroom-shaped coherent Honji vortices for *β* in the range of 150 and 550 and turbulence flow at *β* = 600. The key characteristics of flow evolution during the development of the instability as well as the instantaneous flow structures under the three flow regimes were demonstrated through flow visualizations. In addition, through a dimension analysis of the governing equations, An et al. was able to demonstrate that the spacing (denoted as *λ*) between the neighbouring mushroom-shaped vortex pairs has a stronger dependence on *KC* than on *β*; they then proposed an empirical relationship between *KC* and *λ*. In addition to discussions on flow development and instantaneous flow behaviours, the steady streaming flow was also evaluated to show the time-averaging effects on the flow field. The results showed that a 3-D steady streaming was only observable for the stable Honji

vortex regime; beyond this range, either reducing β to result in the 2-D potential flow or increasing β to cause the chaotic flow would result in a 2-D steady streaming field. The reason for resulting in a 2-D steady streaming field at larger β cases where strong interactions and movements of the unstable vortical structures were observable for the instantaneous flow field was attributed to the cancellations of the overall three-dimensionality in the whole field when applying a long-time averaging. This study is of most relevance to the Honji instability studies covered in Chapter 4 and Chapter 5 of the present thesis, as shall be mentioned later.

Also considering low values of governing parameters, Elston et al. [20] explored the various instability modes in the range $KC < 10$ and $\beta < 100$ using direct numerical simulations combined with a Floquet analysis. The Floquet analysis is frequently used to tackle the instability problem for causing the 2-D to 3-D flow transition. They found that the symmetric breaking flow could be either 2-D or 3-D for the (KC, β) values concerned, and that for a β value roughly larger than 50, a 3-D instability arose primarily in the 2-D symmetric base flow. Elston et al.'s study indicated that the demarcation line dividing the absolute 2-D flow with the early 3-D unstable flow should cross the H-Line at $\beta \approx 50$. However, as shown in Figure 1.2, the S-Line according to Sarpkaya's empirical formula and the H-Line from Hall's analytical solution crosses at $(KC, \beta) = (1.6, 171.5)$. It should be remembered that Sarpkaya [18] obtained the empirical formula for the S-Line based on experimental observations where the 3-D flow structures failed to be captured. Also, Sarpkaya's experiments were conducted at high values of β ($10^3 < \beta < 10^6$), and thus may not be suitable for predicting the 2-D flow field at low values of (KC, β) such as that concerned by Elston et al. [20].
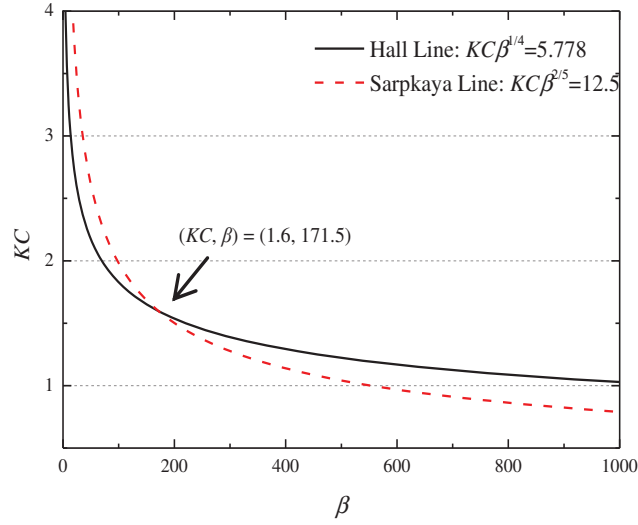
Figure 1.2 Dependence of KC on β for Hall's formula and Sarpkaya's formula in the range of $0 < KC < 4$ and $0 < \beta < 10^3$.

Suthon and Dalton [22] extended numerical simulations on Honji instability to high values of β (β = 1035, 6815 and 9956 for $0.1 < KC < 2.0$). They applied a finite-difference spectral-method scheme to discretise the dimensionless governing equation system of the primitive variables form, i.e. the Navier-Stokes equation and the continuity equation. In order to facilitate a better comparison with experimental observations, Suthon and Dalton used streaklines rather than the conventional vorticity iso-surfaces for visualizing the flow. The most prominent contribution in their study was providing an insight into the mechanism that forms and sustains the Honji instability. The origin of the 3-D vortical structures under the instability regime was related to both the boundary layer and the outer flow. They provided elaborate demonstrations for the vortical structures around the circumference, which are in the form of 3-D dipole tubes and are mushroom-shaped at each 2-D circumferential plane. The evolution of the vortical structures considering the mechanism of the generation and sustaining of the Honji instability in relation to the boundary layer as well as the outer flow was also discussed.

Subsequently, in a follow-up study [23], Suthon and Dalton looked deeper into the mechanism for causing the Honji instability by quantifying a critical criterion for triggering of the instability. Through careful evaluation and analysis of the numerical

results obtained through a similar method to their earlier study mentioned above [22], they found that the Honji instability is caused by a mechanism of the Lord Rayleigh type [30], but is different from the Taylor [31], Dean [32] and Görtler [33] types. This finding supported the suggestion of Sarpkaya for giving the instability its own name – the "Honji instability". Suthon and Dalton [23] also mentioned that the requirements for trigging the Honji instability involved two aspects, i.e. both the Lord Rayleigh's stability criterion of $d\Gamma^2/dr < 0$ and the critical values of (KC, β) (so far the best estimation for the critical values for different flow regimes is predicted by the H-Line and the S-Line) must be met.

1.2.1.1 Effects of angle of attack (α)

Although Honji instability at various (KC, β) values has undergone extensive investigations, the understanding of the Honji instability is still relatively limited with previous relevant studies exclusively considering the limiting situation when the incoming oscillatory flow is perpendicular to the cylinder. To the author's best knowledge, investigation of the Honji instability under possible effects of an oblique inflow has attracted little attention, though in practical circumstances oscillatory flow is unlikely to be directed precisely at right angles to the obstructing body. The oblique angle, or angle of attack, is often defined as the angle between the free stream and the perpendicular flow component, as shown in Figure 1.3.
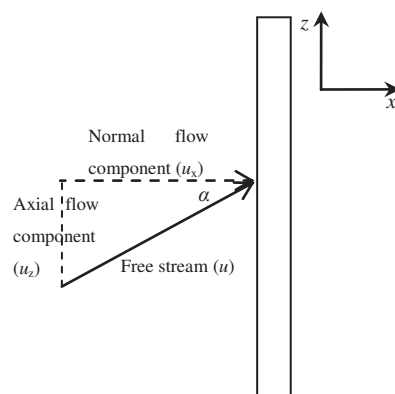
Figure 1.3 Definition sketch for oblique inflow with an angle of attack α.

There exist some previous studies on inclined flow around a yawed circular cylinder, however most of them consider the effects of flow incidence angle on hydrodynamic

forces and vortex shedding phenomena at relatively large values of (KC, β), and very often are concerned with steady flow conditions [34-42]. Among these studies, one research worth mentioning is that of Zhao et al. [41]. Using a Petrov-Galerkin finite element method, Zhao et al. studied the sinusoidal oscillatory flow around a circular cylinder at different oblique angles in the range of 6.75 < KC < 30 and a constant Re of 2000. Vortex shedding can be observed for the interested governing parameter range, with the shedding mode determined by the value of KC. Zhao et al. gave a discussion on the flow behaviours and the associated hydrodynamic forces under effects of varying values of angle of attack for the calculated vortex-shedding modes. They found that the oblique angle exerted little effect on the resultant vortex shedding modes. In addition, through evaluations of the calculated in-line and lift forces, their results indicated that the Independence Principle (or the Cosine Law[1]) [34] is applicable for the in-line force at an angle of attack up to 60°, and for the lift force at an angle of attack as large as 45°. However, at an oblique angle of 60°, both the maximum value and the mode-averaged value of the non-dimensionalized lift force showed some differences from that obtained for a perpendicular flow, indicating that the Independence Principle is violated for the lift force for an angle of attack at 60°.

1.2.1.2 Effects of shape ratio (K)

In the case of an oblique inflow, the free stream sees an elliptic cross-section. A consideration then naturally arises for the situation when the cylinder is of an elliptic shape. To the best knowledge of the author, possible alterations on the Honji instability brought by variation in cross section of the cylinder have never been covered before.

Different studies on elliptic cylinders at low Reynolds number have been conducted, although not specifically on the topic of Honji instability. Many analytical studies for

---

[1]The Independence Principle, or the Cosine Law, states that for a cylinder placed in an oblique flow, the normalized force coefficients in the direction perpendicular to the cylinder are identical to that obtained for a cylinder normal to the flow.

flow around elliptic cylinders are conducted at low Reynolds numbers either in uniform flow, or in oscillating flow but not in the Honji regime. For a steady flow, Shintani et al. [43] reported an analytical study on a steady flow approaching an elliptic cylinder perpendicularly in the limit of $Re \to 0$ ($Re = 0.1$). They applied a matched asymptotic study based on Umemura [44], and discussed in particular the effects of both the shape factor K (the ratio of minor axis to the major axis of the elliptic cross section of the cylinder) and fluid inertia on the resultant flow structures. For a varying shape factor including a limiting case of zero thickness (viz the ellipse becoming a flat plate), they found that the twin vortices spread wider as the cross-section of the cylinder became flatter with a smaller K.

In addition to the shape factor K, another influencing factor considered in studies regarding flow around elliptic cylinders is the direction of the incoming flow with respect to the ellipse. A cross-sectional angle of attack, α_0 (note, different from the axial angle of attack α defined for the previously mentioned oblique inflow problem) is then defined by an angle between the free stream and the major axis of the elliptic cross-section. There are many theoretical predictions on elliptic cylinders considering oscillating flow approaching the cylinder with specific values of α_0. For example, in Taneda's [45] comprehensive study on basic unsteady flows around 2-D bodies, he attempted a theoretical solution for a cylinder of K = 0.5 oscillating at $\alpha_0 = 30°$ in a flow at rest, and gave visualizations of the flow field using streamline patterns. Taneda reported that, for an elliptic cylinder oscillating in a uniform flow, there exists an 'isolated permanent dead water region' in the downstream. Another analytical study given by Badr [46] investigated an elliptic cylinder with K = 0.6 and α_0 at either 30° or 60°, in an oscillatory flow at low Reynolds number from 10^2 to 10^3 and *KC* number of 2 and 4. Badr's study presented the evolution of the developed flow structures near the cylinder surface using streamlines and vorticity distribution. Hydrodynamic forces were also considered by giving distributions of pressure and force coefficients.

Numerical studies on elliptic cylinders under the Honji instability regime are also rare. Evaluation of the few previous papers on oscillatory flow around elliptic cylinders shows that, while the flow is likely to undergo a 2-D to 3-D transition for *Re* value between $10^2 < Re < 10^3$, most numerical simulations found in the literature only

assumed the flow to be 2-D. This is mostly because of the restrictions of inadequate computational resources at the time such studies were conducted. Examples include Nair and Sengupta [47] for uniform flows at Re = 10,000, and a follow-up study of Nair and Sengupta [48] at Re =3000 and 10,000. Nair and Sengupta [47] conducted a 2-D simulation to study the onset of asymmetry in the flow field (resulting from flow instability) and found that, compared with a circular cylinder, the asymmetry developed earlier around an elliptic cylinder for a perpendicular incidence (i.e. $\alpha_0 = 0°$). They also found that the asymmetry development had a higher rate as the ellipse became thicker (i.e. larger K). Their later study [48] of a 2-D direct numerical simulation further extended their previous study [47] by introducing the influences of the Re number, the angle of attack α_0 and the shape ratio K of the ellipse.

With the boost of supercomputing technology in recent years, an increasing number of 3-D simulations have emerged. The laminar 3-D transition of a uniform flow around an elliptic cylinder was discussed by Sheard [49], who studied the case under Re = 500 and an incidence angle α_0 between 0° to 90°. In particular, it is worthwhile mentioning an interesting application of a 3-D simulation for a higher Re value proposed by Flynn and Eisner [50], which related an elliptic cylinder in flow to the scenario of a human body immersed in contaminant airflows. In their study, Flynn and Eisner regarded the human form as elliptic in the cross section. With a Re number as high as $Re = 1.35 \times 10^4$, they applied a k-epsilon model in the finite element package called Fidap, and studied the resultant turbulence kinetic energy. They were able to give a verification and validation study for the time-averaged velocity field in the very near wake. Although interesting results are provided by the studies just mentioned along with other similar research on an elliptic cylinder exposed in various types of flows (examples including [51-53]), no previous 3-D simulations have been found regarding elliptic cylinders under the Honji instability marking the transition from 2-D flow to 3-D flow, which is our present interest.

To the best knowledge of the author, the linear stability analysis reported by Hall [17] is the only study considering the Honji instability around an elliptic cylinder. Hall produced a dependence curve of the critical Taylor number on the shape factor K and angle of attack α_0 (see Figure 4 and Figure 5 in Hall [17]) and predicted that the flow

would become unstable at different circumferential locations depending on the shape of the cylinder and the incidence angle α_0. In particular, for the case of $\alpha_0 = 0°$, Hall found that flattening of the cross-section of the cylinder (by decreasing K) inhibits the Honji instability. In addition, as the shoulders (upwind and lee-wake sides) of the cylinder become sharpened at smaller K values, the fluids near the shoulders may break into a 3-D instability at governing parameters lower than those needed for a 3-D instability to develop near the crown of the cylinder. Hall's theory was derived in the limiting case of small *KC* and large β without consideration of the non-linear effects. An in-depth discussion on Hall's theory is covered in Chapter 5 considering oscillatory flow around an elliptic cylinder.

1.2.2 Flow behaviours and hydrodynamic forces in vortex shedding flows

Understanding the flow structures around and the fluid induced forces on a single cylinder in an oscillatory flow under the vortex shedding regime is of both academic as well as practical importance. Therefore, this type of flow has always been a heated topic and undergone extensive investigations both experimentally and numerically [21, 54-62]. An accessible summary of some interesting phenomena with respect to flow structures and vortex properties has been given by Zdravkovich [63].

The relation between the near-cylinder flow structures and the resultant hydrodynamic forces has been documented by previous researches. Zdravkovich and Namork [64] and Sarpkaya [25] have reported that an asymmetric wake resulted from vortex shedding and convection may cause the lift force to increase. Williamson [56] conducted experiments on a sinusoidal flow around both an isolated cylinder and a pair of identical cylinders in a subcritical flow regime, and found that the number of large vortices being shed in each half cycle is closely associated with the magnitude and frequency of the measured lift force.

Compared with the isolated cylinder case, the understanding of the resultant hydrodynamic forces for a common application of a dual-cylinder system with either identical or different diameters remains far from complete [65], especially considering that many of the investigations of flow around two neighbouring cylinders are concerned with steady flow conditions. Examples include the 2-D numerical studies of

16

Zhao et al. [66] (at a low *Re* of 500, with respect to the main cylinder) and Zhao et al. [67] (for a turbulent flow at high *Re* of 5×10^4) for steady flow past a pair of cylinders of differing diameters; in both studies, the properties of the force coefficients and vortex shedding patterns were discussed as the smaller cylinder (or the piggyback cylinder) was moved relative to the larger. Zhao et al. reported that the key factors influencing the flow field around a pair of cylinders include the gap ratio, the diameter ratio and the direction of the incoming flow.

For oscillatory flow scenarios, Williamson [56] conducted experiments on two identical cylinders moving harmonically in an otherwise quiescent fluid, and reported that, when the two cylinders were in close proximity, large alteration of the vortex-shedding patterns was observed, which then resulted in a great change in both the lift and in-line forces. Another study by McIver and Evans [68] provided an approximation method for calculating forces on fixed vertical cylinders in a plane wave, and reported that the interactions between the cylinders could have strong influences on the flow structures and the resultant fluid forces. Less is known about the case when the two neighbouring cylinders are of unequal diameters. Carstens and Sayer [65] used a linear potential theory to study the hydrodynamic interactions and gave their results in terms of the added mass and damping between two unequal vertical cylinders in oscillatory flow. Williamson [69] investigated the fluid forces on two neighbouring cylinders with unequal diameters, and focused on ascertaining the hydrodynamic interference effects of the flow field of the larger cylinder on the smaller one.

1.3   Research objectives

As can be seen from the literature review given above, although extensive studies have been conducted on oscillatory flow around cylindrical structures covering a large range of governing parameters, understanding of the flow behaviors subject to certain conditions remains far from complete. The incompleteness lying in the present knowledge of these practically important problems has motivated the research presented in this thesis, of which the main objectives are described briefly in the following subsections.

1.3.1 **For the hydrodynamic instability**

Understanding the Honji instability is of both academic as well as industrial importance in that: the flow experiences a fundamental change as it transmits from 2-D to 3-D, resulting in substantial modifications of flow structures which will then alter the hydrodynamic forces exerted on the underwater cylinder. Careful examination and clear understanding of the variations of flow structures near the cylinder provides information on intrinsic mechanisms and physical explanations for the transition process, and is therefore a prerequisite for force evaluation and other studies. However, as discussed in Section 1.2.1, previous studies on Honji instability are still rare and limited, presumably due to the fact that, for one thing, it is hard to be achieved through laboratory experiments; for another, conducting numerical simulations on Honji instability requires a huge amount of computer resources in order to reveal the delicate flow structures formed during the 2-D to 3-D transition.

This thesis, with the aid of powerful supercomputers, provides a numerical study to comprehensively investigate the Honji instability under conditions commonly encountered in practice. The study on Honji instability considers two aspects under which the attributes of the near-cylinder fluid structures are likely to be affected. First, the effects of an angle of attack are evaluated to examine the influences of obliqueness of the incoming flow. Second, the cross-sectional shape of a cylinder is investigated, and the resultant flow fields under different elliptic cylinders with different flatness are discussed.

1.3.1.1 Objective 1. Evaluating the effects of angle of attack (α)

One primary aim of the present study is to extend our understanding of the Honji instability to when the incident flow is slightly oblique to the cylinder, i.e. at a small angle of attack (α). Oscillatory flow oblique to an isolated cylinder is examined when the flow transits from 2-D to 3-D under the effects of the Honji instability. The major concern is to gain a detailed description of the effects of an oblique inflow on the resultant flow evolution as well as the instantaneous flow field. In addition, possible explanations on the observed findings of the obliqueness effects will also be given.

1.3.1.2 Objective 2. Evaluating the shape effects of an elliptic cylinder (K)

Arising from a geometric analogy with the oblique inflow case, the resultant flow field for an elliptic cylinder with different shape ratios are discussed under the Honji instability regime. The main aim is to provide detailed flow visualizations for the Honji vortical structures (namely, the QCS and the CS) near an elliptic cylinder in order to reveal the effects of the flatness of the cylinder for the cases evaluated. Numerical results obtained for elliptic cylinder cases provide a first-ever attempt to validate Hall's [17] theory considering the elliptic effects on the instability causing the 2-D to 3-D transition. Possible reasons for inducing the shape ratio effects are also explored.

1.3.2 **For the dual-cylinder system in vortex shedding regime**

As mentioned in Section 1.2.1.2, effects of the presence of a nearby smaller cylinder on the flow patterns and fluid forces of the main cylinder under oscillatory flow conditions are still unclear despite their apparent engineering relevance. Existing numerical studies regarding steady flow at low *Re* or oscillatory flow at low (*KC*, *β*) around a dual-cylinder system are dominated by calculations using 2-D direction numerical simulations, for which Lei [9] has provided a summary of the key outcomes, plus an evaluation of the 2-D and 3-D modelling.

1.3.2.1 Objective 3. Evaluating the effects of a nearby smaller cylinder

This thesis also provides an investigation on flow behaviours around two neighbouring cylinders of unequal sizes at low values of (*KC*, *β*) using 2-D numerical simulations. The (*KC*, *β*) range concerned for the dual-cylinder study leads to a vortex shedding regime. This particular research aims to address the influences of a nearby smaller (piggyback) cylinder on the resultant flow fields and hydrodynamic forces on the primary cylinder. This objective relates directly to a practically important problem of prediction of possible force alterations caused by the existing of a piggyback cylinder near the main cylinder.

1.4 Thesis outline

A brief overall structure of the present thesis is given in Figure 1.4. The background information and motivations for conducting the research work presented in this thesis are covered in Chapter 1. Subsequently, the theory and the methodology applied to conduct the calculations of the study are introduced in Chapter 2 and Chapter 3. Following that, main results from calculations and associated discussions that serve the three objectives listed in Section 1.3 are presented in Chapter 4, Chapter 5 and Chapter 6, respectively. The thesis then finalises with main conclusions summarised in Chapter 7 along with some suggestions for relevant future studies. A more detailed outline for the major body of the thesis is given as follows.

- In **Chapter 2** the methodologies used in this research are described in detail. The numerical scheme and validation of the numerical method are presented. The mathematical theory and the finite element method adopted in the computer programs are explained, and a mesh validation is conducted to evaluate the influences of mesh density on the calculated results, based on which a most appropriate mesh was chosen.

- **Chapter 3** introduces a perturbation method to be applied to selected cases for the aim of accelerating the development of the instability (for the wake 3-D cases) as well as checking the convective instability of the flow field (for confirming the obtained 2-D flow field).

- **Chapter 4** concerns the effects of an axial flow component on the Honji instability, where the modification of the development of the instability as well as the resultant flow structures under different values of angle of attack (α) are discussed.

- Following the previous chapter, **Chapter 5** is then devoted to consider the influences of the cross-sectional shape of an elliptic cylinder on the Honji instability. Flow behaviours under different values of the shape ratio of the cylinder's cross-section are described and explained. The resultant flow fields under the two geometrically similar scenarios are compared. In addition, evaluations of Hall's [17] theory are discussed using the results obtained.

- **Chapter 6** deals with a 2-D numerical simulation on a dual-cylinder system of unequal sizes for the aim of investigating the alterations of the resultant flow fields as well as hydrodynamic forces of the main cylinder under the effects of a smaller cylinder in the vicinity.

- Finally, main findings arising from the present study are briefly summarised in **Chapter 7**. Some final remarks and suggestions for future studies are also presented.

Chapter 1.

Overall introduction & thesis objectives

Oscillatory flow at low values of (KC, β)

Hydrodynamic instability causing 2-D
to 3-D flow transition

(3-D)

Vortex shedding regime

(2-D)

Chapter 2 & 3.

Numerical method

Objective 1.

Effects of angle
of attack

Geometrically

analogous

Chapter 4.

Objective 2.

Effects of shape
factor

Chapter 5.

Objective 3.

Effects of a piggybacking
cylinder

Chapter 6.

Chapter 7.

Final remarks and future work

Figure 1.4 Sketch showing thesis structure and organisation.

CHAPTER 2
METHODOLOGY

2.1   Aim of this chapter

In this chapter, we will first briefly give some general background information in research methods for fluid studies. Then we will focus on providing detailed information on the specific numerical method applied in the present study.

2.2   Introduction

There are mainly three typical approaches to conduct research concerned with behaviours of fluid flows, namely, physical experiments, theoretical analysis and numerical simulations. The earliest and currently still most widely adopted method is conducting physical fluid experiments in a laboratory. Early attempts to study the flow behaviours by conducting experiments provide us with some fundamental concepts and understanding about the important basics. Another conventional approach is to produce mathematical solutions. The analytical or theoretical solutions are able to produce satisfactory descriptions of the flow behaviour for some simple cases such as potential flows. However, the limitation of analytical solutions is that this method is only valid for some specific or limited cases, or has to be applied under certain simplifications (such as linearization), due to the complexity resulted from the non-linear nature of the real problem. Then numerical treatment of various flow problems began to emerge with the advent of computers in the early 1950s. The theory behind numerical modelling is referred to as computational fluids dynamics (CFD), which is based on understanding and appropriate mathematical processing of the governing equations along with properly-applied boundary and initial conditions. Ever since it was proposed, numerical simulation method has been a much interested topic and developing fairly fast. This is probably because of its handiness and time-and-cost efficiency that keeps improving with the huge growth of computer power in recent years.

The basic tools for CFD mainly include finite difference method (FDM), finite element method (FEM) and finite volume method (FVM), listed according to the time sequence of their origins. Comparing between these methods, FDM is acknowledged to be simple in formulation and computation, and therefore is chosen by the majority. However, with current development of the FEM along with the increased computer capacity, FEM has seen an increasing popularity in recent years. The formulation of FVM is related to both FDM and FEM. The three methods can be used both individually and with combined knowledge. In fact, because of evident benefits, there is a trend in recent years to combine these methods when solving a certain problem. However, it should be noted that to the present, there are still unsurpassable limitations in all three methods mentioned above. One example is the numerical treatment of high-Reynolds-number flow using direct numerical simulation, which would involve enormous calculations because of mesh requirements and is still unattainable at the present stage.

In this thesis, FEM is adopted for calculations of the fluid field and therefore is our focus of discussion from now on. After the initial introduction and application of FEM on structural analysis in the 1950s, this method began to be used to simple flow problems, first seen with Zienkiewicz and Cheung [70]. Various improved approaches and methods were then proposed which facilitated the evolvement of FEM. Based on whether the weighting functions are the same as the trial functions or not, there are the Galerkin methods and the weighted residual methods. Examples for the Galerkin methods (weighting functions the same as the trial functions) are the streamline upwind Petrov-Galerkin method ([71], [72]) and Taylor-Galerkin methods [73]. Examples for weighted residual methods (weighting functions different from the trial functions) include spectral element methods [74], least square methods [75] and finite point method [76], etc. The method used by this study is the streamline upwind Petrov-Galerkin FEM, as will be discussed in detail later on.

The incompressible flow concerned here oscillates around blunt bodies at low Re number. Specifically, our interests fall in studying the flow behaviour in the regime where the 2-D to 3-D transition occurs due to hydrodynamic instabilities. For an intrinsically unstable flow in practice, transition to 3-D flow occurs because of small 3-D disturbances. There are obvious advantages in studying fluid instability problems

numerically rather than through physical experiments. This is because it is greatly challenging to try to control the experimental conditions for instability studies, as the marginal fluid field is very sensitive to small disturbances, which are almost impossible to avoid completely in physical experiments. It is challenging to distinguish the 3-D behaviours resulted from the intrinsic instability within the flow and those due to unwanted environmental influences. There are numerous possibilities for disturbing the stable flow field in actual flow experiments, such as non-uniform incoming flow, presence of surface roughness and running conditions of the experiments. However, these issues do not exist or can be controlled for numerical simulations.

2.3 The numerical scheme

In this study, the oscillatory flow field is calculated by solving the Navier-Stokes equations using a streamline upwind Petrov-Galerkin Finite Element Method (PG-FEM). Direct numerical simulation (DNS) is conducted by simulating viscous flow without turbulence modelling. The current thesis adopts a calculation model previously developed by Zhao et al. [40] in FORTRAN 90. The simulations are conducted on the high-performance supercomputer cluster provided by iVEC supercomputer facility in Western Australia. The efficiency of the calculations is greatly increased by applying the parallel-computing technique based on OpenMPI, namely, the message-passing interface for the parallel processing. The accuracy of the present method has been validated in a number of previous projects [21, 40, 61, 62, 66, 67, 77-83] it has been applied to, as shall be mentioned later.

2.3.1 **The physical model**

The physical problem concerned in this study is the behavior of an oscillatory flow around a smooth fixed cylinder of infinite length at low *KC* and *β* numbers. The physical model is represented by a computational domain shown in Figure 2.1. Flow past a cylinder of infinite length is simulated by a finite domain and a periodic boundary condition at the two ends of the cylinder. All calculations were performed on a domain of size 40*D* × 20*D* ×4*D*, with 40*D* in length (flow direction), 20*D* in width (cross flow direction), 4*D* *in height,* where *D* is the cylinder's diameter. The height of the

computational domain is a sectional length of a theoretically infinite-long cylinder. The cylinder, as can be seen from Figure 2.1, has its axis in the *z*-direction and lies in the center of the *x-y* plane with these coordinates oriented so that the free stream velocity oscillates in the *x-z* plane. The cylinder is located at the center of the computational domain. The computational domain size is checked and confirmed for its sufficiency to be free from inlet and outlet boundary influences on the computed flow field.
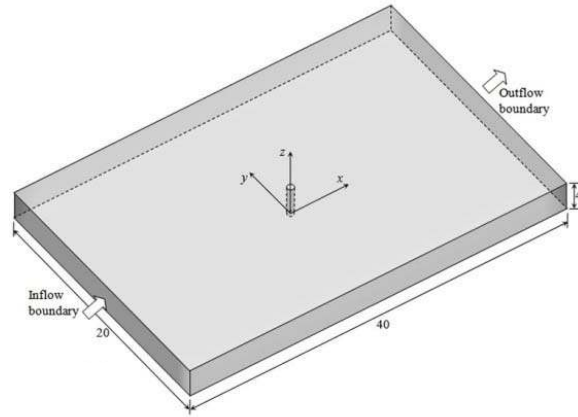
Figure 2.1 Definition sketch of the computational domain, with a dimension of 40*D* × 20*D* ×4*D*.

2.3.2   The governing equations

The governing equations for the incompressible flow field are the 3-D Navier-Stokes equations. The primitive variables are non-dimensionalized using the cylinder diameter *D* and the amplitude of the oscillatory velocity in the *x*-direction (U_{mx}) following the equations

$$x_i = x_i'/D, u_i = u_i'/U_m, p = p'/\rho U_m{}^2, t = t'/T, Re = U_m D/\nu, KC = U_m T/D \qquad 2.1$$

Using above non-dimensionalization method, the non-dimensional Navier-Stokes equations are written as

$$\frac{1}{KC}\frac{\partial u_i}{\partial t} + u_j\frac{\partial u_i}{\partial x_j} = -\frac{\partial p}{\partial x_i} + \frac{1}{\beta KC}\frac{\partial^2 u_i}{\partial x_j{}^2} \qquad\qquad 2.2$$

$$\frac{\partial u_i}{\partial x_i} = 0 \qquad\qquad 2.3$$

where p is the pressure and u_i is the velocity in the x_i-direction, $(x_1, x_2, x_3) = (x, y, z)$ and u_i stands for the velocity in the x_i-direction. The governing equations are solved through the PG-FEM described in detail in the following contents. The incompressible oscillatory flow past a fixed cylinder under various scenarios is computed at $KC = 2$ and $\beta =200$, 300 and 400. The first step of solving the equations is to apply a spatial discretization of the domain field.

2.3.3   Computational mesh

The computational domain is divided into eight-node tri-linear hexahedral elements, as shown in Figure 2.2. The 3-D computational mesh is constructed by slicing the computational domain into a number of identical 2D planes that are perpendicular to the cylinder axis, and each of these slices is discretised into four-node quadrilateral elements (Figure 2.2a). Dense mesh is applied in area close to the cylinder surface in order to obtain detailed observation of the flow structures, while a relatively coarser mesh is applied in the far field. The size of the elements for the 2-D plane and the axial density of the 3-D mesh are determined through a careful mesh-dependence study, which will be discussed in Section 2.3.6.1.
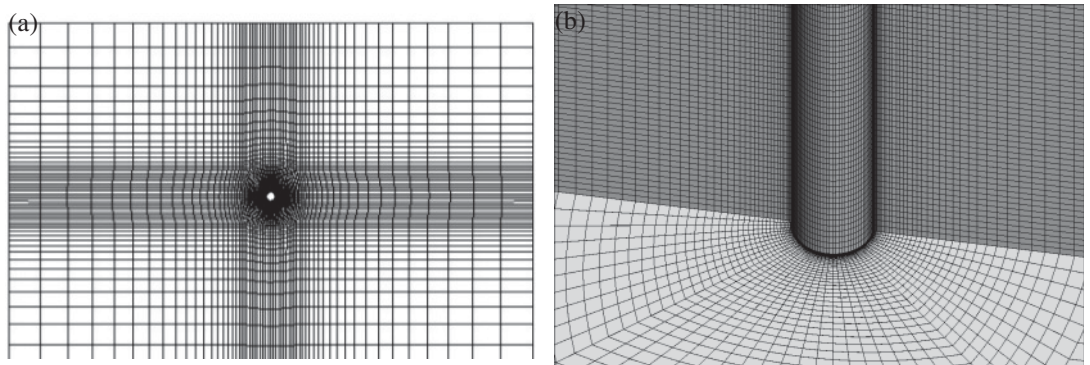
Figure 2.2 Demonstration of the computational mesh. (a) 2-D mesh in the axial plane; (b) 3-D mesh.

2.3.4 **Petrov-Galerkin finite element method**

The PG-FEM described below is the same as that applied in Zhao et al. [40], which also provides the major elements of the method. As mentioned before, the validation of this method has been well established from various studies including Zhao et al. [40, 41, 62, 66, 67, 79, 83], An et al. [21, 61] and Yang et al. [80], to name but only a few.

2.3.4.1 FEM Formulation

The FEM begins with introducing a shape function (also known as interpolation, trial or basis function). In order to obtain the finite element equations, the primitive variables pressure and velocity of the partial differential equation are approximated as a linear combination of the shape function by $f = \sum \Phi_k f_k$, with f being pressure or velocity, the subscript k denoting the global node number, therefore f_k is the value of f at k^{th} node and Φ_k is the shape function at k^{th} node.

The original governing Equation 2.2 is formulated into finite element equations using weighted residual methods. Aiming to minimize the error or the residual of the governing equations to zero, the weighted residual methods apply an inner product of the weighting function and the residual, and then set the integral of the inner product to zero. This process is mathematically expressed as

$$(W, R) = \int_0^1 WR\mathrm{d}x = 0 \qquad\qquad 2.4$$

It is easy to understand that this method is sometimes called the 'projection method', as the integration shown in Equation 2.4 simply means that 'the error at each point in the domain orthogonally projected onto a functional space spanned by the weighting function summed over the entire domain is set equal to zero' (p249, [84]).

Using W as the weighting function, Ω as the computational domain, Γ as the domain boundary and $\frac{\partial u_i}{\partial x_n}$ (or $u_{i,n}$) as the gradient of u_i in the outwards direction normal to the boundaries, the resultant variational or weak form of Equation 2.2 can be written as

$$\int_{\Omega} (W \frac{\partial u_i}{\partial t} + W u_j \frac{\partial u_i}{\partial x_j} + \frac{1}{KC\beta} \frac{\partial W}{\partial x_j} \frac{\partial u_i}{\partial x_j} + W \frac{\partial p}{\partial x_i}) \mathrm{d}\Omega - \int_{\Gamma} W \frac{\partial u_i}{\partial x_\perp} \mathrm{d}\Gamma = 0 \qquad 2.5$$

Next we determine the element shape function. The element shape function obtained under different coordinate system varies. The coordinate system should thus be selected to ensure smallest amount of algebra involved in formulation of finite element equations. In the present study, the standard rectangular Cartesian coordinate system is applied. To obtain the shape function within an element, the actual hexahedron elements are transformed into isoperimetric cubic elements using a non-dimensional local coordinate. The origin of the local isoperimetric coordinates is located at the centroid of the element and has a range of $\xi_{1,2,3} = [-1,1]$ as shown in Figure 2.3. The transformation between two coordinates are realised through geometrical Jacobian rule, given in Equation 2.6.
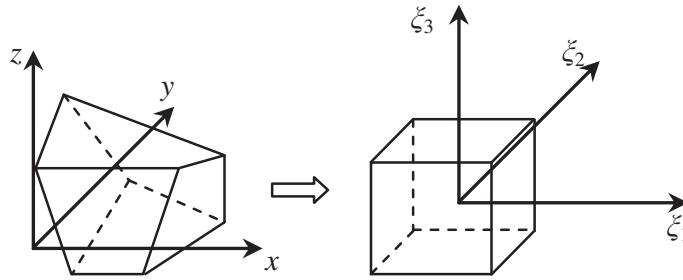
Figure 2.3 Sketch of transformation from between two coordinate systems, (x, y, z) to $(\xi_1, \xi_2$ and $\xi_3)$.

$$\begin{bmatrix} \dfrac{\partial f}{\partial x} \\ \dfrac{\partial f}{\partial y} \\ \dfrac{\partial f}{\partial z} \end{bmatrix} = [J]^{-1} \begin{bmatrix} \dfrac{\partial f}{\partial \xi_1} \\ \dfrac{\partial f}{\partial \xi_2} \\ \dfrac{\partial f}{\partial \xi_3} \end{bmatrix} \qquad 2.6$$

where J is the Jacobian matrix given by

$$[J] = \begin{bmatrix} \dfrac{\partial x}{\partial \xi_1} & \dfrac{\partial y}{\partial \xi_1} & \dfrac{\partial z}{\partial \xi_1} \\ \dfrac{\partial x}{\partial \xi_2} & \dfrac{\partial y}{\partial \xi_2} & \dfrac{\partial z}{\partial \xi_2} \\ \dfrac{\partial x}{\partial \xi_3} & \dfrac{\partial y}{\partial \xi_3} & \dfrac{\partial z}{\partial \xi_3} \end{bmatrix}$$

2.7

Following the Jacobian rule, in the isoperimetric element for a linear variation of the geometry and variable, the isoperimetric shape function has the form

$$\Phi^{(e)}{}_k = \frac{1}{8}(1 + \xi_{Ni}\xi_i)$$

2.8

The transformation between two coordinates are realised through geometrical Jacobian. Following the rule that the derivatives of $\dfrac{\partial f}{\partial x_i}$ can be determined from the tensor product of the inverse of the Jacobian (J) and the derivatives of $\dfrac{\partial f}{\partial \xi_i}$, Equation 2.5 representing the weighted residual formulation can then be written in the transformed local coordinates as

$$\int_{\bar{\Omega}} (W\frac{\partial u_i}{\partial t} + Wu_i(\frac{\partial u_i}{\partial \xi_a}\frac{\partial \xi_a}{\partial x_j}) + \frac{1}{KC\beta}(\frac{\partial W}{\partial \xi_a}\frac{\partial \xi_a}{\partial x_j})(\frac{\partial u_i}{\partial \xi_b}\frac{\partial \xi_b}{\partial x_j}) + W\frac{\partial p}{\partial \xi_a}\frac{\partial \xi_a}{\partial x_i})J d\bar{\Omega} - \int_{\bar{\Gamma}} W\frac{\partial u_i}{\partial x_\perp}I d\Gamma = 0 \quad 2.9$$

in which $d\Omega = Jd\bar{\Omega}$ and $d\Gamma = Id\bar{\Gamma}$, J and I denote the Jacobians for the points located in the inner domain the on the boundaries, respectively.

Next we discuss the weighting function (test function) to be applied. It is known that the conventional Galerkin methods using the shape function as the weighting function leads to unstable and inaccurate solutions under some situations. Especially for convection-dominated flows, spurious node-to-node oscillations or 'wiggles' occur in the solutions which fails the 'best approximation' [71]. To preclude the wiggles, the weighting function is defined differently from the shape function. The Petrov-Galerkin scheme applied here uses a weighting function defined by adding a streamline upwind perturbation to the standard Galerkin weighting functions. The artificial perturbation is

constructed to act only in the flow direction to eliminate the possible crosswind diffusion. The streamline upwind Petrov-Galerkin weighting functions for the momentum equations then take the form

$$W = (N_1 + \widetilde{W_1})(N_2 + \widetilde{W_2})(N_3 + \widetilde{W_3})$$

2.10

where $W = N_1 N_2 N_3$ ($N_{1,2,3}$ represents the one-dimensional shape function in $\xi_{1,2,3}$ direction) is the weighting function for the simple Galerkin finite element method, which is modified by the added streamline perturbation $\widetilde{W}_{1,2,3}$. Considering only first order of $\widetilde{W}_{1,2,3}$, Equation 2.10 can be written as

$$W = (\widetilde{W_1}N_2 N_3 + N_1 \widetilde{W_2} N_3 + N_1 N_2 \widetilde{W_3})$$

2.11

The definition for the three-dimensional perturbation terms can be demonstrated through the definition of a one-dimensional problem, where $\widetilde{W_1}$ is defined as

$$\widetilde{W_1} = \gamma U_1 \widetilde{\xi}_1 \Delta_1 \frac{\partial N_1}{\partial x}$$

2.12

where Δ_1 is the characteristic size of the elements in $\xi_{1,2,3}$ coordinates, $\widetilde{\xi}_1$ is the artificial diffusion coefficient, defined as $\widetilde{\xi}_1 = \coth(\psi) - 1/\psi$ and $\psi = U_1 \Delta_1 / 2k (k = \frac{1}{KC\beta} \frac{\partial^2 \xi_1}{\partial x^2}) . \gamma$ is a constant chosen to be $1/\sqrt{15}$ so that the phase error is minimum [85].

After deciding on both the shape function and the perturbed weighting function, the updated finite element formula under the streamline upwind Petrov-Galerkin formulation can be written as

$$\int_{\overline{\Omega}} ((W + \widetilde{W})\frac{\partial u_i}{\partial t} + (W + \widetilde{W})u_i(\frac{\partial u_i}{\partial \xi_a}\frac{\partial \xi_a}{\partial x_j}) + \frac{1}{KC\beta}(\frac{\partial(W + \widetilde{W})}{\partial \xi_a}\frac{\partial \xi_a}{\partial x_j})(\frac{\partial u_i}{\partial \xi_b}\frac{\partial \xi_b}{\partial x_j}) + (W + \widetilde{W})\frac{\partial p}{\partial \xi_a}\frac{\partial \xi_a}{\partial x_i})J\mathrm{d}\overline{\Omega}$$

$$- \int_{\overline{\Gamma}} (W + \widetilde{W})\frac{\partial u_i}{\partial x_\perp}I\mathrm{d}\Gamma = 0 \qquad\qquad 2.13$$

The numerical integration of the transformed Equation 2.9 is achieved by performing the Gaussian quadrature. For a quantity given by $\int_{-1}^{1}\int_{-1}^{1} f(\xi_1, \xi_2, \xi_3)\mathrm{d}\xi_1\mathrm{d}\xi_2\mathrm{d}\xi_3$, the Gaussian quadrature can be expressed as

$$\int_{-1}^{1}\int_{-1}^{1} f(\xi_1, \xi_2, \xi_3)\mathrm{d}\xi_1\mathrm{d}\xi_2\mathrm{d}\xi_3 = \sum_{j=1}^{n}\sum_{k=1}^{n}\sum_{l=1}^{n} w_j w_k w_l f(\xi_{1j}, \xi_{2k}, \xi_{3l}) \qquad\qquad 2.14$$

Chosen the Gaussian points to be 2, the weight coefficient w_k then becomes 1.0 and abscissae are ±0.57735.

2.3.4.2 Time-advancement

The governing equations are integrated forward in time to determine the evolution of the flow field, using a fractional step method. The adequacy of this method to be successfully applied to FEM is demonstrated by previous studies, including Donea et al.[86], Ramaswamy [87] and Ramaswamy and Jue [88].

The fractional step method is performed in a three-step sequence as given below. It can be seen that the perturbation term $\widetilde{w}$ is only applied in the first step for predicting the velocity, while for step 2 and 3 the simple Galerkin method is applied. This suits the aim of applying the upwind scheme simply for precluding the wiggles caused by the convective term.

- Step 1, a predicted or intermediate velocity is calculated by omitting the pressure term when time integrating the momentum equation. At this step, the intermediate velocity does not necessarily satisfy the incompressibility condition. Corresponding formulation:

$$\int_{\overline{\Omega}} ((W + \widetilde{W}) \frac{1}{\Delta t} (\hat{u}_i^{n+1} - u_i^n) + (W + \widetilde{W}) u_i^n (\frac{\partial u_i^n}{\partial \xi_a^n} \frac{\partial \xi_a^n}{\partial x_j^n})$$

$$+ \frac{1}{KC\beta} (\frac{\partial (W + \widetilde{W})}{\partial \xi_a^n} \frac{\partial \xi_a^n}{\partial x_j^n}) (\frac{\partial \hat{u}_i^{n+1}}{\partial \xi_b^{n+1}} \frac{\partial \xi_b^{n+1}}{\partial x_j^{n+1}})) J d\overline{\Omega} - \int_{\overline{\Gamma}} (W + \widetilde{W}) \frac{\partial \hat{u}_i^{n+1}}{\partial x_\perp^{n+1}} I d\Gamma$$

$$= 0$$

2.15

in which Δt is the computational time step, the superscript n and $n+1$ stands for the calculated results at the time $n\Delta t$ or $(n+1) \Delta t$.

- Step 2, pressure is calculated by solving a pressure Poisson equation:

$$\frac{\partial^2 p^{n+1}}{\partial x_j x_j} = \frac{1}{\Delta t} \frac{\partial \hat{u}_i^{n+1}}{\partial x_i}$$

2.16

for which the finite element formula can be written as

$$\int_{\overline{\Gamma}} W \frac{\partial p}{\partial x_\perp} I d\overline{\Gamma} - \int_{\overline{\Omega}} \frac{\partial W}{\partial x_j} p_j J d\overline{\Omega} = \int_{\overline{\Omega}} W \frac{1}{\Delta t} \frac{\partial \hat{u}_i^{n+1}}{\partial x_i} J d\overline{\Omega}$$

2.17

- Step 3, the intermediate velocity is corrected by solving the momentum equation with only the pressure term as calculated in step 2:

$$\int_{\overline{\Omega}} (W \frac{1}{\Delta t} (\hat{u}_i^{n+1} - u_i^n) + W (\frac{\partial p}{\partial \xi_a} \frac{\partial \xi_a}{\partial x_i}) J d\overline{\Omega} = 0$$

2.18

2.3.5 Boundary conditions

All computational runs are initiated with zero velocity and pressure fields to obtain self-developed flow field. Motion is induced into the system by imposing desired boundary conditions.

At the inlet and outlet boundaries, flow is prescribed as sinusoidal oscillatory. Unless otherwise suggested (see Section 4.3.2), the following formula applies on the inlet and outlet boundaries as shown in Figure 2.1:

For velocity variables

$$(u_x, u_y, u_z) = (1,0,0)\sin(2\pi t/T)$$

2.19

For pressure variables

$$\frac{\partial p}{\partial x} = \frac{2\pi}{KC}\cos(2\pi t)$$

2.20

The flow is solved subject to no-slip requirements on the cylinder, where the velocity is zero in all directions. Symmetric conditions are enforced on the two bounding surfaces parallel to the *x-z* plane (see Figure 2.1), i.e. the velocity in the *y*-direction is zero. Special consideration is given at two ends of the cylinder (two boundaries parallel to the *x-y* plane). The conventional free-slip boundary condition is not suitable for the cases where the incoming flow is not perpendicular to the cylinder, as it prohibits the flow component in the spanwise or axial direction. In this study, the periodic boundary condition is used at the two end boundaries. Under the periodic boundary condition velocity and pressure gradients at one end of the cylinder are the same as their counterparts at another end. In this way, the cylinder in the finite domain can represent a cylinder of infinite length.

2.3.6 Validation and verification of the numerical model

The results obtained through FEM must be convergent, stable and accurate. It is of vital importance to carry out mesh-dependence study and model verification when conducting numerical simulations.

2.3.6.1 Mesh dependence study

The numerical results are greatly influenced by the mesh size. The temporal and spatial discretization must be carefully designed to achieve convergent solution, maintain numerical stability and obtain accurate numerical results. Mathematical accuracy can be improved by refining the mesh. However, the time cost for the simulations at extreme dense mesh must be considered when such refinement is applied. The compromise between the accuracy and efficiency is usually determined based on the aim of the particular study. In general, mesh size is always attempted to be as coarse as possible by way of mesh validation on the basis that the calculation results are least affected.

As mentioned in Section 2.3.3, considering both the accuracy of the results and time efficiency, alongside with our aim of study, fine mesh is applied near the cylinder and coarse mesh is applied in the far field. The present study applied the same domain size and discretization method as that of An et al. [21]. Although An et al. gave a discussion on mesh validation when choosing the computational mesh, for the present study, careful mesh dependency experiments were still performed in a similar fashion but with different mesh prescriptions.

Table 2.1 A comparison of different meshes evaluated. $\Delta e/D$ is the distance between the first nodal point and the cylinder diameter in the radial direction of the cylinder; N_{cy2D} is the number of elements on the cylinder circumference in the cross section of the domain; N_{p2D} and N_{e2D} are the total number of nodal points and elements respectively in the cross section of the domain; N_{p3D} and N_{e3D} are the total number of nodal points and elements respectively in the 3-D domain; N_{cy3D} is the number of 2-D mesh layers; and $\Delta z/D$ is the axial density along the cylinder.

Mesh	$\Delta e/D$	N_{cy2D}	N_{p2D}	N_{p3D}	N_{e2D}	N_{e3D}	N_{cy3D}	$\Delta z/D$
a	0.0016	80	7460	305,860	7280	291,200	40	0.100
b1	0.0012	96	8996	368,836	8800	352,880	40	0.100
c	0.0008	102	9764	400,324	9540	381,600	40	0.100
b2	0.0012	96	8996	539,760	8800	529,320	60	0.067
b3	0.0012	96	8996	719,680	8800	719,680	80	0.050
b4	0.0012	96	8996	863,616	8800	846,912	96	0.038
b5	0.0012	96	8996	1151,488	8800	1129,216	128	0.030

Mesh validation for the present study was carried out for seven different meshes as listed in Table 2.1. The process for the mesh validation mainly includes two steps. First, the two-dimensional cross-sectional plane as shown in Figure 2.2a was examined by

changing the nodal point number around the cylinder circumference (a1, b and c in Table 2.1) while mesh resolution in the axial direction remained constant. Then, after choosing the appropriate two-dimensional resolution, the axial density was investigated using the two-dimensional resolution chosen (Mesh a1~5 in Table 2.1).

Test calculations were run for the case of $\beta = 400$ and $KC = 2$ for up to 100 oscillation periods. This value for β was chosen because it is the largest among all the simulation cases to be investigated in the present study. With KC fixed, a higher β results in a more unstable flow field likely to involve turbulent behaviours of fluid particles, and therefore requires the finest mesh resolution. According to An et al.[21], the flow with $\beta = 400$ and $KC = 2$ is in the interactive Honji vortices regime where the flow structure is unstable. As a result, a more promising approach to study the mesh dependency is to compare statistical data calculated from different cases rather than using the primitive values of velocity and pressure.

Following the previous discussion, we choose the quantities of the root-mean-square (RMS) Morison force coefficients C_M and C_D and the axial correlation length $L_{px,y}$ of pressure coefficient with regards to two measurement lines for validating the meshes. The Morison coefficients C_M and C_D are used to decompose the resultant drag (or in-line) force per unit length of the cylinder, F_D, defined in Equation 2.21. Then the definitions for C_M and C_D can be given in Equation 2.22.

$$F_D = \int_0^{2\pi} (-p\cos\theta + \tau_0 \sin\theta)Rd\theta \qquad 2.21$$

$$\frac{2F_D}{\rho DU^2{}_M} = C_D|\sin\omega t| \sin\omega t + \frac{\pi^2 C_M}{KC}\cos\omega t \qquad 2.22$$

The axial correlation length reflects the average lengths of the cells in which vortical structures occur. The correlation length along the cylinder axis can be defined by

$$L = \int_0^\infty R(z)dz \qquad\qquad 2.23$$

In which R(z) represents the correlation coefficient, defined by

$$R(z) = \frac{\overline{p'(z_0)p'(z_0 + \Delta z)}}{\sqrt{\overline{p'^2(z_0)}}\sqrt{\overline{p'^2(z_0 + \Delta z)}}} \qquad\qquad 2.24$$

in which the overbar denotes averaging by time, z_0 is the reference axial location, Δz is the axial distance between the two measurement points, and p' is the fluctuating part of the unsteady pressure. Correlation lengths are recorded at two measurement lines. L_{px} (L_{py}) denotes L_p calculated along the line of first nodal points close to the cylinder when $y/D = 0$ ($x/D = 0$).

The calculated C_M and C_D, and $L_{px,y}$ based on the seven meshes are compared in Figure 2.4 and Figure 2.5 respectively. For all meshes evaluated, the absolute values are given in Figure 2.4a and Figure 2.5a while the relative values of ΔC_M and ΔC_D, and $\Delta L_{px,y}$ are given in Figure 2.4b and Figure 2.5b for the purpose of comparison. As listed in Table 2.1, first the 2-D resolution is studied between meshes a1, b and c. It is seen that although the differences resulting from different 2-D resolutions are not obvious in $L_{px,y}$ in Figure 2.5, the calculated C_M and C_D show that about 0.5% difference occurs between the most coarse mesh a1 and the finest mesh c. In the present study the intermediate mesh b is then chosen as the 2-D mesh to be applied in the next step, the axial density examination. Table 2.1 lists the axial variation for meshes b1, b2, b3, b4 and b5. It is found that the $L_{px,y}$ is influenced most when decreasing $\Delta z/D$ from Mesh b1 to Mesh b5, with a decrease of about 1.5%. Further evaluation of Figure 2.4b and Figure 2.5b shows that increasing the mesh resolution from Mesh b3 to Mesh b5 induces less than a 0.5% change in C_D, C_M and $L_{px,y}$ values. However, the computational cost for Mesh b5 is approximately 40% higher than that for Mesh b3. The results show that the deviation between using Mesh b3 and Mesh b5 is negligible, compared with the additional computational cost. As a result, for the present study, Mesh b3 was chosen which was

proved to be numerically accurate and temporally economic in computational cost, and it suits the main interest of the present study.

The time step for the simulation was set at $dt = 0.005$, which is the same as that used in the work of An et al.[21], and is considered to be both temporally accurate and stable at the low values of governing parameters concerned in this study.

(a)
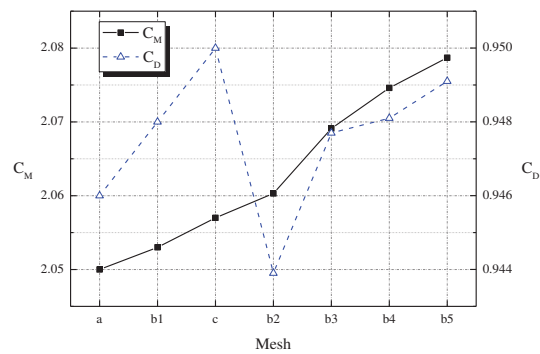
(b)
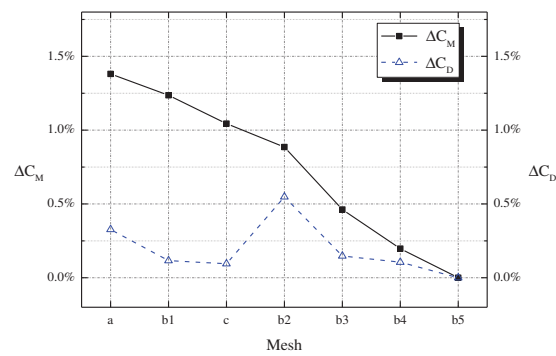
Figure 2.4 Calculated Morison coefficients values for different meshes (a) and derivations based on Mesh 7 (b).

(a)
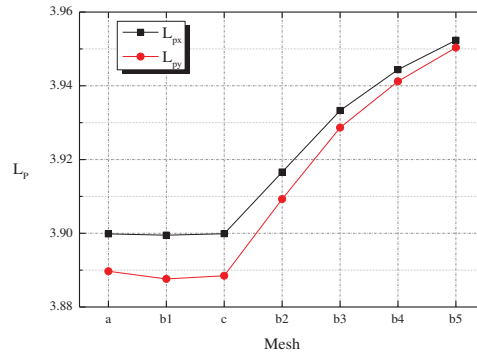
(b)
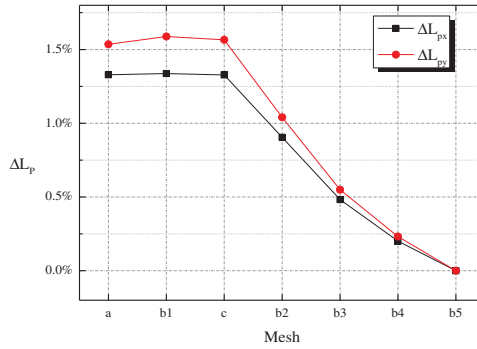
Figure 2.5 Correlation Length of P (pressure) for different meshes (a) and derivations based on Mesh 7 (b).

2.3.6.2 Verification of the numerical scheme

As mentioned before, the current numerical scheme has been applied to various projects and the results obtained for different scenarios have been compared successfully with those similar studies in the literature. It is proved to be capable of simulating the actual physical problems concerned. Some publications using the current numerical scheme are listed below to demonstrate the verification for the numerical method.

One case most relevant to the present study is An et al.'s [21] study on oscillatory flow around a circular cylinder at low Re number. The parameter range covered in their study is $KC = 2$ and $100 \leq \beta \leq 600$. Using the current numerical scheme, An et al. successfully describes the detailed flow structures for the Honji instability, which agrees well with

previous physical experiments [14, 15, 18, 24]. Both the instantaneous fluid field and the time-averaged steady streaming phenomena are successfully captured and discussed in that study.

A DNS study using this numerical scheme was first applied to study a 3-D flow past a yawed cylinder conducted by Zhao et al. [40]. In that study, a fixed cylinder with an inclined angle between 0° and 60° is immersed in a steady flow at Re = 1000. The calculated wake flow structures are found to compare well with those observed from flow visualization in previous studies. Later in Zhao et al. [89], the 3-D numerical simulation is applied to an oscillatory flow at higher Re number of 2000 and KC number ranging from 6.75 to 30. In Zhao et al.'s paper they first studied the flow regimes for a perpendicular incoming flow under different KC number, and then discussed then effects of the oblique angle on the vortex shedding regime and resultant hydrodynamic forces. Using the results obtained from the numerical model, Zhao et al. evaluated the independence principle under the chosen inclination angles and the KC number concerned.

It should be mentioned that the numerical model has been proved to work well under various circumstances, sometimes with slight modifications such as applying turbulence models. Examples of other applications using the current numerical model include 2-D simulations [80], near wall or seabed simulations [79] and combined current and oscillatory flow [62]. This shows the versatile capability of the numerical scheme.

2.4   Post-processing

Post-processing the computational results involves visualization of the calculated flow field and some quantitative analysis of the fluid properties. Both the flow evolution history and the instantaneous fluid field are examined.

The raw results calculated by each parallel processor are first composed to get the whole flow field at the chosen moment. This can be done either in the supercomputer system or at a single desktop computer. Detailed flow structures can be gained through flow visualization of the calculated flow field, which are represented by the primitive

variables velocity and pressure. The vorticity components calculated from the primitive variables and are also used to demonstrate the vortical structures. Flow visualizations are obtained using largely Tecplot, a commercial CFD visualization and post-processing software, conducted on a desktop. Quantitative or discrete data processing is gained through post-processing codes written in FORTRAN and MatLab. Origin and Excel are also involved in post-processing mainly for quantitative analysis.

2.4.1   Three-dimensionality demonstration

The prime purpose of the present study is to investigate the hydrodynamic instability that causes the flow transition from 2-D to 3-D in the flow field near the cylinder. In this study, the third dimension refers to the axial direction. During the calculations, small disturbances are resulted from residuals at each time step. If the 2-D flow is intrinsically unstable under certain governing parameters, those disturbances will accumulate and develop, leading to the transition from 2-D to 3-D flow.

The onset of 3-D instability is marked by the rising of irregular structures along the cylinder's axis. Several phenomena represent the three-dimensionality of the flow. Using the primitive variable velocity, the flow is found to be 3-D when the axial flow component appears and begins to increase. The intensity of 3-D can be measured by the strength of the axial flow component. Another method to express the 3-D feature is through demonstration of the irregular vortical structures.

2.4.2   Visualization of the vortical structures

Other than the increase of the axial flow component, the presence of axially irregular vortices is also a feature showing the 3-D nature of the resultant flow field. Identification of the 3-D flow instability is represented by vortical structures formed and vary along the cylinder span.

The vortical structures are visualised using the instantaneous iso-surfaces of the unit amplitude of the three non-dimensional vorticity components (ω_x, ω_y and ω_z) in this study. The three vorticity components represent the specific rotation of the fluid

particles about different axes as are defined by $\omega_x = (\frac{\partial w}{\partial y} - \frac{\partial v}{\partial z})$, $\omega_y = (\frac{\partial u}{\partial z} - \frac{\partial w}{\partial y})$ and $\omega_z = (\frac{\partial v}{\partial x} - \frac{\partial u}{\partial y})$. The three-dimensionality can be reflected by the axial variation of the iso-surface of ω_x (ω_y and ω_z) $= \pm 1$, as shall be demonstrated in the results discussion.

<div align="right">

CHAPTER 3

</div>

<div align="right">

A PERTURBATION METHOD ARISING FROM DIRECT STABILITY ANALYSIS

</div>

3.1   Aim of chapter

In this chapter we will propose a perturbation method to be applied for selected cases in the main calculations discussed in Chapter 4 and Chapter 5. The purpose is to establish a perturbation method that will facilitate the acceleration of the calculation and assist in determining the intrinsic stability of the flow field, while at the same time retain the key flow properties in the calculated results as if without perturbation.

3.2   Introduction

This chapter provides a new numerical method for tackling the problems of hydrodynamic instability, such as the Honji instability which is our main concern. This method introduced in this chapter originates from a direct stability analysis, which serves as a good approach for studying instability problems. Direct stability analysis is previously adopted for studies on the instability characteristics of the natural convective thermal boundary layer [90-97]. The key element of the approach is to introduce a perturbation to either the governing equations or to the boundary conditions, and then the flow field under the effects of the perturbation is examined. A similar perturbing approach is applied to some of our main calculations based on our interest. The aims for us to apply the perturbations in addition to the free-developing (i.e. calculations without perturbation) results mainly include two aspects.

For one reason, perturbing the flow field can help to accelerate the calculations. In Chapter 2 it was mentioned that CFD is a robust tool in conducting studies on hydrodynamic instability problems due to its cost-effectiveness and controllability. However, in numerical simulations, hydrodynamic instability (such as the Honji instability which induces the flow field to take a 2-D to 3-D transition) is triggered

through accumulation of numerical residuals, which happens when the flow is intrinsically unstable under the flow regime determined by the governing equations. Since the residuals are usually small, this process may be very long before the instability is finally induced, especially for the cases under marginal governing parameters. To improve this situation, an artificial perturbation is introduced to accelerate the flow development.

Another purpose is to evaluate the intrinsic stability of the flow field and the properties of the hydrodynamic instability developed. There are two types of hydrodynamic instabilities, namely, absolute instability and convective instability. In particular, for the Honji instability which accounts for the 2-D to 3-D flow transition, absolute instability refers to a case that flow remains 3-D, following an artificially applied 3-D initial instability. The convective instability refers to a case that flow gradually develops into 3-D with an on-going perturbation being applied to the flow field. If neither absolute instability nor convective instability develops, the flow is intrinsically stable.

This chapter deals with the definition of an on-going perturbation that fulfils the main purposes as given above. The perturbing method used here is similar to that applied in the direct stability analysis [98], i.e. the perturbation comes into effect by adding a source term in the governing equations. Details of the mathematical formulation are given in Section 3.3. It is noted that the perturbation has to be chosen carefully so that the resultant flow field is not fundamentally altered and is still conceptually correct. Validation of the method is conducted by comparing the flow developing process as well as the resultant instantaneous flow field with those obtained without perturbation (i.e. free-developed).

For ease of reference, angle θ is defined in Figure 3.1 to represent circumferential locations on the cylinder. According to the definition, the positive x-axis stands for the value of $\theta = 0°$ and the positive y-axis stands for the value of $\theta = 90°$. The half-circumferential range from $\theta = 0°$ to $180°$ (the upper half plane) is named the 'top half-plane'; and the other half (from $\theta = 180°$ to $\theta = 360°$) is regarded as the 'bottom half-plane'.
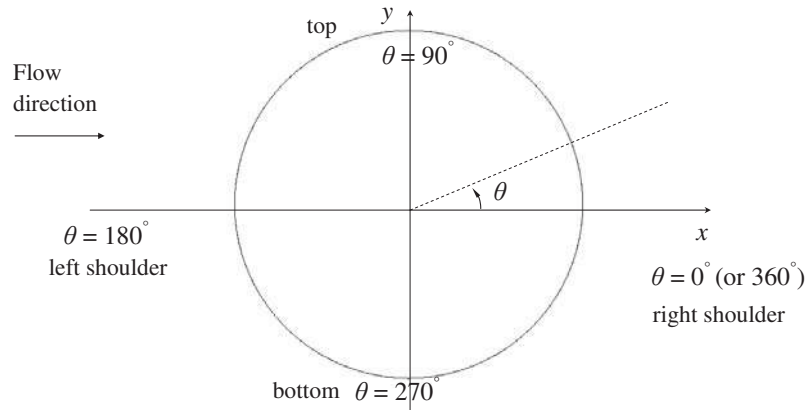
Figure 3.1 Definition sketch of the phase angle θ.

3.3   Mathematical formulation

3.3.1   **Governing equations**

In this study, an axial random perturbation was added in the dimensionless Navier-Stokes equations, which were then solved together with the non-dimensionalized continuity equation. It is known that the Honji instability is a 3-D instability demonstrated by an axial variation of the near-cylinder flow field. Therefore, the perturbation as a source term was only added in the z-component momentum equation. The dimensionless momentum equations for the perturbed flow field then read

For x and y axes

$$\frac{1}{KC}\frac{\partial u_x}{\partial t} + u_x\frac{\partial u_x}{\partial x} + u_y\frac{\partial u_x}{\partial y} + u_z\frac{\partial u_x}{\partial z} = -\frac{\partial p}{\partial x} + \frac{1}{\beta KC}(\frac{\partial^2 u_x}{\partial x^2} + \frac{\partial^2 u_x}{\partial y^2} + \frac{\partial^2 u_x}{\partial z^2}) \qquad \text{3.1a}$$

$$\frac{1}{KC}\frac{\partial u_y}{\partial t} + u_x\frac{\partial u_y}{\partial x} + u_y\frac{\partial u_y}{\partial y} + u_z\frac{\partial u_y}{\partial z} = -\frac{\partial p}{\partial y} + \frac{1}{\beta KC}(\frac{\partial^2 u_y}{\partial x^2} + \frac{\partial^2 u_y}{\partial y^2} + \frac{\partial^2 u_y}{\partial z^2}) \qquad \text{3.1b}$$

For z axis

$$\frac{1}{KC}\frac{\partial u_z}{\partial t} + u_x\frac{\partial u_z}{\partial x} + u_y\frac{\partial u_z}{\partial y} + u_z\frac{\partial u_z}{\partial z} = -\frac{\partial p}{\partial z} + \frac{1}{\beta KC}(\frac{\partial^2 u_z}{\partial x^2} + \frac{\partial^2 u_z}{\partial y^2} + \frac{\partial^2 u_z}{\partial z^2}) + SP \qquad \text{3.2}$$

in which SP stands for the perturbation as a source term. The continuity equation remains the same as that given in Equation 2.3.

The perturbed governing equations together with the initial and boundary conditions as specified in Section 2.3.5 are solved using the Petrov-Galerkin's FEM described in Chapter 2. The source term SP is first determined through a series of test runs discussed in the following section. The governing parameter group $(KC, \beta) = (2, 200)$ is chosen for the calculations for the evaluation of the perturbed method.

3.3.2   Definition of the perturbation

Several aspects need to be considered when applying the perturbation. First the location where the perturbation is added is determined. Perturbation needs to be placed in a position that does not interfere with intrinsic nature of the hydrodynamic instability. Therefore, we choose the shoulders of the cylinder out of the consideration that Honji structures mainly develop in the range near the top and bottom of the cylinder, i.e. at approximately 90° from the shoulders region. The perturbation term is applied to points located in the range of $0.5 < |x/D| < 0.5025$ and $-0.05 < y/D < 0.05$ at the cylinder shoulders (i.e. $\theta = 0°$ and 180°). In addition, it is speculated that the Honji instability is a convective instability which associates with small disturbances generated at the leading edges of the cylinder. If that is the case, deliberately prescribing small disturbances at the shoulders may help to trigger the Honji instability. Both sides of the shoulders are

46

included, in order to keep the symmetry of the oscillatory flow field. For the 2-D cross-sectional mesh, there are 39 nodal points perturbed on each side of the shoulder. In total 6318 nodes are perturbed in the 3-D mesh. In addition, the perturbation should be random along the cylinder span to avoid assigning a pre-defined frequency to the flow field. Finally, for the purpose of keeping consistence with the sinusoidally oscillatory free stream, the perturbation should include a sinusoidal function in phase with the free stream.

Following the previous discussion, an primitive expression for the perturbation SP can be written as

$$SP = A*\text{Random}[0,1]*\sin(2\pi ft) \hspace{4cm} 3.3$$

in which A is the amplitude of perturbation to be determined later on, Random[0,1] stands for a random number in the range of 0 to 1, and $\sin(2\pi ft)$ is a sinusoidal function in phase with the free stream where t is the dimensionless computational time and f is the frequency of the perturbation, which is also given as random.

3.3.3 Tests for the source term

Test runs are conducted for the case of $(KC, \beta) = (2, 200)$, under which it has been reported [21] that the flow falls into the stable Honji regime where the distinct mushroom-like Honji vortical structures can be observed around the cylinder surface.

3.3.3.1 Randomness check

As mentioned before, the perturbation applied should be random along the cylinder span in order to avoid influencing the intrinsic frequency of the Honji instability. Figure 3.2 presents two plots demonstrating that the perturbation prescribed is random. To show that the perturbation term added in the governing equations as given in Equation 3.3 is random, SP is plotted against the cylinder length for several early steps in Figure 3.2a. The SP values shown are obtained from an axial line of the first nodal points next to the cylinder at $\theta = 0°$, which is within the perturbed region. To show that the resulting flow field is also random at the perturbed points, Figure 3.2b shows the contours of u_z/U_{mx} in

a circuit plane around the cylinder circumference recorded on points next to the cylinder surface for the first time step. At this instant, a slightly larger u_z/U_{mx} is seen at two shoulders of the cylinder (i.e. $\theta = 180°$ and $\theta = 0°$, or $360°$) due to the added perturbation, and the axial random variation of u_z/U_{mx} can be observed. In the rest of the flow field other than the perturbed area, u_z/U_{mx} is zero. The randomness of the perturbation is obvious as demonstrated in both figures.

(a)
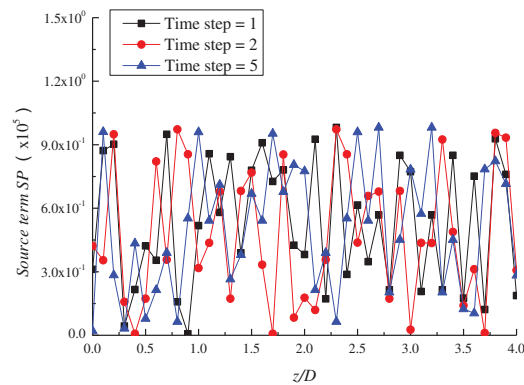
(b)
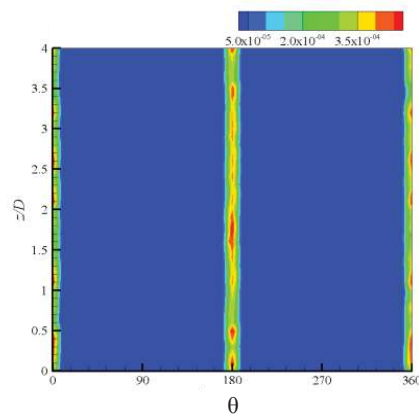
Figure 3.2 Demonstration of the random perturbation through (a) plot of source term (*SP*) amplitude along the cylinder span for three early time steps and (b) plane view of instantaneous contours of u_z/U_{mx} around the cylinder at the 1st time step. Probed at a circuit of the first nodal points next to the cylinder surface.

3.3.3.2 Determination of the amplitude A

In Equation 3.3 for the definition of the perturbation to be prescribed, the amplitude *A* should be evaluated carefully. To satisfy our main aims in applying the perturbation, the amplitude should neither be too large to maintain convergence of the calculation, nor too small to accelerate the flow development. The value of the amplitude of perturbation is regarded as appropriate when the system response is linear [94, 98]. Tests were run for the amplitudes *A*, 0.5*A* and 2*A* to see the effects on the resultant flow field. At first, the base amplitude *A* was set at 0.001, which was found to be too small to have any influence on the flow development. Several runs were conducted as *A* is increased from that value (test runs including *A* = 0.005, 0.1, 0.15, 0.2, 0.3, 0.4, 0.8), and it was observed that when *A* = 0.2 the flow development could be reasonably accelerated. Therefore the base amplitude was prescribed as 0.2. Next, in order to ensure the system response was linear, calculations for 0.5*A* (0.1) and 2*A* (0.4) were also conducted. Calculations for the three cases were run for 100 flow periods, and the characteristic properties of the resultant flow field were compared, including the time for the onset of Honji instability, the dominant wavenumber, and the standard deviation of the axial velocity component at selected points along the cylinder circumference.

First, the flow developments under different amplitudes of the perturbation are compared. The development of the flow was visualised by monitoring the time history of the relative axial velocity component u_z/U_{mx} along a probe line which is parallel to the axis of the cylinder and close to its surface at $\theta = 90°$ with $(x/D, y/D, z/D) = (0, 0.51, 0\text{-}4)$. The position of the probe line is sketched in Figure 3.3. This line locates within the Honji vortical structures once the instability occurs. The non-dimensionalized axial velocity component u_z/U_{mx} is measured along this line at the same phase of the flow oscillation cycles. In the results presented in Figure 3.4, this velocity is recorded at *T/4* into the oscillation period, i.e. at the moment when the free stream has the maximum amplitude. The recorded u_z/U_{mx} then has the attribute $(0, 0.51, z/D, N_i+T/4)$, in which $(0, 0.51, z/D)$ specifies the location of the measured points and N_i is the number of the flow oscillation cycle, where $N_i = 0, 1, 2, …, 100$ as shown in Figure 3.4. Both the temporal and spatial evolution of the flow structures can be demonstrated in this type of figure. In this method, the strength and direction of u_z/U_{mx} are reflected by the colour shade of the

contours, and the three-dimensionality of the flow can be observed by the change of colour patterns as the latter indicates the variation of the axial velocity along the cylinder span. When the flow develops to be 3-D, vortices form along the cylinder span, which are represented by the stripes in Figure 3.4.
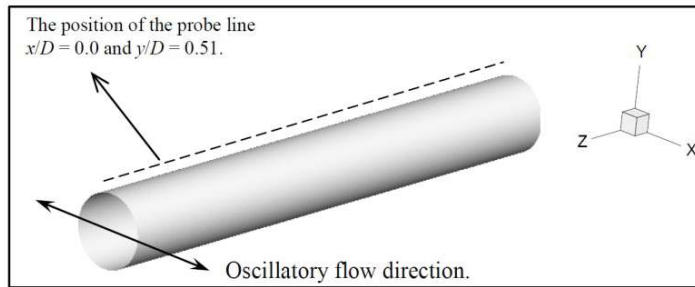
Figure 3.3 Sketch of the probe line at $\theta = 90°$ with $(x/D, y/D, z/D) = (0, 0.51\ 0\text{-}4)$. Data is recorded for the points along the probe line represented by the dash line in this figure.
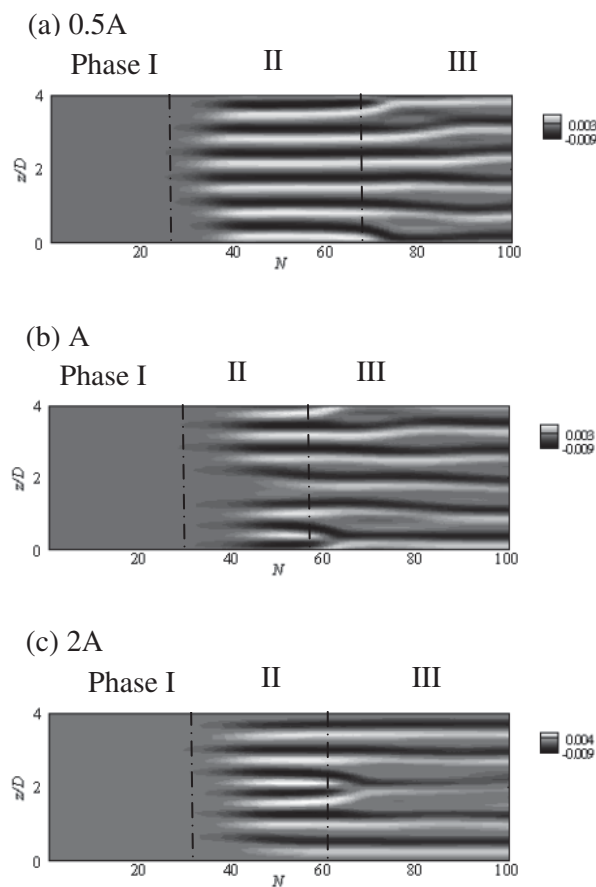
Figure 3.4 Evolution of the 3-D Honji vortices along the probe line shown in Figure 3.3, under different perturbation amplitudes: $0.5A$, A and $2A$, where $A = 0.2$.

As shown in Figure 3.4, the flow development can be divided into three main phases as labelled in each figure: phase I, phase II and phase III. First, when the calculation starts, the featureless 2-D flow (phase I) remains until the accumulation of the numerical residuals is sufficiently large to turn the flow into phase II, which begins with the onset of three-dimensionality (represented by the variation of the contour shade). The three-dimensionality initially appears as the evenly distributed vortex pairs along the cylinder span during Phase II. This is a transient stage, which soon ends with the onset of interactions between the unstable neighbouring vortices. The vortex interactions are signalled by the 'fork-like' structures observed in Figure 3.4, which are formed as a result of the merging of neighbouring vortices. The vortex interactions mark the beginning of a new phase - phase III, when vortices begin to shift along the cylinder span, and merging of neighbouring vortices causes a slight decrease in the number of vortices compared to that in phase II.

The flow developments calculated with different perturbation amplitudes show small variations as observed in Figure 3.4. This is not necessarily an effect of the amplitudes because, in fact, small variations are expected due to the randomness of the perturbation. Despite the slight distinctions between the results obtained under different amplitudes, Figure 3.4 shows that the three spatial-temporal figures have the same essential attributes mainly reflected in two aspects. Firstly, the time for the onset of the Honji instability for all cases is roughly $N = 30$, i.e. the duration of phase I under different amplitudes is roughly 30. Secondly, both in the transient phase II and in the final quasi-steady phase III the number of vortex pairs formed along the cylinder span is the same for all the three cases. As can be observed, once the 3-D features appear, for all cases in phase II there are six pairs of vortices along the cylinder span, represented by the six stripes. Then two neighbouring pairs merge during a transitional stage, thus leaving five pairs of Honji vortices, when the flow field enters a quasi-steady stage (phase III).

Next we compare the characteristic wavenumbers obtained from results at different amplitudes. Figure 3.5 gives the results of the computed FFT (Fast Fourier Transform) for the three cases at $N = 100$ along the probe line shown in Figure 3.3. As is seen in Figure 3.5, for all perturbations with different amplitudes, the same non-dimensional wavenumber is obtained, with a value of roughly 1.2. Over a cylinder span of $4D$, this

wavenumber gives five ($1.2×4 = 4.8 ≈ 5$) vortices, consistent with Figure 3.4. Recall that the initial perturbation applied is random and similar to white noise at the beginning of the calculations, therefore, it can be deduced that a dominant wavenumber of 1.2 is an intrinsic characteristic for the Honji instability developed in the near-cylinder flow at the specified governing parameters. The consistence between the three cases observed in Figure 3.5 indicates that the change of amplitudes does not result in variation of the characteristic wavenumber.
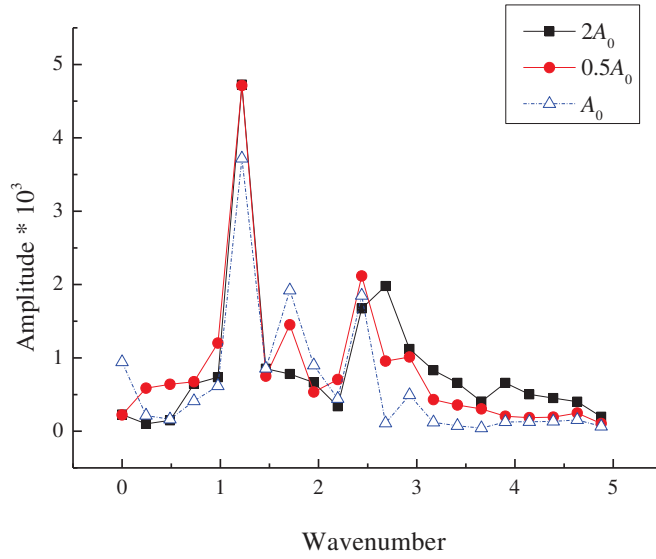
Figure 3.5 Comparison of the FFT results between different amplitudes at $N = 100$.

Although the previous discussions have primarily demonstrated consistent results between using different amplitudes, in order to confirm that the base amplitude chosen is appropriate, it is important to ensure that the response of the system is linear with different amplitudes. For this aim, the instantaneous spatial growth of the axial velocity component along the cylinder circumference is examined. For the selected θ values, we calculate the standard deviation of the non-dimensionalized axial velocity component u_z/U_{mx} at the recorded points along the cylinder span. The formula for this calculation is given in Equation 3.4, in which N_z is the number of nodal points for a single line along the cylinder, $u_z(n)$ is the value of u_z at the nth point, and $\overline{u_z}$ is the mean value calculated along the specific probe line. The measured points in each axial probe line consist of the first nodal points next to the cylinder surface, similar to that shown in Figure 3.3. The results are given in Figure 3.6, which shows the logarithmic plot of the calculated

standard derivation of u_z/U_{mx} (denoted as u'_{zstn}) against the chosen points around the circumference of the cylinder.

$$u'_{zstn} = \sqrt{\frac{\sum_{i=1}^{N_Z}(u_z(n)-\overline{u_z})^2}{N_Z}} \qquad \text{3.4}$$
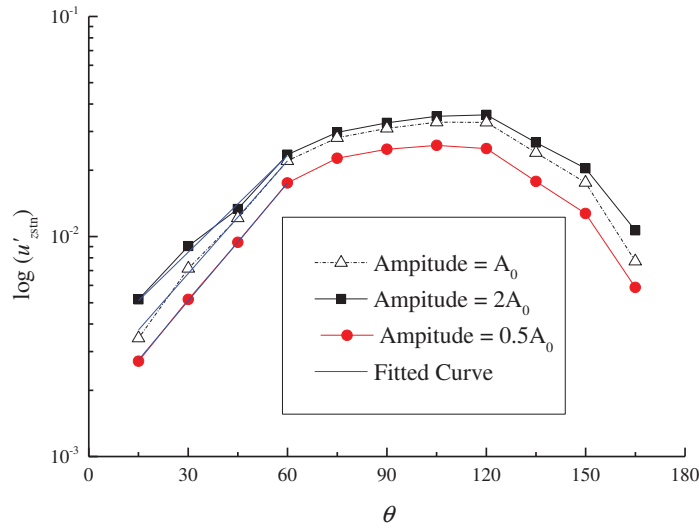
Figure 3.6 Standard deviation of the dimensionless axial velocity component u'_{zstn} verses spatial phase angle θ in logarithmic scale along with the fitted curve at $N = 100$. Data recorded for selected points around the circumference between the two shoulders ($\theta = 0°$ and $180°$) of the cylinder with an interval of $15°$.

As can be seen in Figure 3.6, along the circumference the variations of the statistical axial velocity calculated for the three cases are similar. Particularly in the range of $\theta \approx 15°$- $60°$, the three cases bear a similar trend of spatial growth along the circumference. The curves in the range of $\theta \approx 15°$- $60°$ shown in Figure 3.6 were fitted with a formula of $u'_{zstn} = ae^{b\theta}$, where a is the initial amplitude and b is the spatial growth rate. The fitted curves are included in Figure 3.6, and the parameter values found through fitting are given in Equation 3.5. It is seen that the relative difference of the spatial growth rate b for the three cases is insignificant (maximum around 10%) compared with the relative variation of the amplitude of the perturbation (a 100% increase from $0.5A$ to A and from A to $2A$). Therefore, for all three amplitudes, b can be treated as a constant, indicating the spatial growth is steady and independent of the amplitude of the perturbation.

According to Lei and Patterson [94], this indicates that the system response can be regarded as linear, and that the resultant flow behaviours are invariant despite changing the perturbation amplitudes. The base amplitude A (0.2) is hence applied for the subsequent calculations.

For 0.5A:

3.5a

$$u'_{zstn} = 0.0018e^{0.045\theta}$$

For A:

3.5b

$$u'_{zstn} = 0.0022e^{0.040\theta}$$

For 2A:

3.5c

$$u'_{zstn} = 0.0024e^{0.044\theta}$$

So far, all the elements of the source term SP which serves as the perturbation are determined. The expression for the perturbation given in Equation 3.3 is now updated to be

$$SP = 0.2*Random[0,1]*\sin(2\pi ft)$$
3.6

with all terms checked and evaluated. In the following section, calculations with the determined perturbation are conducted.

3.4   Resultant flow field with and without perturbation

The flow field calculated with a prescribed perturbation is compared with the free-developing flow field to check the effects of the additional perturbation on the main features of the resultant flow field. Following the test runs, the cases concerned are calculated under the governing parameters of $(KC, \beta) = (2, 200)$. The calculations are run for 100 flow periods to allow the flows to develop into the quasi-static phase III.

Both the flow development and the instantaneous flow properties calculated with and without the prescribed perturbation are compared and discussed.

3.4.1 **Flow development**
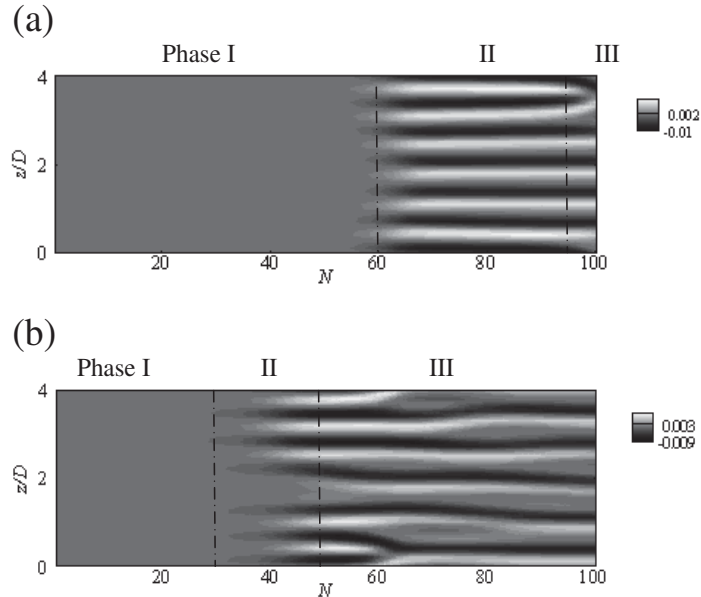
Figure 3.7 Flow development for the cases of (a) free-developing flow and (b) perturbed flow at $(KC, \beta) = (2, 200)$. Probed along the line of $(x/D, y/D, z/D) = (0, 0.51\ 0\text{-}4)$ as demonstrated in Figure 3.3.

The flow developments over 100 oscillation periods are compared in Figure 3.7 for the free-developing case and the perturbed case. The figures are again obtained along the probe line shown in Figure 3.3. The three different phases in the flow developing process can be identified for both cases. The main features of each phase have been described in Section 3.3.3.2 and shall not be repeated here.

Comparing the two cases, it is obvious that adding the perturbation reduces the duration of phase I, and the flow enters a 3-D phase II much earlier. This is because the added perturbation promotes the accumulation of the numerical residuals, and therefore triggers the three-dimensionality to develop earlier. Compared with the free-developing case, the perturbation brings the onset of 3-D forward from about 60th to about 30th flow period. In addition, the transient phase II is also shortened by the perturbation, lasting for only about 20 periods from $N = 30$ to 50, while for the free-developing case, phase II runs for more than 30 periods from $N = 60$ to roughly 95. After the transient phase II

persists for some periods, the balance between the evenly-distributed vortices is broken, and the flow enters phase III, where the vortices are unstable and shift along the cylinder span, causing the interactions between them. The 'fork-like' structures observed in the stripes stand for the merging of the two existing vortices. The instantaneous 3-D structures for this phenomenon is covered in Section 4.4.1 rather than here as it is not directly related to our concern for the present chapter.

As seen from Figure 3.7, the interactive phase III begins at around $N = 50$ for the case with the added perturbation, which is more than 40 periods earlier compared with the free-developing case. Considering all the three phases experienced by the flow until the quasi-static Honji regime is reached, it is concluded that, in general, adding the perturbation accelerates the flow development by about $40 \sim 50\%$.

Another observation worthwhile mentioning is that the number of vortex pairs formed throughout the 3-D stages is not altered by adding the perturbation. As can be seen in Figure 3.7, the number of resultant vortex pairs formed along the cylinder in both phase II and III is the same for the two cases. In phase II, both cases have six vortex pairs evenly distributed along the cylinder. When phase III starts, the number of vortex pairs is reduced to five as a result of vortex interaction. For a more precise comparison on the vortical structures, the characteristic wavenumber obtained through the FFT calculations is given in the next section.

3.4.2 Instantaneous flow behaviours

This section presents the comparison of the instantaneous flow properties between the free-developing and perturbed flows, including the characteristic wavenumber obtained through FFT, the pressure distribution along a near-cylinder circle around the circumference, the distribution of the three velocity components along probe lines, the circumferential distribution of the statistic axial velocity, and the visualization of the 3-D flow field.

3.4.2.1 Characteristic wavenumber
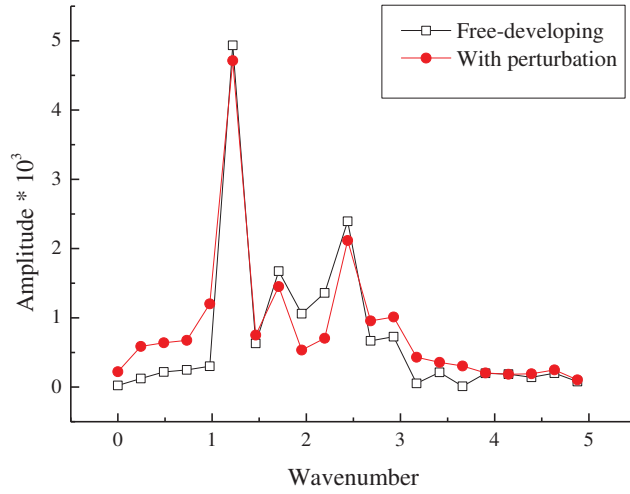
Figure 3.8 Characteristic wavenumber for the free-developing case and the perturbed case at $(KC, \beta) = (2, 200)$.
Calculated through FFT at $N = 100$.

The characteristic wavenumbers in phase III for the two cases obtained through FFT are compared in Figure 3.8. As is observed from Figure 3.8, both cases with and without perturbation bear the same dominant wavenumber of 1.2 (the maximum value from the curve), corresponding to five main vortex pairs (the same as demonstrated in Figure 3.7). In addition, the second peak value and even the third peak value of the two FFT curves match very well, and the trends of the whole curves for the two cases are also very similar. Recall that the perturbation prescribed is a random value both in space and in time, it is thus found that the random perturbation is filtered out as the flow field finally evolves into a Honji instability similar to the results of the free-developing case, with a characteristic wavenumber of 1.2. This means that the characteristic wavenumber reflecting the frequency of the Honji structures is not modified by adding the perturbation.

3.4.2.2 Pressure distribution
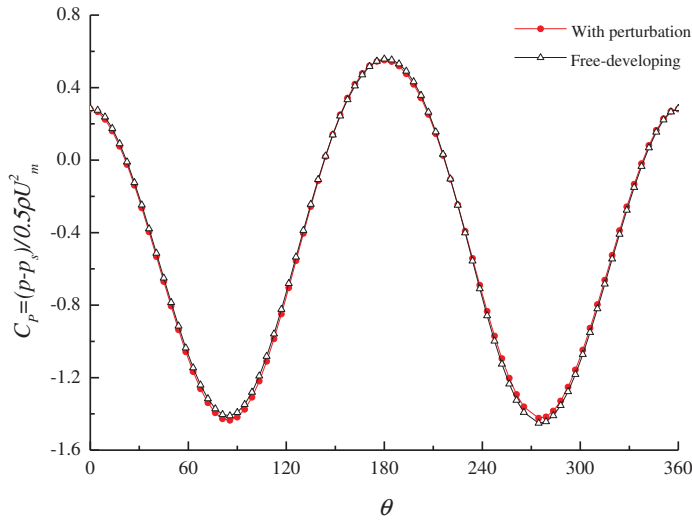
Figure 3.9 Pressure distribution along the cylinder circumference for the free-developing case and the perturbed case at $(KC, \beta) = (2, 200)$. Calculated at $N = 100$ and probed in the plane of $z/D = 2$.

Figure 3.9 presents the circumferential distributions of the mean pressure coefficient C_p for the two cases at $N = 100$. The measurement points are in the cross-sectional plane of $z/D = 2$, the axial location of which is indicated in Figure 3.13. The definition of C_p is given in Equation 3.7, in which P_s is the reference pressure taken from the pressure at the far field.

$$C_p = (P\text{-}P_s)/(0.5\rho U^2_M) \qquad\qquad 3.7$$

As demonstrated in Figure 3.9, the pressure distributions around the circumference calculated for the two cases agree quite well. It is observed that, for both cases, Cp bears a symmetric distribution with respect to the centre line (the *x*-axis) The largest value of Cp is found at $\theta = 180°$, which is the present front portion of the cylinder in relation to the instantaneous flow direction (which is the same as shown in Figure 3.1). The value of Cp is slightly smaller at $\theta = 0°$, i.e. the rear of the cylinder in relation to the flow direction, where Cp is close to zero. This means the pressure at the front of the cylinder is close to the far field value. Near the top and bottom of the cylinder ($\theta = 90°$ and $270°$), Cp shows negative peaks, and has the largest distinction from the far field, as a result of

the Honji vortical structures. Although small differences between the peak values are found, they are in fact negligible and the overall trend of the circumferential distribution of Cp repeats that without the perturbation.

3.4.2.3 Distribution of the velocity components

The non-dimensionalized velocity components, namely u_x, u_y and u_z, at $N = 100$ calculated for both the free-developing case and the perturbed case are compared along two probing lines in the cross-sectional plane of $z/D = 2$. Results are plotted in Figure 3.10 for the probe line of $\theta = 0°$ at the cylinder shoulders in the range of the added perturbation, and in Figure 3.11 for the probe line of $\theta = 90°$ at the cylinder crown within the range of the Honji instability. At the instant shown, the flow is at its peak, and the values of the velocity components at the far field is $(u_x/U_{mx}, u_y/U_{mx}, u_z/U_{mx}) = (1, 0, 0)$.

For the case of $\theta = 0°$ shown in Figure 3.10, the distributions of u_x, u_y and u_z for the two cases agree fairly well, especially for the streamwise component of u_x and axial component of u_z. It is observed from Figure 3.10a that u_x increases from zero at the cylinder surface to the value of one in the streamwise direction along $y/D = 0$. The other two velocity components, namely u_y and u_z, are both zero at the far field. However, in the region close to the cylinder, a positive u_y can be observed in the range of approximately $0.5 \leq x/D \leq 1$. Within this range, it is noticed that the positive u_y for the perturbed case is slightly larger than that measured for the free-developing case, which is attributed to the added perturbation. The relative difference between the maximum values of u_y/U_{mx} for the perturbed and free-developing case is roughly 17%. This is because that the free-developing case at $N = 100$ is not as fully developed as the perturbed case. However, as shown in the figure, the general trend of the velocity distributions agree well with each other.

For the distribution demonstrated in Figure 3.11, the recorded points close to the cylinder fall in the range of the Honji vortical structures. Therefore in the near-cylinder region, when increasing from the zero value resulting from the prescribed no-slip boundary condition at the cylinder surface, the component u_x becomes larger than the free stream (= 1) due to the formation of the Honji vorticity, and is restored to a value of

one at locations further away from the cylinder. The distributions of u_x from both cases have good consistency as shown in Figure 3.11a. For the other two components u_y and u_z, the velocity distributions close to the cylinder surface bear both a positive and negative value, again due to the formation of the vortical structures. Despite the negligible small differences observed in Figure 3.11b,c, the trends of the distribution curves are very similar. The velocity distributions within the Honji vortical structures obtained from both cases have good consistency for all three components.

It is found that adding the perturbation results in no significant alteration of the distribution of the primitive velocity components either in the region after the cylinder where perturbation is applied or in the cylinder crown where the Honji vortices evolve. Still, a more rigorous comparison is given on the calculated standard deviation value of the axial velocity component in the next section.

(a)
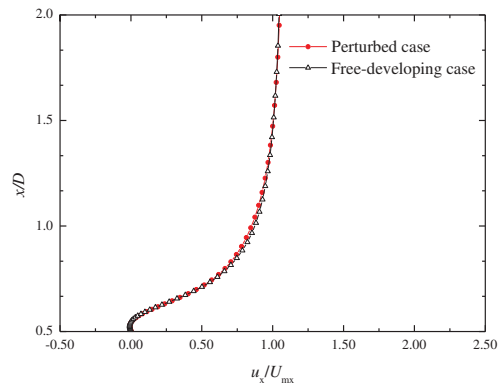
(b)
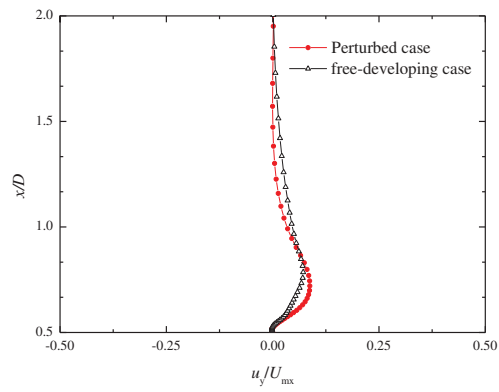
(c)
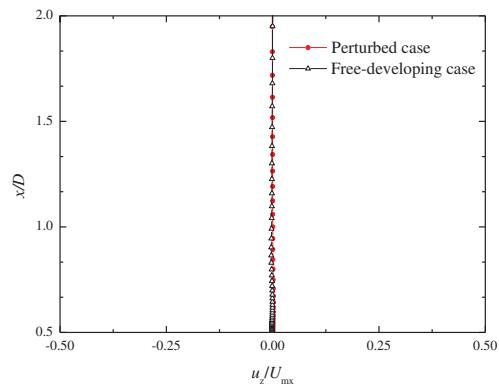
Figure 3.10 Instantaneous velocioty components plotted against x/D (along $\theta = 0°$) in the cross-sectional plane of z/D $= 2$ at $N = 100$. Ambient $|u_x/U_{mx}| = 1$, $|u_y/U_{mx}| = 0$, $|u_z/U_{mx}| = 0$.

(a)
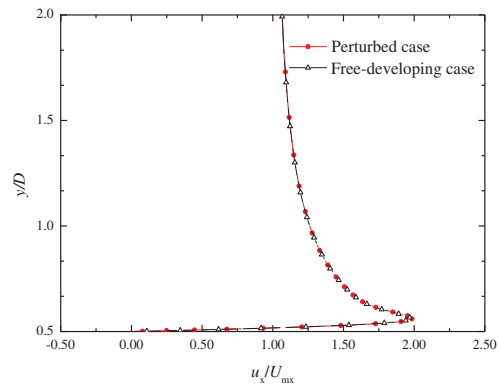
(b)
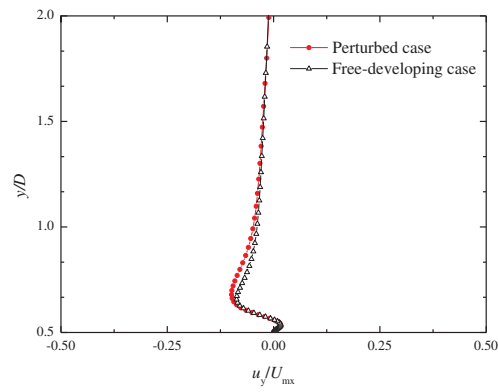
(c)
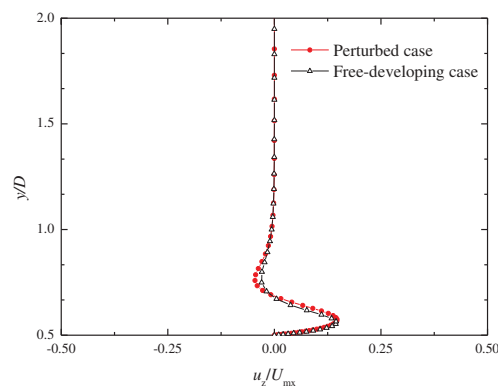
Figure 3.11 Instantaneous velocioty components plotted against y/D (along $\theta = 90°$) in the cross-sectional plane of $z/D = 2$ at $N = 100$. Ambient $|u_x/U_{mx}| = 1$, $|u_y/U_{mx}| = 0$, $|u_z/U_{mx}| = 0$.

3.4.2.4 Circumferential distribution of the statistic axial velocity

A quantitative description that compares the free-developing flow with the perturbed case is given using the standard deviation of the axial velocity component (u'_{zstn}), which can be calculated using Equation 3.4. As mentioned before, this value reflects the spatial growth of the instability around the cylinder circumference.

Results obtained from the two cases are presented in Figure 3.12, from which it can be observed that the trends of the two curves are very close. Around the half circumference, for both cases the value of u'_{zstn} grows in the range of $\theta = 0°$ to $110°$, with the largest growth rate observed from $30°$ to $80°$ and a relatively flat slope afterwards until $110°$. After that point, the value of u'_{zstn} decreases quickly to zero at the opposite side of the cylinder when the locations are out of the Honji vortical range. Although the two cases show similar growing trend, there exist small differences in the absolute values of the calculated u'_{zstn}. The largest difference in the value of u'_{zstn} between the two cases is found at around $110°$, where u'_{zstn} for the perturbed case is larger than u'_{zstn} for the free-developing case by 9.8%. Therefore, the additional perturbation exerts no effects on the spatial growth trend caused by the instability in this case.
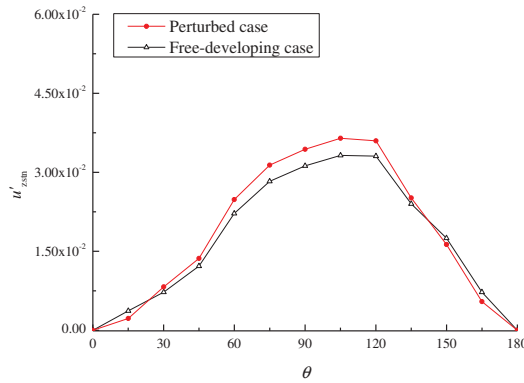
Figure 3.12 Instantaneous distribution of standard deviation of the axial velocity component (u'_{zstn}) verses spatial phase angle θ around half circumference of the cylinder at $N = 100$, for selected data points with a uniform interval of 15°.

So far, we have discussed the flow development and instantaneous flow properties such as the distributions of pressure and velocity components. The comparison between the free-developing case and the perturbed case shows good consistency. It is also necessary to present the 3-D flow structures obtained under the two cases for the evaluation of the effects of prescribing the additional perturbation.

3.4.2.5 Three-dimensional flow structures
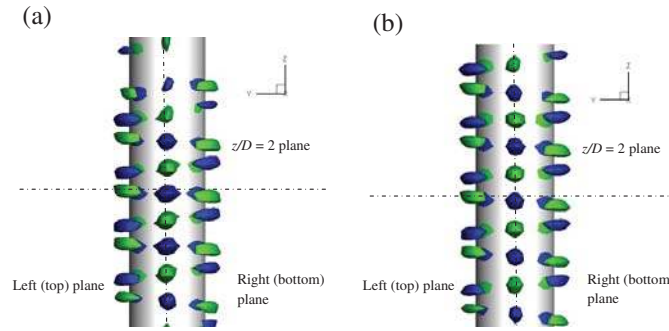
Figure 3.13 Instantaneous structures of iso-surface of ω_x near the cylinder for (a) perturbed case and (b) free-developing case at $(KC, \beta) = (2, 200)$. Plotted at $N = 100$. The view direction is illustrated by the coordinate system in each figure, which indicates that the figures are plotted in the direction of the major axis of the elliptic cross section. With respect to the x-axis, the left is regarded as the top plane (i.e. the circumferential range from $\theta = 0°$ to $180°$ as previous defined) and the right the bottom plane (i.e. the circumferential range from $\theta = 180°$ to $360°$).

To further confirm that the resultant flow field is not altered by the perturbation, the instantaneous flow structures at $N = 100$ in the quasi-static phase III are compared between the perturbed case and the free-developing case. The flow field is visualized using the iso-surface for the vorticity component ω_x presented in Figure 3.13. Here the x-component of vorticity, ω_x, is defined as $\omega_x = (\frac{\partial u_z}{\partial y} - \frac{\partial u_y}{\partial z})$. In Figure 3.13 the iso-surfaces are given for the unit value of $\omega_x = \pm 1$, with the two colours denoting two opposite directions of rotation.

As seen in Figure 3.13, the resultant vortical structures from the two cases are very similar. All the features that can be observed in the instantaneous flow field for the free-developing case (Figure 3.13a) can also be observed for the case calculated with perturbation (Figure 3.13b). For both cases, the resultant 3-D flow fields take the form of two arrays of five two-layer vortex pairs distributed at opposite sides of the cylinder. Each two-layer vortex structure consists of a pair of counter-rotating vortices, which are

rib-like in the top layer, and in the form of flat patches in the bottom layer. As observed in Figure 3.13, for both cases the two arrays are in a staggered arrangement.

Nevertheless, a closer examination of Figure 3.13 shows two slight distinctions between the resultant flow fields from the two cases. It is observed that the five vorticity pairs on two sides of the cylinder are all complete and distinct for the perturbed case, while there is one vortex pair with half missing and only a single vortex remaining for the case of the free-developing case. This is in consistence with the flow development shown in Figure 3.7a, from which it can be seen that, at $N = 100$ (the instant shown in Figure 3.13), a merging of two vortices for the free-developing case just finishes, which explains the remaining single vortex in Figure 3.13a. In addition, the vortices formed under the perturbed flow field (Figure 3.13b) generally appear to develop into a slightly fuller shape than the free-developing case (Figure 3.13a). This is probably caused by effects of the additional perturbation on slightly enhancing the instability of the fluid particles at the perturbed area, and those particles are then convected to the Honji region to result in stronger Honji vortices. Also, as mentioned previously, the addition of perturbation causes the instability to develop faster. However, these small distinctions do not alter the consistence of the main characteristics of the resultant vortical structures from the two cases both with and without the perturbation.

3.5 Conclusions

This chapter describes a method of introducing a lasting perturbation to the free-developing flow field. This method borrows the idea from the direct stability analysis previously adopted for studying thermal dynamic stability problems [94, 98].

Under the chosen parameter group of $\beta = 200$ and $KC = 2$, the mathematical formulation and evaluation for the definition of an appropriate perturbation are discussed. Applied as a source term in the governing equations, the perturbation is lasting during the calculations in order to check the convective instability of the flow field. Also for this aim, the perturbation is applied at the shoulders of the cylinder so that it is out of the region at which Honji vortices form. The perturbation term is defined as given in Equation 3.3, and each term in the definition formula is evaluated based on two aspects:

one, the instability can be induced earlier and two, the main characteristics of the resultant flow field remain unchanged . Finally, the perturbation is determined to be with amplitude of 0.2, with a sinusoidal component consistent with the free stream, and is random along the cylinder span.

Effects of the perturbation on the resultant flow field are evaluated by comparing the results obtained for both a free-developing flow field and a perturbed flow field under $(KC, \beta) = (2, 200)$. Calculations are run for 100 oscillation periods for both the cases with and without the perturbation. It is found that a full development process for the 3-D Honji instability can experience three different stages, namely, phase I, phase II and phase III. Phase I stands for the featureless two-dimensional flow before three-dimensionality appears. Phase II marks the onset of three-dimensionality caused by the Honji instability, which takes the form of evenly, distributed vortex pairs. Phase III is represented by the breaking of the balance between the evenly distributed vortices, and interactions between neighbouring vortices can be observed in this phase. Flow visualization in phase III shows that the two vortex arrays on two half planes of the cylinder distribute in a staggered manner with respect to the cylinder's main axis. The three-phase flow development is typical for the calculations under the Honji instability, as shall be discussed in the following chapters.

It is shown that applying a carefully chosen and evaluated perturbation fulfils our main objectives for applying the perturbed method. First, adding the perturbation at the two shoulders of the cylinder ($\theta = 0°$ and $180°$) saves computational time as it induces the instability earlier, as demonstrated by the comparison of the flow developments between the free-developing case and the perturbed case; second, this method provides a way of introducing a lasting perturbation which enables us to check against the convective instability and hence to determine the intrinsic stability of the flow. Since adding the perturbation at the cylinder shoulders induces the vortical structures at the vertex of the cylinder to occur earlier, the Honji instability is regarded as a convective instability.

At the same time, through comparisons conducted on several aspects including the flow development, quantitative values (such as pressure and velocity components) and visualization of the instantaneous flow structures, it is found that the additional

perturbation poses no significant influence on the free-developing field as to alter the key features of the resultant flow field. Hence the perturbation method is regarded as successful and, when necessary, can be applied to some of the main calculations discussed in the following chapters.

The perturbation method is used in addition to the free-developing calculations in the main calculations described in both Chapter 4 and Chapter 5, where the perturbation method is used for checking against the convective instability for the cases that the flow field remains 2-D over 200 flow periods, so that the intrinsic stability of the flow field can be confirmed. In Chapter 5, for calculations of the flat cylinder case where the 3-D features are very weak, perturbation is also applied to stimulate the flow development. Another aim of applying perturbation for this case is to check if the Honji vortical structures can develop when slight perturbation is applied at the cylinder shoulders, i.e. to check against convective instability of the flow field.

CHAPTER 4

HONJI INSTABILITY UNDER OBLIQUE INFLOW

4.1   Aim of chapter

In this chapter, we will examine the effects of an axial flow component on the resultant flow field under the governing parameters where Honji instability occurs around a circular cylinder immersed in a perpendicular oscillatory flow.

4.2   Introduction

Although many investigations of Honji instability at low KC and β values have been conducted which are of vital importance in providing some fundamental ideas, the understanding of this issue remains far from complete. Previous studies mainly focus on the situation where the flow approaches the cylinder perpendicularly. This chapter is going to examine an oblique oscillatory flow around a circular cylinder under Honji instability regime.

There are few investigations concerning the features of Honji instability with regard to oblique incidence or flow past yawed cylinders. Previous studies on yawed cylinders addressing the issue of the effects of angle of attack mainly concern either steady current over an inclined cylinder or oscillatory flows around a cylinder at relatively large KC or β numbers where vortex shedding flow dominates. The majority of these studies focus on the discussion on the hydrodynamic force and the validation of the independence or cross-flow principle ([7], which states that the perpendicular force component on the cylinder is only related to the flow velocity component normal to the cylinder axis and is invariant of the angle of attack) rather than giving a detailed description of the flow field [35-40, 42, 62, 99].

The primary aim of the present chapter is to extend our understanding of the Honji instability to the case where the incident flow is not perpendicular to the cylinder. Numerical simulations are carried out to investigate the influence of the incidence angle of the incoming flow on the Honji instability that occurs when the flow transits from 2D to 3D. The effect of angle of attack is assessed by introducing a suitable axial flow component parallel to the axis of the cylinder, to which point we shall return later. The present study is the extension to the study by An et al. [21], where oscillatory flow perpendicular to an isolated cylinder is examined in the subcritical flow regime and the transition from 2-D flow to 3-D flow through Honji instability is observed. In the contents below, comparisons are made among the simulated flow fields of different oblique angles at β = 200, 300 and 400 and KC = 2. The governing parameters covered by the numerical calculations in the course of this study are illustrated in Figure 4.1.
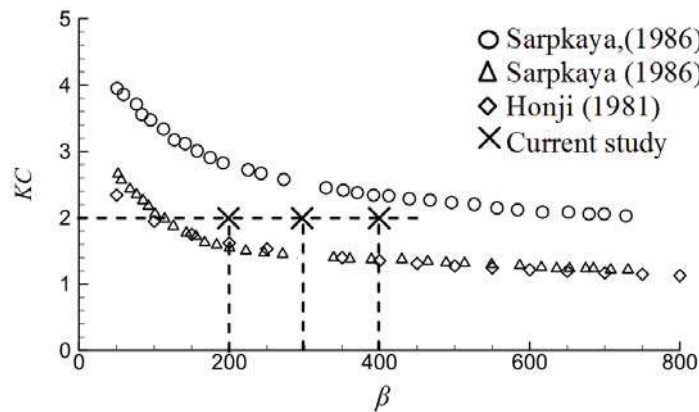
Figure 4.1 Flow regimes depending on KC and β.

4.3   Methodology

The computational problem is to solve the incompressible Navier-Stokes and continuity equations (given in Chapter 2 and Chapter 3).

4.3.1   **Computational domain**

The computational domain applied in this section is similar to that shown in Figure 2.1. Its dimension is $40D \times 20D \times 4D$ in the x-, y- and z- directions respectively. As

mentioned in Section 2.3.1, the free stream oscillates parallel to the *x-z* plane. For the oblique inflow concerned in this chapter, the flow velocity can be decomposed into two mutually perpendicular directions. As a result, the free stream has sinusoidal velocities in both the *x* (streamwise) and *z* (spanwise or axial) directions, as given in Equation 4.1. The flow incidence angle (oblique angle or angle of attack, α) is defined as the angle between the *x*-axis and the free stream velocity as shown in Figure 4.2. In this study, the velocity component normal to the cylinder span is the *x*-component of the inflow velocity (u_x). The nondimensional amplitude of the oscillating flow component in the *x*-direction is set to be a unit constant ($U_{mx} = 1$) throughout the calculations and the incidence angle α is obtained by varying the amplitude of the axial flow in the *z*-direction.

4.3.2 Initial and boundary conditions

The initial and boundary conditions are specified as that described in Section 2.3.5 with only one exception, i.e. the inlet and outlet boundary condition for flow past a circular cylinder at an oblique attack is given by

$$(u_x, u_y, u_z) = (1,0, \tan \alpha) \sin \frac{2\pi t}{T}$$

4.1

The angle of attack is defined as $\alpha = \tan^{-1} \frac{u_z}{u_x}$. Following this definition, larger incidence angle implies larger amplitude of the axial flow velocity. Figure 4.3 shows the incoming flow field under an attack angle of α.
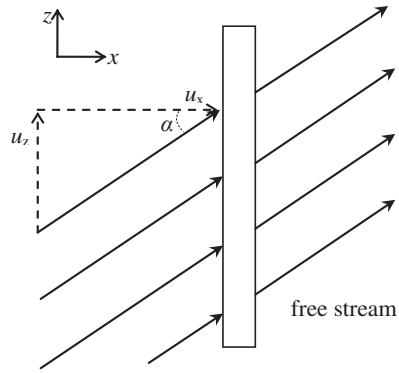
Figure 4.2 A definition sketch for the angle of attack α.

(a) $\alpha = 0^{\circ}$

(b) $\alpha = 10^{\circ}$

(c) $\alpha = 20^{\circ}$

(d) $\alpha = 30^{\circ}$
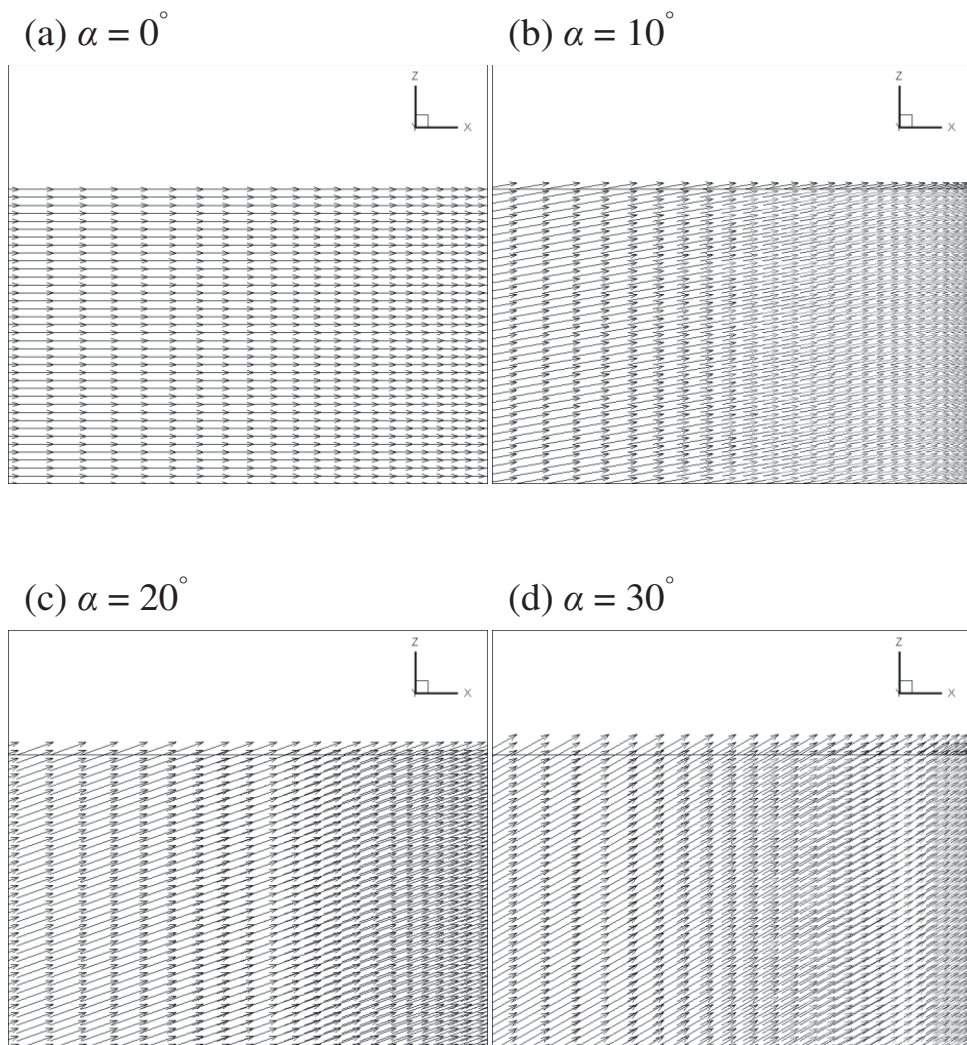
Figure 4.3 Velocity vectors from far-field (left) towards the cylinder (right) viewed normal to the oscillation plane for different incidence angles.

Numerical simulations are conducted to investigate the effects of flow incidence angle on flow characteristics around the cylinder at $KC = 2$ and $\beta = 200$, 300 and 400. According to An et al. [21], 3-D Honji instabilities exist in this KC and β range for a perpendicular approaching flow (i.e. $\alpha = 0°$). The angle of attack, α, is in the range of $0°$ to $40°$ in the present study. The values of α chosen actually depend on the β value because, at a constant KC, the latter is related to the intrinsic three-dimensionality of the flow, as will be shown in the discussions given below.

4.4   Flow development over 200 periods

The three-dimensionality of the flow can be observed from the variation of the axial velocity along the cylinder span. Flow development is represented by the same approach of spatial-temporal figures used in Section 3.3.3. In total, 200 flow oscillations are calculated for all the cases to allow sufficient development of the flow field, and the results are presented in Figure 4.7, Figure 4.8 and Figure 4.9.

4.4.1   **Flow development for $\alpha = 0°$**

The flow behaviours for the perpendicular inflow cases are first examined before comparing the differences resulted from various α values. It is observed that over the $200T$, the development of the instability can be divided into three main phases labelled in Figure 4.7 to Figure 4.9: phase I (for the 2-D featureless flow), phase II (for the transient evenly-distributed vortices stage) and phase III (for the interactive stage with axially shifting vortices). Descriptions of the characteristics for the three phases are given in Section 3.3.3.

The generation of the new vortices and merging of the existing vortices observed in phase III results in the 'fork-like' structures shown in Figure 4.4a. The instantaneous flow structures at three instants during the transient period are illustrated in Figure 4.4b,c,d, where we can see that an additional half vortex pair (circled in Figure 4.4b,c,d) appears between two existing vortex pairs and finally merges with the one of the same sign, causing the latter to be slightly stretched at $N = 120$ (Figure 4.4d). This process causes one vortex pair (the one with the same sign as the transient half period) to shift

along the cylinder, when other main vortex pairs remain to be at their original axial locations until they merge with the transient vortex pair to be generated next to each of them. The generation and merging of the vortex pairs, happening at two sides of the cylinder simultaneously (circled in blue dashed lines in Figure 4.4b,c,d), results in a slight shift of all pairs along the cylinder span. The transient vortex pair consists of two counter-rotating vortices similar to the other main vortex pairs. The reason why only half of the vortex pair can be observed in Figure 4.4 is attributable to the inequality of the two counter-rotating halves, i.e. the vorticity intense of one half of the vortex pair is simply smaller ($\omega_x < 1.0$) than that shown in the unit iso-surface for $\omega_x = 1.0$, as mentioned in the following paragraph.

The mechanism of the generation of transient vortex pairs and merging of main vortices is explained through the process demonstrated in Figure 4.5. When the flow is intrinsically unstable, the numerical residuals during the calculations will accumulate and finally result in the transition from 2-D to 3-D. At early stage of the calculations, the flow first remains 2-D, until the accumulation of the residuals becomes sufficient to trigger the first appearance of three-dimensionality represented by the transient phase II, which appears in the form of vortex pairs evenly distributed along the cylinder. This type of structure lasts for some time before the balance between these equally spaced vortex pairs are broken by the increasing numerical residuals as the instability develops, which leads to the more active vortices.

As shown in Figure 4.5a, the first vortex shifting is then observed which results in the merging of two neighbouring vortices (denoted by V_{01} and V_{02}, with the first subscript representing the finished number of merging and the second subscript indicating the vortex sequence number along the cylinder). This process is the same as that described in An et al. [21] for the case of $\beta = 300$. The merging results in a new vortex pair (denoted by V_1, from V_{01} & V_{02}) that is stronger than the other main vortex pairs and located in the middle of the original locations of the former V_{01} and V_{02} (Figure 4.5b). As a result, the distance between V_1 and its neighbouring vortex pair (V_{03}) is larger than the average spacing between the main vortex pairs so that a new vortex pair is allowed to emerge. At the same time, the distance between V_1 and V_{03} is smaller than the axial dimension of a proper main vortex pair; hence, the local vortex pair generated cannot

fully develop and is finally ingested by the neighbouring stronger vortex pairs, i.e. this new vortex pair is only transient.

Figure 4.5c shows that the new transient vortex pair (T_1) is consisted of two halves of counter-rotating vortices originating from two neighbouring vortex pairs, namely, V_1 and V_{03}. Recall that V_1 resulted from merging is more intense than the original main vortex V_{03}, therefore the half vortex T_{1r} close to and arising from V_1 is stronger than its counter-rotating part (T_{1l}). The inequality of the two halves (T_{1r} & T_{1l} as given in Figure 4.5c remains through the transient growth of T_1 for the next several periods with the most distinct formation seen at $N = 110$ (Figure 4.5c).

Finally, as seen at $N = 115$ in Figure 4.5d, the weaker half T_{1l} is completely ingested and suppressed by the stronger half T_{1r}. T_{1r} then draws and connects to the same-signing half of the main vortex V_{03}. Merging of T_1 and V_{03} causes a temporary stretching of the same-signing half of V_{03} as well as an axial shifting of the whole V_{03}, as observed in Figure 4.5d,e. At the same time, formation of V_{03} also marks the beginning of generation of another new transient vortex nearby, and the whole process will repeat itself again in the space between V_2 and V_{04}, where a new transient vortex pair T_2 is spawned as shown in Figure 4.5e,f.

The flow regime at $(\alpha, \beta) = (0°, 200)$ is regarded as a stable Honji regime because the interactions among the vortices in phase III are very weak. This is because the additional vortex pair generated temporally is weak and small compared with the main five vortices (as seen in Figure 4.4c, and therefore does not cause a fundamental change to the total wavenumber. The consistency in the characteristic wavenumbers obtained during the evolution of the transient vortex pair at instants in Figure 4.4 is evidenced by Figure 4.6 where the FFT (Fast Fourier Transform) of the axial velocity component is given. From Figure 4.6 we can see that, although the generation of the additional vortex causes the wavenumber to have a tendency towards 1.5 at $N = 105$ and 110, this vortex is so weak and transient that it does not change the dominant wavenumber, which is 1.2 for all three Ns shown in Figure 4.4 and Figure 4.6. Considering the cylinder length to be $4D$, the wavenumber value of 1.2 gives about five ($1.2 \times 4 = 4.8$) vortex pairs, in consistence to that shown in Figure 4.4. The transient vortex pair only exists for about

15 flow periods. At $N = 120$ only five main vortex pairs remain (Figure 4.4d). Therefore, the amplitude spectrum in Figure 4.6 corresponding to $N = 120$ shows a very dominant wavenumber of 1.2.
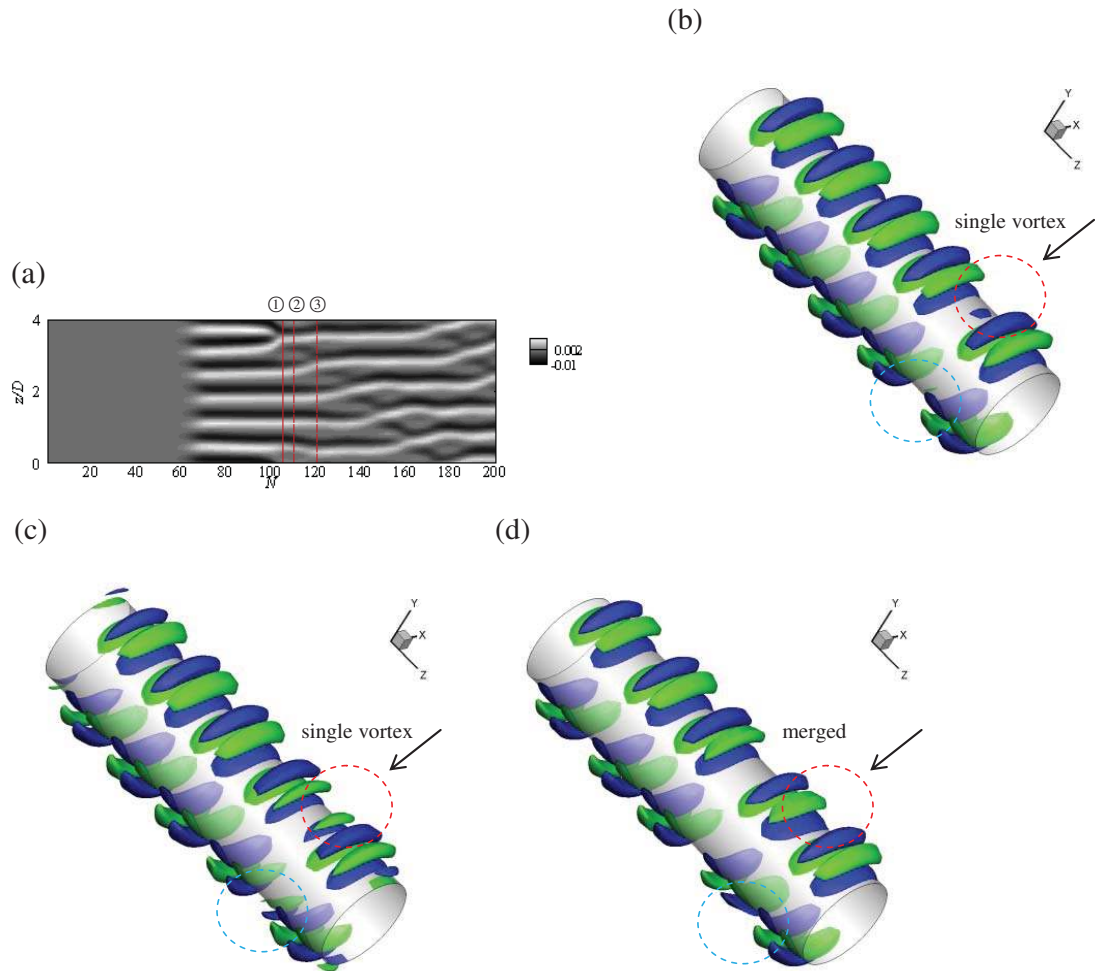
Figure 4.4 Demonstration of the generating and merging of an additional vortex in Phase III. Presented for the case of $(\alpha, \beta) = (0°, 200)$. The dashed circle in red is the probed side as in (a) locations of probing labelled in the spatial-temporal development figure. The dashed circle in blue is the opposite symmetric pair. (b) ω_x at $t/T = 105.25$, a new vortex pair is about to appear. (c) ω_x at $t/T = 110.25$, the additional vortex pair coexists with the main pairs. (d) ω_x at $t/T = 120.25$, end of merging.
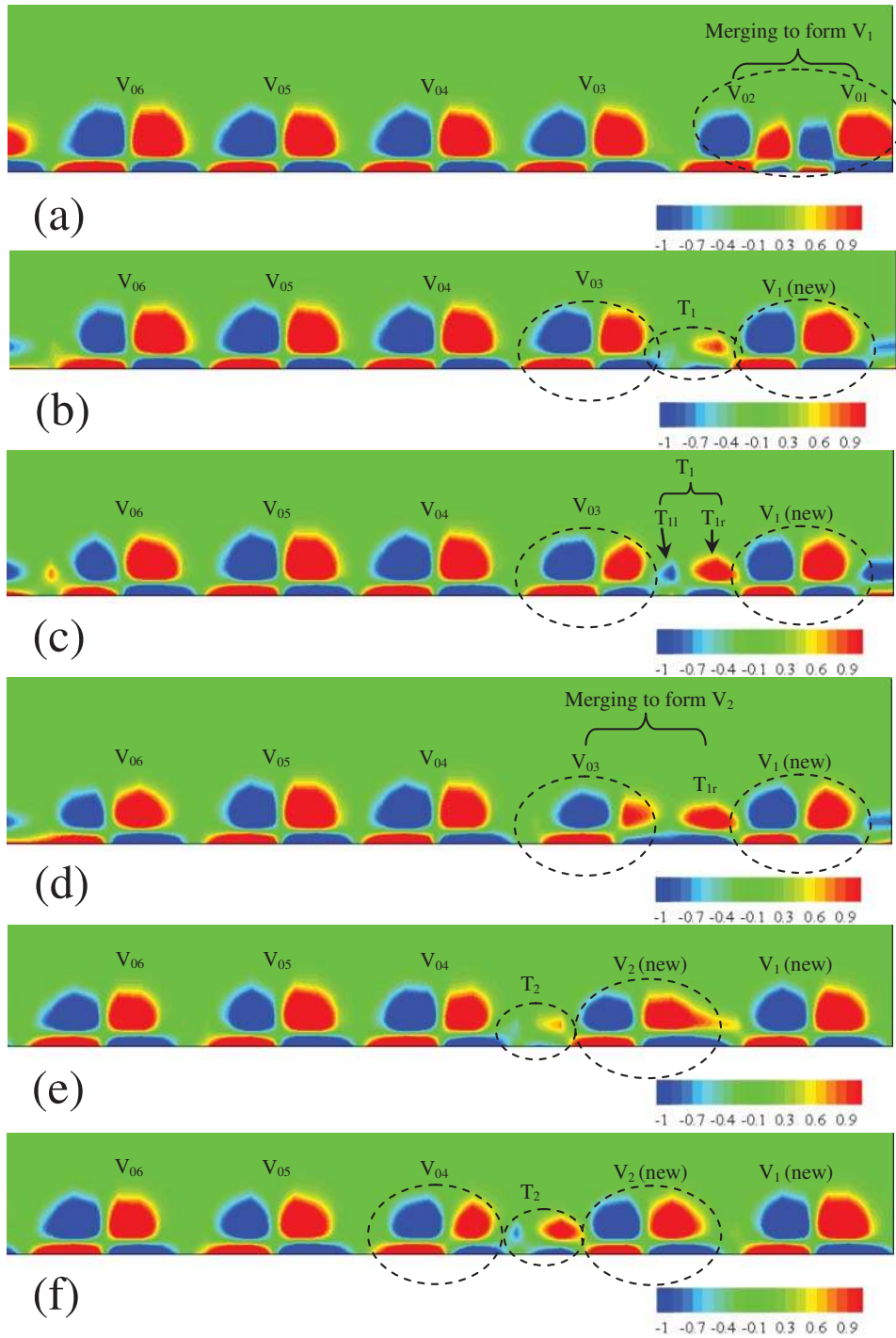
Figure 4.5 Plane view demonstrating the generating and merging process of a transient vortex pair T_1 in Phase III. (a) $t/T = 100$, the first merging of two neighbouring vortices. (b) $t/T = 105$, early appearance of the additional transient vortex pair. (c) $t/T = 110$, development of the transient T_1, with two unequal halves clearly seen. (d) $t/T = 115$, ingestion of the weak half T_{1l}. (e) $t/T = 120$, merging of the remaining half T_{1r} and the neighbouring main vortex pair V_{03}. (f) $t/T = 125$, completed one vortex interaction and shifting of V_{03}.
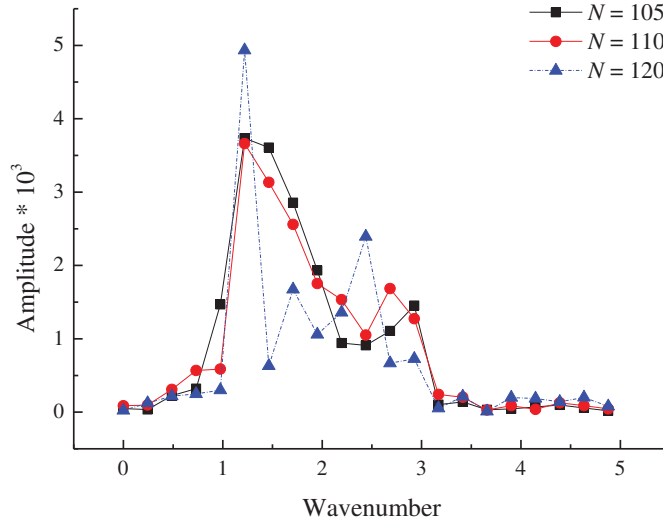
Figure 4.6 Wavenumber calculated through FFT (Fast Fourier Transform Algorithm) during the evolution of one transient vortex at the corresponding moments of Figure 4.4a.

4.4.2 Comparison between different values of α

Figure 4.7 compares the evolution of u_z/U_{mx} for a flow with parameters β =200 and KC = 2 and the angles of attack at $\alpha = 0°$, 10° and 20°. It can be seen from Figure 4.7 that, if the incidence angle of the flow is increased from 0° to $\alpha = 10°$ the initial 2-D structure changes to 3-D flow slightly later, with phase II starting at about $N = 70$ for $\alpha = 10°$ compared with $N = 60$ for $\alpha = 0°$. It is noticed that for $\alpha = 10°$, although the first merging of two equal vortex pairs happens at $N \approx 100$, marking the onset of phase III and leaving six evenly distributed vortex pairs along the cylinder span, the persisting interactions between two pairs of neighbouring vortices is not observed. Neither observed is the shifting of all vortex pairs after generation and merging of an additional transient vortex never appears until $N = 200$. The less active vortex behaviours indicate the weakening of the flow instability. It is noted that there are six vortex pairs formed along the cylinder, compared with five in the perpendicular inflow case. The flow is further stabilised when α is increased larger to 20°, see Figure 4.7c. For $\alpha = 20°$, the flow remains in the 2-D phase I throughout the calculation and no evidence of 3-D flow is observed. The instability never occurs with α higher than 20° and the flow development is the same as presented in Figure 4.7c.
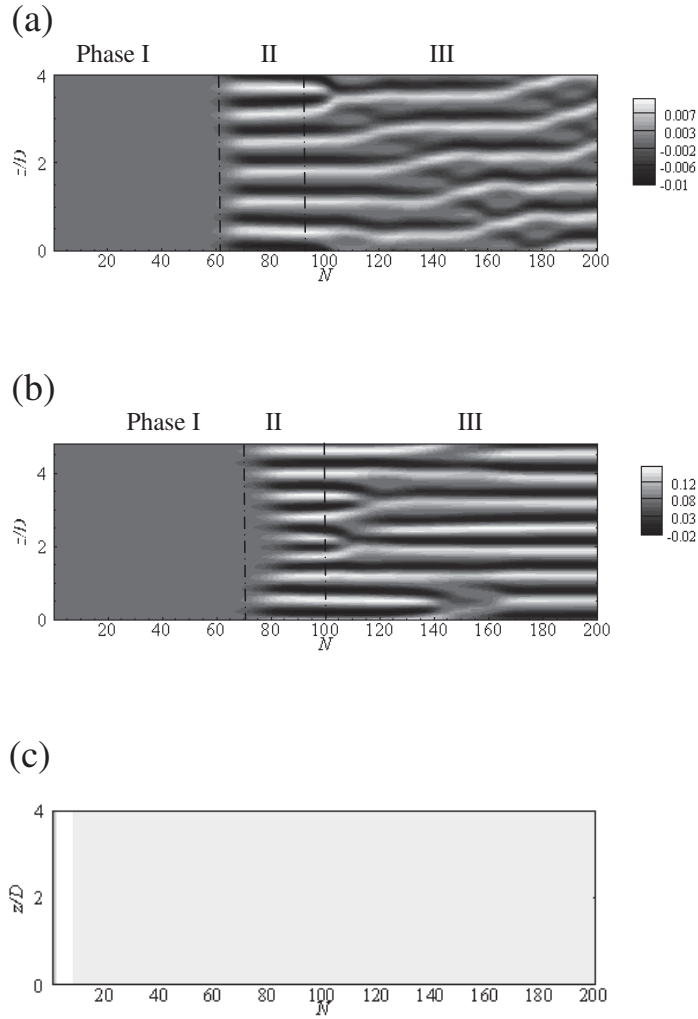
Figure 4.7 Evolution of the relative axial velocity component u_z/U_{mx} at β =200 and for angles (a) $\alpha = 0°$ (b) $\alpha = 10°$ and (c) $\alpha = 20°$.

The analysis of the vortex structures for $\alpha = 0°$, $10°$, and $20°$ suggest that larger angle of attack or an increase in the axial flow velocity weakens the Honji vortices. Further evidence of this observation is provided by calculations at higher β values of 300 and 400, for which results are given in Figure 4.8 and Figure 4.9 for different values of α.

To evaluate the effects of increasing β, the cases of $\alpha = 0°$ for β =300 and β =400 are first examined. As is expected, the 3-D instability becomes stronger as β increases while KC is kept constant, as reflected by the earlier start of phase II and stronger interactions among the vortices. When $\alpha = 0°$, phase II starts earlier and is much shorter for $\beta = 300$ and $\beta = 400$ (lasting for about 10 and 5 flow periods respectively), compared with the β = 200 case where phase II takes over about 30 flow periods from N = 60 - 90. In

addition, for $\beta = 300$ and $\beta = 400$, strong interactions between vortices can be seen in phase III, and the interaction at $\beta = 400$ is stronger than that at $\beta = 300$ (see Figure 4.8a and Figure 4.9a).

Now the effects of increasing α for each β are discussed. In consistence to what is previously mentioned for varying α at $\beta = 200$, it is observed that the increase of α also reduces the 3-D instability of the flow for higher β values. As seen from Figure 4.8 and Figure 4.9, the interaction between vortices in phase III apparently weakens as α is larger. At $\alpha = 20°$ for $\beta = 300$ (Figure 4.8b), the interaction among the vortices is not as strong as that of $\alpha = 0°$, and the weaker regular-ordered evolution indicates a reduced three-dimensionality. The flow development for $\alpha = 20°$ at $\beta = 300$ (Figure 4.8b) appears very similar to that of $\alpha = 0°$ at $\beta = 200$, with the shifting of vortex pairs clearly seen in phase III. However, six vortex pairs distribute along the cylinder span for $20°$ at $\beta = 300$ compared with only five for $\alpha = 0°$ at $\beta = 200$. The case of $\alpha = 30°$ for $\beta = 300$ seems to be dominated by the 2-D phase I as seen in Figure 4.8c. For $\beta = 400$, a decreasing trend for three-dimensionality can also be seen with the increasing of α, reflected by the less irregularity of the velocity contours as α increases. For $\beta = 400$, the Honji modes occur at $\alpha = 30°$ where the flow develops into a phase III with six equally spaced vortices, but are suppressed once the angle of attack exceeds $40°$.
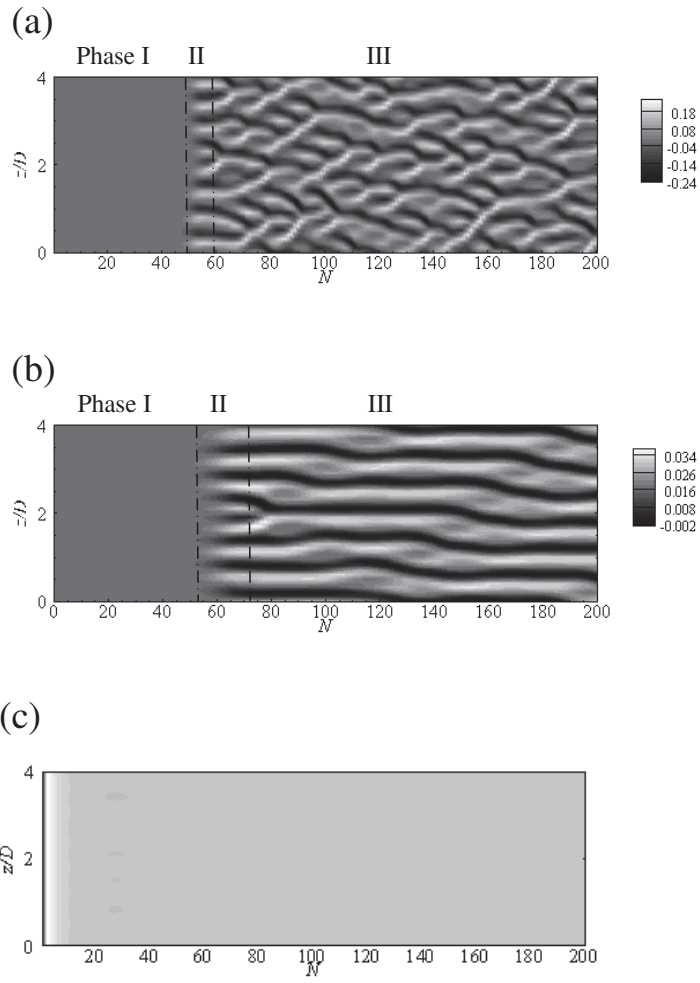
Figure 4.8 Evolution of the relative axial velocity component u_z/U_{mx} at $\beta =300$ and for angles (a) $\alpha = 0°$, (b) $\alpha = 20°$ and (c) $\alpha = 30°$.
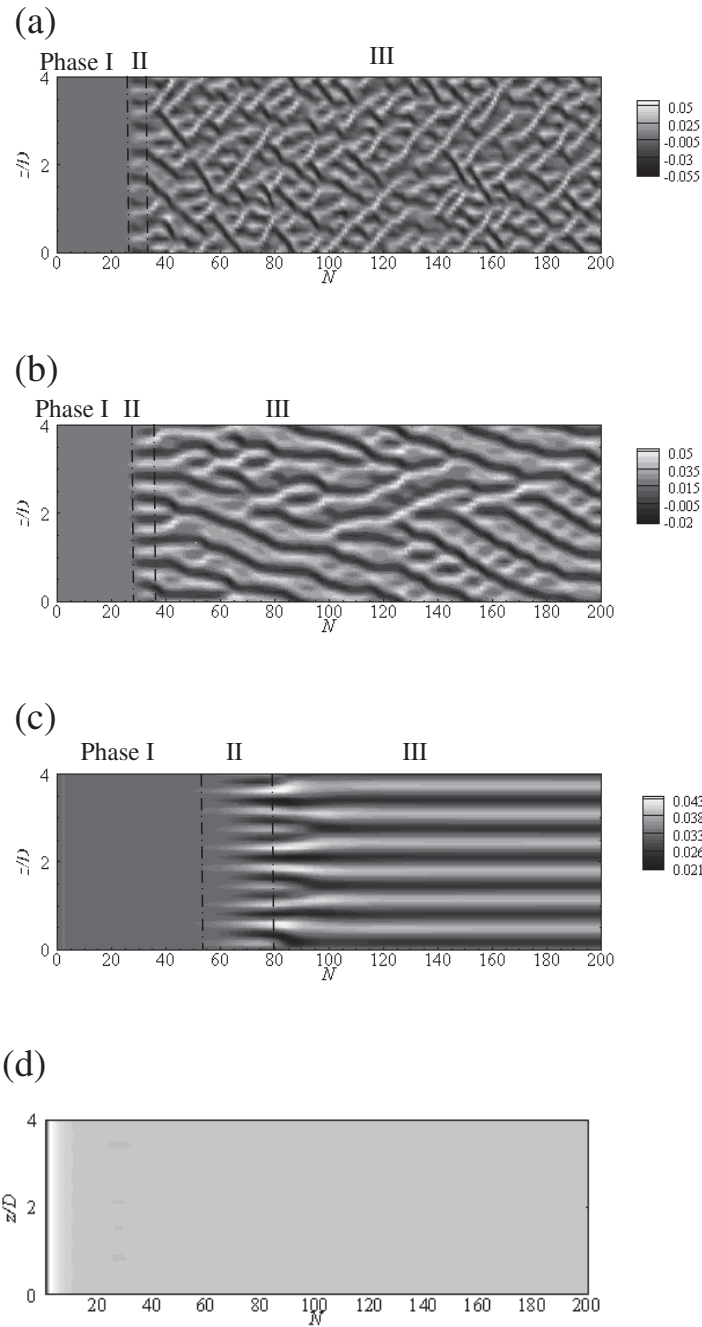
Figure 4.9 Evolution of the relative axial velocity component u_z/U_{mx} at β =400 and for angles (a) α = 0°, (b) α = 20°, (c) α = 30° and (d) α = 40°.

As mentioned in Section 2.1, in order to check the intrinsic stability for the cases of (α, β) = (20°, 200), (30°, 300) and (40°, 400), it is essential that these cases are evaluated against their possibility of being absolute unstable and convective unstable. First, for checking absolute instability, these cases were calculated with a pre-assigned 3-D flow field as the initial condition to see if the 3-D features amplify or diminish as the

calculation progresses. Figure 4.11 shows that the axial variation of u_z/U_{mx} is wiped off within 20 flow periods for all three cases and the flow resumes a 2-D featureless flow. It is noted that although Figure 4.11 only demonstrates the results probed at $\theta = 90°$, it has been checked that around the circumference from $\theta = 0°$ to $\theta = 360°$ no axial variation remains. This result shows that the flow is absolute stable. Next for checking the convective instability, we conduct calculations by perturbing the flow field using the method described in Chapter 3. It is found that no Honji instability is triggered in the perturbed flow field after 100 flow periods and that the flow remains 2-D, as indicated by the development figures as shown in Figure 4.7c, Figure 4.8c, and Figure 4.9d. The flow is hence exempted from being convective unstable. Therefore, it is confirmed that the Honji instability is suppressed for the cases of $(\alpha, \beta) = (20°, 200)$, $(30°, 300)$ and $(40°, 400)$, and that the flows are intrinsically stable.

(a)

(b)

(c)
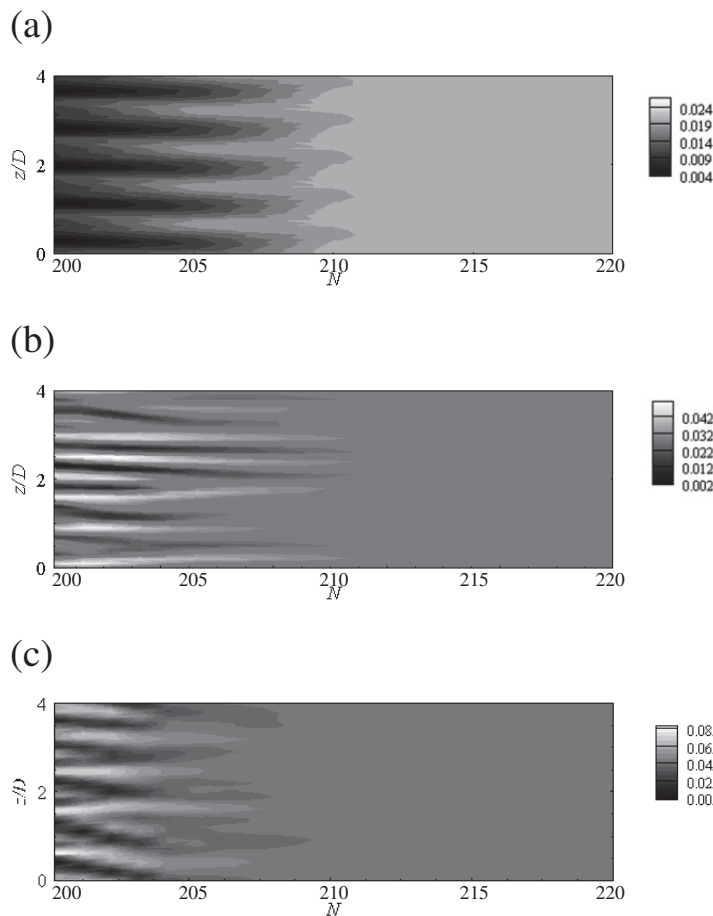
Figure 4.10 Contours of the relative axial velocity component u_z/U_{mx} for demonstrating the 3-D dissipation under large α for the cases of $(\alpha, \beta) = $ (a) $(20°, 200)$, (b) $(30°, 300)$ and (c) $(40°, 400)$.

The conclusion is that the larger the frequency parameter β, the larger axial flow component is required to suppress the 3-D Honji structure to grow until finally at some threshold, this instability mechanism can no longer operate.
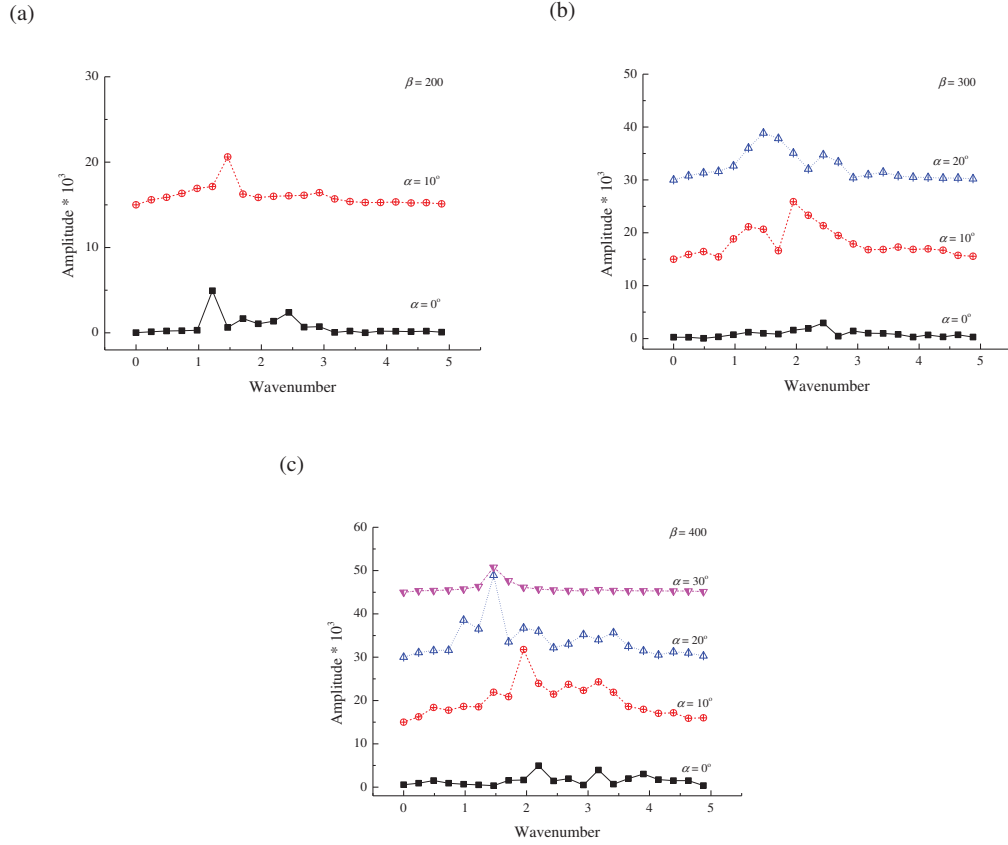
Figure 4.11 Characteristic wavenumber obtained from FFT under different α for (a) β =200, (b) β =300 and (c) β =400 at $N = 200$. An offset between different α is applied in each figure for aim of clarity.

The characteristic wavenumber obtained through FFT for the cases where the Honji instability exists is presented in Figure 4.11. The effects of increasing α are clearly seen for each β case evaluated here. At $\beta = 200$, a single dominant wavenumber is observed at both $\alpha = 0°$ and $\alpha = 10°$. The dominant wavenumber changes from 1.2 to about 1.5, as α is increased from 0° to 10°. As mentioned before (see Section 4.4.2), at $N = 200$ six evenly distributed vortex pairs are observed for $\alpha = 10°$ because of the weakened instability, resulting in a wavenumber of 1.5. For the perpendicular incidence cases for β = 300 and 400 which are strongly unstable, no dominant wavenumber is identified. As α grows, a dominant wavenumber begins to stand out, and the value of wavenumber decreases with an increase in α, indicating that fewer vortex pairs are distributed along

the cylinder span. The dominant wavenumber read from Figure 4.11 and the number of vortex pairs counted from the instantaneous flow structures for each case is listed in Table 4.1. The number of vortex pairs is in consistence with the calculated dominant wavenumber. For $\beta = 200$, the flow field of $\alpha = 10°$ (with six evenly distributed non-interacting vortices) is more stable than that of $\alpha = 0°$ (with five interacting vortices) as discussed in Section 4.4.2. The dominant wavenumber increased from 1.2 to 1.5 due to the increase of the number of vortex pairs. For $\beta = 300$ and 400, a decrease in instability with an increase of α is indicated by the fact that fewer interactions between vortices can be observed (represented by the standing out of a dominant wavenumber) and that fewer vortices are formed along the cylinder at large α.

Table 4.1 Comparison of calculated wavenumber and the number of vortex pairs counted for all cases studied.

β	200		300		400	
	wavenumber	Number of vortex pairs	wavenumber	Number of vortex pairs	wavenumber	Number of vortex pairs
$\alpha = 0°$	1.2	5	2.4	10	2.2 or 3.2	9 or 13
$\alpha = 10°$	1.5	6	2	8	2	8
$\alpha = 20°$			1.5	6	1.5	6
$\alpha = 30°$					1.5	6

4.4.3   Flow regime dependence on α and β

The results obtained thus far are sufficient to identify three regions in a α-β space as sketched in Figure 4.12. Based on our observations, three distinct flow regimes are defined as the following:

- Regime I for the unstable Honji regime;

- Regime II for the stable Honji regime;

- Regime III for the two-dimensional vortex-free regime.

Regime I arises at relatively large β and small α, where the flow is in the highly unstable Honji flow regime where neighbouring vortices interact strongly and frequently (merging and splitting). In contrast, within regime II, stable vortex modes hold which are seen as the typical mushroom-like structures. Last, within regime III, and at comparatively large values of α, the Honji mechanism is suppressed and featureless 2-D flow dominates throughout the calculations.

It should be mentioned here that Figure 4.12 is provided only as a general guidance, and the boundaries between the various regimes are somewhat speculative. This is because in order to locate the boundaries more accurately it would require extensive and lengthy calculations that are unlikely to be particularly instructive, especially when it is realised that the precise positions of the transitions between the regimes are also functions of KC.
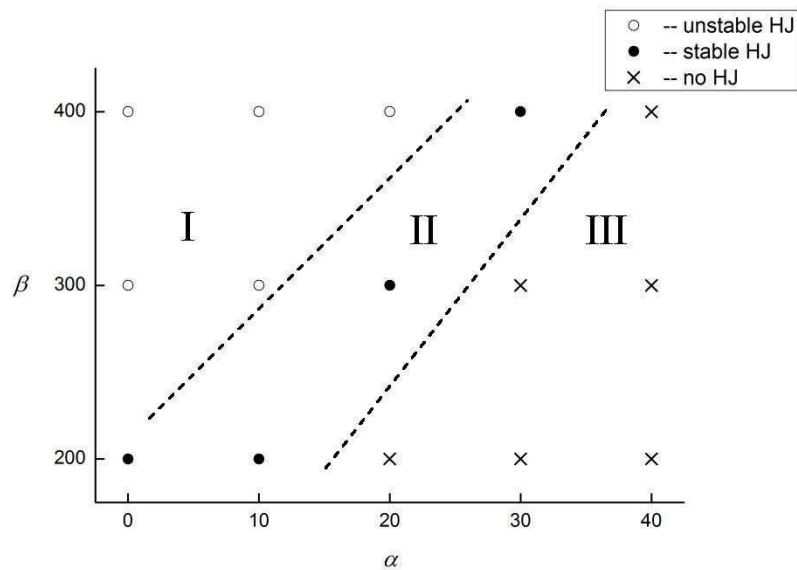
Figure 4.12 Sketch of the approximate geometry of the three flow regimes in α-β parameter space for $KC = 2$.

4.5 Developed flow structures

Further information relating to the nature of the vortical structures formed around the cylinder can be obtained from visualization of the typical instantaneous flow structures.

In the following the vortex evolution within one oscillation period is discussed. The results given are for $\beta = 200$ and 400 but the same observations also apply to the case of $\beta = 300$, which is not discussed here to avoid repetition.

4.5.1 Description of the instantaneous structures

The 3-D vortical structures are viewed in terms of the iso-surface of the x-component of vorticity ($\omega_x = 1$) as illustrated in   for $\beta = 200$, and in Figure 4.14 for $\beta = 400$. The vortices are much more active at higher β (400) than lower β (200), and strong interaction between the vortices is observed at $\beta = 400$ for $\alpha < 30°$. The interaction is impeded by the existence of an axial flow component. As mentioned previously, stable Honji structures occur when $(\alpha, \beta) = (0°, 200)$, $(10°, 200)$ and $(30°, 400)$. These structures appear as pairs of rib-like counter-signing vortices wrapping diametrically opposite sides of the cylinder, composed of two layers in the radial direction (see a, b and Figure 4.14d). For the oblique flow cases, the stable and regular vortical structures along the cylinder span are different from the typical Honji vortices formed under normal incidence, as shall be discussed later. At $(\alpha, \beta) = (20°, 200)$ and $(40°, 400)$ the flow does not possess any 3-D property and remains purely 2-D. For these cases the cylinder is wrapped by axially invariant vorticity contours, as is seen from c and Figure 4.14e.
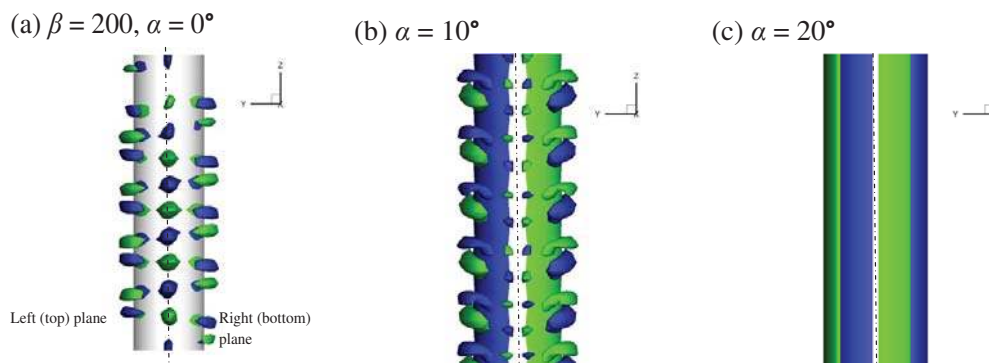
Figure 4.13 Instantaneous structures of iso-surfaces of ω_x near the cylinder at $KC = 2$ and $\beta = 200$ for various values of the incident angle α. (a) $\alpha = 0°$, (b) $\alpha = 10°$ and (c) $\alpha = 20°$. Plot at $N = 200$. The view direction is illustrated by the coordinate system in each figure.
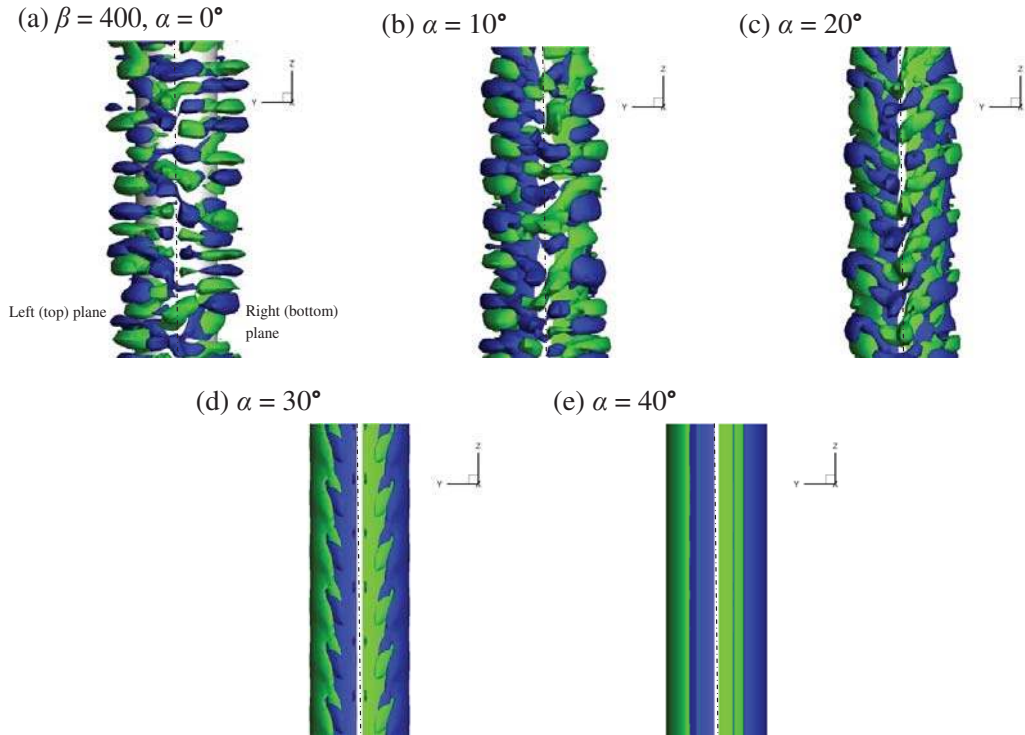
Figure 4.14 Instantaneous structures of iso-surfaces of ω_x near the cylinder at $KC = 2$ and $\beta = 400$ for various values of the incident angle α. (a) $\alpha = 0°$, (b) $\alpha = 10°$, (c) $\alpha = 20°$, (d) $\alpha = 30°$ and (e) $\alpha = 40°$. Plot at $N = 200$. The view direction is illustrated by the coordinate system in each figure.

It can be concluded that the 3-D features of the flow under oblique flows (i.e. $\alpha \neq 0°$) differ from those corresponding to $\alpha = 0°$ in several ways. First, it is obvious that the vorticity distribution in oblique flow acquires a sheet flow that lies below the rib-like vortices attached to the cylinder surface. This sheet flow leads to the existence of a uni-directional vorticity in the boundary layer. At $\alpha = 0°$ the two vortices in each pair are equally strong and symmetric and are perpendicular to the cylinder axis. In the oblique attacks, the vortex pairs are unbalanced and the two vortices in each pair are of unequal strengths and wrap around the cylinder (see most clearly in b). Last, for $\beta = 200$, the vortex pairs are distributed along the cylinder in a staggered manner when $\alpha = 0°$, but sit side-by-side when the incoming flow is oblique. This is because as shown in the flow development figures, that at $N = 200$, for $\alpha = 0°$ the flow has reached phase III with persisting vortex interactions, while for $\alpha = 10°$ six evenly-distributed vortex pairs along the cylinder span is observed. The vortex distribution is staggered because of the shifting of vortices caused by the generating and merging of the transient vortex. Since the flow at $\alpha = 0°$ is intrinsically more unstable than that at $\alpha = 10°$, the vortices are first

diametrically symmetric at phase II (similar as that shown in b), then become staggered in phase III as a result of vortex interactions.

4.5.2   Evolution of the two-layer structures within one flow period

The evolution of the two-layer vortical structure wrapping the cylinder surface in one period of the flow is studied in planes of $x/D = 0$ (perpendicular to the x-axis) and $z/D = 2$ (perpendicular to the z-axis). The locations of the z/D (cross-sectional) plane are indicated by the dashed lines in the $x/D = 0$ planes. It should be noted that the cross-sectional plane at a certain z/D value only reflects the evolution of specific vortices which can be shown in that plane. For the stable cases at $\beta = 200$, the vortices shown on cross-section planes such as $z/D = 2$ may reasonably present the behaviour of others as the vortices remain relatively identical along the cylinder span. However, for the strongly irregular cases of $\beta = 400$, the behaviours of the vortices in plane $z/D = 2$ only represent themselves, not the rest of the vortices at other axial locations. Nevertheless, for such cases we still analyse the behaviours of vortices on a chosen z/D in the hope of understanding the possible characteristics of a single unit under the unstable Honji regime through samples.

4.5.2.1 Vortices in x/D = 0 plane

The distribution of all the vortices along the cylinder span within one flow oscillation period is demonstrated in plane of $x/D = 0$ from Figure 4.15 to Figure 4.19. In each of these figures seven instants within one flow period are shown. In particular for the first half-period, five moments with an interval of $T/8$ are presented while only three moments with a $T/4$ interval in the next half period are given for aim of avoiding repetition. Figure 4.15 presents the plane view for all the vortices formed along the cylinder for the normal incidence case at $\beta = 200$. In consistence with the previous discussion, for $\alpha = 0°$ the flow near the cylinder surface gains a structure consisting of two layers of equal-sized vortex pairs, and the two-layer vortical structures are staggered with respect to the cylinder's axial centre line. Both layers contain a pair of symmetric counter-rotating vortices and the two layers are counter-rotating as well to form a dipole-like four-vortex two-layer structure. The top layer extends further in

88

space to be more circular and the bottom layer underneath is much flatter and has a slightly longer axial span. The top pair identifies the stable Honji structure in which the vortex pair adopts the standard mushroom-like shape that results from the rolling-up of the shear layer. In contrast, the bottom layer that is attached to the cylinder surface presents the vorticity within the boundary layer formed along the axial direction. It is seen that the two-layer dipole-like vortical structure remains stable and stationary along the cylinder span throughout the period, and the oscillatory fluid velocity only alters the vorticity magnitude in the vortex pairs. At $t^*=1/4$ where the ambient flow reaches its maximum value, the vortex pairs also appear to be the strongest. The flow evolution is repeated after every half oscillatory flow period.

The results for $\alpha = 10°$ are demonstrated in Figure 4.15. It is noted that in the first half-period ($t^* = 0 \sim 1/2$), the axial flow component points to the right-hand side direction in the figure; in the next half period it reverses. As observed in Figure 4.16, the distinct dipole-like vortical structures disappear. Recall that b shows the existence of a sheet flow for this case. In Figure 4.16, it is seen that unlike the symmetric dipole-like structures formed at $\alpha = 0°$, for this oblique inflow case, the sheet flow due to the axial flow component causes the imbalance in the two-layer vortical structures. The mechanism for causing the imbalance is easy to understand. When the axial flow moves along the cylinder span, the boundary layer generates strong vorticity near the cylinder surface. At the same time, due to the relatively strong axial flow during the half period, only very weak counter-rotating vortices are produced, except when the flow speed is small (at flow reversals, or after $T/4$). Hence the bottom layer is dominated by the sheet flow with uni-directional vorticity. At this α, the axial flow can reduce half of vortices (with opposite rotating direction) in the top layer, but is not strong enough to totally suppress those vortices with opposite rotation. As a result, the two-layer structure exists in a very unbalanced fashion, and becomes flatter in the radial direction due to the axial flow component. The vortex flow structure in the second half-period is in a mirror image with that in the first half period with respect to the centre of each two-layer structure, and the whole evolution repeats after one flow oscillation.
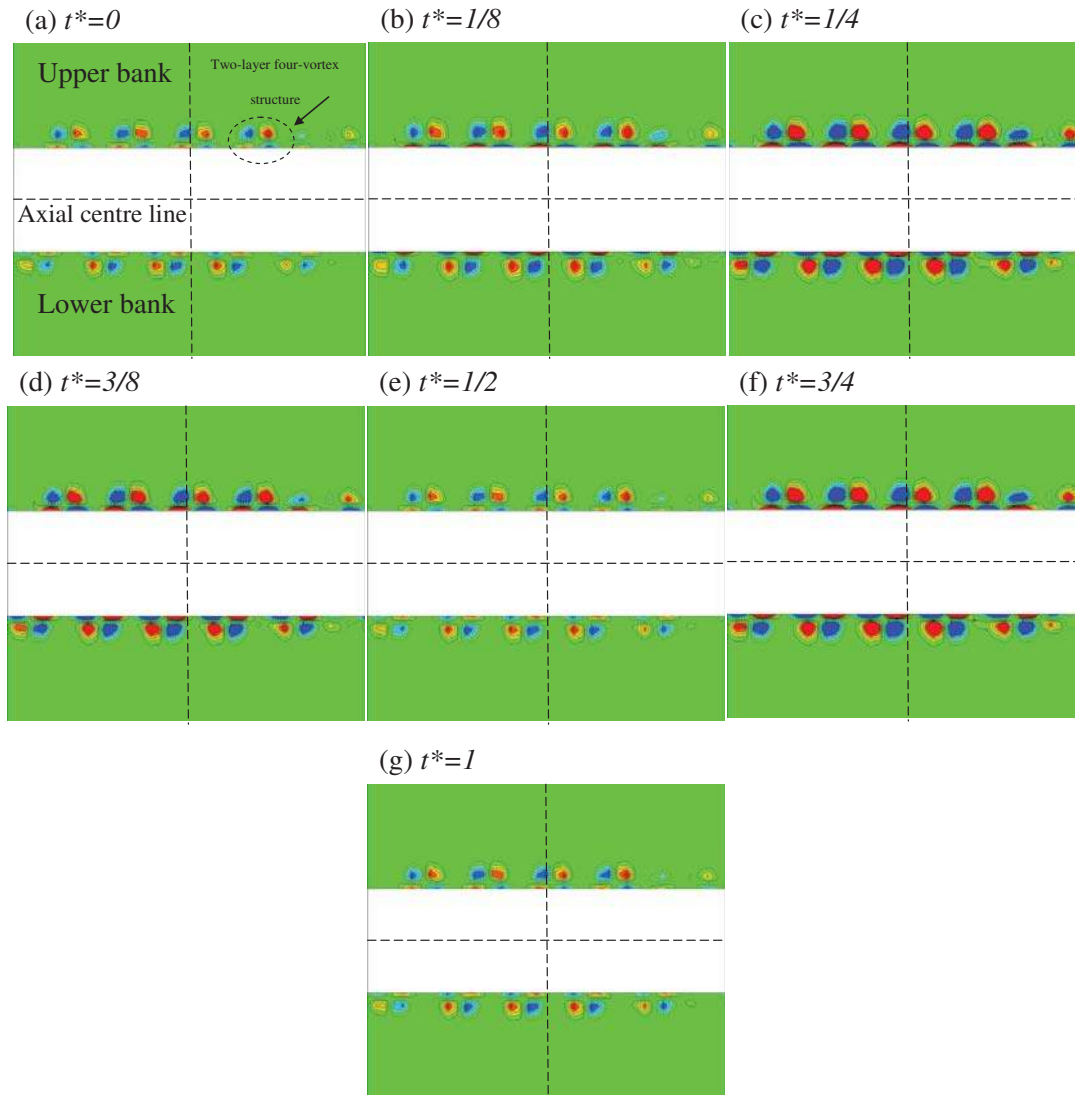
Figure 4.15 Instantaneous contours of *x*-component of vorticity in *x/D* = 0 plane for *β* = 200 and *α* = 0° within one flow period. -1.5 < ω_x < 1.5. *t** = *t/T* - 200. For the first ½ period the interval is Δ*t** = 1/8 and for the second half period Δ*t** = 1/4.

(a) t*=0   (b) t*=1/8   (c) t*=1/4

Upper bank

Axial centre line

Lower bank

(d) t*=3/8   (e) t*=1/2   (f) t*=3/4

(g) t*=1

Figure 4.16 Instantaneous contours of x-component of vorticity in x/D = 0 for β = 200 and α = 10° within one flow period. -1.5 < ω_x < 1.5. t* = t/T - 200. For the first ½ period the interval is Δt* = 1/8 and for the second half period Δt* = 1/4.

The observations described previously for the case of $\beta = 200$ are similar to the case of $\beta = 400$. In Figure 4.17, it is found that the vortex structure near the cylinder at $\beta = 400$ for $\alpha = 0°$ also shows a two-layer structure, with the top layer being much more developed than the bottom layer. Due to the stronger three-dimensionality at this β value, the flow falls into the unstable Honji regime, which can be demonstrated by the much more irregular vortices distribution. The vortices are distributed irregularly along the cylinder surface. More vortex pairs form along the span compared with the case of β

= 200. Therefore, the span of each vortex and the distance between vortex pairs are smaller. In addition, the top layer vortices extend further away from the cylinder in the radial direction and become slender in the axial direction of the cylinder. Although Figure 4.9 shows a strong interaction between vortices, it is observed from Figure 4.17 that within one oscillation period the vortices are stationary in the axial location of the cylinder.
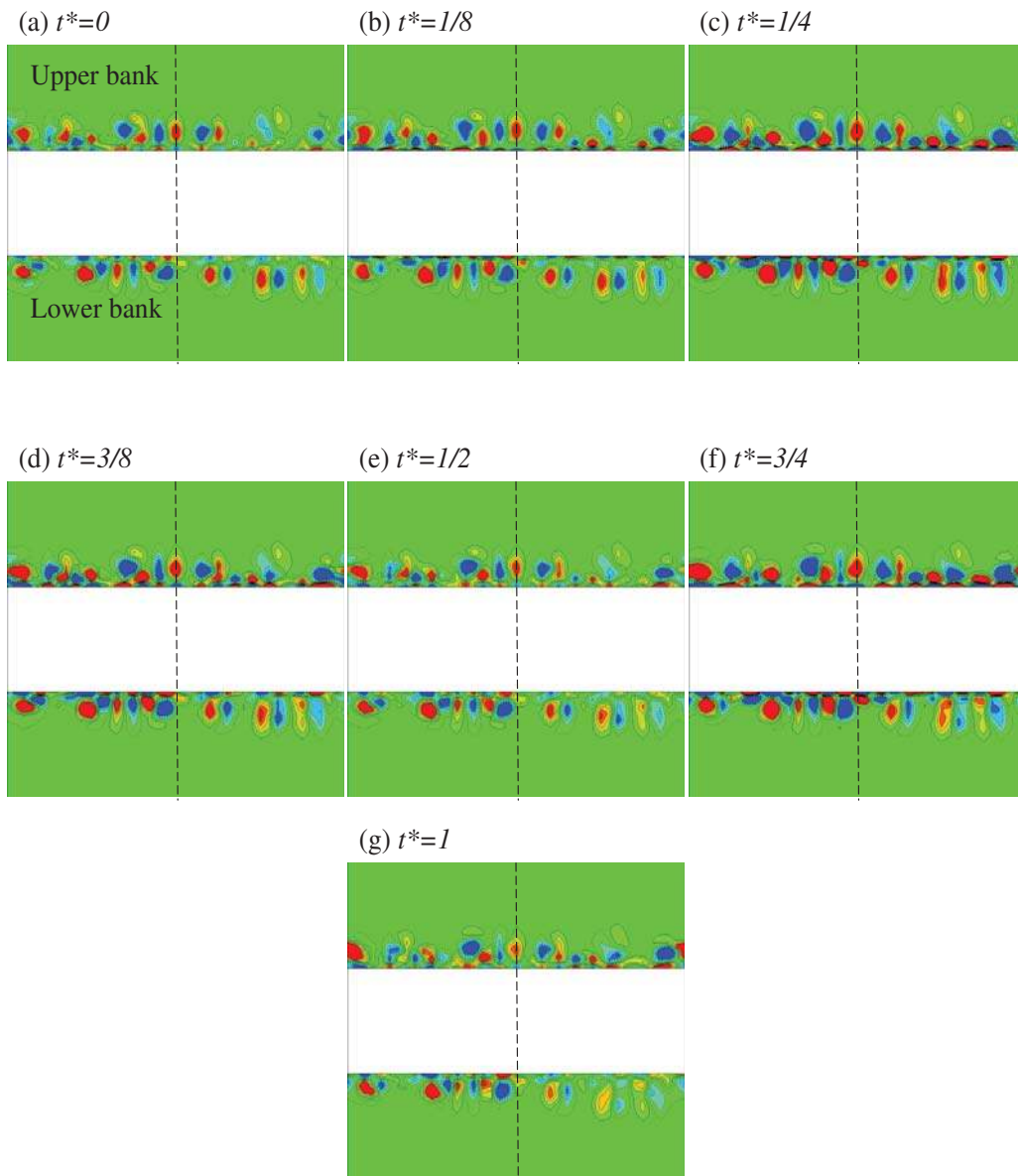
Figure 4.17 Instantaneous contours of x-component of vorticity in $x/D = 0$ plane for $\beta = 400$ and $\alpha = 0°$ within one flow period. $-1.5 < \omega_x < 1.5$. $t^* = t/T - 200$. For the first ½ period the interval is $\Delta t^* = 1/8$ and for the second half period $\Delta t^* = 1/4$.
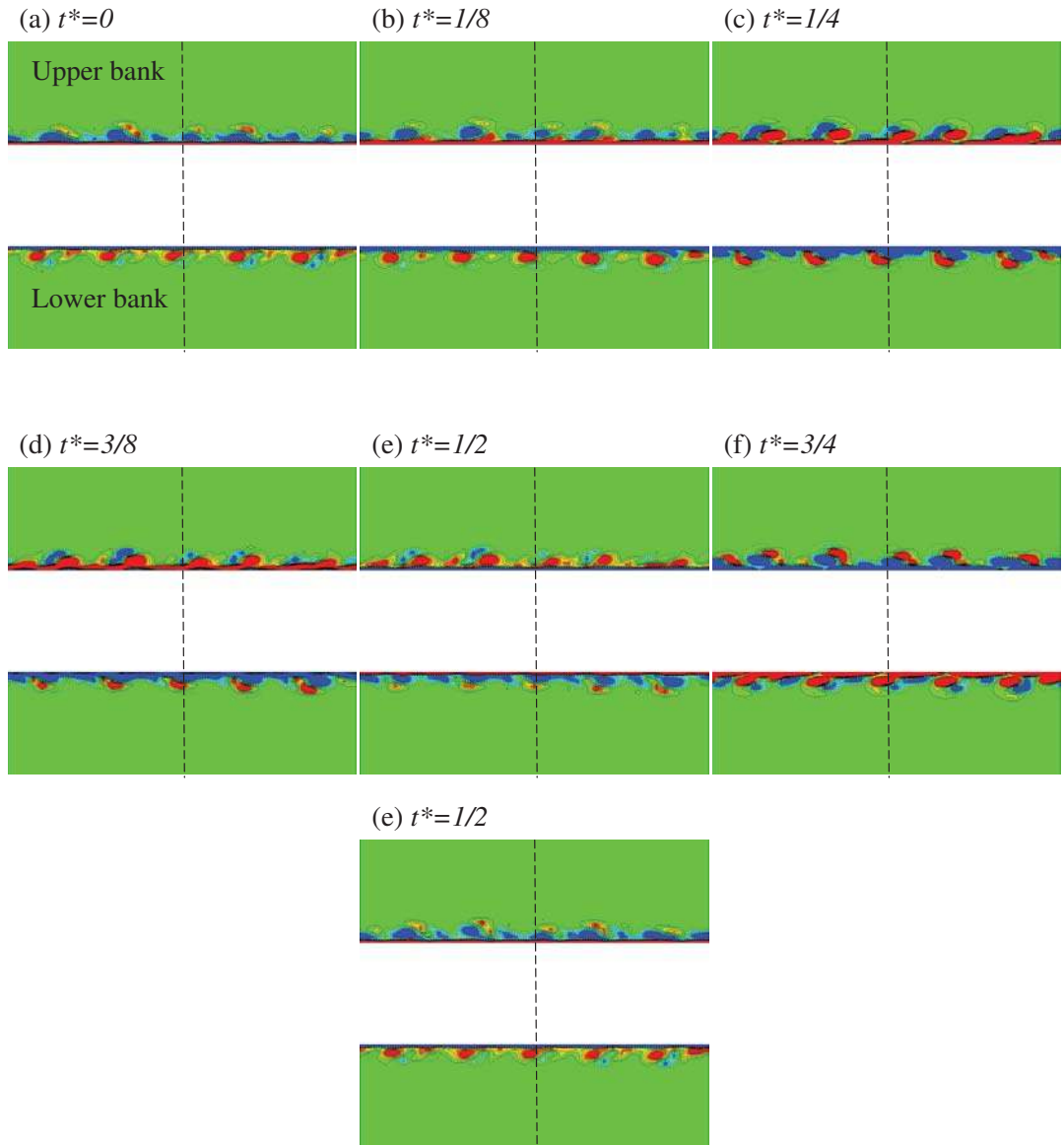
Figure 4.18 Instantaneous contours of x-component of vorticity in $x/D = 0$ plane for $\beta = 400$ and $\alpha = 20°$ within one flow period. $-1.5 < \omega_x < 1.5$. $t^* = t/T - 200$. For the first ½ period the interval is $\Delta t^* = 1/8$ and for the second half period $\Delta t^* = 1/4$.

The case of $\beta = 400$ and $\alpha = 10°$ is found to be very similar to that of $\beta = 200$ and $\alpha = 0°$ and is hence not presented here. The case of $\alpha = 20°$ and $30°$ are given in Figure 4.18 and Figure 4.19. As the axial velocity component is increased, the irregularity weakens, and the vortical structures are more independent and distinctive with greatly reduced interactions between neighbouring vortex pairs. For these two cases with strong axial flow component, the vortices become oblique while the distance between two neighbour vortices becomes larger. The vortices also appear to be flatter at larger α. With the

cancellation and ingestion of the opposite fluid by the axial flow component, for $\alpha = 20°$, the left-right counter-rotating distribution of the vortex pairs almost turns into top-bottom counter-rotating vortex pairs; and for $\alpha = 30°$ the sheet flow completely merges with half of the vortex pairs and leaves the other halves to be revealed only at certain moments when the free stream is strong enough.

(a) $t^*=0$ (b) $t^*=1/8$ (c) $t^*=1/4$

Upper bank

Lower bank

(d) $t^*=3/8$ (e) $t^*=1/2$ (f) $t^*=3/4$

(e) $t^*=1/2$
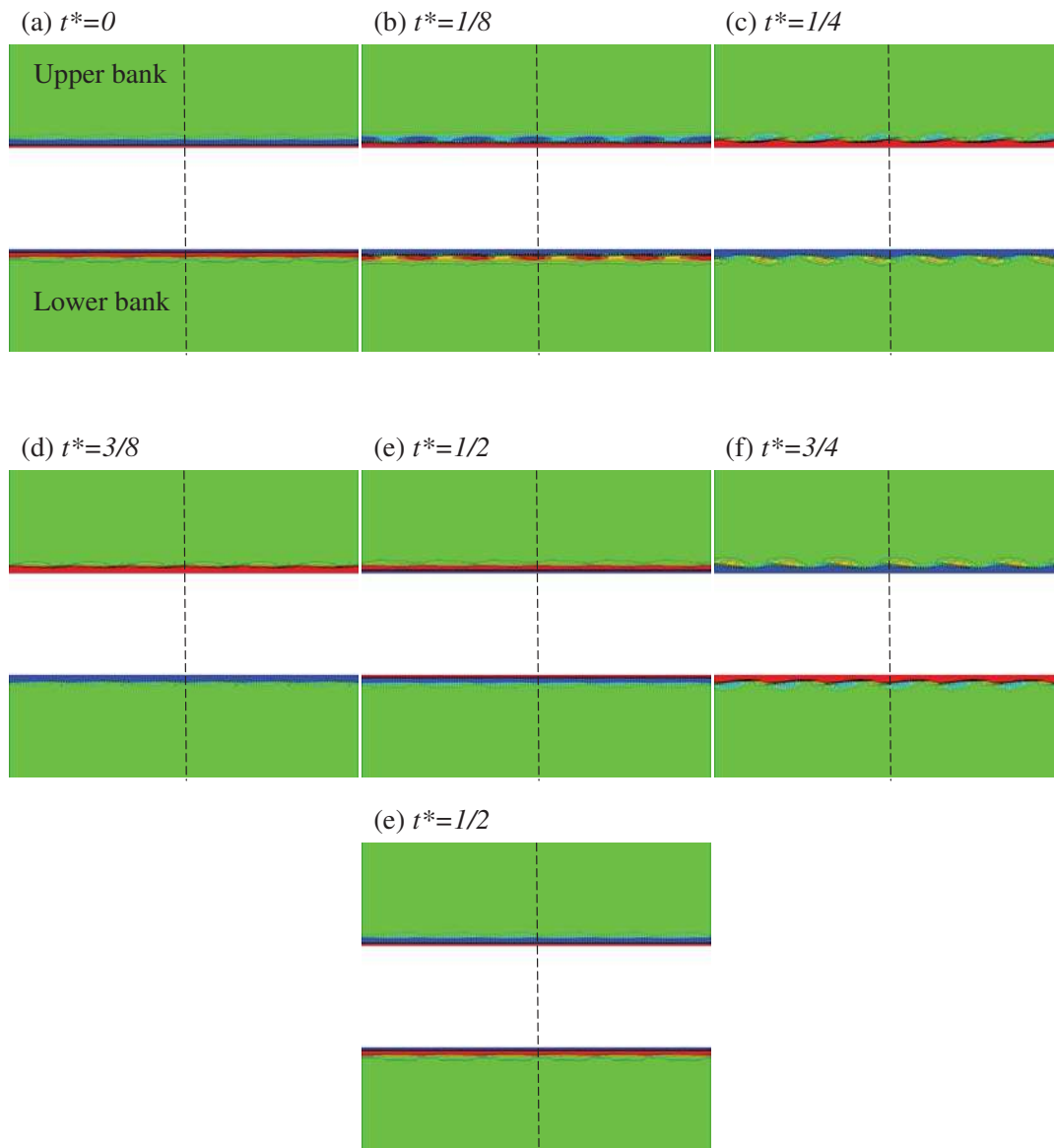
Figure 4.19 Instantaneous contours of x-component of vorticity in $x/D = 0$ plane for $\beta = 400$ and $\alpha = 30°$ within one flow period. $-1.5 < \omega_x < 1.5$. $t^* = t/T - 200$. For the first ½ period the interval is $\Delta t^* = 1/8$ and for the second half period $\Delta t^* = 1/4$.

4.5.2.2 Vortices at cross-sectional view

From the instantaneous 3-D figures (and Figure 4.14), we can see that for all the cases, the radial dimensions of the vortical structure are unequal along the cylinder circumference, i.e. at certain circumferential locations the vorticity has a larger spatial extent in the radial direction than at others. Therefore, the distribution of iso-surfaces of vorticity components appears to be "pointed". This feature is also reflected in the cross-sectional area figures from Figure 4.20 to Figure 4.24, from which we can see the unequal radial extent of one vorticity along the cylinder circumference, especially for the greater extended top layer representing the mushroom-like Honji vortices. Vortex behaviours around the cylinder circumference can be assessed by studying the cross-sectional contours of vortices over one oscillation period. The cross-sectional planes are chosen to cut through the centre of a vortex, and the measurement locations are indicated in the $x/D = 0$ figures given in Figure 4.15 to Figure 4.19.

In Figure 4.20 for the cross-sectional view of $(\alpha, \beta) = (0°, 200)$ at $z/D = 2$, the cylinder circumference is seen wrapped by only one vortex (Figure 4.20) throughout the half period. This is because the vortices distribute along the cylinder in a staggered manner for this case, as is mentioned before. The two-layer structures can be seen with the top layer in the shape of a dolphin. It seems that the 'dolphin's head' (focus of the vorticity, or the larger end) follows the flow direction for the half period given. When the previous oscillation period finishes (Figure 4.20a), the focus of the top vorticity locates at about $\theta = 120°$ at the beginning of the half period shown. Then as the flow starts again in an opposite direction to the previous period, the 'head' is washed across the cylinder following the flow during that half; at the same time its strength increases due to the on-going enhancing of the accelerating ambient flow until $t^*=1/4$. At this moment, the vorticies are the strongest. Then the ambient velocity reduces in speed while keeping its direction, and the vortices are then further washed down around the cylinder by the flow, until at $t^*=1/2$. After that, flow reverses in the next half oscillation period and the procedure repeats in the opposite direction. Although the transfer of the vortices along the cylinder circumference is for both the top and bottom layers, it is apparently much stronger for the top layer, as observed in the figure. This is because the top layer is

further away from the no-slip constraints of the cylinder surface and the boundary layer, therefore more prone to be affected by the oscillatory ambient flow.

(a) $t^*=0$
(b) $t^*=1/8$
(c) $t^*=1/4$

(d) $t^*=3/8$
(e) $t^*=1/2$
(f) $t^*=3/4$

(g) $t^*=1$
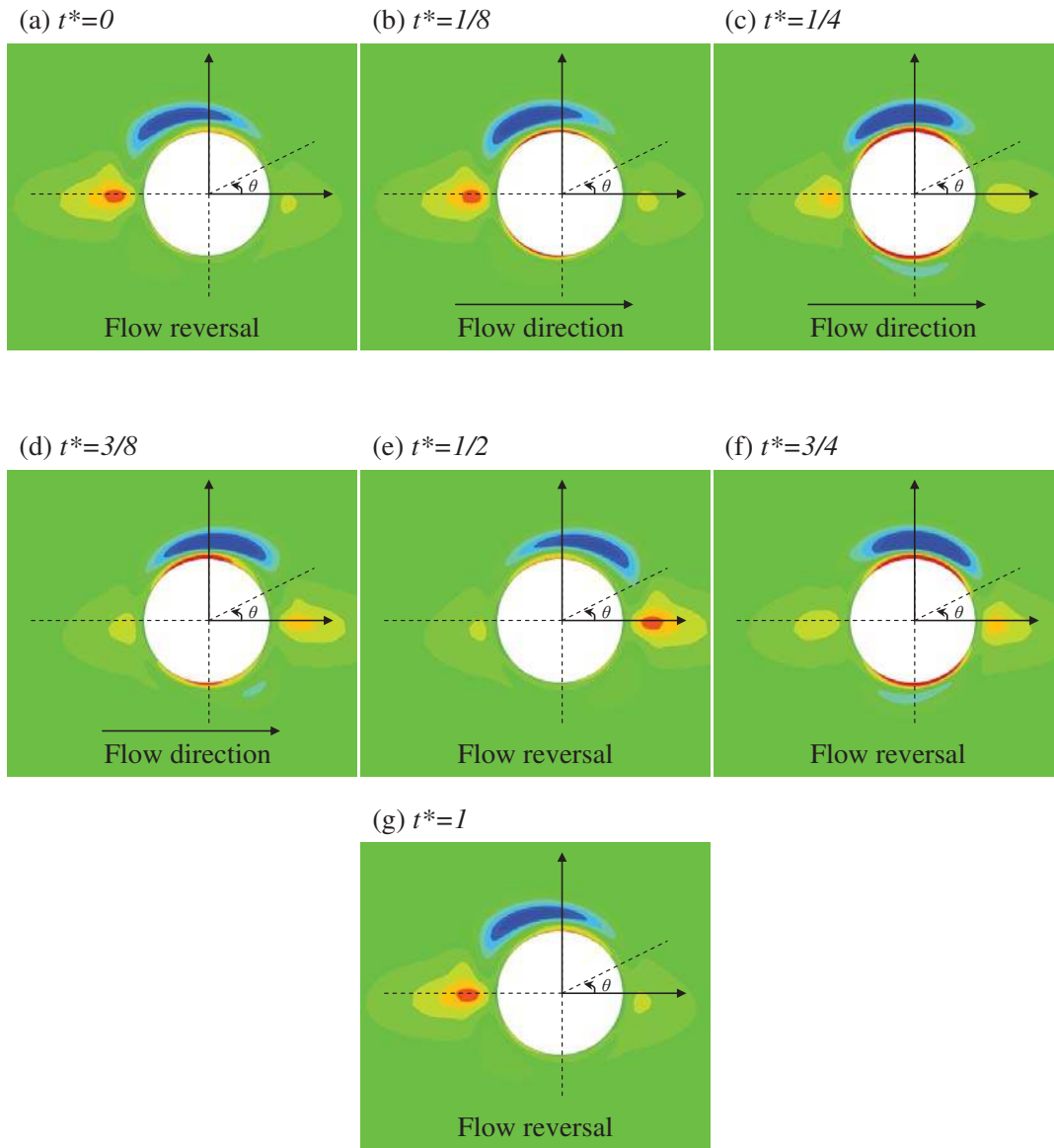
Figure 4.20 Vortex evolution in plane $z/D = 2$ by vorticity contours of ω_x for one oscillation period. For $\beta = 200$ and $\alpha = 0°$. $t^* = t/T$-200 and $-1.5 < \omega_x < 1.5$. For the first ½ period the interval is $\Delta t^* = 1/8$ and for the second half period $\Delta t^* = 1/4$.

The vortices distribution is in a symmetric manner for the case of $(\alpha, \beta) = (10°, 200)$. As shown in Figure 4.16, the cross plane chosen for $\alpha =10°$ cuts through a pair of two-layer structures which are up-down symmetric with respect to the x axis. Therefore, two symmetric vortices can be seen surrounding the cylinder in Figure 4.21. With the existence of an axial flow component, the top layer vorticity appears to be weaker and

shorter while the bottom layer is stronger and covers a larger circumference than that of $\alpha = 0°$. As shall be mentioned later, the bottom layer plays the role of the source of energy and momentum for the top vortices. As the flow accelerates so the two layers grow, but the bottom layer experiences a more apparent growth than the top one. It is also observed that the top layer is less extended in space and hence is pressed closer to the cylinder than that of $\alpha = 0°$, which means the two-layer vortical structures are flatter under the effect of an axial flow component.

(a) $t*=0$ 　　　　 (b) $t*=1/8$ 　　　　 (c) $t*=1/4$

(d) $t*=3/8$ 　　　　 (e) $t*=1/2$ 　　　　 (f) $t*=3/4$

(e) $t*=1/2$
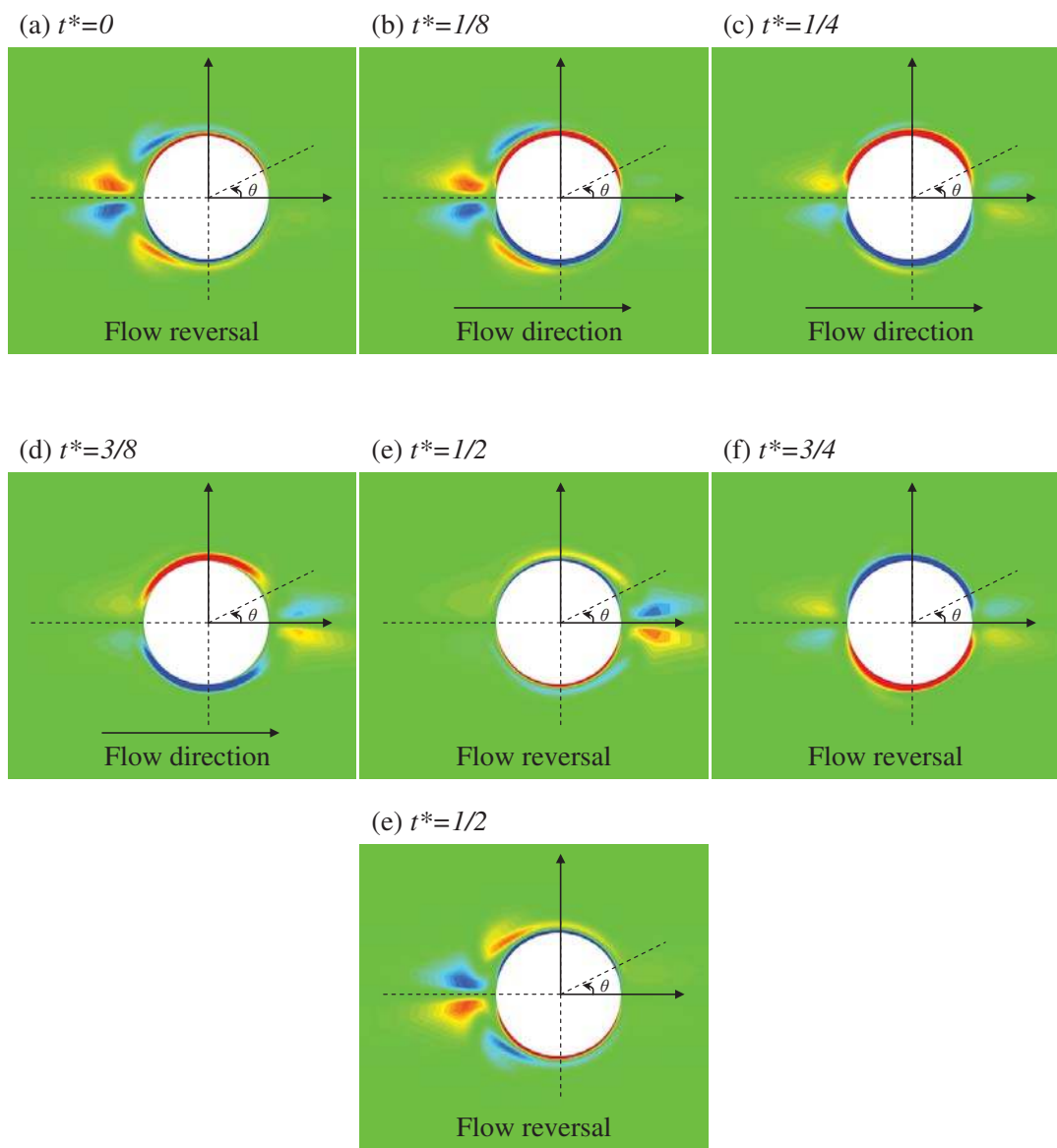
Figure 4.21 Vortex evolution in plane $z/D = 2$ by vorticity contours of ω_x for one oscillation period. For $\beta = 200$ and $\alpha = 10°$. $t* = t/T\text{-}200$ and $-1.5 < \omega_x < 1.5$. For the first ½ period the interval is $\Delta t* = 1/8$ and for the second half period $\Delta t* = 1/4$.

(a) $t^*=0$

(b) $t^*=1/8$

(c) $t^*=1/4$

A

B

θ

θ

θ

Flow reversal

Flow direction

Flow direction

(d) $t^*=3/8$

(e) $t^*=1/2$

(f) $t^*=3/4$

θ

θ

θ

Flow direction

Flow reversal

Flow direction

(g) $t^*=1$

θ

Flow reversal
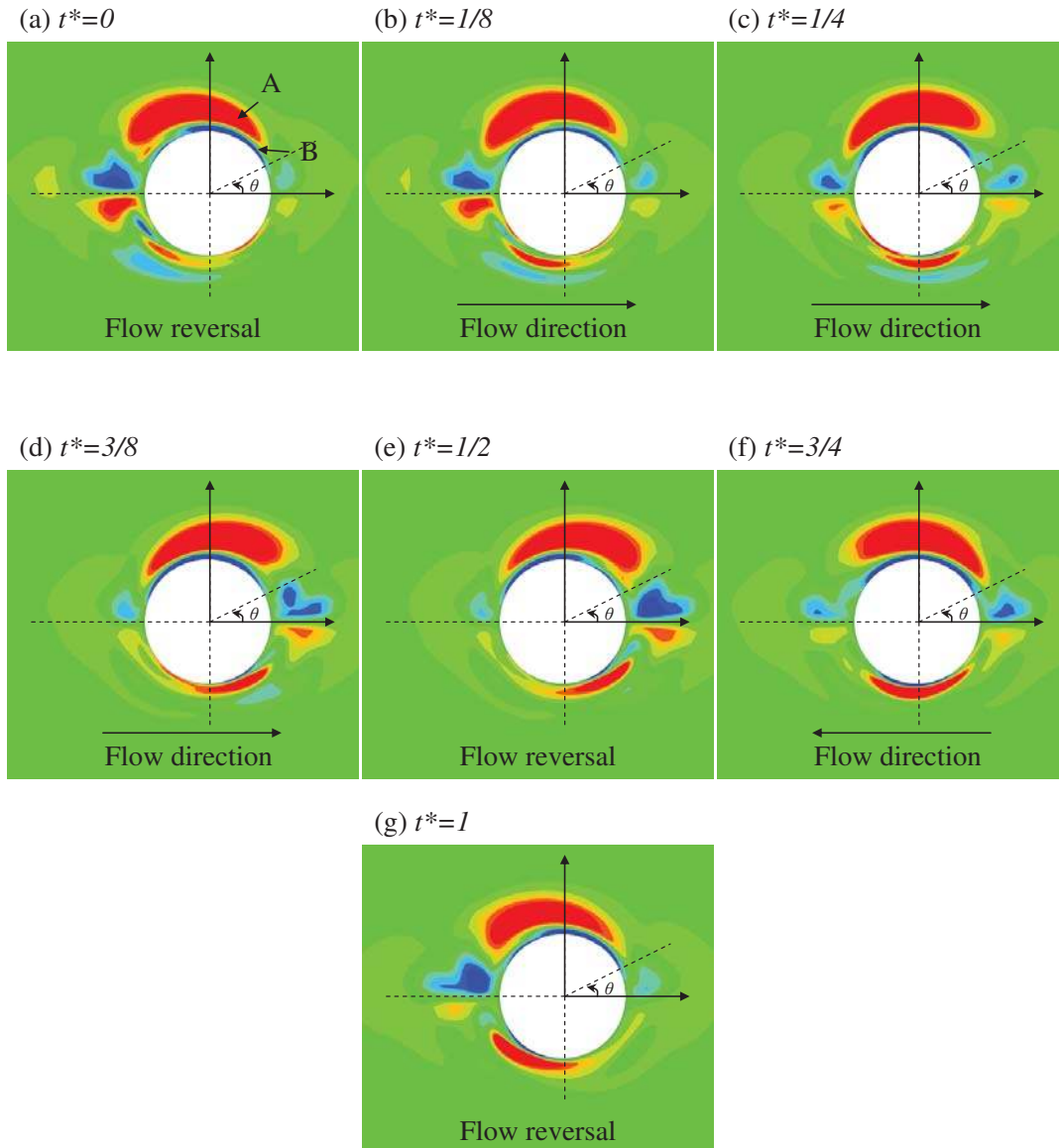
Figure 4.22 Vortex evolution in plane $z/D = 2$ by vorticity contours of ω_x for one oscillation period. For $\beta = 400$ and $\alpha = 0°$. $t^* = t/T$-200 and $-1.5 < \omega_x < 1.5$. For the first ½ period the interval is $\Delta t^* = 1/8$ and for the second half period $\Delta t^* = 1/4$.

The cross-sectional plane at $z/D = 2$ for $(\alpha, \beta) = (0°, 400)$ is given in Figure 4.22. The location of the measurement cross section is indicated in Figure 4.17. The top-layer vorticity (denoted as vorticity 'A') viewed is also in a 'dolphin-like' shape with the radial extent varies with circumference. Throughout the oscillation period, the overall circumferential coverage of A remains more or less unchanged, covering about 1/4 circumference spaning roughly from $\theta \approx 45°$ to $\theta \approx 135°$. During this process, the bottom layer vorticity B transfers in an opposite direction to that of the top layer. Vortex

B also seems to cover roughly 1/4 circumference, similar to vortex A. In addition, it is observed that A and B are not aligned in the radial direction; rather, there is a small offset between the two. Bottom vorticity B is slightly thinner where the focus of the top vorticity A lies, i.e. where the top vorticity A has a larger radial span.
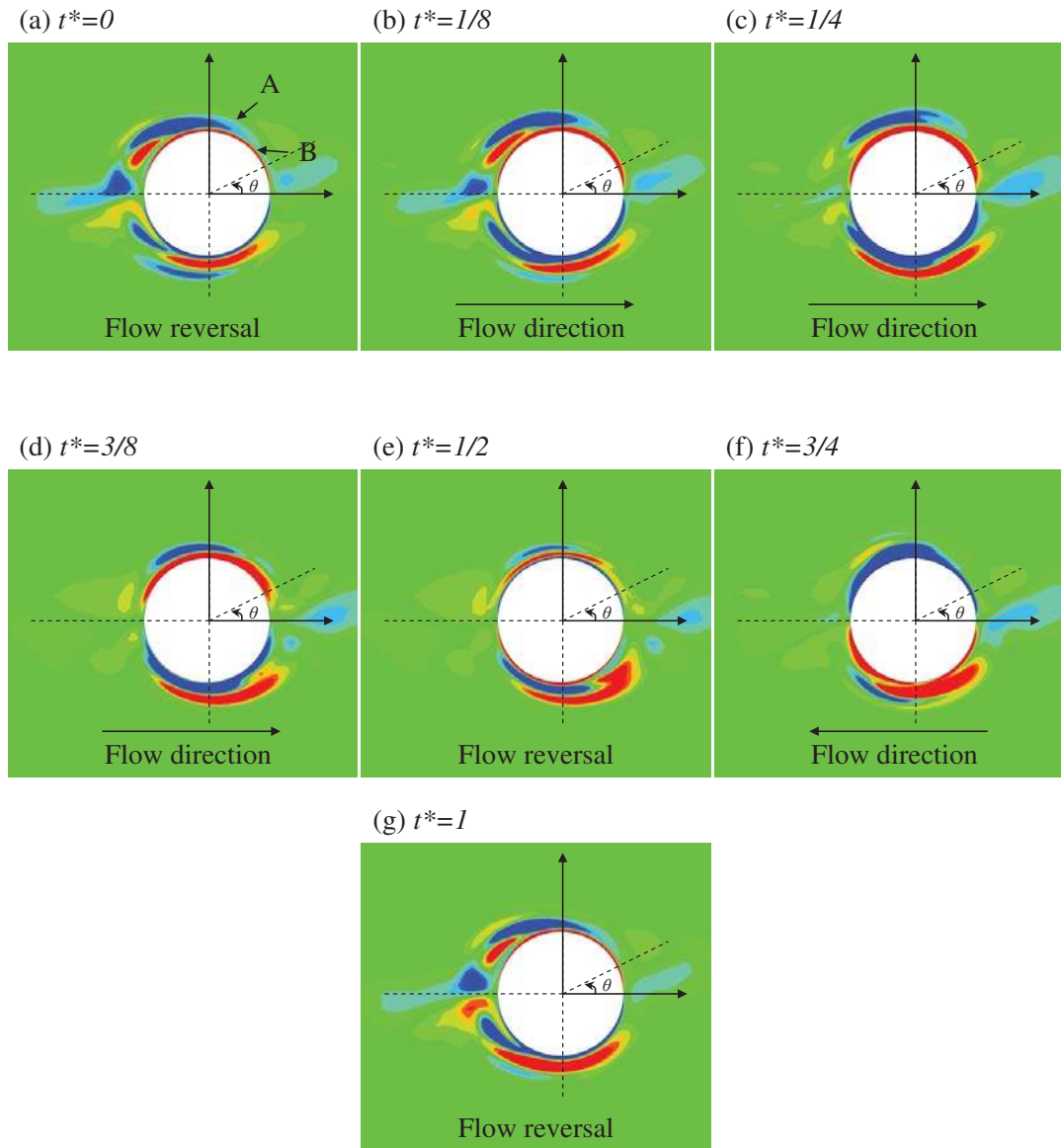
Figure 4.23 Vortex evolution in plane $z/D = 2$ by vorticity contours of ω_x for one oscillation period. For $\beta = 400$ and $\alpha = 20°$. $t^* = t/T$-200 and $-1.5 < \omega_x < 1.5$. For the first ½ period the interval is $\Delta t^* = 1/8$ and for the second half period $\Delta t^* = 1/4$.

Cases of $(\alpha, \beta) = (20°, 400)$ and $(30°, 400)$ are presented in Figure 4.23 and Figure 4.24, respectively. The varying trend of the resultant flow field with the increase of α is similar to that observed at $\beta = 200$. As α increases, the bottom layer increases its

99

strength and circumferential coverage, and grows stronger and larger in both circumferential and radial directions than the top layer. However, the two-layer structure as a whole becomes flatter (less extended in the radial direction) at larger α, similar to the observations from the $x/D = 0$ planes.

(a) $t^*=0$

Flow reversal

(b) $t^*=1/8$

Flow direction

(c) $t^*=1/4$

Flow direction

(d) $t^*=3/8$

Flow direction

(e) $t^*=1/2$

Flow reversal

(f) $t^*=3/4$

Flow direction

(g) $t^*=1$

Flow reversal
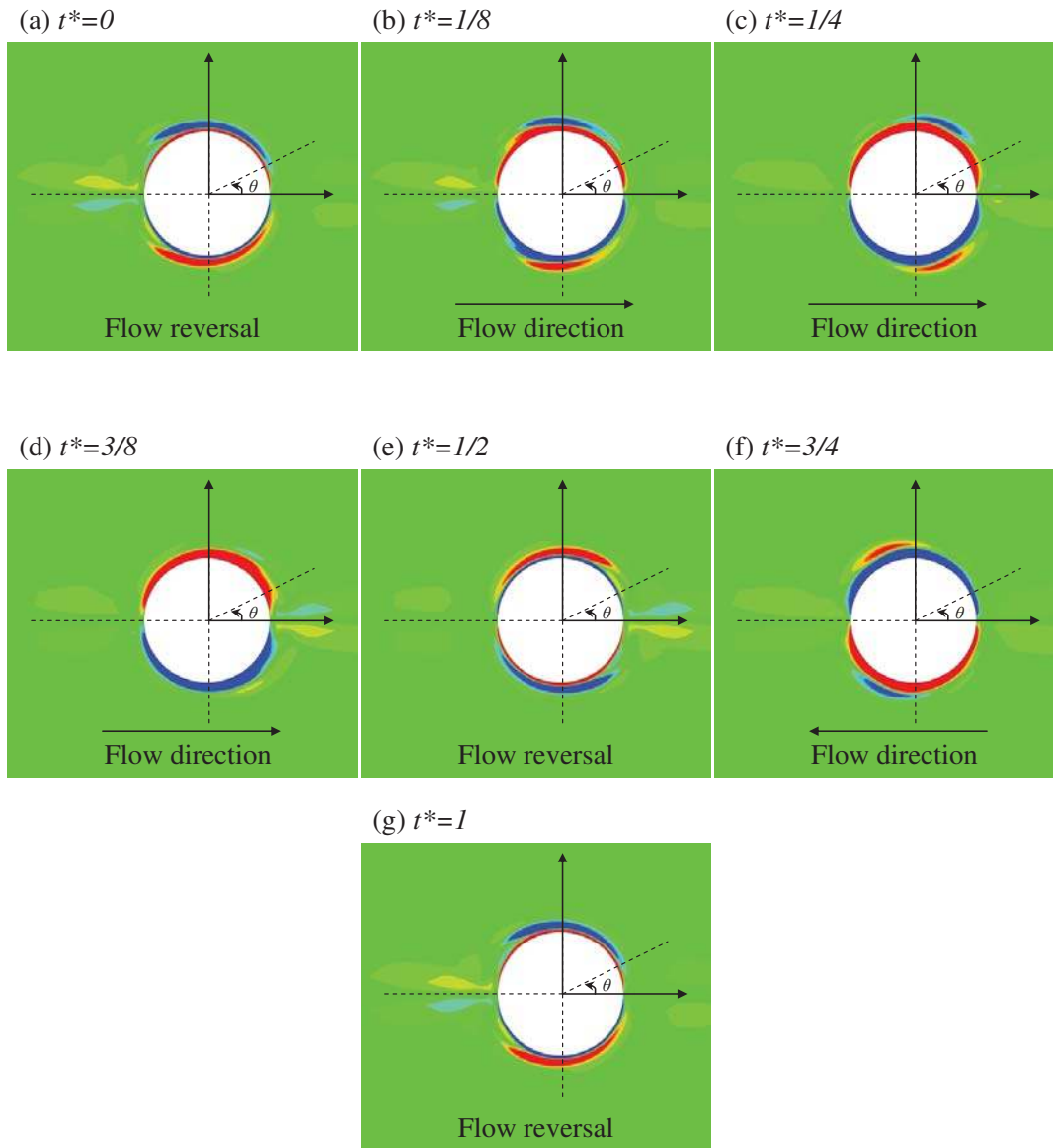
Figure 4.24 Vortex evolution in plane $z/D = 2$ by vorticity contours of ω_x for one oscillation period. For $\beta = 400$ and $\alpha = 30°$. $t^* = t/T$-200 and $-1.5 < \omega_x < 1.5$. For the first ½ period the interval is $\Delta t^* = 1/8$ and for the second half period $\Delta t^* = 1/4$.

4.5.3   Energy transfer within one Honji vortex pair
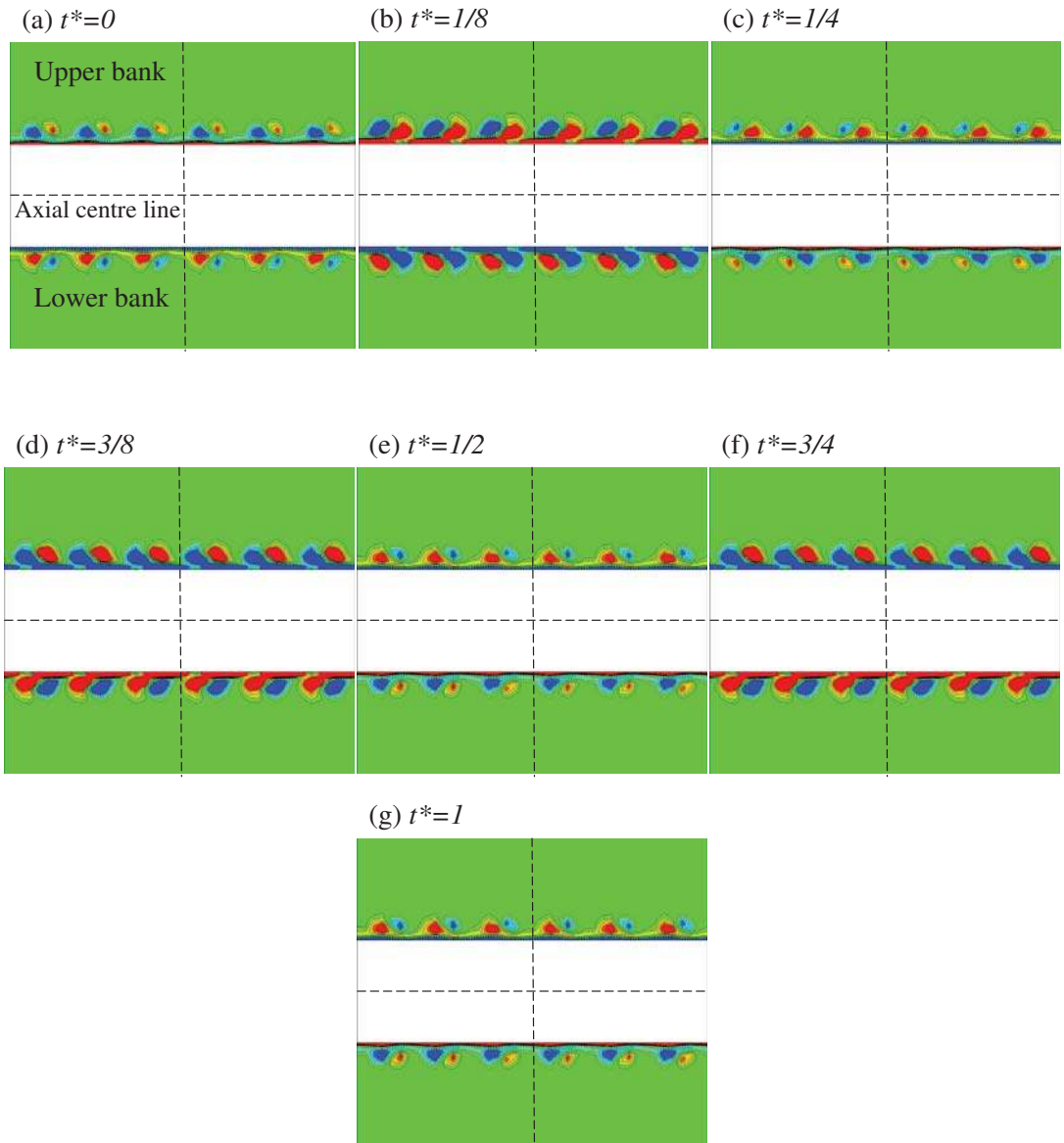
The variation of the vortical structures with α is closely related to the energy transferring within the two layers. The evolution of a single vortex pair within half flow period is examined and its structure at four instants over the half period are shown in terms of vorticity contours (Figure 4.25) and streamlines (Figure 4.26). The cases studied here are two in the stable Honji regime: $(\alpha, \beta) = (0°, 200)$ and $(10°, 200)$.

Close-up views of a dipole-like four-vortex structure for the case of $(\alpha, \beta) = (0°, 200)$ are given in Figure 4.25a, visualised by contours of ω_x. For $\alpha = 0°$, this structure facilitates the bottom layer, which is smaller in size but more intense, to be a source of energy and momentum for the top mushroom-like vortices. The vorticity in the bottom layer entrains the flow from the outer field through rotation to the centre of the bottom pair and then pushes the flow upwards into the top pair (see also [21] and [23]). In this way vorticity is fed into the top layer to sustain the latter. As can be speculated, this transfer process benefits from the symmetric nature of the dipole-like structure.

This mechanism is depicted vividly by the streamlines plotted in Figure 4.26a, where the flow near the cylinder surface rises up perpendicularly to its span before separating equally into two opposite directions to form the counter-rotating vortices of each Honji vortex pair (top layer vortices). In addition, the upper vortices also help in drawing fluid from the outer field during its rotation into the centre of the four-vortex structure. This part of fluid is also washed up together with the fluids drawn by the bottom pair. The symmetric Honji vortex pair can be observed throughout the half-period for $\alpha = 0°$ from the streamline visualisation in Figure 4.26a.

(a) $\alpha = 0°$

(b) $\alpha = 10°$
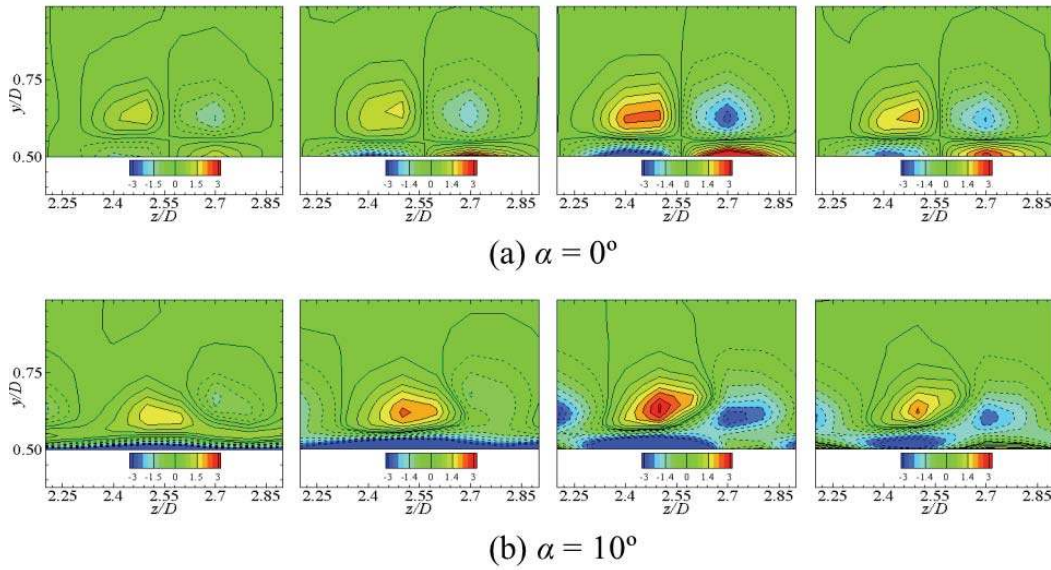
Figure 4.25 Vorticity contours of ω_x for one Honji vortex pair for (a) $\alpha = 0°$ and (b) $\alpha = 10°$ at $t/T - 200 = 0$, 1/8, 1/4 and 3/8 at $\beta = 200$ for the plane of $x/D = 0$.

(a) $\alpha = 0°$

(b) $\alpha = 10°$
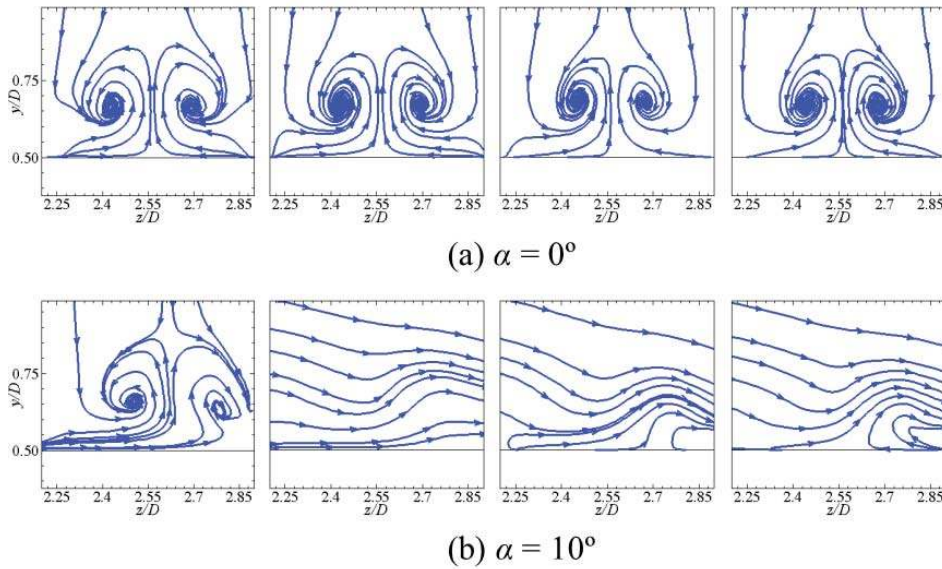
Figure 4.26 Streamlines of one Honji vortex pair for (a) $\alpha = 0°$ and (b) $\alpha = 10°$ at $t/T - 200 = 0$, 1/8, 1/4 and 3/8 for $\beta = 200$.

The evolution of the vortical structures considering the energy transfer is now discussed. Considering both Figure 4.25a and Figure 4.26a, it is seen that the variation of the Honji structure is consistent with flow oscillation. At the start of the oscillation, when the mean flow is zero, the pair of vortices is weak because the whole vorticity field is at a low value. As mentioned before, the strength of the top vortex pair depends on both the

102

bottom layer and the strength of the ambient flow. Therefore, once the oscillation starts, both the ambient flow and the flow within the bottom layer intensifies, enabling more energy supply and resulting in the growth of the top vortex pair (representing the mushroom-like Honji vortices). When the free stream reaches the first peak value (at t^* = 1/4), the vorticity within the two-layer dipole-like vortices is the strongest. Then the ambient flow velocity starts to reduce, and less supply is provided for the Honji vortex pair, which therefore weakens until the minimum value again at the flow reversal (t^* = 1/2). The whole process then repeats itself for the following half period. During the whole process, the scale and shape of the vortical structure remain almost unchanged while its vorticity intensity varies.

Modifications to the flow structures are noted when $\alpha = 10°$, see Figure 4.25b and Figure 4.26b. The unbalanced vortex pair, with one vortex of the pair playing a clearly dominant role, is observed from the vorticity contours figure (Figure 4.25b), and the mushroom-shaped Honji vortices fail to form as demonstrated by the streamlines figure (Figure 4.26b). The disappearance of the Honji vortices is a consequence of the existence of the axial velocity component, which inhibits the energy transfer towards the top layer in several ways. First, as seen in Figure 4.25b, under the effects of the axial flow component, the bottom and top layer are both unbalanced with the bottom layer almost dominated by a uni-directional flow, and a merging of the same-sign vorticity from diagonal vortices of the top and bottom pairs exists. This structure causes the energy and mass transfer passage to be biased and most supply is directly imported into the dominant vortex (which merges with the bottom layer) in the top layer, resulting in the unequal vortices in the upper layer. In addition, another important supply for the formation and sustenance of the top-layer vortices provided by the outer flow is also limited as the axial velocity is an effective obstacle to the entrainment of the fluid from the outer field by the vortices. Last, the axial flow also exerts directly on the vorticity field generated by normal flow component by cancelling the opposite vorticity part and flattening the same vorticity, and results in the streamlines shown in Figure 4.26b. Subsequently the two-layer vortical structures under oblique inflow are not only unbalanced, but also smaller compared with the normal incidence case.

4.6   Dimension of the Honji vortices

As is already noticed, the dimension of the Honji vortices is affected by addition of an axial flow component. Full description of the dimension can be gained through measurements of the three quantities: a radial extent (Δd_r), an axial extent (Δd_z) and a circumferential extent (Δd_c), as defined in Figure 4.27. Among these three extents, the radial and axial extents are both plane extent at *x/D* = 0.

It is noted that the dimension of the Honji vortices changes with time within one period. The dimensions given below are the maximum value in one oscillation, i.e. at the *T/4* when the free stream is at its peak value. Measures are only given for the cases falling in the stable HJ regime, which includes (α, β) = (0°, 200), (10°, 200), (20°, 300), and (30°, 400). For these cases, the vortices arrange in a regular distribution along the cylinder span, and all vortex pairs are identical in size and strength, hence the measurements of one pair are taken to represent all Honji vortex pairs along the cylinder span. The dimensions of the Honji vortices measured are summarised in Table 4.2.
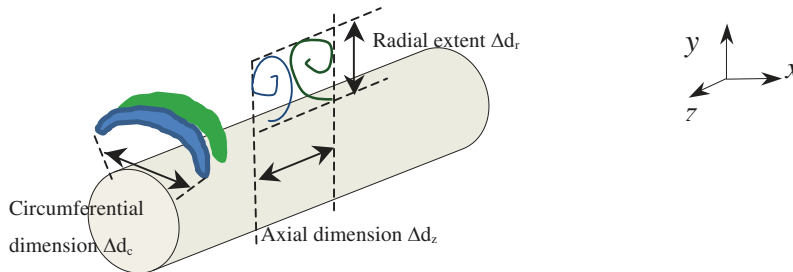
Figure 4.27 Definition sketch of the dimensions of the Honji vortical structures.

4.6.1   **Plane extent at x/D = 0**

The dimension of the cross section of a Honji vortex pair is determined by measurements of the plane extent, which includes a radial extent (Δd_r) and an axial extent (Δd_z). As defined in Figure 4.27, the radial extent is the typical height of the two-layer vortex pairs. The measured radial dimension for the cases studied are plotted and compared in Figure 4.28.

Table 4.2 The dimensions for one vortex pair for the selected cases. Δd_r is the radial dimension, Δd_{rc} is the height of centre of the vortex (see Figure 4.28a), Δd_{rc} is the radial height of the bottom layer (see Figure 4.28b) and Δd_z is the axial dimension of the vortex pair. Measured in plane $x/D = 0$.

	$\beta = 200$				$\beta = 300$		$\beta = 400$	
	$\alpha = 0°$		$\alpha = 10°$		$\alpha = 20°$		$\alpha = 30°$	
	Left	right	Left	right	Left	right	Left	right
Δd_r	0.35D	0.35D	0.27D	0.27D	0.2D	0.2D	0.1D	0.05D
Δd_{rc}	0.13D	0.13D	0.13D	0.1D	0.13D	0.1D	0.1D	N/A
Δd_{rb}	0.05D	0.05D	0.06D	0.03D	0.05D	N/A	0.05D	N/A
Δd_z	0.61D		0.61D		0.61D		0.61D	

For the unbalanced cases ($\alpha > 0°$), the two vortices in the top layer are not parallel. The lower vortex merges with the sheet flow in the bottom layer bearing the same sign, and therefore its vorticity centre is lower and closer to the bottom layer (reflected by Δd_{rc}). In addition, as α increases, the bottom layer entrains more of the same-signing top layer vorticity, and therefore becomes stronger and thicker (reflected by Δd_{rb}); on the contrary, its thickness is limited by the existence of the axial flow component, as the latter cancels and ingests the opposite-signing vorticity. The combined effects results the overall height (Δd_r) of the vortex pairs to be smaller and the two-layer structures as a whole are flatter.
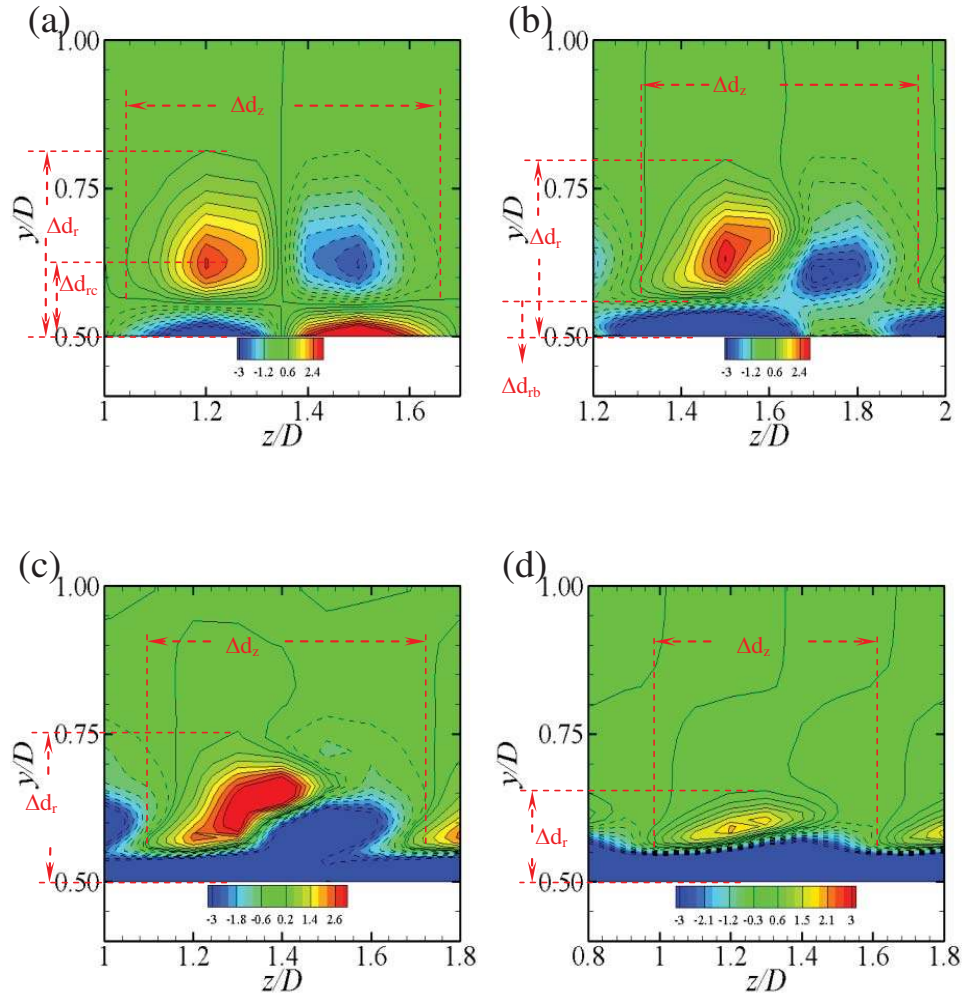
Figure 4.28 Comparison of plane dimensions for one pair of Honji vortices for (a) $(\alpha, \beta) = (0°, 200)$, (b) $(\alpha, \beta) = (10°, 200)$, (c) $(\alpha, \beta) = (20°, 300)$ and (d) $(\alpha, \beta) = (30°, 400)$ at $KC = 2$. Plot at $N = 200$.

For the axial extent of the vortices, it is seen from Table 4.2 that the variation of Δd_z is not apparent among the measured cases. Recall that for $(\alpha, \beta) = (0°, 200)$ there are five main vortex pairs along the cylinder span, and for the other stable cases there are six. The lack of variation of Δd_z between these cases means the axial dimension of each two-layer vortical structure remains unchanged between these cases, and the average distance between the vortex pairs is reduced slightly as more vortex pairs form along the cylinder.

4.6.2 Circumferential extent

In order to examine the vorticity distribution along the cylinder circumference, Figure 4.29 shows a plane view of the vorticity distribution against the cylinder span z/D and the phase angle θ recorded for a circuit of the nodes around the cylinder. The measurement points are located at the centre of the top of the vortical crown, where the mushroom-like vortices develop from obtaining momentum and energy from the bottom layer as well as the outside flow field. All cases given in Figure 4.29 apply the same range of ω_x, therefore the relative difference in the circumferential extent at different α values can be obtained.
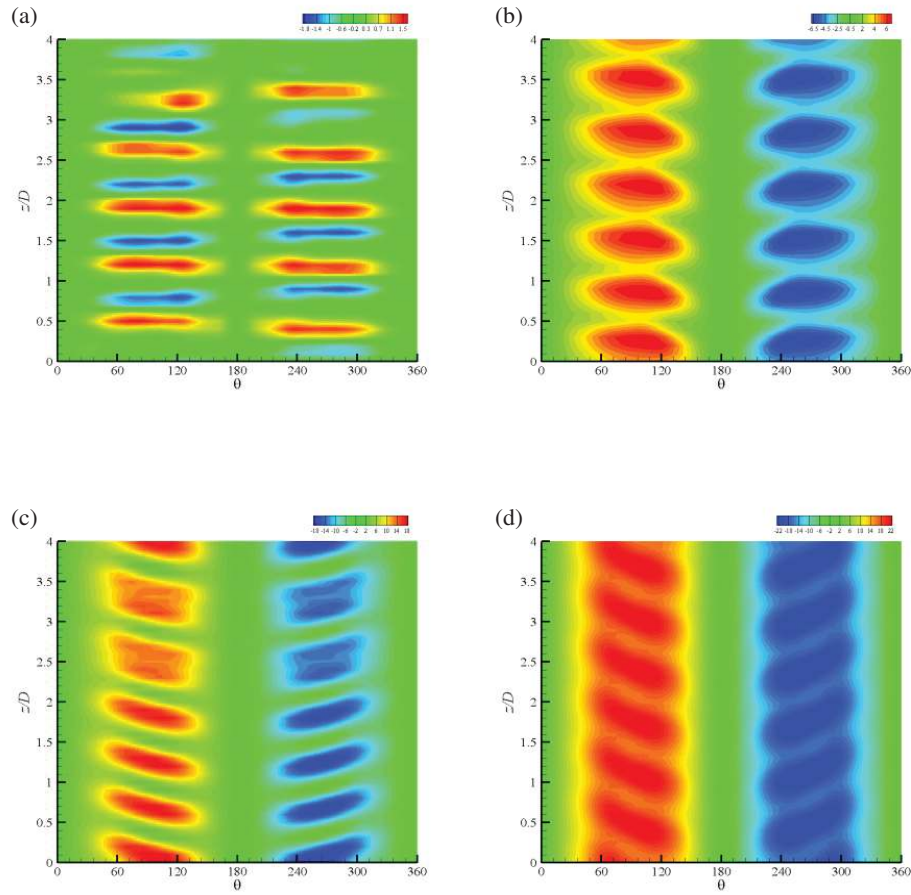
Figure 4.29 Comparison of circumferential dimensions visualised by contours of ω_x plotted along the cylinder circumference over the whole length of the cylinder for (α, β) = (a) (0°, 200), (b) (10°, 200), (c) (20°, 300) and (d) (30°, 400) at $KC = 2$. Plot at $N = 200$. The circuit plane probed is at the centre of the top layer vortices of the two-layer Honji vortical structures.

For the case of (0°, 200), the previously staggering distribution of the five main vortices is also observed in circumferential distribution give in Figure 4.29a. The distance between the vortex pairs is unequal, due to the interaction with the transient vortex. For the oblique inflow cases shown in Figure 4.29b,c,d, the six evenly-distributed vortex pairs are symmetric with respect to the centre line ($\theta = 180°$ line). Comparing between Figure 4.29a for (0°, 200) and Figure 4.29b for (10°, 200) a slight decrease in the circumferential coverage can be observed for larger α. Similar trend is also observed at other β values when increasing α. However, as is noticed between Figure 4.29b,c,d and compared in Table 4.2, differences are negligible between these stable cases of $(\alpha, \beta) =$ (10°, 200), (20°, 300) and (30°, 400). For all these cases, one vortex typically extends 42% of the whole circumference (in the range of about 150° of the total 360°).

In addition, from Figure 4.29, the imbalance caused by larger α can also be observed: with the increase of α, the dominance of one vortex grows. The counter-rotating vortex pairs distributed along the cylinder span observed at (0°, 200) change into an array of uni-directional vortices. The most unbalanced case among all these stable cases falling in the stable Honji regime is $(\alpha, \beta) = (30°, 400)$. As can be seen in Figure 4.29d, the single-signing vortices almost cover the cylinder span as a whole stripe.

For the cases of $\alpha > 0°$, an interesting phenomenon observed for the vortex distribution shown in Figure 4.29 is that, in addition to being symmetric, they are also oblique with respect to the cylinder axis. It is noticed that the obliqueness in the vorticity orientation shown in Figure 4.29 is not in consistence with the incidence angle, but with a difference of about 5°. The measured inclination angle in Figure 4.29 is approximately 5°, 15° and 25° for $(\alpha, \beta) = (10°, 200), (20°, 300)$ and $(30°, 400)$, respectively. This is because, for an oblique approaching flow, as the flow reaches the cylinder, the flow direction is bent to be more perpendicular to the cylinder's surface. This phenomenon is also reported by Sumer, B.M. and J. Fredsøe [7]. As a result, the inclination angle for the flow adjacent to the cylinder is smaller than its original angle of attack as in the far field.

4.7   The 2-D columnar flows at different β

According to the calculations, the intrinsic three-dimensionality of the oscillatory flow around a circular cylinder may be suppressed by the addition of an axial flow component, when the latter is sufficiently strong. The resulting flow field is then a purely 2-D columnar flow wrapping around the cylinder with no evident variation along the cylinder span. This flow field close to the cylinder surface can be regarded as a 2-D oscillatory boundary layer flow. It appears that at larger β number the flow is more prone to 3-D instability so that a stronger axial flow is required to suppress the onset of the Honji instability. The present calculations show that the 2-D flow can be observed for the cases of $(\alpha, \beta) = (20°, 200)$, $(30°, 300)$ and $(40°, 400)$.

The cross-sectional views for the three axial-flow resulted 2-D cases are presented in Figure 4.30. This figure shows that the oblique 2-D cases also assume a two-layer structure; however, this structure is clearly different from the 3-D four-vortex dipole-like two-layer structures. For the 2-D two-layer structure shown in Figure 4.30, both the top and bottom halves of the cylinder surface are surrounded by two layers of sheet flow in opposing directions resulting from uni-directional flow past the cylinder surface. This two-layer structure is only observed at flow reversals, and breaks off once the flow starts, when each half of the cylinder is seen covered by a single vorticity only. A comparison between Figure 4.30a, b and c shows that, with larger axial flow component, the top sheet layer is stronger and covers larger part of the cylinder circumference. The top layer serves as the bottom layer in the previous oscillation. When the flow starts, the top layer dissipates and the bottom layer grows to become the only vorticity covering the cylinder.
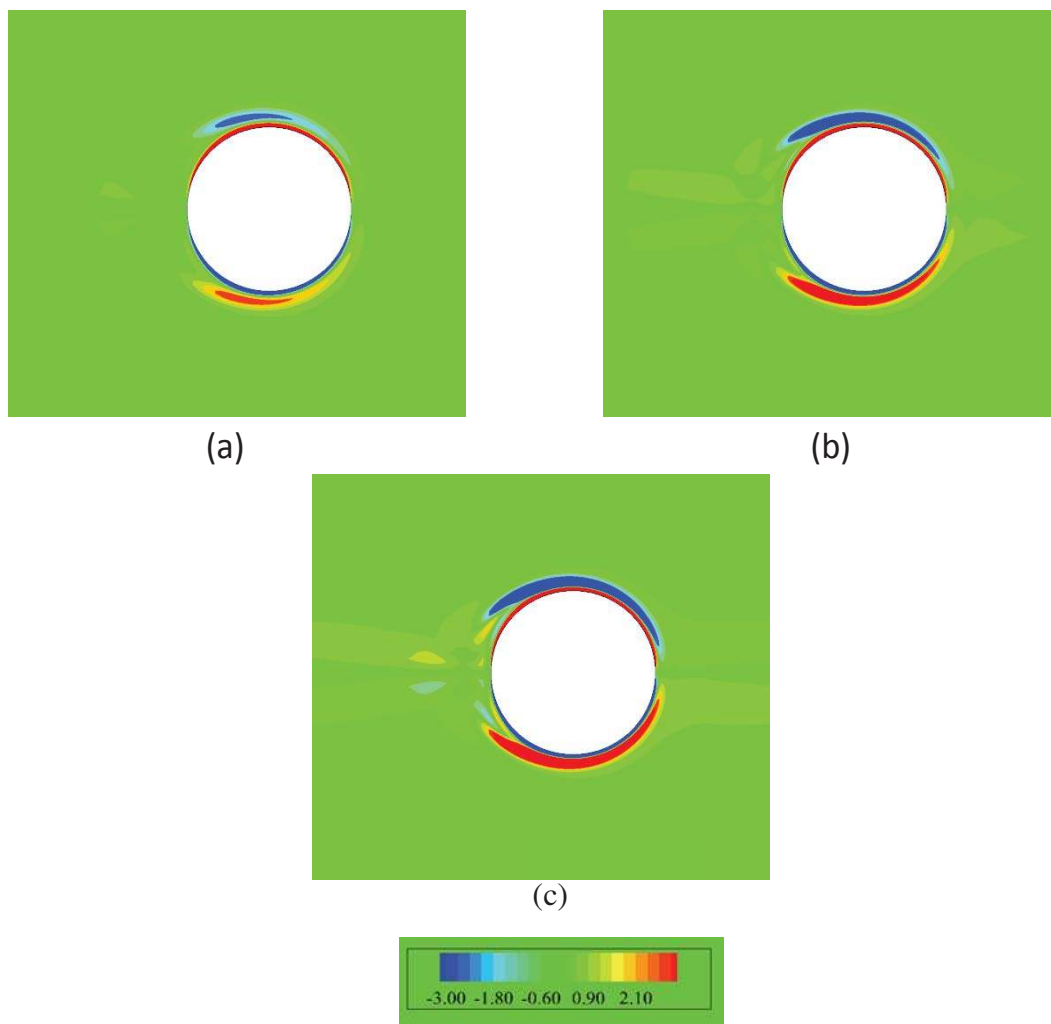
Figure 4.30 Instantaneous contours of ω_x in $z/D = 2$ plane for $(\alpha, \beta) =$ (a) $(20°, 200)$, (b) $(30°, 300)$ and $(40°, 400)$ at $t/T = 200$. $-1.5 < \omega_z < 1.5$.

The non-dimensional axial velocity component u_z/U_{mx} is plotted against y/D close to the cylinder in Figure 4.31. It is seen that for all three cases, the variation of u_z/U_{mx} is confined to the approximate range $0.5 < y/D < 0.8$. u_z/U_{mx} increases first and then decreases at larger y/D, resulting in opposite-signing vorticities along the y-axis as observed in Figure 4.30. The component u_z/U_{mx} vanishes at $y/D = 0.5$ owing to the no-slip condition applied at the cylinder surface, and is also virtually zero beyond $y/D \approx 0.8$, in consistence with the far-field flow at the measurement moment. Also observed from Figure 4.31 is that, for greater β and α, the variation of u_z/U_{mx} becomes more abrupt with a larger peak value happening at a smaller y/D, i.e. closer to the cylinder surface. The sharp change at larger β and α leads to a stronger vorticity, in consistence with that

in Figure 4.30. The value of u_z/U_{mx} for the case of $(\alpha, \beta) = (40°, 400)$ increases and decreases fastest with a peak value of $u_z/U_{mx} \approx 0.29$ at $y/D = 0.52$. The case of $(\alpha, \beta) = (30°, 300)$ falls in the middle with a peak value of $u_z/U_{mx} \approx 0.21$ at $y/D = 0.53$. The case of $(\alpha, \beta) = (20°, 300)$ is the last to reach the peak value $(u_z/U_{mx} \approx 0.13$ at $y/D = 0.54)$ and to disappear in the far field. This indicates that the 2-D oscillatory boundary layers have similar thicknesses, which are only slightly decreased by increasing the axial flow.
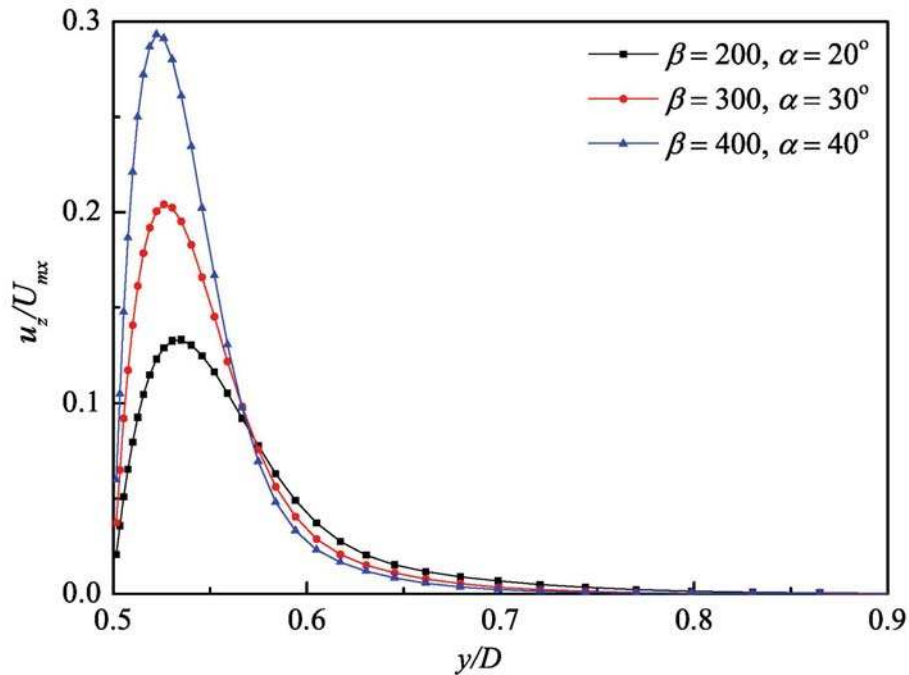
Figure 4.31 Relative axial component u_z/U_{mx} against y/D in plane $z/D = 2$ for all three 2-D columnar flow cases. Plot for $t/T = 200$.

4.8 Conclusions

The aim of this chapter is to extend the study of Honji instability to the case when the far-field oscillatory flow is directed at an oblique angle to the stationary cylinder immersed in an oscillatory flow. Effects of the angle of attack (α) have been studied by introducing an axial velocity component in the flow field. The governing parameters concerned are at $KC = 2$ and $\beta = 200$, 300 and 400. Using a Petrov-Galerkin FEM as described in Chapter 2, the calculations are run for 200 flow oscillation periods for all

the cases in the present study. For the cases that the flow remains 2-D after 200 flow periods, the perturbation method described in Chapter 3 is used to confirm that the flows are intrinsically stable.

First, the flow development for the 200 periods calculated is presented. For the cases where Honji instability operates, the flow developing process can be divided into three phases, namely, a 2-D phase I at the beginning of the calculation, a phase II with evenly-distributed vortex pairs and a phase III where interactions between neighbouring vortices are observed. The calculations show that the imposition of an axial flow component of basic flow tends to have a stabilising effect on the fluid motion for the cases where Honji instability occurs. Further increasing the value of α to a critical value can totally suppress the onset of Honji instability. It is speculated that for any value of $\beta \times KC$ there is a cut-off value of α beyond which the Honji mechanism is completely shut down.

It is then summarised that as the angle of attack α varies so the developed flow pattern falls into one of three distinct classes (in the order of a decreasing three-dimensionality): an unstable Honji regime, a stable Honji regime and a featureless purely 2-D regime. The unstable Honji regime is marked by the strong interactions between vortices along the cylinder span. The cases with relatively high β and low α fall into this regime, which include the cases $(\alpha, \beta) = (0°, 300), (10°, 300), (0°, 400), (10°, 400)$ and $(20°, 400)$. The stable Honji regime finds the cases with relatively low β or large α, including $(\alpha, \beta) = (0°, 200), (10°, 200), (20°, 300)$, and $(30°, 400)$, with the prominent feature that the vortical structures along the cylinder span remain distinct and conduct no strong interactions between neighbouring vortices. The 2-D regime assumes when α is large enough, for the cases of $(\alpha, \beta) = (20°, 200), (30°, 300)$ and $(40°, 400)$, where the flow is simply 2-D columnar flow around the cylinder. The boundaries between these zones are roughly mapped out in Figure 4.12; however, determination of the exact critical values is withdrawn here because it requires countless test runs that are impossible to be completely covered using the present numerical method.

The instantaneous flow structures have been studied by way of vorticity visualization near the cylinder. It is seen that the vortical structure near the cylinder surface is

composed of two layers, namely, a relatively flat bottom layer and a more extended top layer. For a normal incidence flow, the two-layer structure is a dipole-like four-vortex structure with good symmetry. For an oblique inflow when the instability is still operative, the observed two-layer structure is significantly modified. Now the upper layer consists of an unbalanced pair of vortices while the lower layer is a uni-directional sheet flow, which generates a single-rotating vorticity under the no-slip constrains at the cylinder surface. A dominant vorticity is seen for the oblique vortical structures, and the merging of the same-signing vorticity from the top and bottom layers can also be observed. For these cases, it is noticed that the vortex array generated along the cylinder is symmetric and oblique to the cylinder span. However, the orientation of the oblique array has a roughly 5° difference with the direction of the flow in the far field.

The dimensions of the vortical structures are also changed by introducing an axial flow component. The radial thickness of the two-layer structure reduces with the increase of α and the whole structure is pressed flatter at the cylinder. It is found that the axial extent of each two-layer vortical structure remains roughly unchanged when α is increased, therefore the distance between the vortex pairs is reduced as there are six vortex pairs along the cylinder for the cases of (10°, 200), (20°, 300) and (30°, 400), compared with only five for the case of (0°, 200). For a given β, the circumferential coverage slightly decreases as the axial flow intensifies. The oblique vortices generated under the oblique inflow cases (for the cases where Honji instability occurs) orient more perpendicular to the cylinder than the free stream in the far field.

Evolution of the two-layer structures within one flow oscillation period is shown in the planes of $x/D = 0$ and $z/D = 2$. It is observed from the plane view of $x/D = 0$ that within one flow oscillation, the vortices remain at their axial locations, and only the strength of vorticity changes with the ambient flow. The periodicity and symmetricity of the vorticity evolution at $\alpha = 0°$ become mirror-image and unbalanced for the oblique cases. Figures of $z/D = 2$ planes show the circumferential evolution of a pair of two-layer structures. For the perpendicular inflow, the top and bottom layer have roughly the same circumferential coverage, while for the oblique inflow cases, the bottom layer covers larger circumferential span than the top layer.

The effects of α on the resultant flow field are explained through its influences on energy transfers within the two-layer structures. The formation and sustenance of the typical 3-D two-layer structure are found to relate to the energy and mass transfer within the structure. The bottom layer, which attaches to the cylinder surface, appears to be the main source of energy and momentum required for the generation and sustenance of the vortical structures in the upper stratum. At $\alpha = 0°$, the perfect symmetric dipole-like two-layer structure is ideal for the supply to be transferred to the upper layer, which is in the form of mushroom-like vortices. However when the oblique Honji mechanism operates, the axial flow cancels and ingests vorticity of opposite sign, and hence causes the supply to be transferred more easily to the dominant part. This results in the unbalanced formation of the upper layer vortices and the total suppression of the upper vortical structures when the axial flow is strong enough.

When the instability is suppressed by the axial flow, a two-layer structure can also be observed but only at flow reversals for the resultant 2-D columnar flow. This 2-D two-layer structure is different from the 3-D two-layer structures in that the top and bottom layers for the 2-D cases are just two sheet flow layers covering the cylinder. It is found that the resulted 2-D oscillatory boundary layer thickness slightly decreases with a larger axial flow component.

INSTABILITY OF OSCILLATORY FLOW AROUND A CYLINDER WITH AN ELLIPTIC CROSS SECTION

5.1 Aim of chapter

The major purpose of the present chapter focuses on examining the effects of the elliptic cross sections under the Honji regime.

5.2 Introduction

This section investigates the effects of a varying cross section of the cylinder when it is elliptic, on the resultant flow structures near a cylinder under low governing parameters where Honji instability is known to occur for a circular cylinder. Chapter 4 considers the effects of an oblique inflow angle on the resultant fluid flow field under Honji instability. A natural and interesting problem would then arise to consider a geometrically analogous situation of a perpendicular flow approaching a cylinder with an elliptic cross section, which is discussed in this chapter. As shown in Figure 5.1, a circular cylinder immersed in an approaching oblique inflow, if viewed in the direction of the free stream, can be regarded as analogous to an elliptic cylinder immersed in a perpendicular inflow with the shape of an elliptic cross section appropriately chosen. The majority of the previous studies of Honji instability almost exclusively concern the circular cylinder case. To the best of our knowledge, studies of Honji instability around an elliptical cylinder are rare [17], despite its vital importance considering that elliptic cross sections are quite common in real industrial applications such as offshore engineering, maritime engineering and aeronautical engineering.
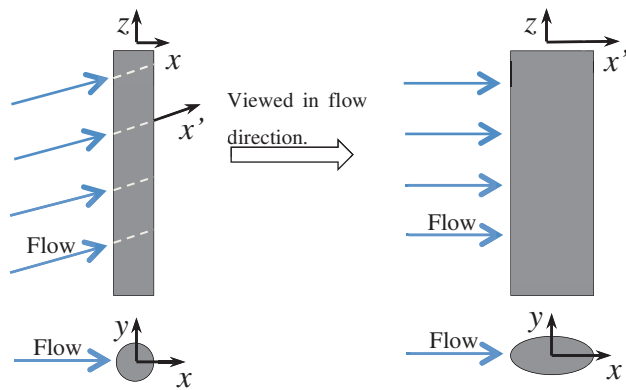
Figure 5.1 Definition sketch showing the analogy of oblique incoming flow over a circular cylinder to perpendicular flow over an elliptic cylinder. Only one dimension of the cylinder is elongated (x direction). y-axis and z-axis remain the same, while x axis is replaced using x'.

The shape factor (K) and the incidence angle (α_0) in the cross-sectional plane are two most important factors considered by most studies concerning flow around an elliptic cylinder. A definition sketch for shape factor K and incidence angle α_0 are depicted in Figure 5.2, together with the phase angle denoted by θ (previously defined in section 3.3.3). Note that, this incidence angle α_0 is different from the angle of attack α discussed in Chapter 4, as the latter is an axial angle. The incidence angle denoted by α_0 is in the x-y plane and defined as that between the flow direction and the major axis of the ellipse. The shape factor is defined as the minor to major axis ratio (see Figure 5.2), so that a smaller K indicates a flatter cross section.
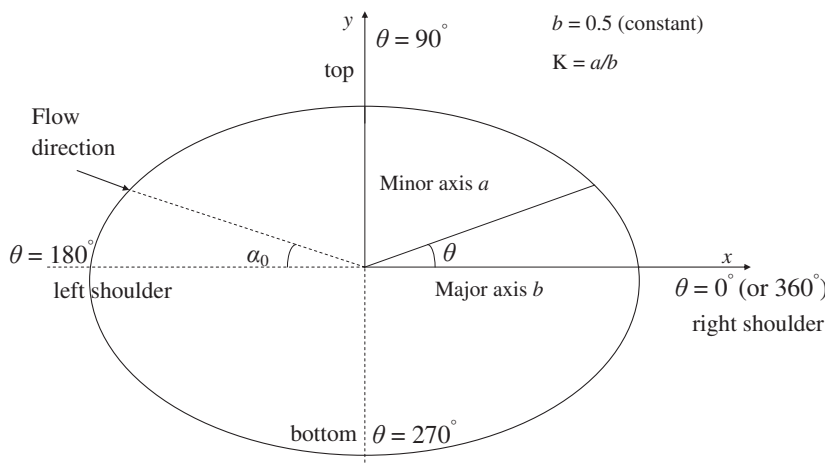
Figure 5.2. Definition sketch of the shape factor K and angle of attack α_0. Following Figure 5.1, if D is the diameter of the circular cylinder, for the elliptic cylinder, the minor axis $a = D$ and the major axis is $b = D/k$.

116

As mentioned in Section 1.2.1, previous research has considered flow around an elliptic cylinder under effects of both the shape ratio K and the incidence angle α_0 under various flow regimes [43, 45-50]. However, work directly related to Honji Instability has been rare. The only work that has been found so far was a theoretical study by Hall [17]. Hall found that the most unstable point around the circumference of the cylinder was dependent on both K and α_0. For the case of an oscillatory flow parallel to the major axis of the cylinder (i.e. $\alpha_0 = 0°$), it was found that the K-Taylor dependent curve representing the onset of the 2-D to 3-D transition appeared to be in a 'cusp-shaped' (reproduced in Figure 5.3). The curve, which bifurcates into two for $K < 0.6^{1/2}$, divides the whole K-Taylor plane into three regimes. Under the lower curve, the flow is 2-D and above the upper curve, the 3-D Honji instability occurs. The area between the two curves stands for the unstable flow with another type of instability happening close to the cylinder's shoulders, as shall be discussed later. The curves show that for an elliptic cylinder with a shape ratio K roughly > 0.5, a higher Taylor number is required for triggering the 2-D to 3-D transition than that required for a circular cylinder (i.e. $K = 1$), indicating that the flow is more stable as the cross-section becomes flatter. According to Hall's analysis, the flow was most stable at $K \approx 0.7$. In addition, the most unstable location also varies with K. At $\alpha_0 = 0°$, when $K > 0.6^{1/2}$, the most unstable point is found at the crown of the cylinder, namely, at $\theta_1 = 90°$ (and symmetrically 270°), while for $K < 0.6^{1/2}$, the flow is more unstable at two other locations (θ_2 and θ_3, which can be calculated from Equation 5.1 proposed by Hall), away from the top and bottom of the cylinder. This means that, as K decreases, flow particles become unstable at θ_2 and θ_3 at a smaller Taylor number, before the points near θ_1 (90° and symmetrically 270°) become unstable when higher Taylor number is reached. In other words, for the same KC, an instability develops at these two points (θ_2 and θ_3) for a smaller β number than at θ_1. It should be noted here that the instability found at θ_2 and θ_3 near the shoulders of the cylinder is different from the Honji instability that occurs at the crown of the cylinder, i.e. at $\theta_1 = 90°$ (and 270°). The properties, behaviours and structures of this 3-D instability near the cylinder shoulders remain unknown in the literature. More details on Hall's formulation for the case of $\alpha_0 = 0°$ are given in Section 5.4.

$$\theta_2 = \sin^{-1}\left(\frac{2K^2}{3(1-K^2)}\right)^{\frac{1}{2}} \text{ and } \theta_3 = 180° - \theta_2 \qquad\qquad 5.1$$
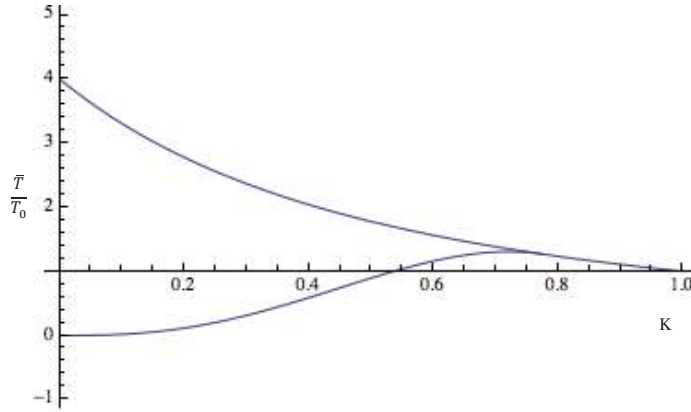
Figure 5.3. Reproduction of Hall's [17] figure 4 for the case of $\alpha_0 = 0°$. Upper curve represents the onset of Honji instability occurring at $\theta_1 = 90°$ (and $270°$), and lower curve represents another type of instability occurring at θ_2 and θ_3, the values of which can be calculated through Equation 5.1.

As a theoretical study, Hall's linear stability analysis focused on developing an analytical solution for the instability causing a 2-D to 3-D transition and deriving the governing parameters dependency curve (e.g. the H-Line given by Equation 1.4). However, no actual flow structures are given. In his paper, Hall mentioned an interest to see corresponding experimental results to confirm the cusp-shaped curve for $\alpha_0 = 0°$. However, no follow-up work on this has been found in the literature.

Inspired by previous studies, particularly the theoretical study of Hall [17], the current study bears four main aims. First, the present study provides detailed descriptions on the resultant flow structures under various thicknesses of the cross-section (K value) for the Honji instability at $\alpha_0 = 0°$. Second, the other type of instability happening near the shoulders of the cylinder is examined for the first time. Third, the results are used to validate the cusp-shaped dependent curve for $\alpha_0 = 0°$ provided by Hall's linear stability theory. The effects of the elliptic shape of the cross section are reflected through analyzing these aspects.

Bearing the main objectives in mind, 3-D numerical simulations are conducted under various values of K at the governing parameter values of interest. In this study, the flow oscillates in the direction of the elliptic cross section's major axis (i.e. $\alpha_0 = 0°$). The shape ratio (K) is varied to examine its influences on the resultant wake structures near the cylinder. Effects of the shape factor on flow structures are discussed at the governing parameters chosen so that both the stable Honji instability regime (at (KC, β)

= (2, 200)) and the unstable Honji regime (at (KC, β) = (2, 400)) observed for a circular cylinder are covered. Following Hall's [17] theory, a critical shape factor of $0.6^{\frac{1}{2}}$ is used as the dividing value for our discussion. For K > $0.6^{\frac{1}{2}}$ the flow is most unstable at the top and bottom points, and the effects of K on the Honji instability are discussed by evaluating the cases of K < cos40°. For K < $0.6^{\frac{1}{2}}$ the effects of the flatness come into power to shift the most unstable locations to points closer to the shoulders of the cylinder. Another type of instability other than the Honji instability occurs at lower governing parameters. This instability is studied at K = cos40° and cos60°.

5.3 Domain and Mesh

(a)   (b)
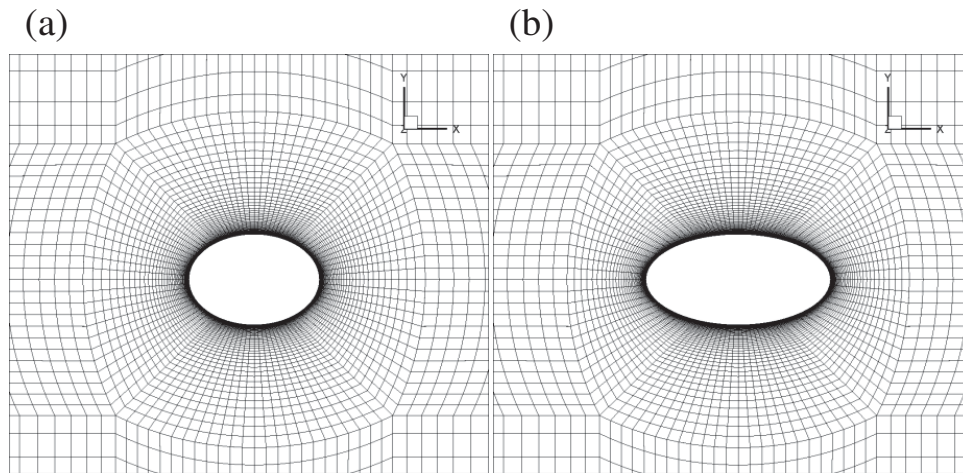
Figure 5.4. Demonstration for mesh in the near-cylinder region for two sampling shape factors (a) K = cos40° and (b) K = cos60°.

The dimension of the domain applied for the present study is again set as $40D \times 20D \times 4D$ (recall that $D = a$, see Figure 5.2), in consistence with the previous chapters. The meshes used for different elliptic cases (K < 1) in this chapter are generated based on the circular cylinder mesh (K = 1), which is the same as used in previous sections. Details of the mesh resolution for the circular cylinder are provided in Chapter 2 and shall not be repeated here. For the elliptic cases calculated in this chapter, similar yet slightly finer mesh than the circular cylinder case is applied so that no further mesh validation for the elliptic meshes shall be given here. Details for achieving the similar mesh is described below.

In the calculations, the shape factor K is varied by keeping the length of the minor axis in y-direction fixed at $0.5D$ and increasing the length of the major axis in x-direction. Following this definition, as the cross section of the cylinder becomes flatter (i.e. K smaller), the circumference is longer; hence the circumferential boundary requires more nodes to ensure that the element sizes do not undergo a dramatic change. The circumferential element size variation between different meshes is smaller than 1×10^{-4}. For the smallest K (i.e. the flattest cross section which has the longest circumference) in the present study, the number of nodal points along the cylinder's circumference is 128, which gives a circumferential density of about 0.03, similar to that of the circular cylinder. As is seen in Figure 5.4, the strategy in mesh generation for elliptic cylinders is similar to that applied to the circular cylinder case: finer mesh is employed in the vicinity of the cylinder's surface, and the mesh becomes coarser at locations further away from the cylinder. To give some general ideas about the discretization under the elliptic cylinder cases, the near-cylinder mesh of two K cases are given as examples in Figure 5.4.

5.4   Discussion of Hall's [17] theory

Since the current numerical simulations are compared with Hall's [17] linear stability analysis, before moving on to our results, we will first evaluate Hall's theory for the case of $\alpha_0 = 0°$ considering first order accuracy. According to Hall, the flow instability and unstable circumferential locations can be examined by considering the maximum values of Equation 5.2 (equation 4.2 given in Hall's paper). In this equation, $f(K, \theta)$ represents $S(\theta)$ as in Hall's notation. Following Hall's formulation, $f(K, \theta)$ is the term containing the phase angle θ, i.e. the functioning term when performing derivatives with regards to θ for the aim of locating the most unstable points.

$$f(K,\theta) = \frac{\sin^2(\theta - \alpha_0)}{(\sin^2\theta + K^2\cos^2\theta)^{\frac{5}{2}}} \qquad 5.2$$

With $\alpha_0 = 0°$, the above equation can be rewritten as

$$f(K,\theta) = \frac{\sin^2\theta}{(\sin^2\theta + K^2\cos^2\theta)^{\frac{5}{2}}}$$

5.3

and plotted in Figure 5.5, which clearly reflects the dependence of the peak values of $f(K, \theta)$ (as given in Equation 5.3) on both K and θ. From Figure 5.5 it is seen that, for a circular cylinder (K=1), the maximum $f(K, \theta)$ value is found at $\theta_1 = 90°$ ($\pi/2$), indicating the most unstable locations are at the vertex of the cylinder. This continues to be the case as K decreases, until after $0.6^{\frac{1}{2}}$ two other peaks of $f(K, \theta)$ occur at two more locations (θ_2 and θ_3). These two θ values are symmetric with respect to $90°$ ($\pi/2$) and can be calculated using Equation 5.1 as provided by Hall. The two new maximum values of $f(K, \theta)$ are larger than that found at $\theta_1 = 90°$, indicating higher instability at θ_2 and θ_3. This type of instability, which differs from the Honji instability, is resulted from the reduced gradient and flatter curvature at smaller K as shall be mentioned later. We will refer to this type of instability as the 'Side instability' in our discussions below.
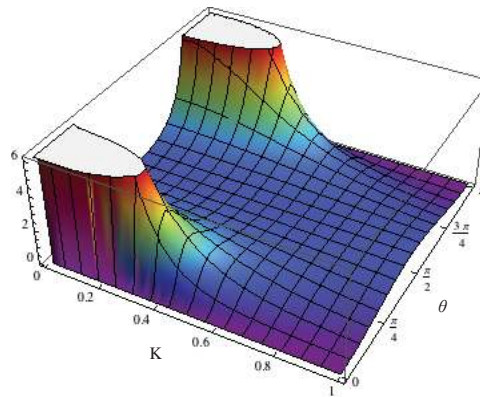
Figure 5.5 Plot of $f(K, \theta)$ as in 5.3 between $0 \leq K \leq 1$ and $0 \leq \theta \leq \pi$.

In his paper, Hall gave a dependency curve of the critical Taylor number on K, as reproduced in Figure 5.3. As shown in Figure 5.3, Hall's prediction finds that when K < $0.6^{\frac{1}{2}}$, the dependence curve bifurcates into an upper curve denoting the onset of the Honji instability, and a lower curve denoting the onset of the Side instability. As is seen from Figure 5.3, for the upper curve denoting the onset of Honji instability, the critical Taylor number increases with the decrease of K, which indicates that the Honji instability is less likely to occur around a cylinder with flatter cross sections. The whole

K-Taylor dependence plane is thus divided into three regions. Below the lower curve, the flow remains 2-D and above the upper curve Honji instability incepts. The region between the two curves represents the flow regime where only the Side instability occurs around the cylinder.

Based on Figure 5.3, the *KC–β* dependence curve can be derived for each K value. Specifically, the second-order-accurate *KC–β* dependence curve for the circular cylinder case (K = 1) is plotted by Hall [17], which is shown to compare well with Honji's [14] experiments. Later Hall's *KC–β* dependence curve with first order accuracy is discussed in other studies concerning the onset of Honji instability including Sarpkaya [15, 18], An et al. [21] and Suthon and Dalton [22, 23]. They all showed that the dependence curve depicted with first order accuracy compares fairly well with the experimental and numerical results and can be used as a brief guidance for determining the flow regime under different *KC* and *β* values. Considering the effects of K for an elliptic cylinder, we now derive the flow regime dependence on *KC*, *β* and K with first order accuracy following Hall's formulation.

According to Hall, the dependence of the critical Taylor number T_c on these parameters reads:

$$T_c = \frac{11.99(\sin^2\theta + K^2\cos^2\theta)^{\frac{5}{2}}}{\sin^2\theta\,(1+K)^2} \tag{5.4}$$

Considering the aforementioned change of the number of maximum values at different K (see Figure 5.5), the dependence of T_c on *KC*, *β* and K are discussed in two K ranges separated by the value of $0.6^{\frac{1}{2}}$. The dependences of Honji instability and the Side instability on *KC*, *β* and K are determined for $K > 0.6^{\frac{1}{2}}$ and $K < 0.6^{\frac{1}{2}}$, respectively.

5.4.1 Dependence for the onset of Honji instability on *KC*, *β* and K

Since the most unstable points occur at $\theta = 90°$ (considering only the range of $0° < \theta < 180°$), substituting $\theta = 90°$ into Equation 5.4 results in

$$T_c = \frac{11.99}{(1 + K)^2} \qquad \text{5.5}$$

Based on the definition of T_c given in Hall [17], we found

$$KC^2 \beta^{\frac{1}{2}} = 11.137 T_c \qquad \text{5.6}$$

The relationship between KC, β and K to first order of accuracy can be obtained by substituting Equation 5.6 into Equation 5.5.

$$KC\beta^{\frac{1}{4}} = 11.556 \sqrt{\frac{1}{(1 + K)^2}} \qquad \text{5.7}$$

from which the critical K required for suppression of Honji instability as a function of KC and β can be derived. Specially, when K = 1 (the circular cylinder case), we have Equation 1.4, as mentioned by Sarpkaya[15, 18], An et al.[21] and Suthon and Dalton[22, 23].

Using Equation 5.7 the dependence of KC on both β and K to the first order of accuracy is plotted as a 3-D contour surface in Figure 5.6. As can be seen, for every smaller K, the KC–β curve is higher than the one with larger K. This means higher KC and β values are needed for Honji instability to occur when K decreases, i.e. the flow is more stable around a flatter cylinder. The critical K value (or the critical flatness of the cylinder) at $(KC, \beta) = (2, 200)$ and $(2, 400)$ are estimated to be 0.54 and 0.30, respectively.
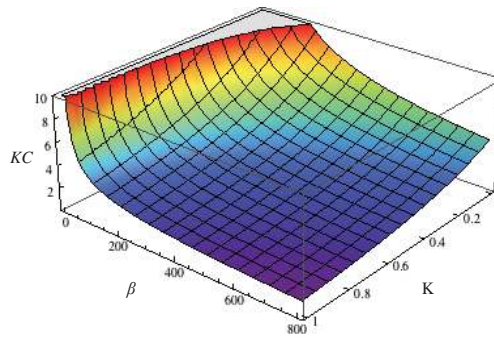
Figure 5.6 Dependence of KC on both β and K as in Equation 5.7. $0 < \beta < 800$ and $0 \leq K \leq 1$.

5.4.2 Dependence for the onset of Side instability on KC, β and K

When K is smaller than $0.6^{\frac{1}{2}}$, the most unstable points move from the crown of the cylinder ($\theta = 90°$ and $270°$) to locations closer to the cylinder shoulders ($\theta = 0°$ and $180°$). The Side instability occurs at these locations which can be calculated from Equation 5.1. Replacing θ with K in Equation 5.4 and considering Equation 5.7, we can get the dependence of KC and β as a function of K as given in Equation 5.8.

$$KC\beta^{\frac{1}{4}} = 11.556 \sqrt{\frac{(\sin^2(\sin^{-1}(\frac{2K^2}{3(1-K^2)})^{0.5}) + K^2\cos^2(\sin^{-1}(\frac{2K^2}{3(1-K^2)})^{0.5}))^{\frac{5}{2}}}{\sin^2(\sin^{-1}(\frac{2K^2}{3(1-K^2)})^{0.5})(1+K)^2}} \qquad 5.8$$

Based on which we can draw the trend of the dependence of KC on both β and K in Figure 5.7.
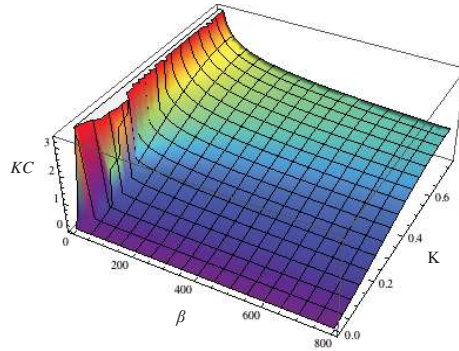
Figure 5.7 Dependence of KC on both β and K as in Equation 5.8. $0 < \beta < 800$ and $0 \le K < 0.6^{1/2}$.

At this point it should be mentioned that Hall's theory was derived based on the assumption of very small KC and very large β. In addition, the results presented by Hall are for the time-averaged flow field. Nevertheless, the analysis by Hall provides us with a theoretical basis for the influence of the governing parameters, namely, KC, β and K on Honji and Side instabilities. However, full description of the instantaneous fluid field must be gained through flow visualisations of either physical or numerical experiments. In the following, detailed flow behaviours and calculated flow field structures are discussed based on numerical simulations under selected governing parameter ranges.

5.5 Effects of K on Honji instability (K > $0.6^{\frac{1}{2}}$)

At K > $0.6^{\frac{1}{2}}$, the flow is predicted to become most unstable at the crown (θ = 90° and 270°) of the cylinder in the form of Honji instability. As shown in Figure 5.6, for a constant (KC, β), the flow becomes more stable with the decrease of K. When K is reduced to a certain threshold at a given (KC, β), further decreasing of K will suppress the Honji instability. The minimum K values for the Honji instability to operate would be respectively K $\geq$ 0.54 at (KC, β) = (2, 200) and K $\geq$ 0.30 at (KC, β) = (2, 400), calculated from Equation 5.7 proposed by Hall.

In the following sections we shall discuss the flow calculated using the current numerical model under different values of K smaller than cos40° (cos40° is close to the value of $0.6^{\frac{1}{2}}$). Descriptions are given for both the flow evolution with time and the developed instantaneous flow structures for the cases concerned. Explanations on the observations for the effects of K are attempted from two aspects as discussed in Section 5.8.

5.5.1 **Flow development over 200 periods**

The evolution of the instantaneous u_z/U_{mx} is sampled for 200 flow periods. The spatial-temporal evolution of the non-dimensional axial velocity component recorded at (x/D, y/D, z/D) = (0, 0.51, 0 ~ 4) are presented in Figure 5.8 for the cases of (KC, β) = (2, 200) and (KC, β) = (2, 400). As mentioned in Chapter 4, for a circular cylinder perpendicular to the oscillatory flow, the flow at the parameter group (KC, β) = (2, 200) falls in the stable Honji regime, where the vortices formed along the cylinder span bear complete and distinctive mushroom-like shapes. For (KC, β) = (2, 400) the flow falls in the unstable Honji regime where the Honji vortical structures formed along the cylinder are unstable and interacting with each other. When the cylinder becomes elliptic, the stabilising effects of decreasing K can be observed for both the case of β = 200 and β = 400.

The evolutions of the flow field shown in Figure 5.8 and Figure 5.9 experience three phases: phase I for the 2-D potential flow, phase II for the orderly distributed vortex pairs and phase III for the interactive vortex pairs. Comparing between the results given

for different values of K, it is clearly shown that the developed three-dimensionality decreases as K becomes smaller (i.e. the cylinder is flatter) for both $\beta = 200$ and $\beta = 400$, which agrees with the theoretical prediction given by Hall [17].

The results for the cases of $\beta = 200$ given in Figure 5.8 are studied first. Comparison of the evolution processes between K = 1 (Figure 5.8a), K = cos10° (Figure 5.8b) and K = cos20° (Figure 5.8c) shows that, as K decreases, the onset of 3-D features marked by the appearing of the evenly distributed stripes is delayed, which is reflected by the elongated phase I. As seen in Figure 5.8, the stripes can only be observed after 60 periods for K = 1, after 90 periods for K = cos10° and after 110 periods for K = cos20°. In phase II, for both K = 1 and K = cos10° we can see six parallel stripes indicating six vortex pairs along the cylinder span. However, there are seven vortex pairs along the cylinder in phase II when K is further decreased to cos20°. There is also one more vortex pair for K = cos20° than K = 1 and K = cos10° when the flow enters the interactive phase III. As K is reduced, the vortex pairs become less active, as reflected by the decreasing interacting frequency with smaller K. During the vortices interaction, the evolution period for one new vortex pair to generate takes about 15 flow oscillations at K = 1, while for K = cos10° it takes slightly longer, about 18 flow oscillations. And for K = cos20° only one merging of the neighbouring vortex pairs is observed within the 200 calculated periods. All this delay of the flow development and elongated process when K is reduced suggests that the flow becomes more stable.

When K is further reduced to cos30°, the 2-D flow dominates throughout the free-developing 200 periods calculated and the flow remains at phase I (Figure 5.8c). We use the two-step method described in Section 4.4.2 to check whether the flow is intrinsically 2-D under this situation. First the test runs are conducted with a pre-assigned 3-D initial condition for this case. It is observed that as the calculations progress, the three-dimensionality is finally suppressed. Then the calculations with a perturbation added at the sides of the cylinder also fail to reveal any three-dimensionality in the flow field after 100 flow periods. It is therefore concluded that the computed flow field is intrinsically stable for K = cos30° at $(KC, \beta) = (2, 200)$. Considering the stronger stabilising effects of smaller K, it is speculated that further reducing K will also result in

the 2-D columnar flow and hence further decreasing K at $(KC, \beta) = (2, 200)$ is withdrawn here.

The flow development for the same K values at $(KC, \beta) = (2, 400)$ are shown in Figure 5.9, from which the same trend of 3-D weakening with smaller K is observed. However, as β is increased to 400, the flow becomes intrinsically more unstable, and the 3-D features appear earlier than those with $\beta = 200$. It is seen that for K = 1, cos10° and cos20°, the flow enters the interactive phase III shortly after calculation starts, after a short transient phase II characterised by stable vortices. Phase III, or the interaction phase, dominates the following calculated periods with a much stronger and higher-frequency interactions between the vortices compared with the smaller β cases. The interactions of the vortices appear random along the cylinder span so that unlike the cases of $\beta = 200$, it is hard to distinguish the generation and merging of individual vortex pairs. Although the differences between the cases of K = 1, K = cos10° and K = cos20° are not obvious, a closer look at Figure 5.9a,b,c does spot a slight delay of the instability development as K decreases. However, as K is further decreased to cos30° (Figure 5.9d), obvious weakening of the irregular 3-D features is observed. Firstly, the onset of 3-D is delayed for more than 30 flow periods than that of larger K values. Secondly, phase II lasts for about 20 periods, which doubles that of larger K cases. Finally, the frequency of interaction in phase III becomes much lower for K = cos30°.

The characteristic wavenumber is studied to give quantitative description of the vortical structures developed at different K. The wavenumbers calculated along the same probing line as shown in Figure 5.9 at $N = 200$ for all cases are compared in Figure 5.10. For $\beta = 200$, as K is decreased from 1 to cos10°, the dominant wavenumber remains unchanged at about 1.2, indicating there are five main vortex pairs along the cylinder span. This agrees with our observations in Figure 5.8. The corresponding wavelength is $1/1.2 \approx 0.83$. The wavelength is reduced as K is reduced to cos20°. The dominant wavenumber read from Figure 5.10 for this case is roughly 1.5, which means there are six vortex pairs generated along the cylinder span, and the wavelength is $1/1.5 \approx 0.67$. For flow cases with strong three-dimensionality at $(KC, \beta) = (2, 400)$ with K = 1, cos10° and cos20°, no dominant characteristic wavenumber is detected because of irregular high-wavelength interactions between the vortices. There are more than one major

values of wavenumber found for these cases as the flow is in a chaotic interaction stage. For a smaller K of the value cos30°, a dominant wavenumber (although relatively weak) emerges as the 3-D of the flow is simply weakened enough to allow the distinguishing of a unique dominant wavenumber. The dominant wavenumber reads for this case is about 2.2, which gives a wavelength of about 0.45.

(a) K = 1

(b) K =cos10°

(c) K =cos20°

(d) K =cos30°
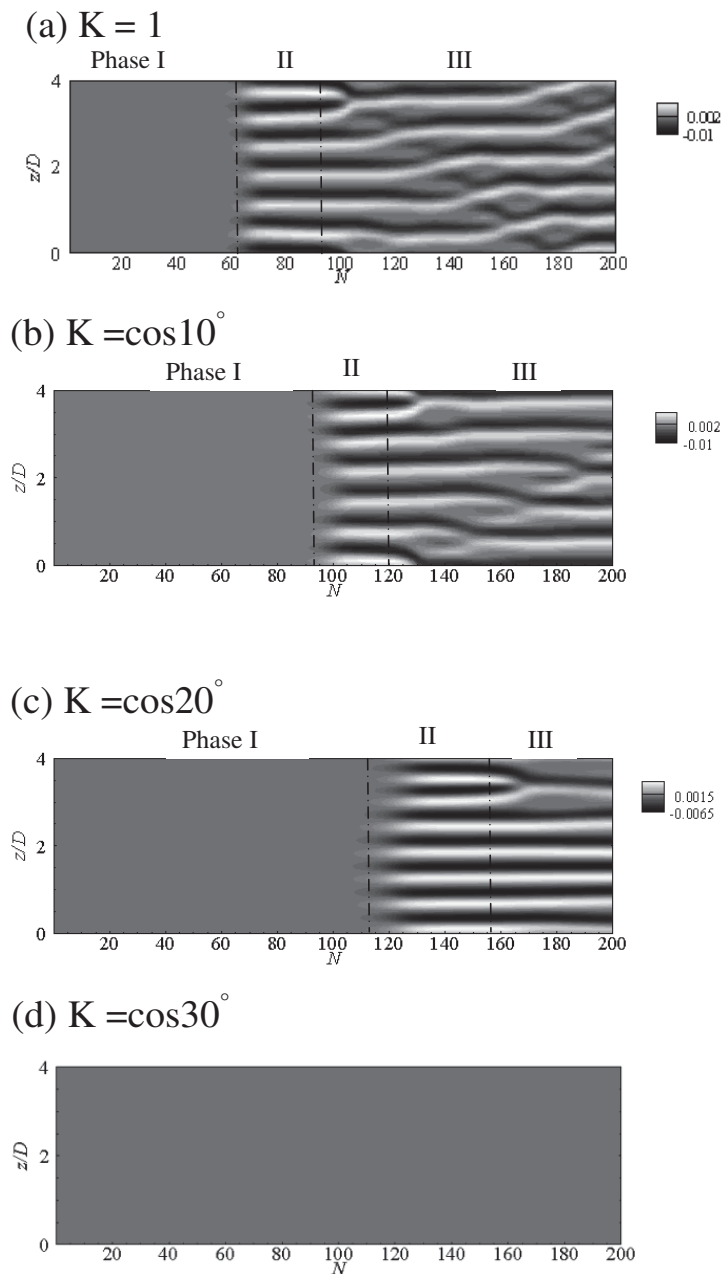
Figure 5.8 Spatial-temporal evolution of the non-dimensional axial velocity component over the 200 periods at $KC = 2$ and $\beta = 200$ for various K values smaller than cos40°. Recorded along a probing line with coordinates of $(x/D, y/D, z/D) = (0, 0.51, 0 \sim 4)$.

(a) K = 1

(b) K = cos10°

(c) K = cos20°

(d) K = cos30°
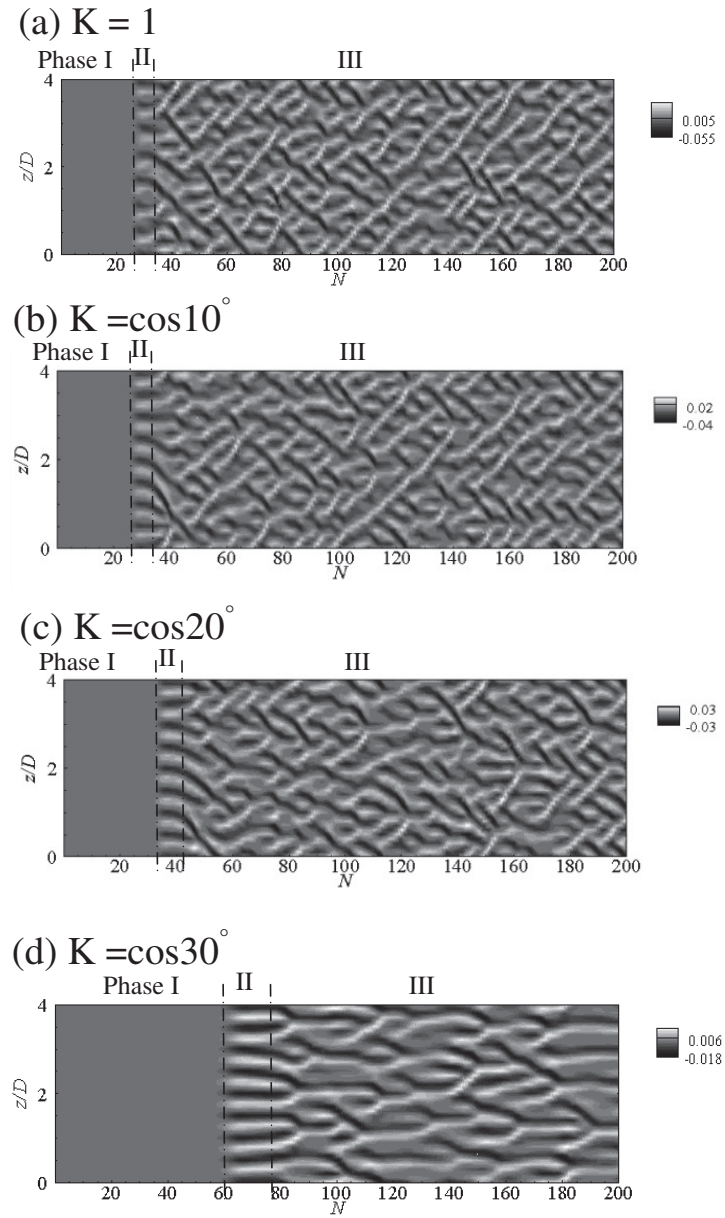
Figure 5.9 Spatial-temporal evolution of the non-dimensional axial velocity component over the 200 periods at *KC* = 2 and β = 400 for various K values smaller than cos40°. Recorded along a probing line with coordinates of (*x/D*, *y/D*, *z/D*) = (0, 0.51, 0 ~ 4).
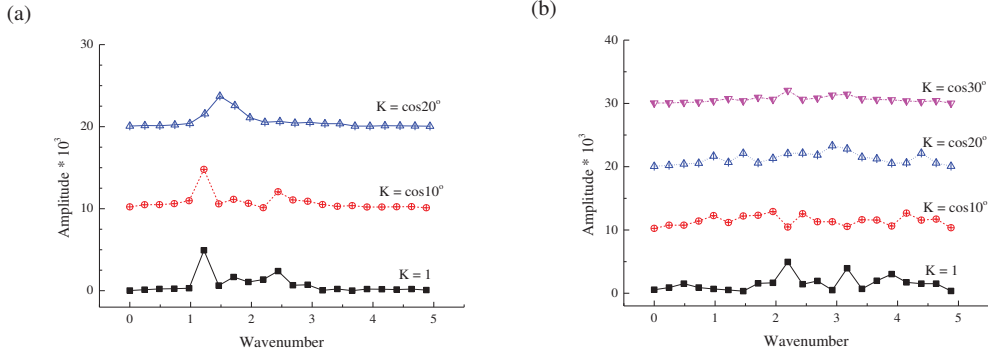
Figure 5.10 Characteristic wavenumber obtained from FFT under different α for (a) $(KC, \beta) = (2, 200)$ and (b) (KC, β) = (2, 400) at $N = 200$. An offset between different K is applied in each figure for aim of clarity.

These observations support the finding that small K is effective in destroying the Honji instability in the flow field near an elliptic cylinder. The detailed instantaneous Honji vortical structures generated under the effects of K is studied in the following section.

5.5.2 Instantaneous 3-D vortex structures

The instantaneous flow structures are studied using the results calculated for the 200th period. Similar to the method used in Chapter 4 the vortical structures formed near the cylinder surface are visualised using iso-surfaces of vorticity (ω_x). The results presented in Figure 5.11 and Figure 5.12 are the views projected to a plane that is perpendicular to the streamwise direction. Since the dimension of the cylinder in the minor axis direction is fixed as one, the width of the cylinder shown in these figures is identical for all K values.

Results for $\beta = 200$ at different shape factors are given in Figure 5.11. As observed in Section 5.5.1, in the 200th flow period the flow has entered a weak interaction phase for K = 1, cos10° and cos20°. Since the flow with $\beta = 200$ is in the stable Honji regime and the interactions between vortex pairs are weak and regular, distinct vortices can still be seen in Figure 5.11. Similar to that reported in Chapter 4, the vortical structures wrapping the cylinder surface are in two layers along the direction perpendicular to the cylinder's span (z-axis). The two layers consist of the rib-like vortical tubes in the top layer sitting on a pair of flat counter-rotating vortices attached to the wall (an illustration of the plane view of this structure can be found in Figure 5.15, which shall be discussed

later on). The top layer with larger radial extent represents the typical Honji vortices in the shape of mushrooms. For K = cos30°, no vortical structures are present because no Honji instability develops and the flow remains in 2-D potential flow (phase I).

Variation of K affects the distribution of the Honji vortex pairs, which arrange in arrays along the cylinder span. For the stronger 3-D cases at $\beta = 200$ (K = 1 and cos10° as in Figure 5.11a, b), the cylinder surface is wrapped by two arrays of five counter-rotating vortex pairs representing the Honji structures. As labelled in Figure 5.11, there is one array of vortex pairs at both the top (left to the x-axis in the figure) and bottom (right to the x-axis in the figure) half plane. The two arrays look similar but are not completely the same due to the interacting behaviours of the vortices in phase III. It is observed that for K = 1 the number of vortex pairs in each array is the same, however for K = cos10° six pairs are in the left array including one being the transient vortex while only 4.5 are in the right array. When K = cos20°, one more vortex pair is present (Figure 5.11c) and each array has six vortex pairs. It seems that the shape and dimension of every single vortex pair remain more or less unchanged for different K values. The existence of an additional vortex pair at small K values results in smaller distances between the vortex pairs than those with larger K cases.

The 3-D structures given in Figure 5.11 are related to the flow development progresses at different K values. It is mentioned in Section 5.5.1 that the flow development at K = 1 is slightly quicker than that at K = cos10° because of the suppressing effects of a smaller K. Regarding the axial shifting and interactions of theses two-layer vortices at the early stage of 3-D development (as discussed in Section 4.4.1), for K = 1, all the five main vortices have finished one interaction with a transient vortex and the associated axial shifting by the time of $t/T = 200$, as shown in Figure 5.8. As a result, five distinct vortex pairs can be seen in Figure 5.11a. However, for K = cos10°, only four shifting and associated merging of vortices have completed by $t/T = 200$, indicating a delay in the flow development. As seen in Figure 5.11b, there are six vortex pairs in the left array, which include five main vortices and one transient vortex pair. Following a similar process as that described in Section 4.4.1, the transient vortex pair labelled in the dashed circle in Figure 5.11b will merge with its neighbour and disappear in later periods. Then the vortices distribution along the cylinder's whole span will look very

similar to that of Figure 5.11a. The flow is more stable and its development further delayed for K = cos20°. At this K, the vortex pairs are more evenly distributed as shown in Figure 5.11c, having just entered the interactive phase III. In addition, the vortex arrays generated on two half planes consist of the same number of vortex pairs. There are six vortex pairs in each array, i.e. one more than the cases of K = 1 and cos10°. However, it is observed that the dimensions of each vortex seem more or less unchanged; hence the neighbouring vortices are closer to each other. Finally, further decrease of K to cos30° leads to the suppression of 3-D instability near the cylinder, as observed in Figure 5.11d.
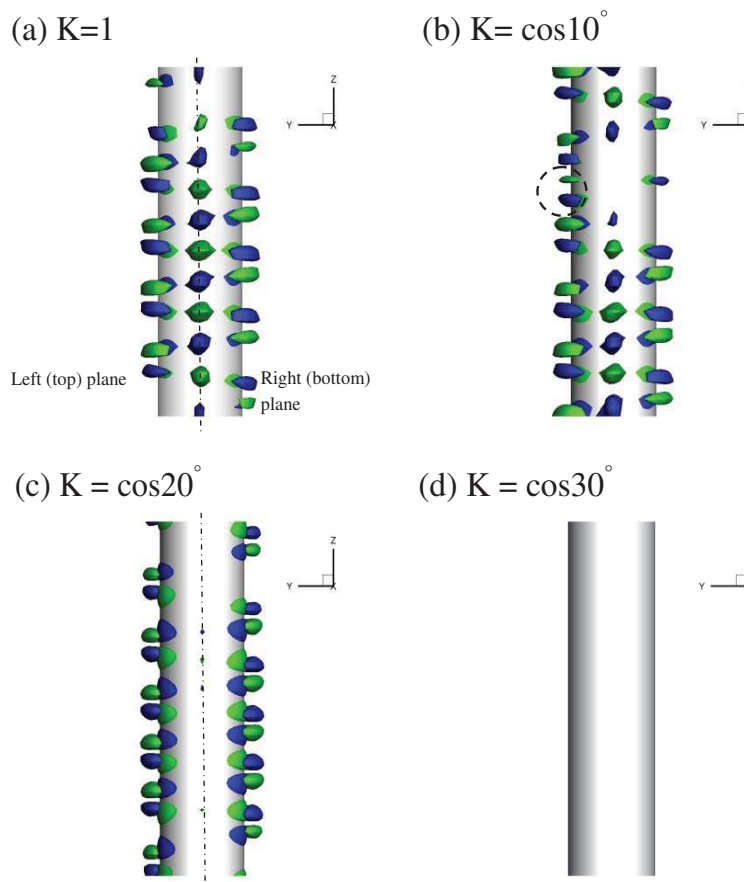
Figure 5.11 Instantaneous structures of iso-surfaces of ω_x near the cylinder for various K < cos40° at (KC, β) = (2, 200). Plot at t/T=200. The view direction is perpendicular to the direction of the major axis of the elliptic cross section. With x-axis as the boundary, its left is regarded as the top plane (i.e. $\theta = 0°$ to 180° as previous defined) and the right the bottom plane ($\theta = 180°$ to 360°).

At $\beta = 400$ and K < cos30° the intrinsic three dimensionality in the near wake is so strong that vortices are strongly irregular with various sizes and strengths as shown in

Figure 5.12a,b,c. Compared with $\beta = 200$, the vortices cover a much larger portion of the cylinder in both the circumferential and axial directions. They extend across the *x*-axis and interact with vortices from the other half plane. In consistence with our previous findings, 3-D behaviours become weaker as K decreases. In consistence with our previous observations, 3-D behaviours become weaker as K decreases. This is reflected by the ease of the vortex irregularity and the decrease of the circumferential coverage of the vorticity contours. For $K = \cos 30°$ the vortices of both the top and bottom half planes remain disconnected with the vortices from the other plane (similar to the $\beta = 200$ case). Fewer interactions are observed and the vortices appear to be in a more distinct shape. However, unlike the cases at $\beta = 200$ which are more regular, the vortex arrays formed on two half planes of the cylinder look quite distinct with different number of vortices and the vortices are in various shapes.

(a) $\beta = 400$, K = 1

(b) K= $\cos 10°$

Left (top) plane

Right (bottom) plane

(c) K= $\cos 20°$

(d) K= $\cos 30°$
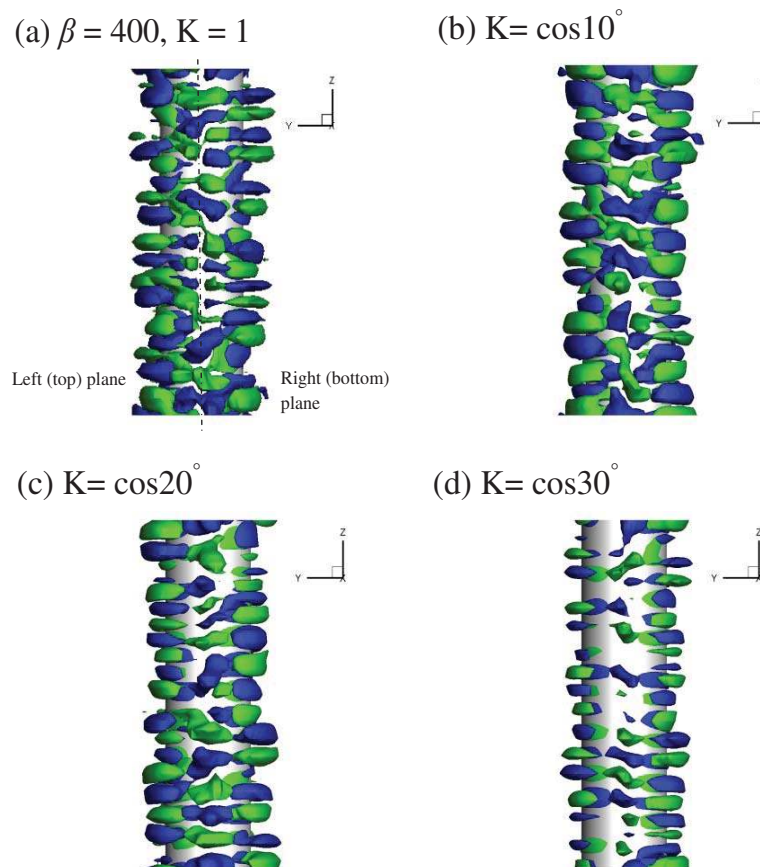
Figure 5.12 Instantaneous structures of iso-surfaces of ω_x near the cylinder for various K < $\cos 40°$ at $KC = 2$ and $\beta = 400$. Plot at t/T=200. The view direction is perpendicular to the direction of the major axis of the elliptic cross section. With *x*-axis as the boundary, its left is regarded as the top plane (i.e. $\theta = 0°$ to $180°$ as previous defined) and the right the bottom plane ($\theta = 180°$ to $360°$).

5.5.3 Circumferential distribution of vorticity at different values of K

This section studies the circumferential coverage of the vortices, using similar figure as Section 4.6.2. It has been noticed from the 3-D instantaneous flow visualizations that the circumferential span is affected by K. In addition, the axial extents of the vortices also seem to vary at different circumferential locations. In Figure 5.13 and Figure 5.14, a plane view of the contours of ω_x for the recorded nodes at circuits located in the centre of the top-layer vorticity along the cylinder span is given for the different values of K studied at $(KC, \beta) = (2, 200)$ and $(KC, \beta) = (2, 400)$. From these extended plane views we can clearly see the circumferential distribution of the 3-D structures for each case.

The results for the cases of $\beta = 200$ are given in Figure 5.13, from which it can be observed that there are some similarities between the vortex distributions obtained at different values of K. First, viewing along the cylinder span, it is seen that the vortices for all cases are horizontal and perpendicular to the cylinder span. Also, the vortices from the two arrays are interlacing and distribute in a staggered manner with respect to the cylinder axis. The counter-signing stripes indicate the counter-rotating vortices within each vortex pair, and these two vortices are equal and symmetric with each other.

Although the circumferential distribution looks similar, several shape effects can be noted when K is varied. First, the strength of the overall vorticity field is weaker at a smaller K, indicating a reduced instability. Furthermore, with the decrease of K the circumferential span of the vortices also sees a decrease. The range of the cylinder circumference covered by the vortical structures is over 70% for K = 1, over 60% for K = cos10° and only about 55% for K = cos20°.

(a) K = 1 (b) K = cos10°

(c) K = cos20°
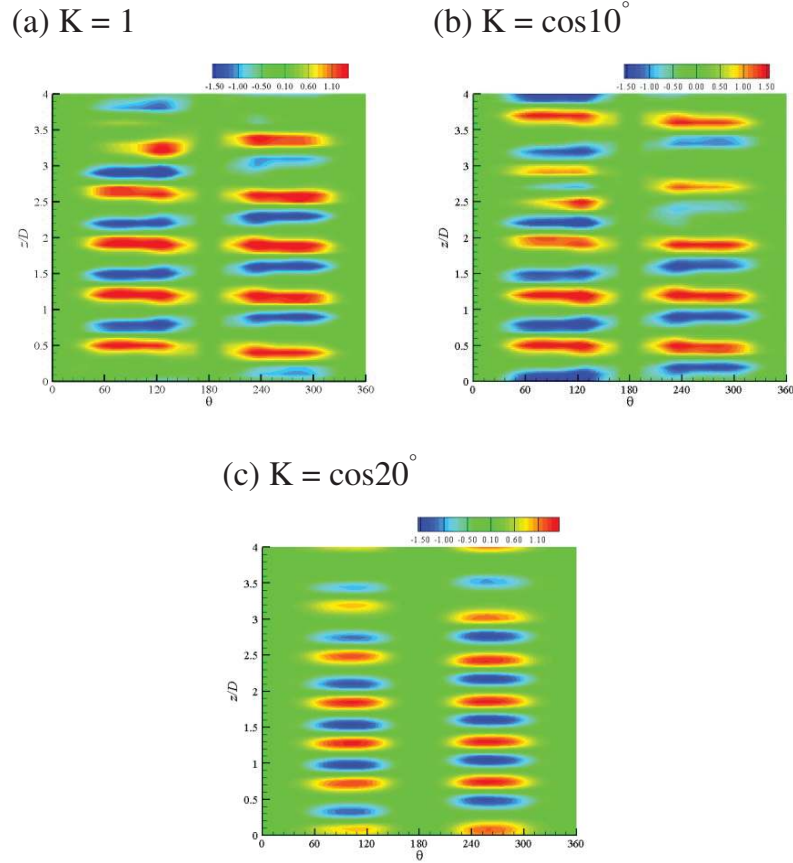
Figure 5.13 Comparison of circumferential dimensions visualised by contours of ω_x plotted along the cylinder circumference over the whole length of the cylinder for $(KC, \beta) = (2, 200)$. Plot in the range of $-1.5 < \omega_x < 1.5$ at $N = 200$. The circuit plane probed is at the centre of the top layer vortices of the two-layer Honji vortical structures.

For $\beta = 400$, the vortices distributions are not as regular as that shown for the $\beta = 200$ cases, due to the strong interactions between the vortices. As can be observed from Figure 5.14, the vortical stripes representing the vortices are of various shapes and sizes along the cylinder span as well as along the circumference (θ). Compared with the cases of $\beta = 200$, it is seen that the stripes become shorter in the axial direction but longer along the circumference. The stripes are much narrower in z-direction because more vortices are generated in each array, and around the cylinder the vorticity contours span so long over the shoulder of the cylinder ($\theta = 180°$) to connect with the same-signing vorticity in the other array. This indicates that the vortices between the top half plane and bottom half plane at certain axial locations pass around the boundary angle of $\theta = 180°$ to interact with each other. All these observations reflect a stronger instability at higher β.

The stabilising effect of decreasing K is indicated by the facts observed which include that the vortex pairs are more orderly distributed, and that at the same time the strengths of the vortices slightly weaken, as indicated by the vorticity contours. It is noticed that when K is decreased from K = 1 to K = cos30°, although the cross section is largely flatter, the circumferential coverage of the vortices remains more or less unchanged. This is resulted from the combined effects of two reasons. For one thing, as K is smaller the flow is more stable and the three-dimensionality of the flow is weaker, which should lead to a decrease of the vorticity strength and a shortening of the circumferential coverage; on the contrary, the flattening of the cross-sectional area and elongation of the curvature result in a stretch of the vortices along the cylinder circumference, which increases the circumferential coverage of the vortical structures.
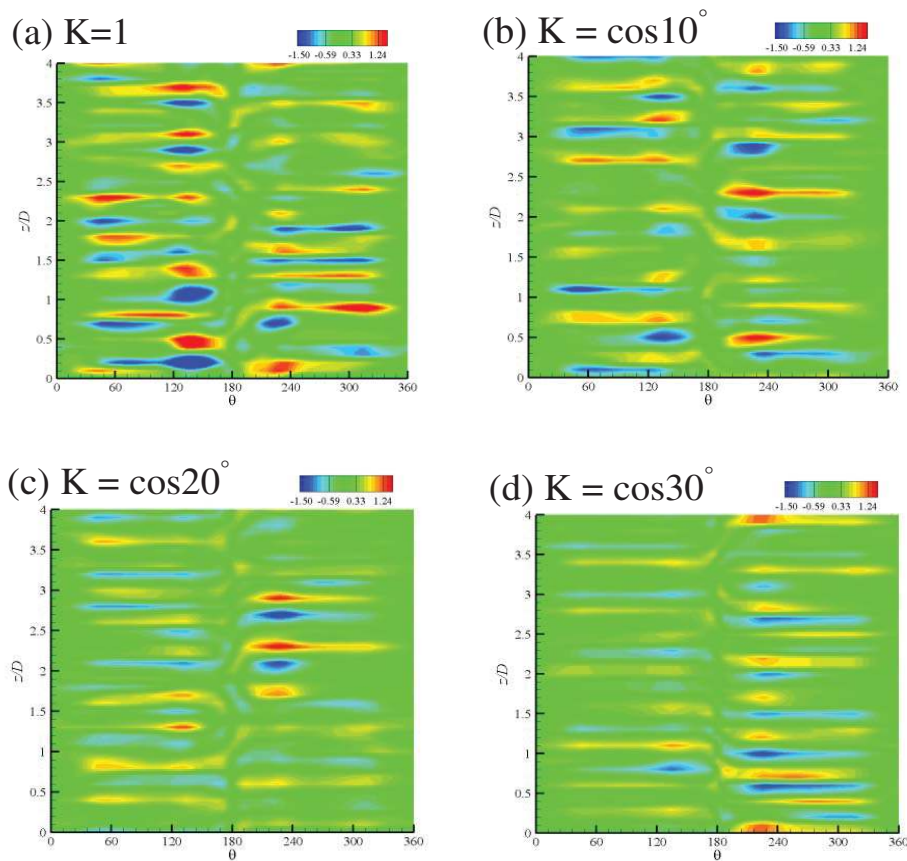
Figure 5.14 Comparison of circumferential dimensions visualised by contours of ω_x plotted along the cylinder circumference over the whole length of the cylinder for $(KC, \beta) = (2, 400)$. Plot in the range of $-1.5 < \omega_x < 1.5$ at $N = 200$. The circuit plane probed is at the centre of the top layer vortices of the two-layer Honji vortical structures.

5.5.4 Evolution of Honji vortex structures within one flow period

The evolution of the two-layer vortical structures within one oscillation period is studied in both $x/D = 0$ plane and the cross-sectional plane of $z/D = 2$.

5.5.4.1 Cross-sectional view of vortices

The vortical structures in the plane of $x/D = 0$ within one oscillation period for a circular cylinder (K = 1) at $(KC, \beta) = (2, 200)$ and $(KC, \beta) = (2, 400)$ have been discussed in Section 4.5.1 and shall not be repeated here. The following discussions are then focused on the cases of K < 1.

For the stable cases at $\beta = 200$ with K = cos10° and cos20°, the vortical structures formed near the cylinder are similar to that of the case K = 1. Distinct two-layer structures are distributed along the cylinder with the top layer more developed and extended in *y*-direction, while the bottom layer is flatter with a slightly longer axial span. The developed flow field obtained for K = cos10° shown in Figure 5.15 demonstrates five main vortex pairs along with an additional transient new pair. Among all the vortex pairs, three of them (almost covering half of the cylinder span) seem to have fully developed at this moment, with a core-to-core interval of roughly $\Delta z/D = 0.8$. Similar to that of K = 1; these three vortex pairs also seem to have similar sizes and shapes with those of K = 1. The other three, which are circled in Figure 5.15, are attached close to each other at this moment and shall interact in later periods. It is speculated that at a later moment the whole vortical field along the cylinder will become just like that of K = 1 with five main vortices distributed along the cylinder span. However, the five-main-vortex distribution is altered when K is further reduced to cos20°. As shown in Figure 5.16, the case of K = cos20° sees six main two-layer vortex pairs on both banks which are in a staggered manner with respect to the cylinder axis. It can be observed from both Figure 5.15 and Figure 5.16 that within the period visualised here, the vortical structures seem to only vary in strength, while the location, shape and size of all vortices are hardly changed. It is found that the interactions between vortices (namely, merging of existing vortices and generating of new vortices) accomplish as the flow evolves but not within one oscillation period.

The plane view for $\beta = 400$ and K =1 is shown in Figure 4.17. For K < 1, the resultant flow fields for cos10° and cos20° are similar, therefore in order to avoid repetition the case of K = cos10° is omitted here. Figure 5.17 gives the evolution of vortices in $x/D = 0$ plane for the case of K = cos20°. As the interaction and irregularity of the vortices weaken when K is reduced to cos20°, the two-layer structures that have a more extended top layer and a flatter bottom layer are in a more regular and distinct shape. The stabilization of the vortex behaviours indicates the flow becomes more stable as K reduces to cos20° from K = 1. At different instants within one period, the size and shape of each vortex show visible variation. With more vortices generated along the cylinder span compared with the cases of $\beta = 200$, the vortices are very close to each other, although no obvious interaction between neighbouring vortices is observed. However, there is neither generation nor dissipation of vortices throughout the oscillation period, and the number of vortices remains unchanged.

As shown in Figure 5.18, further stabilization of the flow field is observed when K is reduced to cos30°. The vorticity field is further weakened compared with larger K values. With a more stable flow, the size and shape of each vortex pair seem to become more similar, and remain unchanged throughout the flow period. In addition, the flow field shows a better periodicity. At all instants during the period, the vortical structures are more distinct and the number of prominent vortex pairs can be identified to be seven on the upper bank and nine on the lower bank of the cylinder span respectively. Recall that the FFT analysis for this case shows a dominant wavenumber of roughly 2.2. This dominant wavenumber indicates approximately ($2.2 \times 4 = 8.8 \approx$) 9 vortex pairs along the cylinder, which is in consistence with the present observation.

The regular vortex structures for the case of K = cos30° at $\beta = 400$ should be distinguished from that obtained at $\beta = 200$. Unlike the cases of $\beta = 200$, the vortices demonstrated in Figure 5.18 have different shapes and sizes along the cylinder, especially in their radial extents (definition sketch given in Figure 4.27); the vortices bear larger variations in the radial span than in the axial span). In addition, there are five prominent pairs of vortices for $\beta = 200$ along the cylinder span so that each vortex pair covers an axial length of about 0.8D, while about 7~9 pairs of vortices can be identified

in Figure 5.18, meaning a distance between the cores of two neighbouring vortex pairs is about 0.5*D*.

(a) *t*=0*

Upper bank

Lower bank

(b) *t*=1/8*

(c) *t*=1/4*

(d) *t*=3/8*

(e) *t*=1/2*

(f) *t*=3/4*

(g) *t*=1*
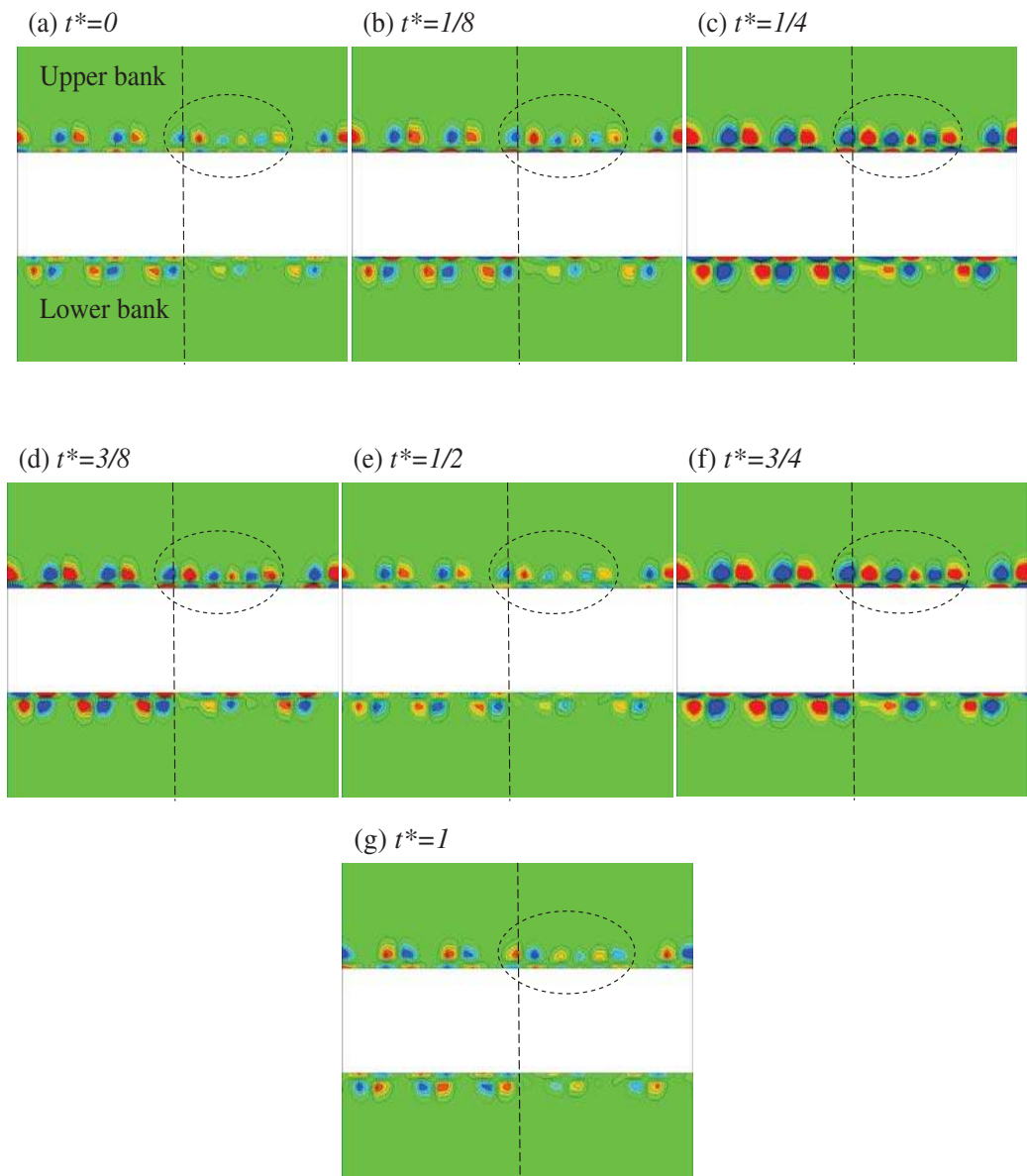
Figure 5.15 Vortex array in plane *x/D* = 0 in vorticity contours of ω_x for one oscillation period. For (*KC*, *β*) = (2, 200) and K = cos10°. *t** = *t/T*-200 and -1.5 < ω_x < 1.5. Circled is the additional transient new pair. For the first ½ period the interval is Δ*t** = 1/8 and for the second half period Δ*t** = 1/4.

(a) *t*=0* (b) *t*=1/8* (c) *t*=1/4*

Upper bank

Lower bank

(d) *t*=3/8* (e) *t*=1/2* (f) *t*=3/4*

(g) *t*=1*
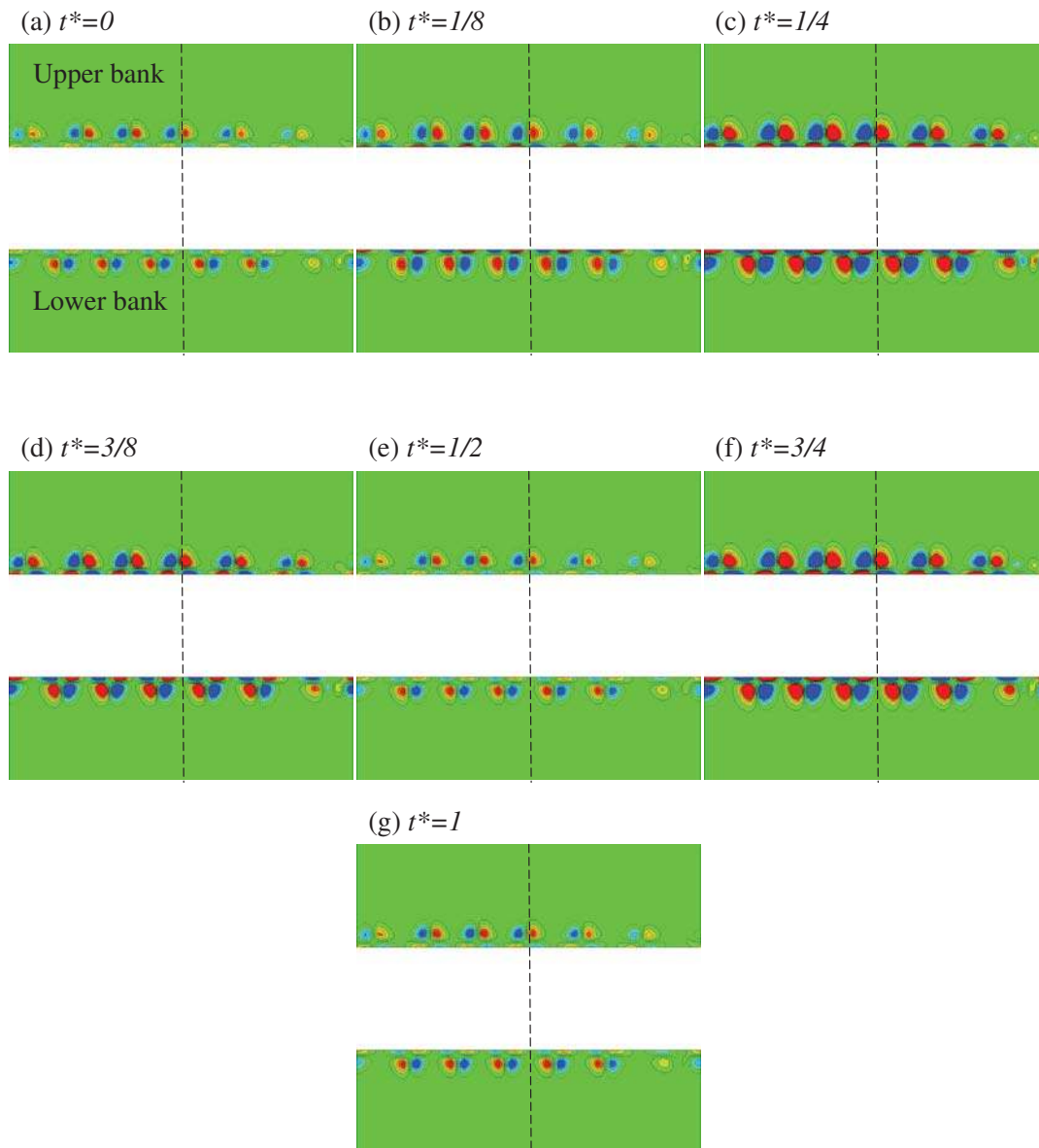
Figure 5.16 Vortex array in plane $x/D = 0$ in vorticity contours of ω_x for one oscillation period. For $(KC, \beta) = (2, 200)$ and K = cos20°. $t^* = t/T$-200 and $-1.5 < \omega_x < 1.5$. For the first ½ period the interval is $\Delta t^* = 1/8$ and for the second half period $\Delta t^* = 1/4$.

(a) *t*=0*　　　　　　　　(b) *t*=1/8*　　　　　　　(c) *t*=1/4*

Upper bank

Lower bank

(d) *t*=3/8*　　　　　　　(e) *t*=1/2*　　　　　　　(f) *t*=3/4*

(g) *t*=1*

Figure 5.17 Vortex array in plane $x/D = 0$ in vorticity contours of ω_x for one oscillation period. For $(KC, \beta) = (2, 400)$ and K = cos20°. $t^* = t/T$-200 and $-1.5 < \omega_x < 1.5$. For the first ½ period the interval is $\Delta t^* = 1/8$ and for the second half period $\Delta t^* = 1/4$.
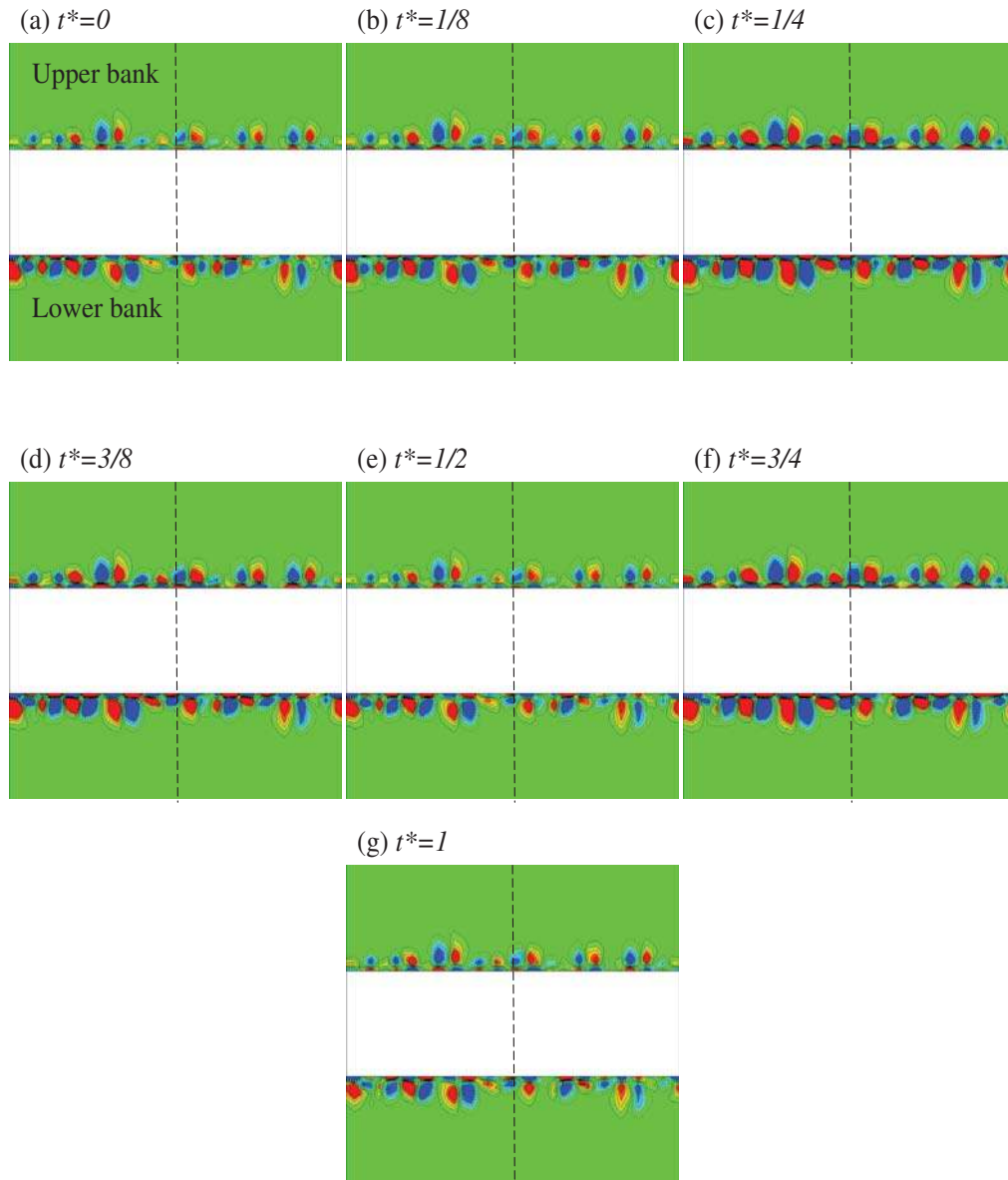
Figure 5.18 Vortex array in plane $x/D = 0$ in vorticity contours of ω_x for half oscillation period. For $(KC, \beta) = (2, 400)$ and K = cos30°. $t^* = t/T$-200 and -1.5 < ω_x < 1.5. For the first ½ period the interval is $\Delta t^* = 1/8$ and for the second half period $\Delta t^* = 1/4$.

5.5.4.2 Vortices at cross-sectional view

Evolution of the radial extent as well as the circumferential coverage of one two-layer vortical structure around the cylinder can be demonstrated in a cross-sectional plane view. Visualizations are given for the cross planes at $z/D = 2$ within one oscillation period. The locations of the visualization planes are indicated by the dashed lines shown in Figure 5.18. Again only the cases of K < 1 are discussed here, because the cases of K = 1 at $(KC, \beta) = (2, 200)$ and (2, 400) have been covered in Section 4.5.2.2.

142

For (KC, β) = (2, 200) at K = cos10° and cos20°, the plane of z/D = 2 runs through a vortex pair in only one array, due to the staggering distribution of the two arrays. Therefore, in Figure 5.19 and Figure 5.20, the two-layer vortical structure can only be observed in the top half plane, and is consisted of a top-layer vorticity that is much more extended in the radial direction and a bottom-layer vorticity that is much thinner. The evolutions of the one sample vortex for K = cos10° and cos20° are very similar. As is also observed for the circular cylinder case during one period of oscillation, for the elliptic cases shown in Figure 5.19 and Figure 5.20, the focus of the top-layer vorticity also moves along with the free stream across the cylinder crown. Although the strongest vorticity is found at the peaks of the ambient flow (t^* = 1/4 and 3/4), the centre of the vorticity reaches the top of the cylinder (i.e. at θ = 90°) at t^* = 3/8 and at this instant the vorticity distribution is symmetric with respect to the y-axis. As the cylinder circumference is further elongated to a smaller K, it is noticed that the vorticity tends to accumulate at the slope before the cylinder crown (e.g. Figure 5.19b and Figure 5.20b), and to stretch when it is across the crown (e.g. Figure 5.19d and Figure 5.20d). This feature becomes more obvious as the cross section of the cylinder turns flatter.

For the case of β = 400, since the results at K = cos10° and cos20° are very similar, therefore discussions for K = cos10° are omitted here. The cross-sectional views for the case of K = cos20° and K = cos30° are given in Figure 5.21 and Figure 5.22, respectively. As indicated by the dash lines in Figure 5.17, the measure plane of z/D = 2 cuts through the centres of a pair of two-layer vortical structures from two arrays located on both banks of the cylinder span. These vortices are middle-sized among all the vortices along the cylinder span. The two vortex pairs happen to be symmetric with respect to the horizontal centre line, and they are also roughly symmetric with respect to the x-axis as can be viewed in Figure 5.21 and Figure 5.22.

(a) *t*=0* (b) *t*=1/8* (c) *t*=1/4*

Flow reversal Flow direction Flow direction

(d) *t*=3/8* (e) *t*=1/2* (f) *t*=3/4*

Flow direction Flow reversal Flow reversal

(g) *t*=1*

Flow reversal
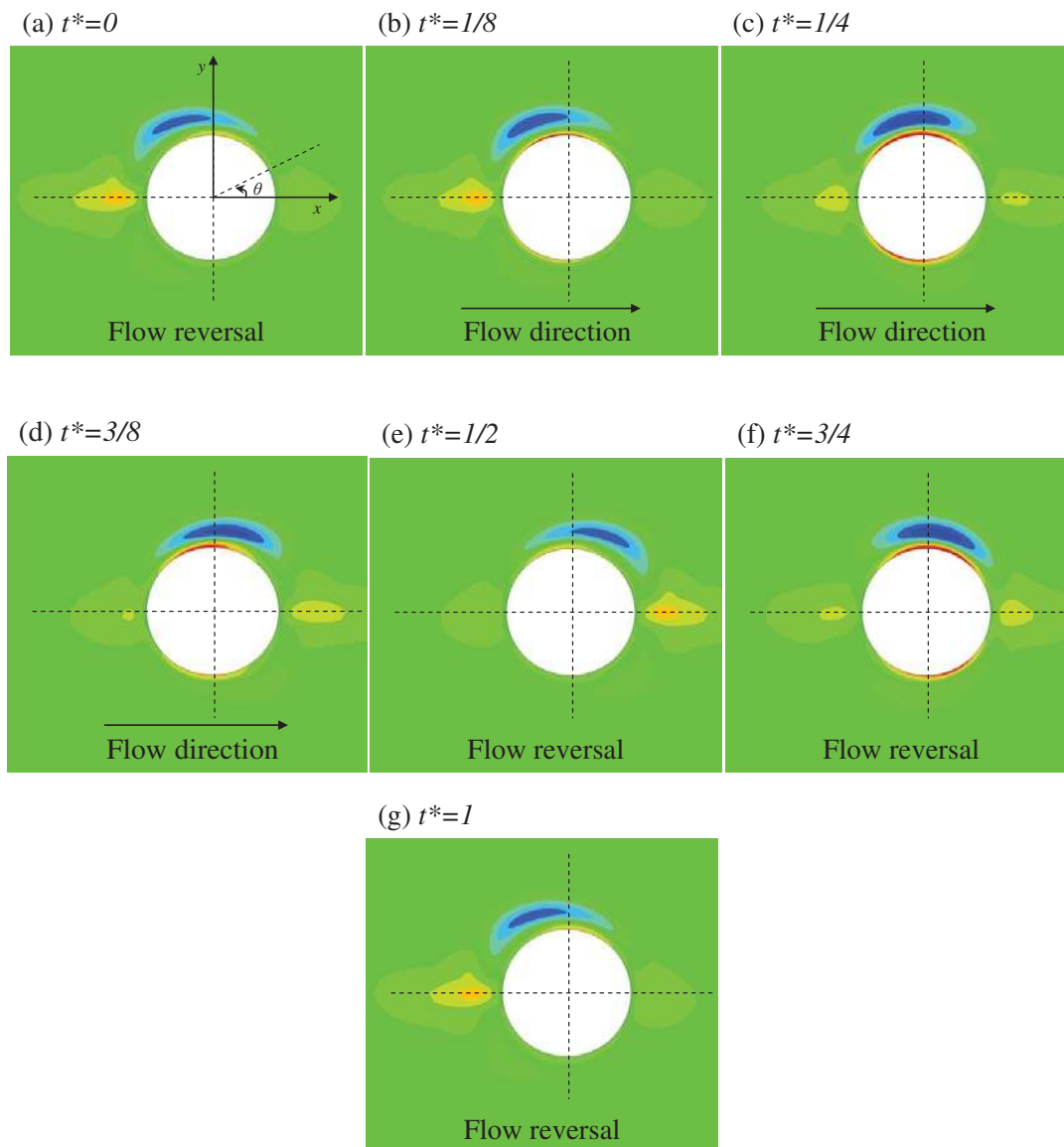
Figure 5.19 Vortex evolution in plane $z/D = 2$ by vorticity contours of ω_x for one oscillation period. For $(KC, \beta) = (2, 200)$ and $K = \cos 10°$. $t^* = t/T\text{-}200$. $-1.5 < \omega_x < 1.5$. For the first ½ period the interval is $\Delta t^* = 1/8$ and for the second half period $\Delta t^* = 1/4$.

(a) *t*=0*

(b) *t*=1/8*

(c) *t*=1/4*

Flow reversal

Flow direction

Flow direction

(d) *t*=3/8*

(e) *t*=1/2*

(f) *t*=3/4*

Flow direction

Flow reversal

Flow reversal

(g) *t*=1*

Flow reversal
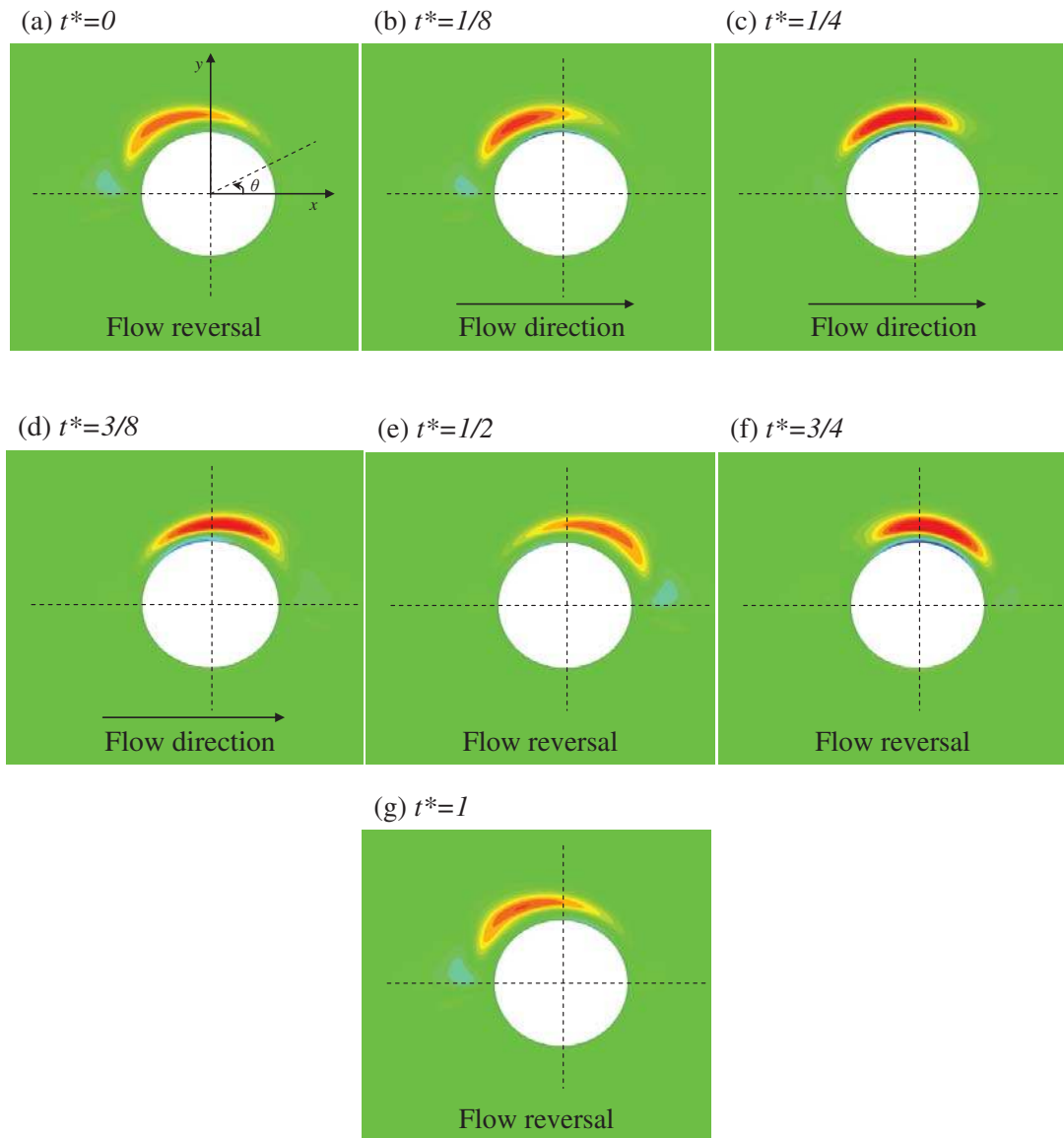
Figure 5.20 Vortex evolution in plane $z/D = 2$ by vorticity contours of ω_x for one oscillation period. For $(KC, \beta) = (2, 200)$ and K = cos20°. $t^* = t/T$-200. $-1.5 < \omega_x < 1.5$. For the first ½ period the interval is $\Delta t^* = 1/8$ and for the second half period $\Delta t^* = 1/4$.

(a) *t*=0*
(b) *t*=1/8*
(c) *t*=1/4*
(d) *t*=3/8*
(e) *t*=1/2*
(f) *t*=3/4*
(g) *t*=1*
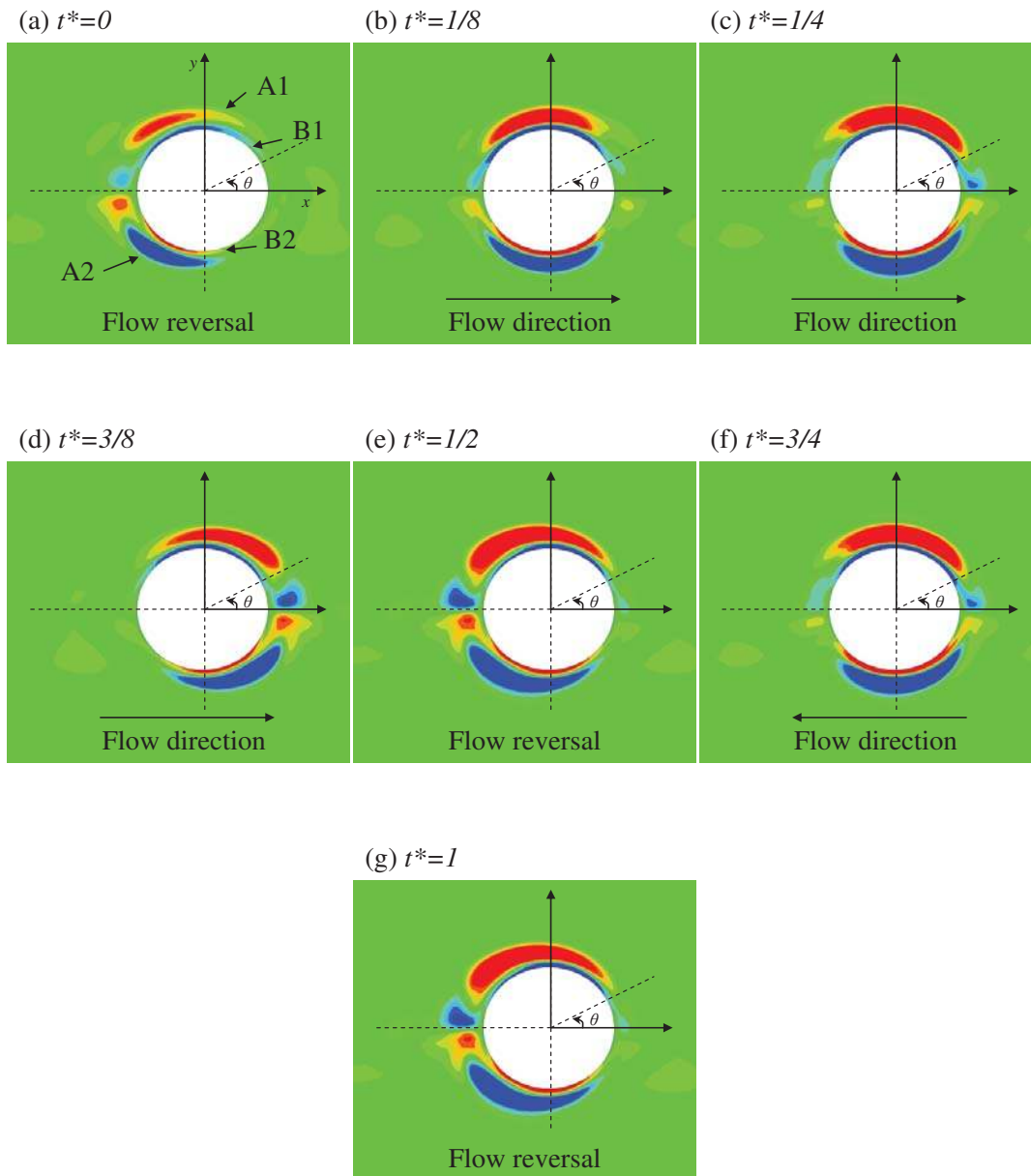
Figure 5.21 Vortex evolution in plane *z/D* = 2 by vorticity contours of ω_x for one oscillation period. For (*KC*, *β*) = (2, 400) and K = cos20°. *t** = *t/T*-200 and -1.5 < ω_x < 1.5. For the first ½ period the interval is Δ*t** = 1/8 and for the second half period Δt* = 1/4.

For the (*KC*, *β*) = (2, 400) cases, it should be noted that the vortex structures vary along the cylinder, hence the cross-sectional views given here are just for one sampling vortex cut through by the measure plane. However, it is still necessary for us to study the behaviours of the sampling vortex in order to get some general ideas on the circumferential evolution for different K values under (*KC*, *β*) = (2, 400).

Figure 5.21 shows the cross-sectional view for the case of $\beta = 400$ and K = cos20°. It is observed that the radial extent of the probed two-layer structure is smaller and the structure is flatter compared with the one studied for $\beta = 400$ and K = 1 shown in Figure 4.17. As can be seen in Figure 5.17, the probing plane cuts through the edge of the vortices at $t^* = 0$ and the centres of the vortices at $t^* = 1/4$ to 1. This indicates that the probed vortices undergo an axial shift of about half-an-vortex length during the oscillation period. As a result, the vorticity shown in Figure 5.21a appears weak at $t^* = 0$ because it is near the vortex edges. Then as the flow velocity increases, the top-layer vortices are swept along the cylinder circumference indicated by the movement of the dolphin-like structures, similar to that previously observed in other cases. As the two-layer vortical structure is washed by the ambient flow and transfers around the cylinder, the uneven circumferential distribution of the vorticity with a focus observed at certain moments indicates the accumulation of the vorticity at locations before the vertex of the cylinder. At moments when the majority of the vorticity reaches the vertex of the cylinder (i.e. at $\theta = 90°$), the vorticity is seen stretched so that it is more equally distributed and the focus of the vorticity disappears.

Recall that for the circular cylinder case, the bottom layers cover a larger circumference than the top layers throughout the period. For the elliptic cylinder with K = cos20°, it is seen from Figure 5.21 that throughout the period, the bottom layer and top layer have almost equal circumferential coverage. However in the radial direction, the bottom layer is again much thinner than the top layer, as a result of being closer to the cylinder surface and confined by the no-slip boundary condition.

(a) *t*=0*

(b) *t*=1/8*

(c) *t*=1/4*

(d) *t*=3/8*

(e) *t*=1/2*

(f) *t*=3/4*

(g) *t*=1*
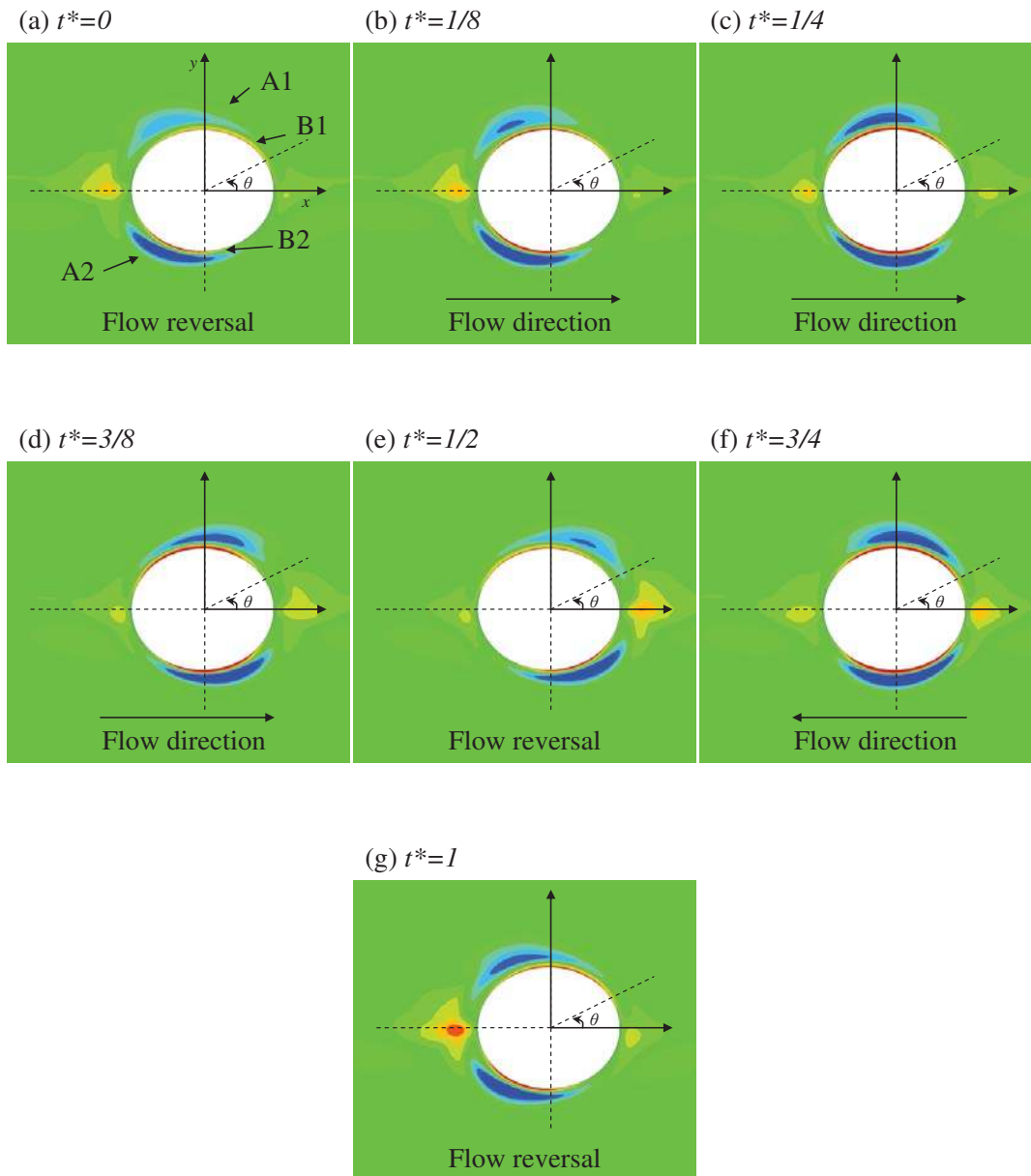
Figure 5.22 Vortex evolution in plane $z/D = 2$ by vorticity contours of ω_x for one oscillation period. For $(KC, \beta) = (2,$ 400) and K = cos30°. $t^* = t/T$-200 and -1.5 < ω_x < 1.5. For the first ½ period the interval is $\Delta t^* = 1/8$ and for the second half period $\Delta t^* = 1/4$.
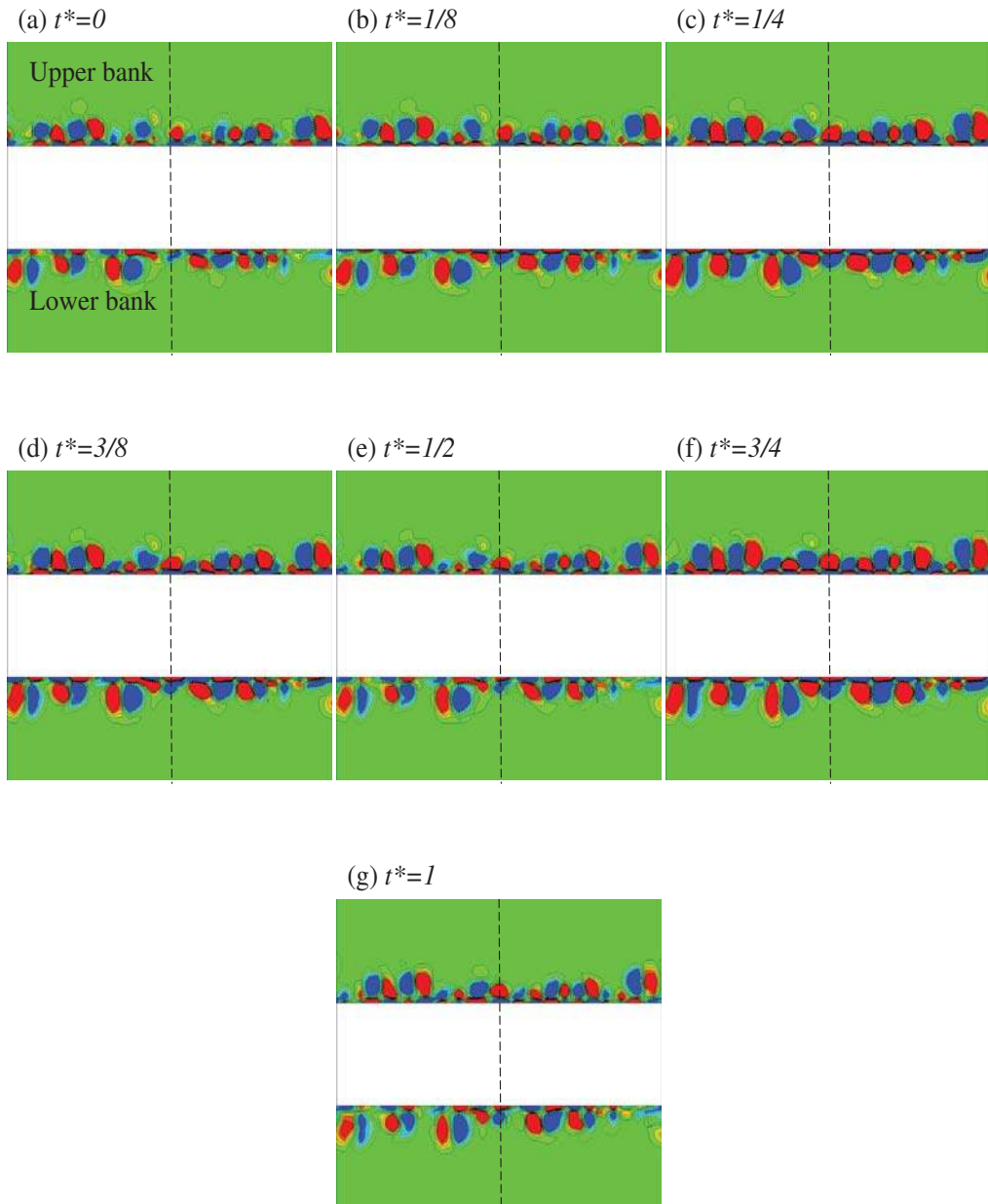
When K is reduced to cos30°, the flow is further stabilized. It can be seen from Figure 5.18 that the measure vortex pair is again middle-sized among all the vortices generated along the cylinder. From Figure 5.22 it is observed that, while the bottom-layer vortices cover a large portion of the circumference, the top-layer vortices reduces its coverage at certain moments. The radial extent of the top-layer vortices also reduced at this case, which is also an indication of reduction in the strength of instability. With a flatter cross section, the top-layer vorticity is distorted into the typical 'dolphin's shape' as described

in Section 4.5.2.2, i.e. the vorticity contour is no longer evenly distributed and non-symmetric with respect to the y axis. The large end of the vorticity is the dolphin's head, representing the accumulation of large amount of vorticity. At the elongated slope is found to be more apparent, see for example Figure 5.22a,b,e. The top layer has its largest circumferential extent at the moment $t^* = 3/8$, as it is stretched when it is swept across the cylinder crown. As a result, at this moment the radial extent of the top-layer vorticity is most uniform around the cylinder yet the smallest within one period.

The accumulation and stretching of the vorticity demonstrate that as the cylinder becomes flatter, the transfer of the vorticity over the top of the cylinder becomes less likely to accomplish. The overall instability of the flow field reduces with the decrease of K, as reflected by the fact that the vortical structures have better periodicity and are weaker in strength. In addition, the radial extent as well as the circumferential coverage of the top layer vortices is smaller compared with those with a larger K value.

5.6   Side instability ($K < 0.6^{1/2}$)

In this section we briefly examine the other instability indicated by the lower curve in Figure 5.3. According to Hall's prediction, when K is too small to induce the Honji instability, another type of 3-D instability may occur closer to the shoulders (or sides) of the cylinder under the effects of an elongated curvature. This indicates that at a small K for a certain value of the governing parameters (KC, β) where the Honji instability is suppressed, the Side instability may be observed. The dependence between KC, β and K for the onset of the Side instability is plotted in Figure 5.7. To evaluate the Side instability, in this study we examine two K values at (KC, β) = (2, 400): one is K = cos40° which is close to $0.6^{1/2}$ and the other is K = cos60°. The results obtained through the present numerical model are compared and evaluated against Hall's theoretical prediction.

5.6.1   **K = cos40°**

At the value of cos40° ($\approx$ 0.766), K is very close to but slightly smaller than the predicted critical value of $0.6^{1/2}$ ($\approx$ 0.774) for the bifurcation of the two instabilities. The

theoretically predicted governing parameters that lead to both the Honji instability and the Side instability at K = cos40° are plotted in Figure 5.23, from which it can be seen that the two curves are very close.
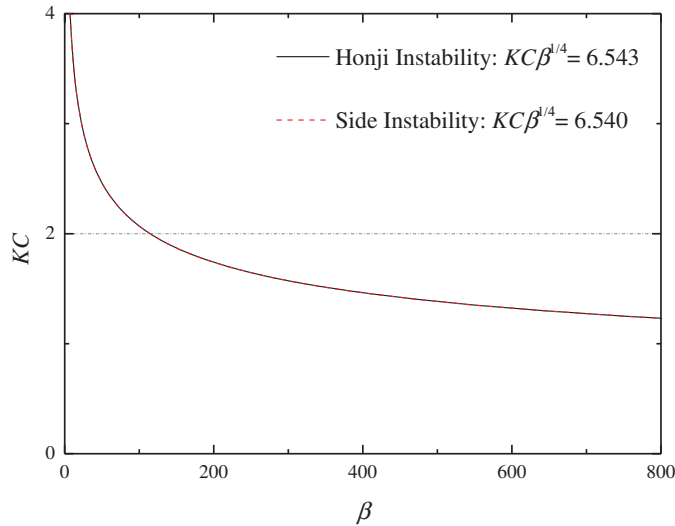
Figure 5.23 Dependence of KC on β for K = cos40° for the Honji instability and the Side instability. Calculated from Hall's theory with first order accuracy.

The spatial-temporal flow development and the instantaneous 3-D structures generated under the case of K = cos40° at (KC, β) = (2, 400) are visualised in Figure 5.24. It is found that for this case, the Honji instability still develops. As is expected, the flow evolution is delayed and the resultant vortices are less active compared with those at larger K values (e.g. K = cos30°). From Figure 5.24a, the onset of 3-D is first observed at around N = 85 with 10 evenly distributed vortex pairs, which become unstable and begin to interact at around N = 110. The 3-D flow field shown in Figure 5.24b shows two vortex arrays distributed along the cylinder representing the Honji vortices. The cross sections of the two arrays on two banks of the cylinder are viewed in Figure 5.24c, from which the typical symmetric two-layer four-vortex Honji pairs are clearly observed. Since K is so small that the 3-D flow around the cylinder is more stable, the vortices are distinct and regular. Compared with those at larger K values (e.g. cos30°), the vortices have become more uniform and similar in size and shape to each other as shown in Figure 5.24b,c. These vortical structures around the cylinder are stretched by the elongated curvature, and therefore have larger circumferential coverage, as can be

clearly viewed in Figure 5.24d. In addition, the accumulation of the vorticity at locations slightly lower than the cylinder vertex is obvious, demonstrated by the large dolphin's head in Figure 5.24d.

According to Hall's prediction, both the Honji instability and the Side instability can develop at $(KC, \beta) = (2, 400)$ with the shape ratio of K = cos40°. However, based on the observations given above, it is impossible to determine the existence of the Side instability. At this K value, since the Honji instability over the cylinder crown is still observed and the accumulated vorticity at the slope before the cylinder crown still connects with the Honji vorticity around the cylinder crown, a complete dolphin's shape is observed in Figure 5.24b,c,d. It is therefore hard to distinguish the vortical structures formed under the Side instability because even if they are generated, they merge with the Honji vortices, which have a large circumferential coverage as seen in Figure 5.24d. This is probably because the critical governing parameters at this K for the two instabilities are very close. However with the cylinder being further flatter, the accumulation of vorticity close to the sides of the cylinder does demonstrate a trend of disconnecting with the Honji instability, which forms at the cylinder crown.
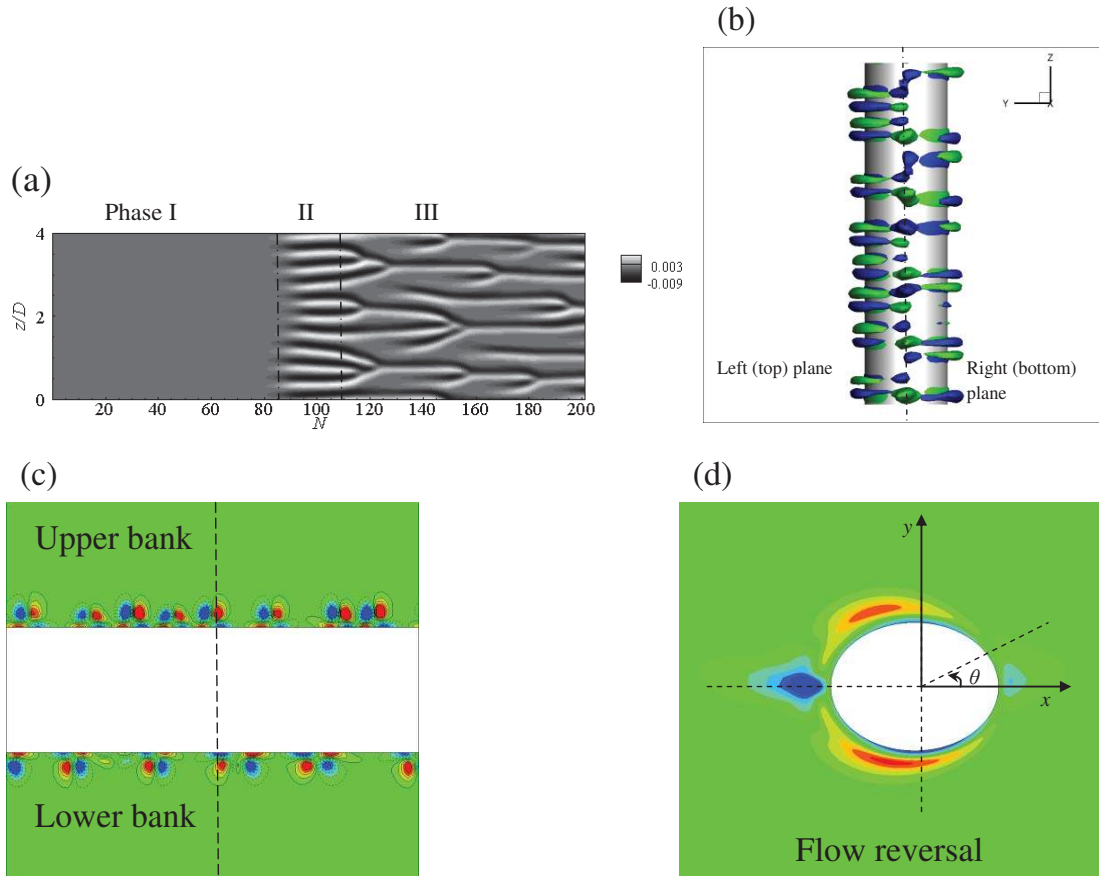
Figure 5.24 Demonstration of the vortical structures formed for K = cos40° at (KC, β) = (2, 400). (a) Spatial-temporal flow evolution over 200 flow periods calculated. (b) Instantaneous 3-D vortical structures visualised by the unit iso-surface of ω_x. (c) Vortices in the plane of x/D = 0 and (d) vorices viewed in the plane of z/D = 2.

5.6.2　K = cos60°

As K reduces from the value at the bifurcation of the two curves in Figure 5.3, the difference between the critical governing parameters for the Honji instability and the Side instability increases. The dependence curves for the two types of instability at K = cos60° by Hall's prediction are compared in Figure 5.25.

Previous results have demonstrated a delayed flow development with the decreasing of K. In order to accelerate the calculations with a small K of cos60°, the calculations are performed with a perturbation method described in Chapter 3. It is found that our calculated results seem to present a flow field that is more stable compared with Hall's prediction. According to Hall's theory as given in Figure 5.25 for this K value, both the Honji instability and the Side instability would occur at (KC, β) = (2, 400). However,

the present results obtained from the numeral simulations show that only a weak Side instability occurs while the Honji instability cannot be observed for the case of (KC, β) = (2, 400) with K = cos60°.
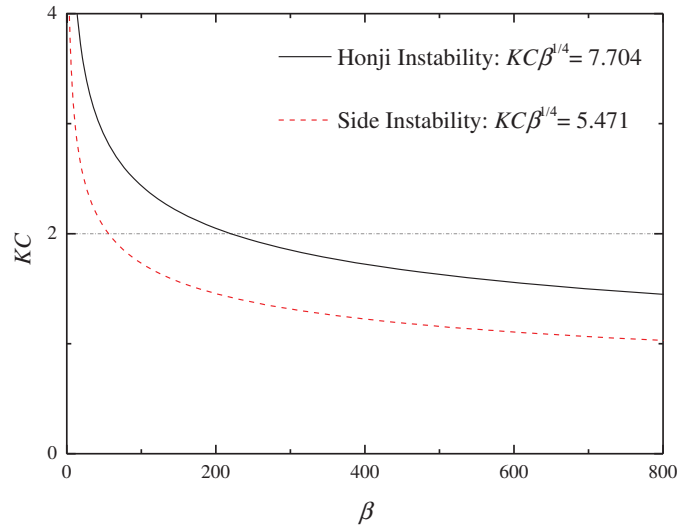
Figure 5.25 Dependence of KC on β for K = cos60° at (KC, β) = (2, 400) for the Honji instability and the Side instability. Calculated from Hall's theory with first order accuracy.

To confirm that the Side instability is an intrinsic flow behaviour, and also to confirm that the Honji instability indeed ceases to form for this case, calculations are performed again with a 3-D initial flow field where Honji vortices exist. The perturbation is also removed in this calculation to allow the flow to develop freely. The time evolution figures and the instantaneous flow structures at the beginning and the end of this calculation are shown in Figure 5.26 and Figure 5.27. The instantaneous flow structures given in Figure 5.27a are obtained under (KC, β) = (2, 1500) with K = cos60°, where the two-layer Honji vortices at $\theta = 90°$ and the side vorticity near the cylinder shoulders coexist yet are separated from each other. This flow field is used as the initial condition for the flow development calculation conducted at (KC, β) = (2, 400), the spatial-temporal evolution process is given in Figure 5.26. It is clearly seen that, as the calculation progresses, the Honji instability (stripes in Figure 5.26a) fades away quickly while the Side instability (stripes in Figure 5.26b) persists although with a slightly decreased intensity at early steps after the calculations are commenced. The resultant 3-D flow field after 20 oscillation periods is visualised in Figure 5.27b where only the

side vortices can be observed. It is thus confirmed that suppression of the Honji instability and development of the Side instability are intrinsic flow features at (KC, β) = (2, 400) for K = cos60°.

The appearance of the Side instability has several differences compared with the Honji instability. Unlike the Honji instability, where the two-layer vortex pairs form, the 3-D structures induced by the Side instability are simply one-layer single rotating vortices in the form of flat patches attached to the cylinder surface. Also, for the cases of larger K values at β = 400 where Honji instability occurs, there are five Honji vortex pairs formed along the cylinder. However at K= cos60° there are only four side vortex patches distributed along the cylinder span as demonstrated in Figure 5.27b. As a result, the distance between the cores of the vortex patches is larger compared with that of the Honji pairs.
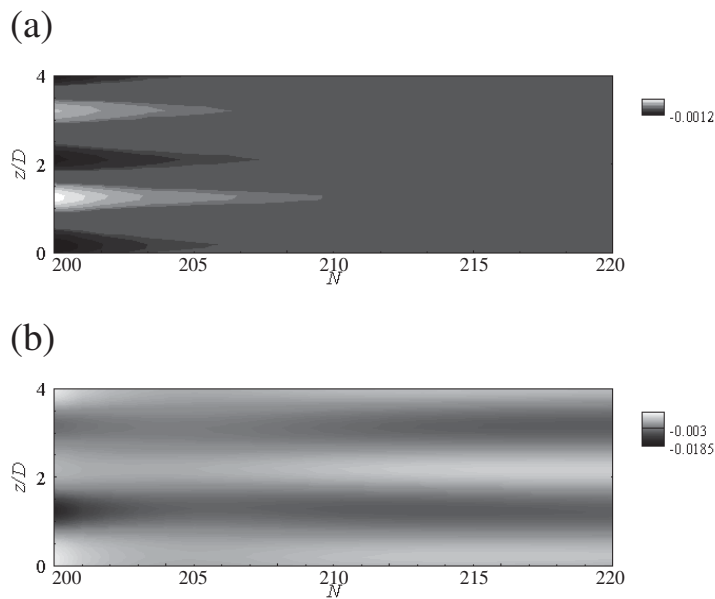
Figure 5.26 Spatial-temporal evolution of contours of the relative axial velocity component u_z/U_{mx} for K = cos60° at (KC, β) = (2, 400) with a 3-D initial condition. (a) For the Honji instability, probed at θ = 90° along the cylinder and (b) for the Side instability, probed at θ = 165° along the cylinder.

(a)   (b)
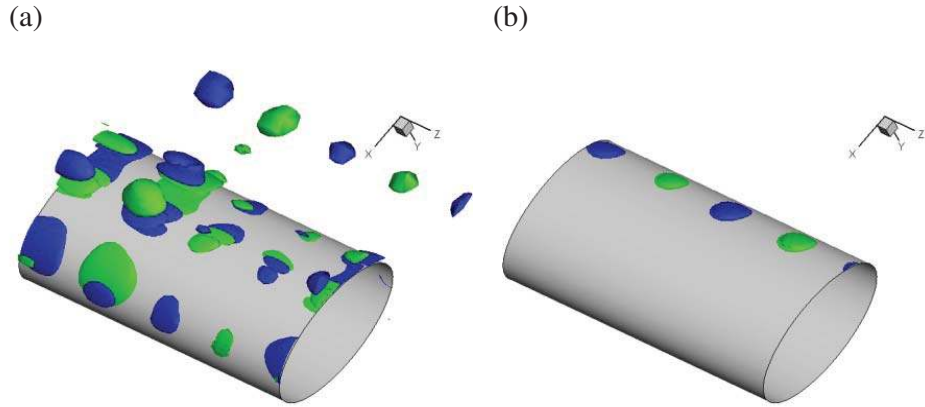
Figure 5.27 Instantaneous structures of unit iso-surfaces of ω_x near the cylinder for K = cos60° at (KC, β) = (2, 400). (a) Results for β = 1500 at N = 200. (b) Resultant flow field for β = 400 after 20 flow periods using (a) as the initial condition.

In addition to the 3-D view of the instantaneous flow structure given in Figure 5.27b, for a full description of the vortical structures, the cross-sectional planes of two vortex patches representing the Side instability around the cylinder circumference with an interval of $\Delta\theta$ = 5° are visualised in Figure 5.28. It is noted that one of the most unstable locations at K = cos60° calculated from Equation 5.1 by Hall's theory is about 152°. This is within the range of about θ = 150° to 170° for the Side instability in the form of axially varying vortex patches to be observed in Figure 5.28. Along the circumference, the vortex patches are flat with small radial extent, and only grow slightly in the axial span. The largest and strongest patch is observed at θ = 165°, where the axial extent is about 0.44D and the distance between two vortex patches is roughly 0.54D. The radial extent at this θ is about 8% of the axial extent.

The one-period evolution process of the vortex patches is demonstrated in a time sequence in Figure 5.29. The oscillation starts in the positive direction of the x-axis. Four evenly distributed vortex patches form at the first peak as seen in Figure 5.29b. These vortex patches are observed close to the shoulders at the current front side (i.e. the side confronting the incoming flow) of the cylinder. These four patches are not identical; rather, two of them are relatively weaker and cannot be observed at certain moments. The patches slightly extend along the cylinder circumference washed by the ambient flow over the half oscillation period before the flow reverses, so that they

slightly stretch while moving towards the top of the cylinder as seen in Figure 5.29c. However the elongated curvature causes the vortex patches to fail to reach to the cylinder crown ($\theta = 90°$) before the opposite oscillation starts. The vortex patches are then washed back to the shoulders by the opposite flow as the latter increases. At the same time, the intensity of the vortex patches are also weakened, causing the two weaker vortex patches to vanish. The flow field at the end of the oscillation looks identical to that at the beginning and the evolution process then repeats in the next period. During the whole process, it is observed that the vortex patches only form at the side which serves as the front side when the first oscillation starts.

(a) $\theta = 175°$

(b) $\theta = 170°$

(c) $\theta = 165°$

(d) $\theta = 160°$

(e) $\theta = 155°$

(f) $\theta = 150°$

(h) $\theta = 145°$
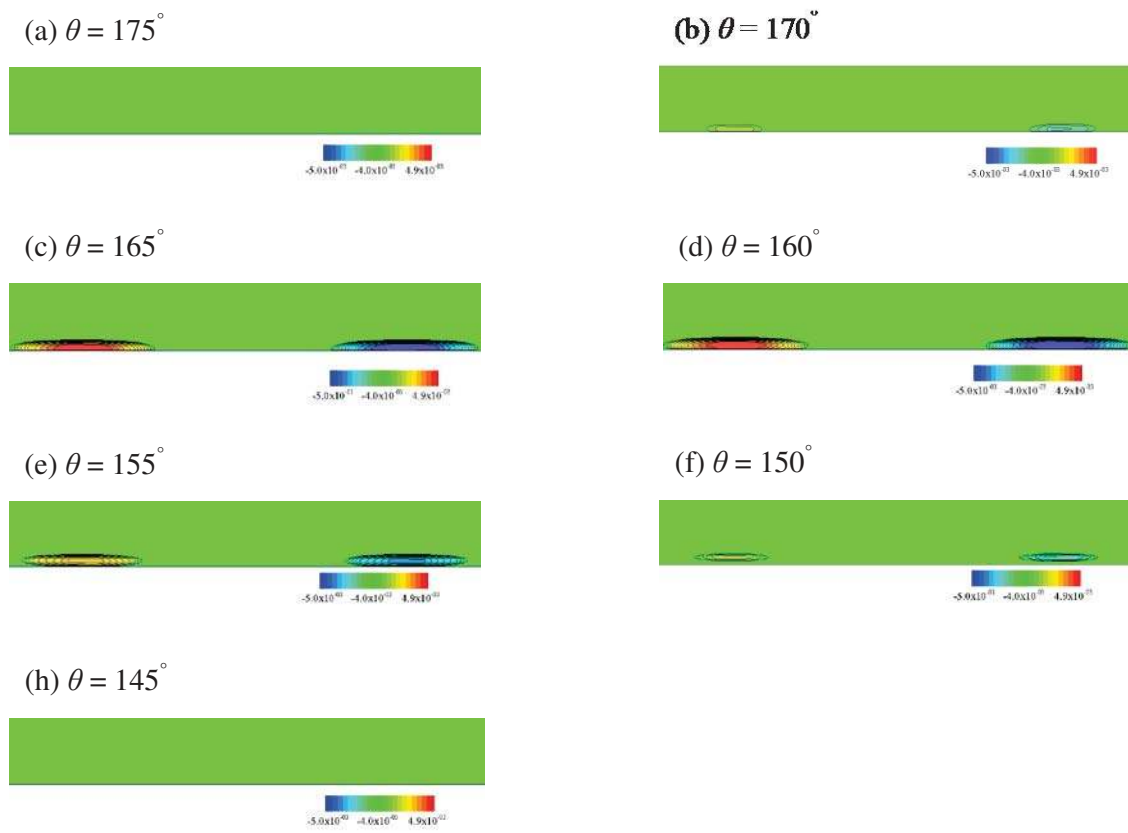
Figure 5.28 Plane views of the instantaneous structures near the cylinder for K = cos60° at (KC, β) = (2, 400) given by contours of ω_x in the planes in the range of $\theta = 145°$ to 175° with an interval of $\Delta\theta = 5°$. The contours shown are in the range of 80% of the maximum ω_x plotted at $N = 200$.
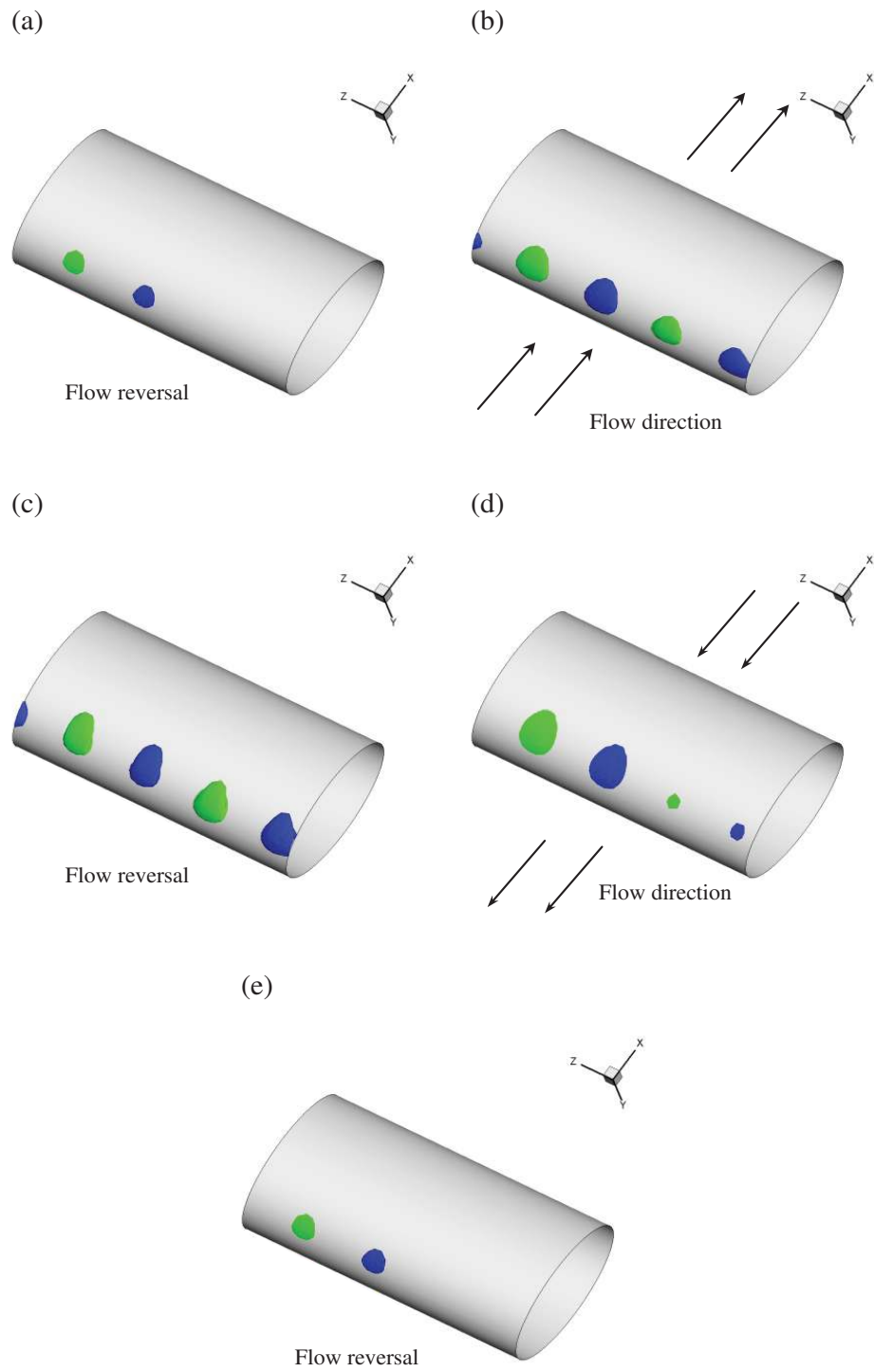
Figure 5.29 Evolution of unit iso-surfaces of ω_x near the cylinder for K = cos60° at (KC, β) = (2, 400). Iso-surface at 80% of the maximum ω_x, which varies in the range of ±0.007 during one period. Plotted for $t^* = t/T - 200$ = (a) 0, (b) 1/4, (c) 1/2, (d) 3/4 and (e) 1.

5.7 Comparison with theoretical prediction

5.7.1 **Contradictions**

So far the numerical results for the cases evaluated have demonstrated Hall's finding that the flattening of the cylinder's cross section can exert a stabilising effect on the transition from 2-D to 3-D flow. However, contradictions are found when comparing between the current calculations and that predicted by Hall's theory with first order accuracy for both the Honji instability and the Side instability discussed in the previous contents.

As mentioned before, the critical shape factor K for suppression of the Honji instability at $(KC, \beta) = (2, 200)$ and $(2, 400)$ are 0.54 and 0.3, respectively, predicted using Hall's theory with first order accuracy. In other words, this means in Hall's theory the Honji instability can be observed at the two (KC, β) groups for a cylinder with any K larger than the values given. However, the calculated flow field seems to be more stable than predicted at different K values. The present calculations have shown that a K value of $\cos30°$ (about 0.87) is sufficient to keep the flow in the 2-D regime for $(KC, \beta) = (2, 200)$ and that the transition from 2-D flow to 3-D flow only occurs at the cylinder shoulders in the form of a so-called Side instability at $K = \cos60°$ (0.5) for $(KC, \beta) = (2, 400)$. This means that the critical K values leading to the suppression of the fluid instability found from the present calculations are larger than that predicted by Hall's first-order linear stability theory.

Further confirmation of this contradiction is also provided by comparing the resultant flow properties at smaller K. For $K = \cos60°$ studied in Section 5.6.2, the theory predicts that the Side instability should be observed at $(KC, \beta) = (2, 200)$, see Figure 5.25. And when the governing parameters are increased to $(KC, \beta) = (2, 400)$, both Honji and side instabilities are expected to occur. However, our numerical simulations showed that the flow is intrinsically 2-D stable for the case of $(KC, \beta) = (2, 200)$ with K $= \cos60°$, i.e. no 3-D instability of any type near the cylinder arises. For the case of $(KC, \beta) = (2, 400)$ with $K = \cos60°$, it is found that only a weak Side instability would occur while the Honji instability cannot be observed. Compared with the present study, it is

seen that Hall's linear stability analysis with first order accuracy seems to 'over-estimate' the instability at relatively lower (KC, β) values evaluated in the present study, from which the flow appears to be more stable than that predicted. Possible reasons for this observed contradiction is given below.

5.7.2 Possible explanations

Before going into the possible explanations, it is worth mentioning the good prediction provided by the current numerical scheme with respect to the circular cylinder case. A 3-D direct numerical simulation of An et al. [21] used the same calculation model to study oscillatory flow around a circular cylinder. It was found that the numerical model was able to identify the three distinctive flow regimes as β varied in the range of 100 to 600 at a constant KC of 2 (same with the present study). Other than demonstrating the detailed flow structures of Honji instability during the transition from 2-D to 3-D, the study also showed good accordance of the predicted flow regime at the corresponding governing parameters with those available in theliterature. This proved that the current numerical scheme is capable of providing direct numerical simulations for the Honji instability observed in an oscillatory flow near a circular cylinder. However, as mentioned in the previous section, there exists some contradicts in the comparison of the current results with the theoretical results of Hall, for which possible explanations are discussed in the following.

The first possible explanation of the over-estimation of the hydrodynamic instability by Hall with respect to the current numerical results is attributed to the assumption based on which Hall's theory was developed, namely the prerequisite that the KC number is very small while β is very large. Even so, at small (KC, β) values such as that concerned in the present study, Hall shows in his paper that the predicted dependence curve of KC and β for the onset of the Honji instability compares relatively well with the experimental results obtained by Honji for the circular cylinder case. However, the theory may not work well with the elliptic cylinder case when another parameter (the shape factor K) is involved, especially when this parameter also serves as another factor which has a stabilising effect on the flow field. It is possible that with the shape factor as an additional parameter, the theory may apply reasonably well for the situation under

a sufficiently large β, but the cases evaluated here with $\beta = 200$ and 400 may not fulfil this requirement. One evidence for this argument is that by slightly increasing β from 200 to 400, the Honji instability can be observed at cos40°. Still, further proof may be provided through experiments which are not found in the literature so far.

Another possible reason for the contradiction in the threshold K values is possibly caused by the neglect of higher-order terms in Hall's equation (in this study only the first-order dependence is given). To show this is the case, the dependence curves plotted with both first order and second order accuracy are compared in Figure 5.30. As can be seen in Figure 5.30a, the two curves calculated are very close, but large differences appear when β is small. For a better comparison, the relative difference of the critical KC is plotted against β in Figure 5.30b. It can be observed that the 2nd order effects drop off significantly as β increases from 0. At $\beta = 200$, the critical KC calculated with 2nd order accuracy (KC_{c2}) is larger than that with 1st order accuracy (KC_{c1}) by approximately 5.6%. A flatter curve shows that results obtained from both cases are more consistent at larger β values (recall one of the prerequisites of Hall's theory is large β). The difference reduces to roughly 4.7% when β is increased to $\beta = 400$, from which point further increase of β only results in a slight difference less than 5%. Particularly, a constant value of approximately 3% for β values larger than 1400 can be observed. This means the higher order terms play a less important role at large β values.
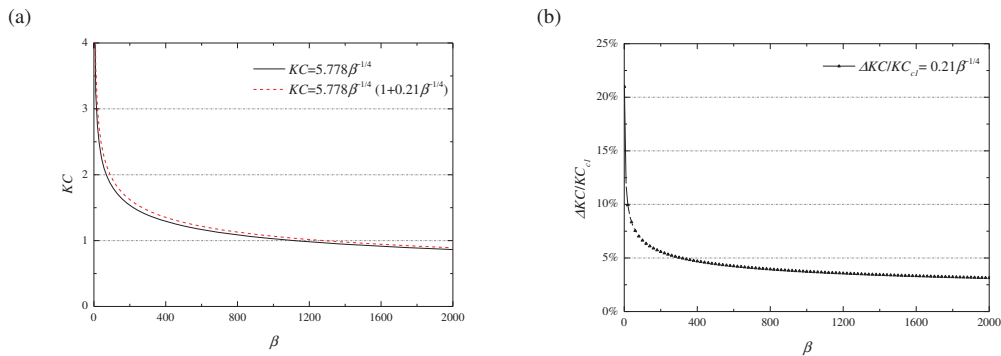
Figure 5.30 Dependence of KC on β for K = 1 for the Honji instability in the range of $0 < \beta \le 2000$. (a) Comparison between the two cases calculated with first order accuracy and second order accuracy. (b) Relative difference of the critical KC with β, in which $\Delta KC=KC_{c2}-KC_{c1}$, in which KC_{c1} is the critical KC obtained with first order accuracy and KC_{c2} is the critical KC obtained with second order accuracy.

It has been demonstrated that, although with the inclusion of the 2nd order term, the critical *KC* value is only increased by about 5.6% for $\beta = 200$ and less than 5% for $\beta = 400$. The predicted KC_{c2} is still smaller than our numerical results, i.e. our calculated flow field is more stable. This bifurcation is attributed to the high-order nonlinear effects. As mentioned by Hall, the high-order nonlinear effects excluded from Equation 1.4 have stabilising effects on the flow field. It should be pointed out that Hall also gave a brief evaluation of his theoretical results, claiming that "it is possible that higher-order nonlinear effects eventually cause these perturbations (to the basic state, added by the author) to equilibrate" and that "our nonlinear calculations do in fact suggest an increasingly likely breakdown in the basic flow structure when the Taylor number is increased".

5.8   Mechanism of the K effects

5.8.1   Geometric variation with K

The results presented so far show the stabilising effects of reducing K, in consistence with the findings of Hall's linear stability analysis. Geometric variations of the cylinder as K reduces include the flatness in the flow direction and sharpness of the cylinder shoulders facing the flow. The resultant flow field near the cylinder is closely related to these geometric variations at different K values.

5.8.2   Mechanism of K effects considering $\frac{\partial p}{\partial x}$

It is known that the Honji instability over the crown of the cylinder ($\theta = 90°$) is related to the separation of the shear layer at the rear of the cylinder when the required governing parameters are matched. The separation is induced by the large value of $\frac{\partial p}{\partial x}$ at the rear when the body is blunt. By gently streamlining the blunt body, separation of the fluid particles can be prevented because the value of $\frac{\partial p}{\partial x}$ reduces.

Following a similar reasoning, the mechanism resulting in the Side instability can be described. As shown earlier, the Side instability happens when K for certain values of

the governing parameters is small enough to suppress the Honji instability, while not too small to induce any three-dimensionality. As the cylinder takes a more streamlined shape, the pressure gradient $\frac{\partial p}{\partial x}$ near the top of the cylinder ($\theta = 90°$) decreases to a critical value that no flow separation occurs. However as the K value reduces, $\frac{\partial p}{\partial x}$ increases at the two shoulders of the cylinder ($\theta = 0°$ and $180°$) where the curvature sharpens. Under the combined effects of these two aspects, finally at a certain K, the Honji instability at $\theta = 90°$ would be suppressed, while the Side instability is triggered near two shoulders of the cylinder. This also explains why the locations of the Side instability are dependent on the particular curvature under a specified shape factor.
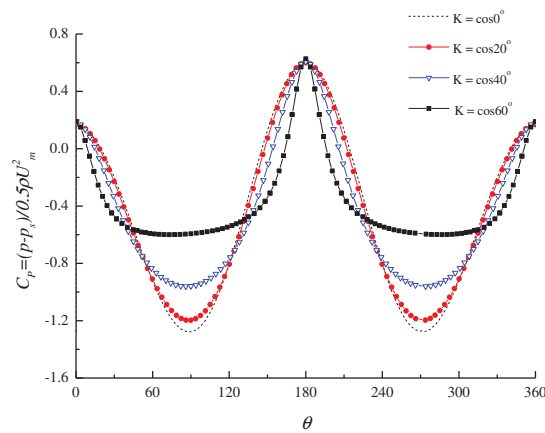
Figure 5.31 Distribution of the pressure coefficient around the circumference for different K values at the first velocity peak $N = 1$ (or $t/T = 0.25$). Measure circuit is composed of the nodal points next to the cylinder edge in the plane of $z/D = 2$.

To assist our discussions here, distribution of the pressure coefficient C_p around the cylinder circumference is plotted in Figure 5.31 for varying K values at the first peak value of the free stream. At this time the flow remains 2-D, therefore Figure 5.31 is identical along the cylinder axis and is applicable for both $\beta = 200$ and 400. The effects of the various K values on the resultant pressure distribution around the cylinder are clearly observed in Figure 5.31. It is shown that the absolute values of C_p at the cylinder shoulders ($0°$, $180°$ and $360°$) are the same for all K values. However, at these locations the variation of C_p is more abrupt for a smaller K value, which means the pressure gradient increases by reducing K. On the contrary, the pressure gradient at the top and bottom of the cylinder ($90°$, $270°$) reduces largely when K is decreased, as indicated by

the flatter curve near these locations shown in Figure 5.31. This explains the increase of $\frac{\partial p}{\partial x}$ at the cylinder shoulders and the decrease of $\frac{\partial p}{\partial x}$ at the vertex of the cylinder, which causes the onset of Side instability and the suppression of the Honji instability, respectively.

An important observation from Figure 5.31 associated with the development of the Side instability is that an abrupt variation appears between every 1/4 circumference (symmetrically, between 0° ~ 90°, 90° ~ 180°, 180° ~ 270° and 270° ~ 360°) as K decreases. Under the effects of the decreasing K, C_p has a trend to remain more constant-like over a larger portion of the cylinder. Take the case of K = cos60° for example, this portion ranges roughly from 30° to 150°. In the range between 0° and 30° and between 150° and 180°, C_p experiences an abrupt change. These two sudden changes happen near the two shoulders of the cylinder, and are resulted from the sharpening of the two shoulders of the cylinder with the flattening of the cross section. The large value of $\frac{\partial p}{\partial x}$ resulted from the abrupt change of C_p at these locations leads to the generation of the local Side instability. It can be observed from Figure 5.31 that, for a different K, the abrupt change of C_p is found at a different θ; therefore the locations of the Side instability vary with the value of K.

5.8.3 Mechanism of K effects considering energy transfers

Another possible explanation of the K effects on the fluid instability can be given by considering the physics of the fluid particle movement. As the cross section of the cylinder gets flatter and the major axis becomes longer while the minor axis remains unchanged, the excursion involved for the fluid particles to move across the top of the cylinder from the front to the rear ends increases, thus more momentum and energy are needed to accomplish such a movement. Insufficient input of momentum and energy would result in the fluid particles to be constrained at one side of the cylinder before the next flow reversal and hence separation is prevented. In addition, a small KC value means the flow period is short, and the duration of flow in one direction is not long enough for the fluid particles to travel to the cylinder crown. Furthermore, a small β value indicates the flow has relatively large viscosity, for which more energy is required in order for the fluid particles to move along the circumference of the cylinder. Under

the combined effects of all these three influencing factors, when a certain condition is met, the fluid particles fail to move far enough to reach the crown of the cylinder to induce the Honji instability, before the next half period starts where the flow runs oppositely and the particles are washed back again. This may then result in the Side instability, which is confined at locations close to the cylinder shoulders.

5.9   Two-dimensional Columnar Flows

It has been noticed that, when K is small enough, the instability never occurs and the flow remains two-dimensional. Now we will discuss the characteristics for the 2-D columnar flow field resulted when the cylinder's cross section is flat enough. The specific value of K to suppress the onset of three-dimensionality depends on the value of (KC, β). For a larger β value at a constant KC, smaller K is required, because the cross section needs to be flatter for inhibiting the stronger 3-D flow at larger β. In our calculated cases, it is found that the flow remains two-dimensional at K = cos30° for $(KC, \beta) = (2, 200)$. For this case, the instantaneous flow structures as well as the one-period evolution of the 2-D flow field near the cylinder will be discussed in the following sections.

5.9.1   **Instantaneous flow structures**

The resultant 2-D flow near the cylinder surface is simply a 2-D columnar flow generated due to the no-slip boundary condition applied at the cylinder surface. In the whole flow field the axial flow never develops, hence the vorticity components ω_x and ω_y remain zero. As a result, in the following contents, rather than ω_x which is used to illustrate the 3-D vortical structures, ω_z is adopted to demonstrate the 2-D columnar flow structures near the cylinder.
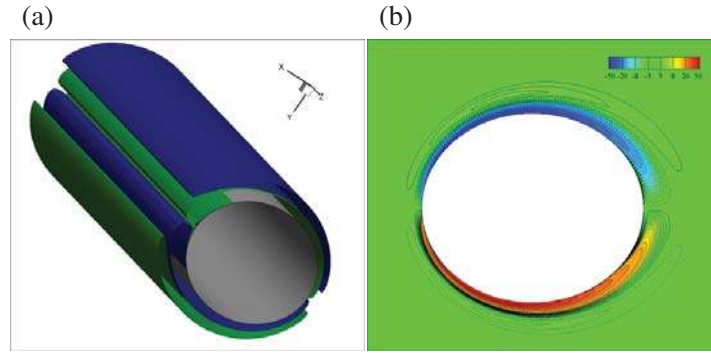
Figure 5.32 The two-dimensional columnar flow wrapping around the cylinder for the case of $(KC, \beta) = (2, 200)$ at K = cos30°, illustrated by the instantaneous structures of vorticity ω_z near the cylinder using (a) unit-amplitude iso-surfaces and (b) contours in $z/D = 2$ plane. Plot at $N = 200$.

The instantaneous 2-D columnar flow structure is demonstrated in Figure 5.32. As is shown, for the 2-D case, the cylinder surface is wrapped by two layers of counter-rotating columnar vortices attached to the cylinder surface forming the sheet-like 2-D boundary layer. This two-layer structure is very flat and the top layer is much more closely attached to the bottom layer compared with the 3-D cases. From the cross section shown in Figure 5.32b it can be seen that the two layers are symmetric with respect to the main axis of the cylinder's cross section. The sheet-like vortices bear a good resemblance to the "attached vortices" reported by Williamson [56] in his experimental study for flow near an oscillating circular cylinder at low KC numbers. The vortex layer denotes the rotation of the fluid particles due to the no-slip constraint applied at the curvature.

5.9.2 Evolution within one period

Evolution of the 2-D columnar vorticity is illustrated in Figure 5.33 by the contours of ω_z at seven moments within one flow period. In the first half period, five moments are chosen ($t^* = 0$ to $t^* = 1/2$). For the second half period (from $t^* = 1/2$ to $t^* = 1$) only one intermediate instant (i.e. $t^* = 3/4$) is included. The evolution of the columnar vortex structures is seen clearly from the first half period, for which more instants are presented. By looking at one complete period we can see the good periodicity of the structure, namely, the repetition of the resultant flow structures at moments with a gap of $T/2$ (e.g. see $t^* = 1/4$ and $t^* = 3/4$).

It is observed from Figure 5.33 that, for all moments during the flow period, the 2-D columnar vortex structures developed around the cylinder circumference are divided into symmetric halves with respect to the horizontal centre line. Therefore, only the vortex pair generated in the top half plane is studied here. The two layers in the top pair are denoted as A1 and B1 at the beginning of the oscillation (Figure 5.33a). At this moment, the structures shown are resulted from the oscillation just completes, and a large top layer vortex A1 with its focus at about $\theta = 180°$ and a thin bottom layer B1 can be clearly seen. A1 has a larger radial extent than B1 at moments close to flow reversal (t^*=0, 1/8, 1/2 and 1) due to the fact that the top layer gets to develop more freely as it is further away from the cylinder boundary.

The onset of the following oscillation sees the transfer of the major vortex across the cylinder circumference following the ambient flow. During this process, B1 starts to increase in thickness and pushes A1 further away from the cylinder, which then becomes thinner. When the flow oscillation reaches its peak at t^*=1/4, B1 grows thicker than A1. In addition, B1 is no longer evenly distributed across the half circumference, rather it has developed a focus at $\theta = 0°$. After t^*=1/4, the flow begins to decrease but the flow direction persists, therefore the vortex continues to move across the cylinder curvature following the direction of the flow. At t^*=3/8, it is seen that A1 is swept past $\theta = 90°$ and seems about to be shed. At the same time, a new bottom layer (C1) underneath B1 emerges. Now B1 becomes the new top layer and C1 the new bottom layer. The previous top layer vortex A1, weak and small, remains loosely attached to the new two-layer structure. With the majority located at the cylinder side, B1 has the tendency to detach from the cylinder surface. However, this will not happen as the oscillatory flow soon reverses. The strength of the vortices reduces with the continuous weakening of the ambient flow until the next flow reversal (t^*=1/2). The process then repeats itself in the opposite direction in the following half period, where the attached weak A1 shall be dissipated but never shed because of the flow reversal.

Evaluation of the evolution process reveals that although the flow structures at the beginning of the one period look the same as that at the end of the period, the vortices are different and are actually newly generated during the oscillation. During the period, the vortices are attached to the cylinder surface while the generation of new vortices and

dissipation of the old vortices occur. The evolution process of the vortices is in consistence with that reported by Williamson for the attached vortices regime.

(a) $t*=0$ (b) $t*=1/8$ (c) $t*=1/4$

(d) $t*=3/8$ (e) $t*=1/2$ (f) $t*=3/4$

(g) $t*=1$
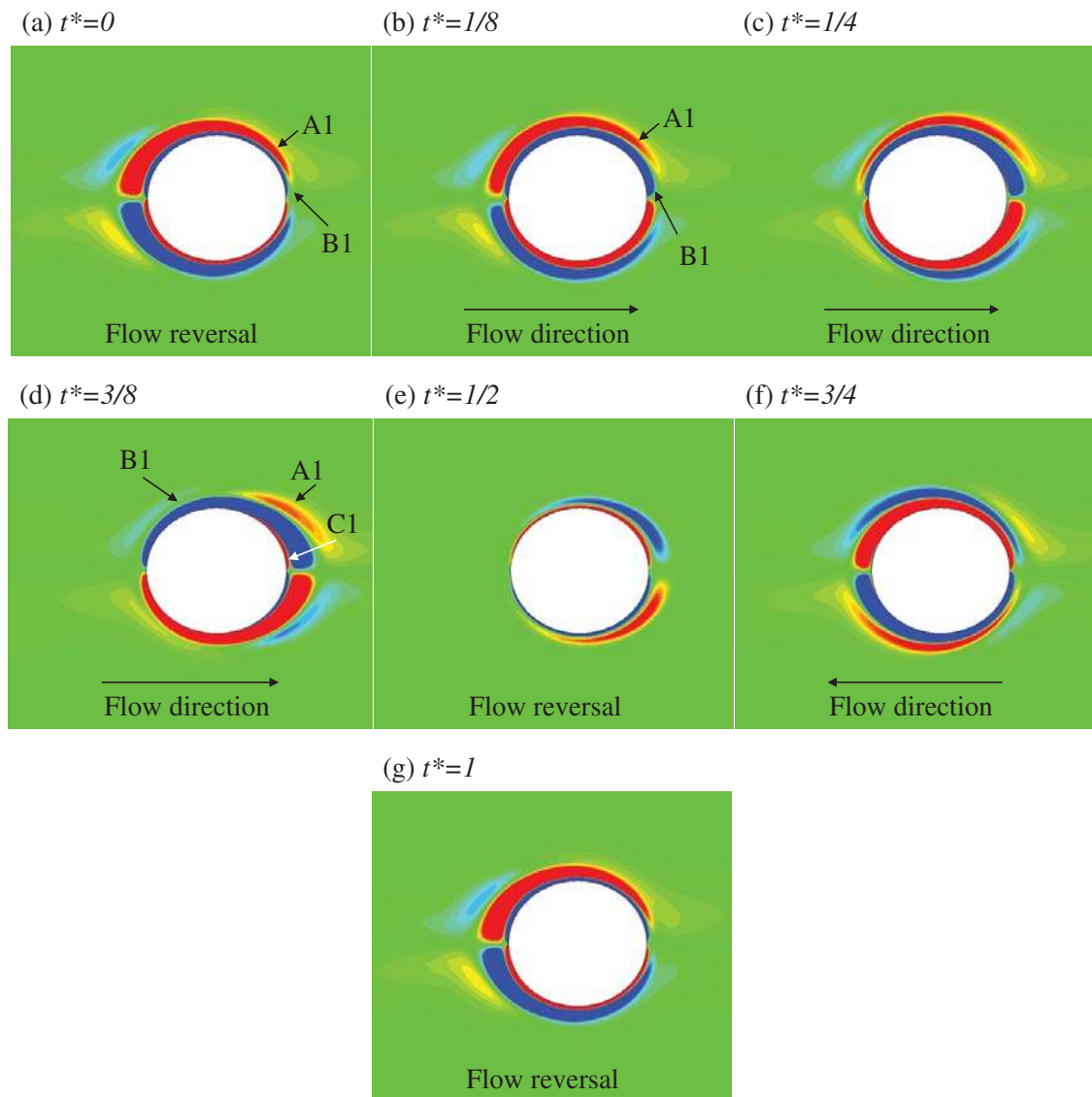
Figure 5.33 Vortex evolution in the plane of $z/D = 2$ by contours of ω_z for one oscillation period. For $(KC, \beta) = (2, 200)$ and K = cos30°. $t* = t/T$-200 and $-2 < \omega_z < 2$. For the first half period the interval is $\Delta t* = 1/8$ and for the second half period $\Delta t* = 1/4$.

5.10 Conclusions

This chapter concerns the resultant flow field for an oscillatory flow around an elliptic cylinder of different cross-sectional shape ratios (K). Effects of the shape ratio on the

transition from 2-D to 3-D flow are investigated at low KC and β values where the Honji instability operates.

A detailed discussion is given to compare the numerical results with those obtained based on a linear stability method suggested by Hall [17]. In consistence with the results by the linear stability analysis, the numerical results showed that the strength of Honji instability decreases with the shape factor K of the cylinder. However, numerical model appears to give different predictions of the critical K value below which Honji instability is suppressed. The reasons for this are attributed to (1) the linear stability method proposed by Hall is based on an assumption of small KC and large β values and (2) the non-linearity of the flow at the parameter ranges are not investigated in the theoretical study.

As a complement to Hall's theory, the present study gives extensive visualizations and descriptions on the resultant 3-D Honji vortical structures around cylinders of different shape ratios. Reduction of K inhibits the 3-D development as well as changes the behaviours of the resultant flow structures. Although it is found that the typical two-layer four-vortex dipole-like vortex pairs representing the Honji vortices can be observed for the 3-D cases for a cylinder with different shape ratios, the vortices around the circumference become stretched by the elongated curvature at small K, and the overall coverage of vortices over the cylinder surface is slightly reduced. The forming of the dolphin's head (representing the accumulation of vorticity) before the cylinder crown grows with the decrease of K, until finally the curvature is flat enough for a 'Side instability' to occur near the shoulder of the cylinder.

The flow features under the Side instability are evaluated for the case of K = cos60° at $(KC, \beta) = (2, 400)$. At this K value, the extent of the elliptic curvature is too large and the shear layer becomes too thin for the flow under this governing parameter value to form vortical structures at the vertex of the cylinder. As a result, the Side instability appears in the form of flat one-layer single-rotating vortex patches attached to the cylinder surface at locations closer to the cylinder's sides facing the incoming flow. While five main Honji vortices can be observed at this particular (KC, β) values for large K values, there are only four vortex patches representing the Side instability along the cylinder span. Once the Side instability occurs, the vortex patches can be observed

throughout the oscillation period, being only slightly stretched along the curvature by the ambient flow.

The mechanisms of reducing K to cause the suppression of the Honji instability and to lead to the Side instability can be accounted for in two aspects, namely, by considering the variation of the pressure gradient and the energy transfer at smaller K. The fluid particles within the high $\frac{\partial p}{\partial x}$ region are more unstable and instability is likely to happen within this area. As K decreases, the pressure gradient along the circumference decreases at the flatter cylinder vertex, while increases at the sharper shoulders. At some point, the pressure gradient at the cylinder vertex is not sufficient to cause the Honji instability; however, at the two shoulders of the cylinder, the pressure gradient may be large enough to cause another type of instability, namely, the Side instability. Considering the physics of fluid particles, more energy of the fluid particles is lost through travelling longer distance over the cylinder's flatter and elongated curvature. Therefore, the energy is not sufficient either for the fluid particles to curl, reverse and shoot upwards along the circumference to the cylinder vertex to generate the Honji vortices, or for transferring energy and momentum upwards in the radial direction to the fluid particles further away from the cylinder to form the top layer of Honji vortices. As a result, for the flow around elliptic cylinder with a sufficiently small K under certain governing parameters, only the Side instability in the form of one-layer vorticity can be generated at a lower location close to the cylinder shoulders.

Also discussed in this chapter are the characteristics of the resultant 2-D columnar flow when K is further decreased. It is found that the cylinder surface is covered by 2-D columnar flows for the case of (KC, β) = (2, 200) at K = cos30°. Neither the Honji instability nor the Side instability occurs, and no axial flow develops for the 2-D flow field. The cylinder surfaced is wrapped by a pair of axially-uniform sheet-like vortices equally dividing the whole circumference. The sheet-like vortices are also in the shape of a two-layer structure with counter-rotating vortices resulted from the no-slip boundary conditions applied at the cylinder surface. The periodic flow evolution demonstrated by the vorticity contours of ω_z shown in the cross-sectional view indicates that the flow is in the attached-vortices regime, as reported by Williamson [56].

CHAPTER 6

THE EFFECT OF A PIGGYBACK CYLINDER ON THE FLOW CHARACTERISTICS IN OSCILLATORY FLOW

6.1   Aim of chapter

In this chapter, 2-D numerical simulations of oscillatory flow around a pair of cylinders of unequal diameters are conducted in order to investigate how the presence of the smaller cylinder affects the resultant flow field as well as the hydrodynamic forces acting on the main cylinder. The contents in this chapter are as published in Yang et al. [80], with small denoting alterations, such as labels of the figures (and the table) and the parameter expressions used, for keeping consistence of the thesis as a whole.

6.2   Introduction

Offshore structures frequently are constructed from various cylindrical components and need to be able to resist forces that can be very large in extreme conditions. The details of the flows and forces present are critically dependent on the precise structure at hand. It appears that relatively little research has been conducted on the study of all but the most elementary cases. The objective of this chapter is to extend the knowledge of the well-studied time-periodic fluid motion which impinges normally on a long, stationary cylindrical tube to the situation when a second cylinder is introduced into the flow. The principal goal is to understand how this additional feature affects the forces and flow characteristics present in the single-cylinder situation.

In more detail, a geometry is envisaged in which there is a primary (relatively large diameter) cylinder but nearby there is a secondary (or 'piggy-backing') cylinder of a smaller diameter. The piggy-backing cylinder is expected to trigger hydrodynamic interference, and therefore change the key properties of the flow structure near the main cylinder. An efficient design of complex structures incorporating multi-pipe components is reliant on a full understanding of the effects the small cylinder may have

on the larger but it seems that analysis of this issue is limited at best and is certainly far from being comprehensive. The present study is intended to shed more light on this important problem.

The knowledge of the flow structures around and the fluid induced forces on a single cylinder in a sinusoidal oscillatory flow is now generally well established and accepted. There have been extensive experimental investigations of this type of flow and some significant results have been detailed by, among others, Keulegan and Carpenter [11], Sarpkaya [54], Maull and Milliner [55], Williamson [56], and Justesen [57]. In addition, numerical studies have been conducted by Wang and Dalton [58], Zhang and Zhang [59], Dütsch et al. [60], An et al. [21, 61] and Zhao et al. [62]. An accessible summary of some interesting phenomena with respect to flow structures and vortex properties has been given by Zdravkovich [63]. In particular, careful practical work enabled Williamson [56] to give a detailed description study of a sinusoidal flow around both an isolated cylinder and a pair of identical cylinders in a subcritical flow regime. Williamson was able to identify a number of distinctive flow patterns depending on the Keulegan-Carpenter (*KC*) number that is defined formally in Section 6.3 below. In particular, he found that the magnitude and frequency of the fundamental lift force are both related to the number of large vortices being shed in each half cycle. The connection between vortex evolution and the force variation had earlier been studied by Zdravkovich and Namork [64] and Sarpkaya [25]: both attributed an increase in the lift force to the wake asymmetry induced by vortex shedding and convection. For the in-line-force, one difficulty associated with achieving a good description of this force arises in the method adopted. In practice, this in-line force is often decomposed into two components using normalized force coefficients as derived within the classic Morison equation [29]. However, this equation applies strictly to steady flow and it is arguable whether it continues to hold in unsteady regimes. This point is further discussed later in the paper.

Compared with the aforementioned investigations the single cylinder case, the hydrodynamic interferences between two cylinders are much more poorly understood despite its clear wide application (see for example, Carstens and Sayer [65]). Moreover, many of the investigations using this more complicated geometry consider steady flow

as opposed to the practically more relevant oscillatory case. Zhao et al. [66] carried out a numerical study of flow past a pair of cylinders of differing diameters in steady flow and discussed the properties of the force coefficients, pressure distribution and vortex shedding patterns as the smaller cylinder is moved relative to the larger. It was found that the key factors that influence the flow field around a pair of cylinders include the gap ratio, the diameter ratio and the angle of attack of the incident flow. Zhao et al. [67] subsequently extended this work to higher Reynolds numbers and incorporated a turbulence model. Studies under sinusoidal oscillatory flow conditions include those by Williamson [56], Bearman et al. [100], Sarpkaya [15], Obasaju et al. [101] and Justesen [57] to mention but a few. Williamson [56] studied the forces on a pair of identical cylinders moving harmonically in otherwise quiescent fluid and found that when the cylinders are in close proximity the vortex-shedding patterns are significantly modified and the lift and in-line forces are significantly affected. McIver and Evans [68] described an approximate method for calculating forces on fixed vertical cylinders in a plane wave, and concluded that the flow structure and fluid forces can be strongly influenced by the interaction effects between the cylinders. Less is known about the case when the two cylinders have unequal diameters. Carstens and Sayer [65] used linear potential theory to study the hydrodynamic interaction in this problem and gave their results in terms of the added mass and damping between two unequal vertical cylinders in oscillatory flow. Williamson [69] also studied the fluid forces on two neighbouring cylinders with unequal diameters, but he focused on ascertaining the hydrodynamic interference effects of the flow field of the larger cylinder on the smaller one.

The present work concentrates on a two-dimensional numerical simulation of a sinusoidal oscillatory flow past a pair of cylinders consisting of a main cylinder and a nearby piggyback of diameter one-fifth that of the principal (see Figure 6.1). The aim is to assess how the presence of the secondary cylinder influences the flow patterns and fluid forces under sinusoidal oscillatory flow conditions. Simulations are carried over a range of Keulegan-Carpenter numbers that span the important flow regimes of both practical and academic interest; details are given in Section 6.3. All the calculations relate to subcritical flow where the flow has a turbulent wake and a laminar boundary layer. Both visualisation and force coefficients are examined in this study.
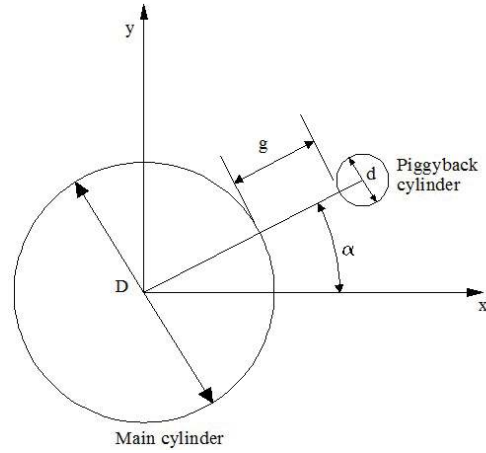
Figure 6.1 The relative positioning of the two cylinders within the computational domain.

The remainder of the paper is organised as follows. In Section 6.3 the governing system of equations is developed and the numerical schemes are described. Then, in Section 6.4, the main results are analysed and these are drawn together in Section 6.5 with some discussion and concluding remarks.

6.3   Formulation

Consider the motion around a pair of infinite cylinders placed in an incompressible fluid that far from the cylinders is oscillatory with amplitude U_m and with angular frequency ω. The period of the oscillation is then $T \equiv 2\pi/\omega$. Two important dimensionless properties of the flow are the Keulegan-Carpenter number KC and the frequency parameter β defined by

$$KC \ = \ \frac{U_m T}{D} \text{ and } \beta \ = \ \frac{D^2}{\upsilon T} \qquad\qquad 6.1$$

respectively; here D is the diameter of the primary (larger) cylinder and υ is the kinematic viscosity of the fluid.

Relative to standard Cartesian co-ordinates scaled on D, the continuity and Navier-Stokes equations can be written as

The continuity equation

$$\frac{\partial u}{\partial x} + \frac{\partial v}{\partial y} = 0 \qquad\qquad 6.2$$

The Navier-Stokes equations

$$\frac{1}{KC}\frac{\partial u}{\partial t} + u\frac{\partial u}{\partial x} + v\frac{\partial u}{\partial y} = -\frac{\partial p}{\partial x} + \frac{1}{Re}\left(\frac{\partial^2 u}{\partial x^2} + \frac{\partial^2 u}{\partial y^2}\right) \qquad\qquad 6.3a$$

$$\frac{1}{KC}\frac{\partial v}{\partial t} + u\frac{\partial v}{\partial x} + v\frac{\partial v}{\partial y} = -\frac{\partial p}{\partial y} + \frac{1}{Re}\left(\frac{\partial^2 v}{\partial x^2} + \frac{\partial^2 v}{\partial y^2}\right) \qquad\qquad 6.3b$$

here u and v denote the fluid velocities normalised by U_m in the x- and y-directions respectively, p is a dimensionless fluid pressure and t is a dimensionless time.

When the cylinders are placed in a moving fluid, the ambient flow exerts a force which is composed of pressure and friction terms. This resultant force is often best examined by finding its components in two mutually perpendicular directions: a lift in the vertical direction and an in-line force in the horizontal. If τ_0 denotes the wall shear stress on the surface of a cylinder of radius R and θ is the usual polar angle measured from the positive x-direction, the lift and in-line forces per unit length of cylinder are given by

$$F_L = \int_0^{2\pi} (-p\sin\theta - \tau_0\cos\theta)R\,d\theta \qquad\qquad 6.4a$$

and

$$F_F = \int_0^{2\pi} (-p\cos\theta + \tau_0\sin\theta)R\,d\theta \qquad\qquad 6.4b$$

respectively. In practice these forces are frequently expressed in terms of corresponding force coefficients C_L and C_F which are simply the requisite forces normalised with respect to $\rho D U_m^2/2$, where ρ is the fluid density.

For a cylinder sitting in an ambient purely oscillatory flow, the in-line force F_F is often characterised by reference to the Morison equation in which the force is decomposed into two parts according to

$$\frac{2F_F}{\rho DU_m^2} = C_D |\sin \omega t| \sin \omega t + \frac{\pi^2 C_M}{KC} \cos \omega t \qquad\qquad 6.5$$

here C_D and C_M are known as the drag and inertia coefficients. In practical cases, these coefficients can be computed via a least-squares calculation using the time history of the measured in-line force.

In all the calculations below β was fixed at 100 for KC = 4, 8, 16 and 24, which means that the corresponding Reynolds number $Re = U_m D/\nu \equiv \beta KC$ lies in the range $400 \le Re \le 2400$.

According to Sumer and Fredøe [7], the flow under the parameters chosen is turbulent, which is the dominant regime in real situations. As pointed out by Sarpkaya [25], the force on a circular cylinder is inertial-dominate for $KC \le 10$; for larger KC it is otherwise drag-dominated. Hence the KC values chosen here cover both regimes. The frequency number β was kept fixed at a relatively low value for computational efficiency. The KC numbers used here are chosen so as to describe flow regimes each with its own distinctive vortex shedding pattern (see Williamson [56]). It is to be hoped that the results presented in this study are of both practical and academic importance in understanding the effects on the physics of flow and the hydrodynamic force on the main cylinder caused by a neighbouring piggyback cylinder.

6.3.1 Numerical methods

The governing equations were solved using a finite element model based upon that developed by Zhao et al. [66]. Complete details of the method can be found in that paper so only the salient points are summarised here. A rectangular computational domain of dimensions $60D \times 30D$ was used, with the centre of the main cylinder fixed at the middle of this domain and the x,y-co-ordinate axes aligned so that the far-field oscillation of the flow is parallel to the x-axis; see Figure 6.1. The piggy-backing cylinder, which has a diameter of $0.2D$, is placed so there is a gap normalised as g/D between the two cylinders and the line joining their centres makes an angle α_p with the positive x-direction.

(a)

(b)
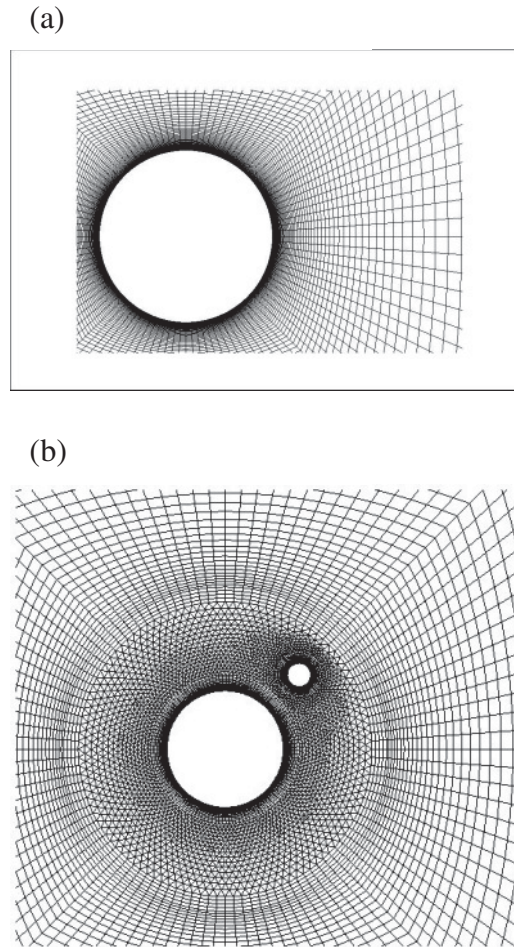
Figure 6.2 An illustrative example of the computational mesh in the vicinity of (a) an isolated cylinder and (b) the pair of cylinders.

Table 6.1 Mesh property for a single cylinder case. N_b: circumferential nodes number; Y_n: element size in the radial direction next to the cylinder boundary; N_p: total number of nodes and N_e: total number of elements in the domain.

Mesh	N_b	Y_n	N_p	N_e
M1	80	0.005	10,020	6,959
M2	110	0.0015	11,378	7,315
M3	130	0.001	13,734	9,333
M4	170	0.0005	16,584	11,758

The typical computational meshes for both an isolated cylinder and the two-cylinder system are illustrated in Figure 6.2. For an isolated cylinder (Figure 6.2a), the computational elements formed a four-node quadrilateral finite element mesh across the entire region. For the two cylinders (Figure 6.2b), structured four-node elements were applied in areas close to the cylinder surfaces and near the edges of the rectangular

domain while remainder of the domain was discretised using triangular elements. As a guideline as to the total number of elements involved, when the gap $g/D = 0.4$, there were 17,435 separate areas concentrated in the form suggested in Figure 6.2. In this case there were 140 nodes distributed around the circumference of the main cylinder and 70 nodes located on the smaller.

The simulation was initiated with the velocity fields set to zero across the entire domain. On the inlet side of the domain the evolution of the unsteady velocity field was prescribed to be $(u, v) = (U_m, 0) \sin \omega t$. At the outflow boundary the gradient of velocity and pressure were set to be zero. The boundary conditions on the remaining two (top and bottom) boundaries, consisted of symmetry requirements that were imposed by demanding that the normal derivatives of the velocity components and pressure be zero. Last, standard no-slip conditions were imposed on the surfaces of the cylinders.

6.3.2 **Validation of the model**

Although the present numerical model has been shown to work well for both an isolated cylinder and for a two-cylinder system in a uniform flow [66, 67], some initial benchmarking was carried out to ensure that reliable results could also be expected under unsteady flow conditions.

First some mesh-density experiments were used to verify that the nodes were sufficiently closely spaced to ensure accurate results. The effect of the mesh density on the resulting precision is considered for the isolated cylinder case. Four different meshes with the same structure but different densities as listed in Table 6.1 were adopted in order to assess the mesh dependency. The mesh structures with different densities have similar geometries to that shown in Figure 6.2a. The *KC* number for the single cylinder validation calculation was 20 and the frequency number β was set to 196. This case corresponds to a *Re* number of 3920, which is higher than the highest *Re* number to be investigated under the piggyback condition ($KC = 24$ and $\beta = 100$, resulting in a $Re = 2400$); also experimental data for validation of the results is available at $\beta = 196$. The convergence of the numerical results was tested by way of an examination of the pressure coefficient C_p (defined as $C_p = (p - p_a)/(\rho D U^2_m/2)$ where p_a is specified as the pressure at a fixed point). The distributions of C_p along the cylinder surface at the phase

of $\pi/4$ for the four meshes listed in Table 6.1 are plotted in Figure 6.3. It is seen that good agreement of the results is achieved between all four of the meshes; indeed the curves for Meshes 3 and 4 almost overlap each other over the whole cylinder surface. Little change of results is identified with any further refinement of the mesh. In view of the twin desires of requiring accuracy of solution while maintaining computational efficiency, Mesh 3 was chosen for all the subsequent calculations.
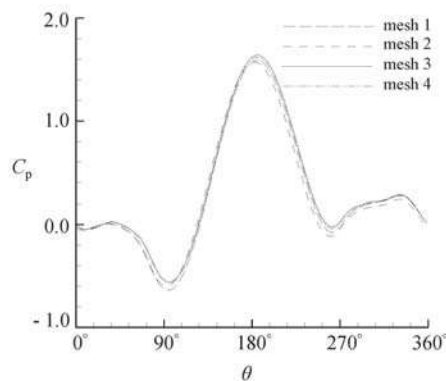
Figure 6.3 Distribution of pressure coefficient C_p along the cylinder surface ($KC = 20$, $\beta = 196$).

Results obtained using the selected mesh were then compared with some in the literature to gauge the performance of the model in predicting the flow behaviour and hydrodynamic forces. The model was validated by comparing the computed flow structure with that seen in the experiments described by Williamson [56] for oscillatory flow around a single cylinder. Without dwelling on the details, it is sufficient to note that Williamson reported a number of key changes in the flow structure as the KC number is increased and that the predictions were able to track these bifurcations with good accuracy and with excellent agreement in the form of the associated flow structure and the vortex shedding phenomena. Furthermore, the transverse and in-line forces calculated using the present computational model were compared with both the experimental results of Obasaju et al. [101] and the numerical results described by An et al. [61], all at $KC = 17.5$ and $\beta = 196$. Figure 6.4 gives a comparison of the results, and good agreement is found for both C_L and C_F. Given that the present computations are two-dimensional whereas the experiments were three-dimensional this provides some justification for concentrating on two-dimensional simulations. In addition, whilst An et al. [61] included a $k\text{-}\omega$ turbulence model in their formulation, this appears to make little

178

qualitative difference to the results despite the fact that the flow parameters are certainly in the regime where turbulence is expected. Thus in order to explore a wide range of parameter combinations for the present piggyback configuration, for the remaining numerical results the coding was restricted to two-dimensional simulations without an explicit turbulence model.

6.4 Results

The presence of the piggy-backing cylinder is anticipated to have a significant effect on the flow that would exist around an isolated cylinder as the interference between the two is likely to provoke changes in the wake structure. The present calculations considered flow simulations at the four values KC = 4, 8, 16 and 24 respectively and, for each of these, examined five gap ratios g/D=0.1,…,0.5. Moreover, this study investigated the flow structures over a range of α_p defined to be the angle between the positive x-direction and the line joining the centres of the cylinders, see Figure 6.1. It is sufficient to restrict α_p to no more than 90°, because the flow reversal inherent in sinusoidal behaviour means that this range is able to account for all the possible flow structures that can arise. With this in mind, it is then possible to identify three basic types of flow configuration. The first, known as the tandem arrangement case, arises when the centres of the cylinders align with the basic flow, α_p = 0°. Next are the staggered arrangements, which were investigated for the three angles α_p = 22.5°, 45° and 67.5°. Last comes the obvious 'side-by-side' arrangement, α_p = 90°, in which the centres of the cylinders are joined by a line perpendicular to the oscillatory flow far away. For ease of reference, the notation (α_p, g/D) is henceforce adopted to refer to the particular cylinder geometry.
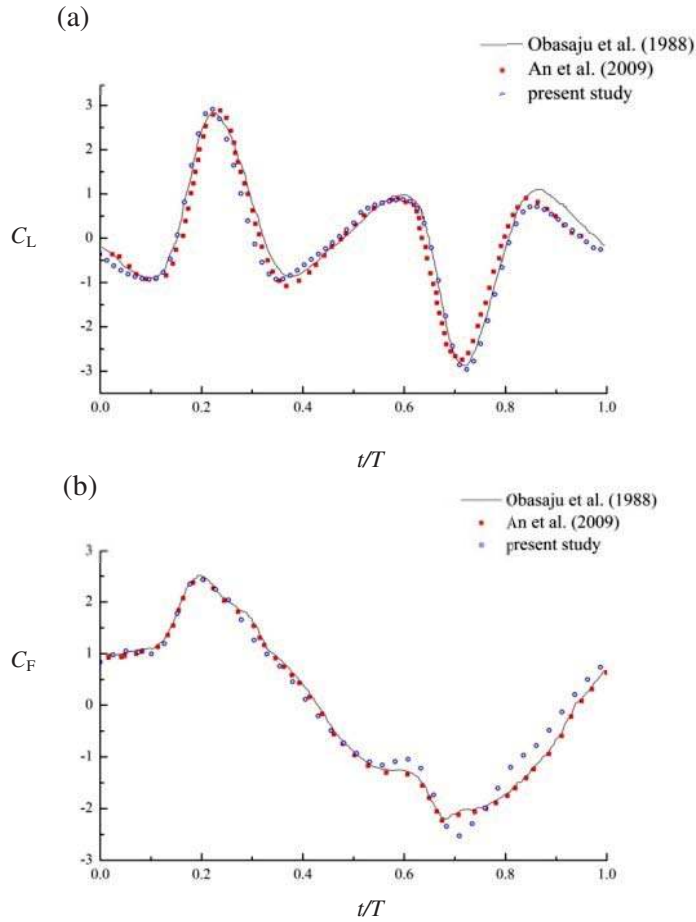
Figure 6.4 Comparison of the calculated force coefficients (a) C_L and (b) C_F with Obasaju et al. [101] and An et al. [61]'s results.

The influence of the piggyback cylinder on the lift and in-line force of the main cylinder is determined by the interactions of the vortex shedding from the two cylinders. At a given β value, the vortex shedding behaviour varies with the KC number. The results of Williamson [56] demonstrate that when $KC = 4$, attached symmetric vortices form around the main cylinder. When KC is doubled the flow is then in a transverse shedding regime with one vortex shed each half-period. When $KC =16$, two vortices are shed in every half-period and this increases to three when $KC =24$. To relate Williamson's research to the present study, his results are based on the KC number definition using the primary cylinder diameter; therefore, in the present study, the KC number with respect to the piggyback cylinder (whose diameter is 1/5 of the primary cylinder) is increased by a factor of five, which suggests that vortex shedding will occur around an isolated piggyback cylinder for all the cases calculated here. It can be predicted that the

wake field due to the small cylinder influences that of the main cylinder, and so affects the force on the main cylinder. Details of the interactions of the flow structures and the resulting force coefficients are discussed below.

6.4.1   The lift force acting on the main cylinder

6.4.1.1 KC = 4

As a general rule the lift force becomes significant only when *KC* number is larger than about 5 [25], so the lift should be negligible for an isolated cylinder at *KC* = 4. In order to assess the effect of the small cylinder on the lift force experienced by the main one we examine the value of C_{Lrms}, which is the root-mean-square value of the lift force coefficient. Figure 6.5 shows the dependence of C_{Lrms} on the piggyback cylinder position when *KC* = 4. The presence of the piggyback cylinder has a significant effect in most cases excepting the situation $\alpha_p = 0°$ when the two in-line cylinders act like a single body and generate a non-vortex-shedding vertical symmetric wake structure, similar to that of an isolated cylinder. The wake symmetry is broken by the piggyback cylinder whenever $\alpha_p \neq 0°$, which leads to a fundamental change in the fluid field, which in turn results in a considerable increase in C_{Lrms} (as mentioned in Section 6.2, the lift is a result of the pressure gradient which increases as the up-down asymmetry of the fluid field grows). The value of C_{Lrms} tends to grow with α_p and this enhancement is more pronounced at the smaller gaps. At larger separations beyond *g/D* = 0.3, it seems that the lift coefficient behaviour for the cases studied fell into two distinct groups. In addition for most values of α_p the maximum lift coefficient arises when *g/D* ≈ 0.3; presumably if the cylinders are closer together there is considerable destructive interference while if they are more widely separated the mutual interaction is quite weak and the flow is similar to that around an isolated main cylinder with an associated zero lift. Previous studies have shown that the asymmetry of the fluid field near the cylinder is caused by either the generation or the shedding of the vortices which means the variation in the lift force acting on the cylinder surface is closely related to the evolution processes occurring in the vortices near the body. Therefore in order to gain insight as to why the lift force is preferentially magnified at (90°, 0.3), it is helpful to trace the development of vortices around the main cylinder and thereby understand how the lift

might be affected by the existence of the piggyback. One strategy to achieve this goal is to study a selection of instantaneous vorticity contours of the $\alpha_p = 90°$ (or side-by-side) arrangement and compare these with the reference isolated cylinder problem. Some useful plots are reproduced in Figure 6.6 for the three gaps $g/D = 0.1$, 0.3 and 0.5.
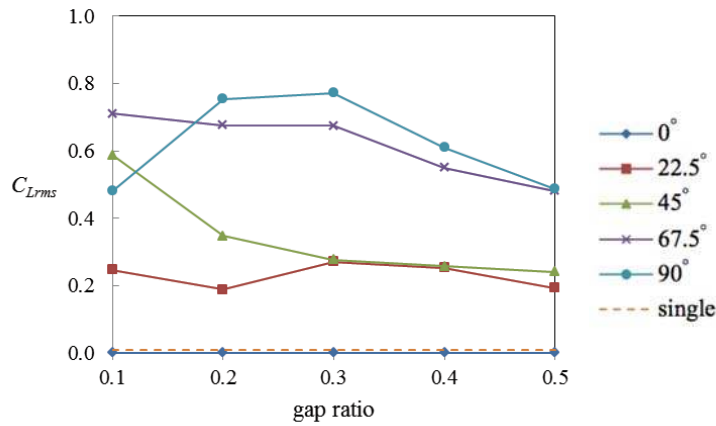
Figure 6.5 Root-mean-square values of the lift force as a function of the gap ratio g/D when $KC = 4$.

For ease of discussion the vortex pair on the main cylinder is referred to as M1 (the upper vortex) and M2 (the lower) and the corresponding pair on the piggyback as N1 and N2. When the small cylinder is placed close to the main, at $g/D = 0.1$, M1 and N2 are quite small and weak compared to their corresponding partners M2 and N1. It can be seen in Figure 6.6a that there is a tendency for N1 and M1 to amalgamate which in turn suppresses vortex N2. The upshot is that the wake flow behaves more-or-less as if the two vortices M2 and the resultant of N1, N2 and M1 behave rather like one large vortex pair around the two cylinders combined in a single body. It is the small difference between the sizes and strengths of the two components of this one large pair that generates a lift force that is quite small.

When the gap ratio is increased to 0.3, the vortices of M1 and N2 are more easily distinguished due to a much stronger gap flow; it is pointed out that N2 is now large enough to form a distinctive pair with its neighbouring vortex, see Figure 6.6c,d. This pair is shed during a half-cycle of the flow oscillation period and a stronger asymmetry in the wake flow is set-up which leads to an enhanced lift coefficient compared to the narrow-gap $g/D = 0.1$ configuration.

However, as the gap ratio is increased yet further to $g/D = 0.5$, the asymmetry of the wake structure reduces again and hence the lift coefficient drops. It can be seen in Figure 6.6e,f that the vortex structure is somewhat more symmetric than its counterpart in Figure 6.6c,d as a consequence of the fact that the flow field around the main cylinder is less affected by the piggyback cylinder as it is moved further away. The vortices formed around the main are hence more independent of the particulars of the wake around the piggyback, thereby forming a more symmetric flow field akin to the single cylinder case.
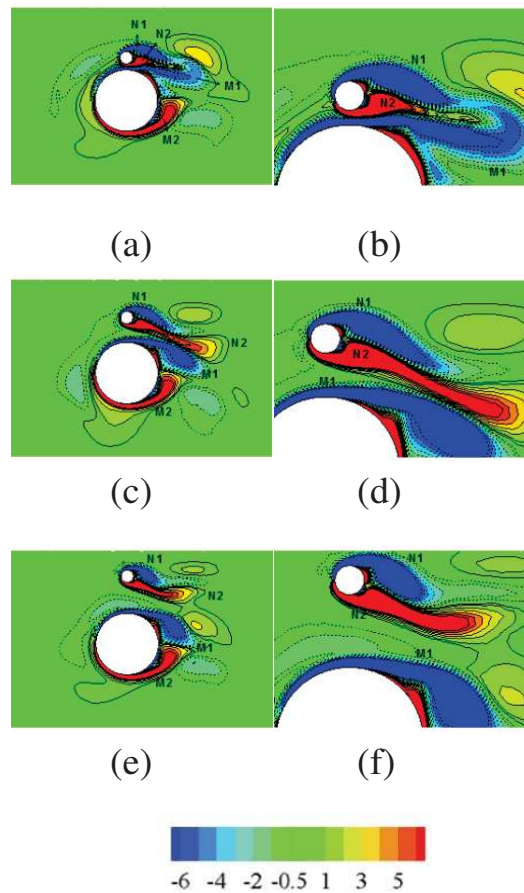
Figure 6.6 Instantaneous vorticity contours and the associated wake structure for the side-by-side arrangement with $KC = 4$. All plots are shown at phase $3T/8$ of the flow period and the left-hand panels relate to gap-widths $g/D = 0.1$, $g/D = 0.3$ and $g/D = 0.5$ (reading down). The corresponding right-hand plots are zoomed-in versions of their left-hand counterparts. In all plots solid contours indicate positive vorticity and dashed contours denote negative vorticity. The labelling of vortices is described in the text. (a, b) $g/D = 0.1$, (c, d) $g/D = 0.3$ and (e, f) $g/D = 0.5$.

6.4.1.2 KC = 8, 16 and 24

Thus far the paper has concentrated on the lift force when $KC = 4$ but now the case of larger KC is addressed. In order to facilitate the following discussion, it is easiest to consider an interference coefficient for the lift force defined to be $C_{Lint} = C_{Lrms}/C_{L\infty}$ in which $C_{L\infty}$ is the root-mean-square value of the lift force coefficient acting on the main cylinder when the piggyback is completely absent from the flow. This coefficient, which is very similar to one adopted by Williamson [56], is a quick gauge of the effects of the piggyback cylinder; clearly a value $C_{Lint} > 1$ indicates the lift on the main cylinder is increased by the piggyback cylinder. It should be noted that this coefficient defined by ratio is proved to be inappropriate for investigation at smaller KC (for the present study, $KC = 4$ as discussed) because then the reference coefficient $C_{L\infty}$ for the isolated cylinder is close to zero as a result of strong symmetry in the wake flow and the ratio is no longer a robust quantity. The dependence of C_{Lint} on the geometries of the cylinders and at various KC numbers is illustrated in Figure 6.7.

(a)

(b)

(c)
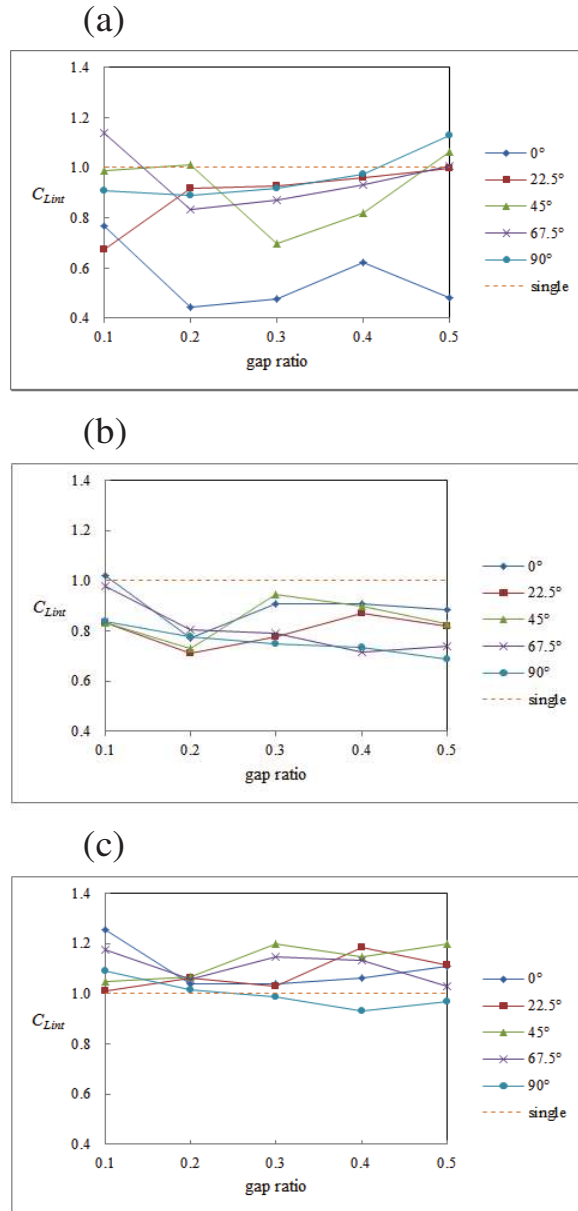
Figure 6.7 The lift interference coefficient C_{Lint} as a function of gap g/D for various values of KC. (a) $KC = 8$, (b) $KC = 16$, (c) $KC = 24$.

At $KC = 8$, see Figure 6.7a, the most dramatic influence of the piggyback cylinder on C_{Lint} is observed when $\alpha_p = 0°$, in which case the lift force is reduced regardless of the gap ratio. For other α_p values the change is less pronounced and the lift force is not very different with that when there is only a single cylinder in the flow. A simple explanation for this observation can be inferred from an inspection of the corresponding flow field as shown in Figure 6.8a,b. When the piggyback cylinder is laid in tandem with the main cylinder (i.e. $\alpha_p = 0°$), the arrangement behaves like a streamline body. It is clear that

under such arrangement the presence of the piggyback cylinder inhibits the shed vortices being swept across to the other side of the wake in a similar manner to the function of a splitter plate. As a result, the main influence of the piggyback cylinder appears to be that the two constituent vortices are more balanced and have improved symmetry with respect to the midline (cf. Figure 6.8a,b). The details of the effect of the piggyback cylinder change with the gap ratio. For g/D up to about 0.2, the gap is sufficiently small for the upper vortex to wrap around the piggyback. As can be seen in Figure 6.7, the maximum reduction of the lift happens when $g/D = 0.2$ for this is the largest gap for the upper vortex to still be able to wrap around the piggyback cylinder. At larger g/D the effects of the piggyback cylinder are weakened, as the spacing is sufficient to prevent vortices from surrounding the small cylinder, and the resulting stronger gap flow allows the lower vortex to pass through the gap region. The upshot is that the wake field loses much of its symmetry and thereby increases the lift (see Figure 6.8c as an example). When the piggyback is placed at a non-zero α_p position it is noticed that the drop in the lift force is much less significant. This is a consequence of the fact that irrespective of the gap value the topology of the vortex shedding is still essentially that of a transverse flow regime; in other words an asymmetric regime reminiscent of that present when only a single cylinder is in the flow (see, for example, Figure 6.8d).

Further sub-plots in Figure 6.7 reveal how the flow develops at yet larger values of KC. By the stage when $KC = 16$ the lift force on the main cylinder tends to be significantly affected and reduced by the presence of the piggybacking cylinder. This influence appears to be least significant when the cylinders are in a tandem arrangement with the secondary cylinder lying directly behind (or in front of) the primary and, in contrast, most important when the cylinders are side-by-side. An examination of the flow field for $\alpha_p = 0°$ when $g/D = 0.1$ and 0.2 (see Figure 6.9b,c) suggests that in these cases the gap is sufficiently small to permit the lower vortex shed by the large cylinder to wrap around the small cylinder. For these gap sizes the two vortex pairs shed during one flow period are similar to those generated behind a single cylinder in as much that the vortex pairs are again located in the first and third quadrants. However, when the gap is increased to $g/D = 0.3$ or 0.4, the two pairs change direction and are shed in the opposite quadrants, possibly as a result of the fact that these gap sizes are critical in the sense that

the piggyback cylinder is located so that it hinders the stretching of the upper vortex while simultaneously elongating the lower vortex. As shown in Figure 6.9d as the gap grows further so a stage is reached when the piggyback sits comfortably within the upper vortex, and the two vortex pairs revert to the top-right and bottom-left quadrants. In general, the vortex pairs are thrown off in the quadrants opposite to those where the stretched vortex is positioned. Moreover, the pressure field generated by the piggyback cylinder when combined with that of the main cylinder tends to lessen the asymmetry of the flow field thereby restricting the overall lift force.
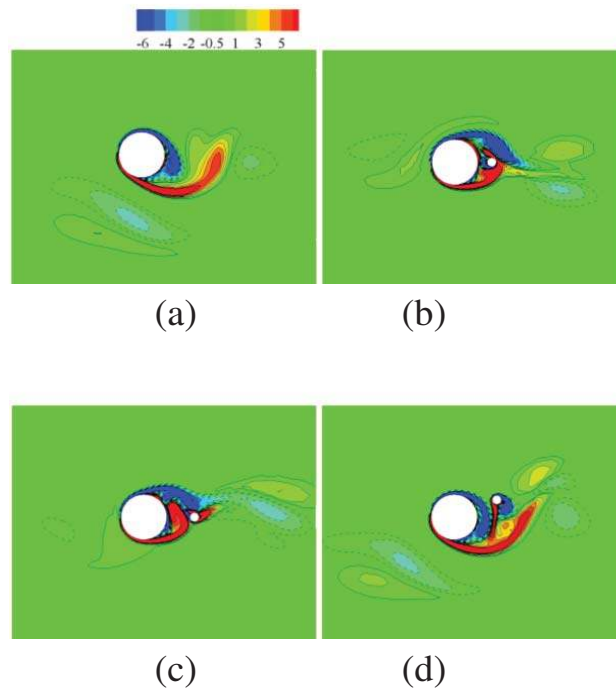
Figure 6.8 Flow structures for $KC = 8$ and at phase $3T/8$ of the flow period. The four cases relate to various positions of the secondary cylinder. (a) Only the primary cylinder present. For other plots $(\alpha, g/D) =$ (b) $(0°, 0.2)$; (c) $(0°, 0.5)$; (d) $(22.5°, 0.4)$.

Once $KC = 24$ the lift is enhanced in almost all cases. An isolated main cylinder within a flow at this KC number gives rise to a vortex shedding regime of three vortices per half-period. Such a wake flow possesses significant asymmetry (as shown in Figure 6.10a). The increase in the lift after the smaller cylinder is added in the nearby field is attributable to the strong vortex field formed near the smaller cylinder when KC is large. It is noticeable in Figure 6.7c that for a gap $g/D = 0.2$, the lift present is almost exactly that for a single cylinder independent of the inclination angle α_p. This suggests strongly

that in this regime the vortices formed by the main cylinder are hardly affected at all by the piggybacking cylinder (good examples of this behaviour are seen for $\alpha_p = 0°$ in Figure 6.10b and for $\alpha_p = 22.5°$ in Figure 6.10c and it is apparent that the small cylinder is not subsumed by the main vortices). At larger gaps, the main vortices occupy the wake of the small cylinder again because the main vortices become increasingly stretched (examples include $\alpha_p = 0°$ in Figure 6.10d and $\alpha_p = 22.5°$ in Figure 6.10e).
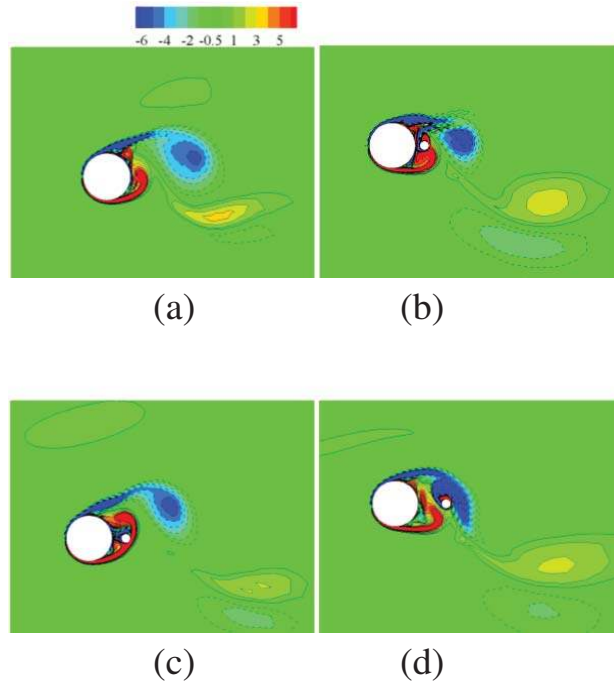
Figure 6.9 Flow structures for $KC = 16$ and at phase $3T/8$ of the flow period. The four cases relate to various distances between the cylindres in all instances $\alpha = 0°$. (a) Only the primary cylinder present. For other plots the gap $g/D =$ (b) 0.1, (c) 0.2 and (d) 0.5.

The computations for values $KC > 4$ suggest that for moderately elevated KC the lift coefficient is slightly reduced with the largest influence occurring when the cylinders are in the tandem arrangement aligned with the oncoming oscillatory flow ($\alpha_p = 0°$). As KC grows so the lift coefficient only changes slightly, but the most dramatic effects occur when the angle α_p dictating the orientation of the cylinders moves away from zero. It is only when KC becomes as large as 24 that the lift coefficient appears to show any tendency to exceed its value when no piggyback cylinder is present.
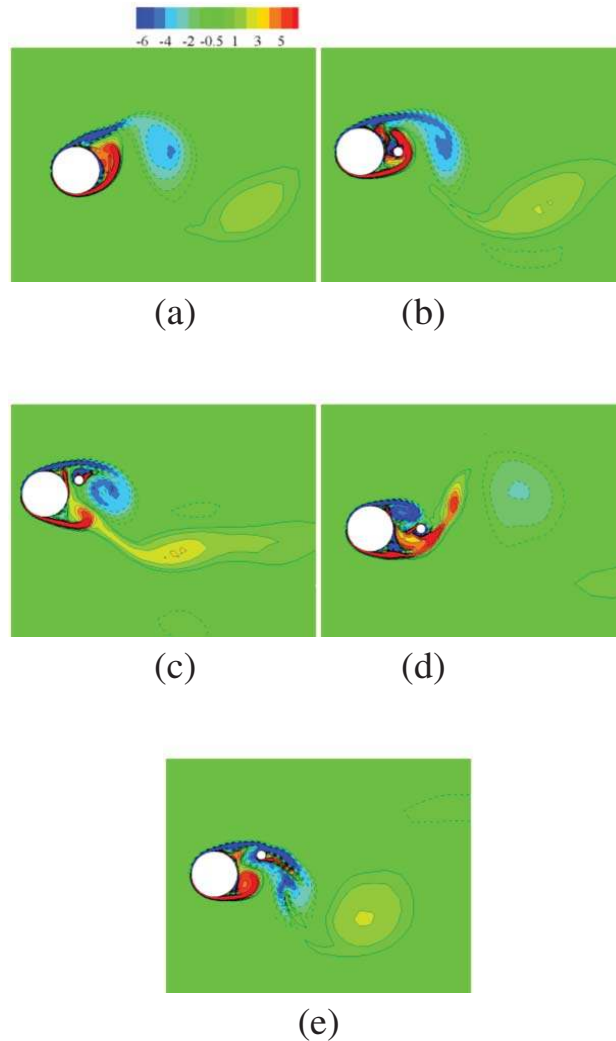
Figure 6.10 Flow structures for $KC = 24$ and at phase $3T/8$ of the flow period. The four cases relate to various positions of the secondary cylinder. (a) Only the primary cylinder present. For other plots (α, g/D) = (b) ($0°$, 0.2), (c) ($22.5°$, 0.2), (d) ($0°$, 0.5) and (e) ($22.5°$, 0.5).

6.4.2 The effect of the piggyback on the in-line force

Traditionally the in-line force experienced by the main cylinder is assessed by appeal to the Morison equation (Equation 6.5) in which the drag and inertia coefficients C_D and C_M are evaluated by fitting with experimental or numerical data. However, there is some debate (see, for example, Williamson [56] or Dütsch et al. [60]) as to whether it is legitimate to use this strategy for the in-line force. There are two grounds for this concern: not only is the method extremely sensitive to the exact phase position of the in-line force peaks but it is also known to perform poorly when the force profile is not

precisely periodic. In view of these aspects, the present study implemented the Morison procedure for irregular flow patterns by calculating period-averaged coefficients. Unfortunately it was found that the computed coefficients vary wildly and could not be considered reliable. This approach was therefore abandoned and a more effective determination of the key coefficients was attempted using a direct computation of the in-line force coefficient C_F (Equation 6.4b).

As noted earlier, the lift force is attributable to the asymmetry present in the vortex field between the upper and lower half planes. In a similar way, the part played by the piggyback cylinder in fixing the in-line force component acting on the main cylinder can be thought of in terms of the asymmetry of the vortex field in the left and right half planes. There is an inherent left-right asymmetry in the vortex field even when there is only the primary cylinder in the flow giving rise to an in-line force coefficient $C_{F\infty}$ which is non-zero for all KC. Thus, in order to most easily illustrate the difference between the flows with and without the piggyback cylinder, it is helpful to define an interference coefficient for the in-line force according to $C_{Fint} = C_{Frms}/C_{F\infty}$. Plots of this quantity as a function of cylinder geometry at different KC numbers are given in Figure 6.11.

Figure 6.11 shows that the in-line force changes more significantly when the gap is small. In addition, a stronger effect is also seen for large inclination angles $\alpha = 67.5°$ or 90° for all KC numbers except for the case when $KC = 16$, at which the reductions in in-line force for small angles are almost as significant as the increases for large angles. An explanation for this observation can be proposed, following a similar approach for the C_L discussion, by analysing the changes of pressure difference between the upwind and lee-wake of the primary cylinder with the absence and presence of a nearby small cylinder.

For the case of an isolated main cylinder, due to the periodicity of the oscillatory flow, the upwind and lee-wake side with respect to the main cylinder take turns to form at the left (or right) plane of flow field near the cylinder every half flow period, and the vortices shed during two half periods are symmetric. Therefore the absolute pressure difference between the upwind and lee-wake sides of the two successive half periods is the same. This symmetry of vortex shedding is disrupted by the inclusion of the

piggyback on one side of the primary cylinder, and the piggyback has its greatest influence when placed close to the primary. The vortex evolution over the first and second half-periods is altered by interference with the secondary cylinder. When the vortex is generated on the same side as the piggyback is located a high pressure centre is formed near the vortex area and is enhanced by the small cylinder.

(a) (b)

(c) (d)
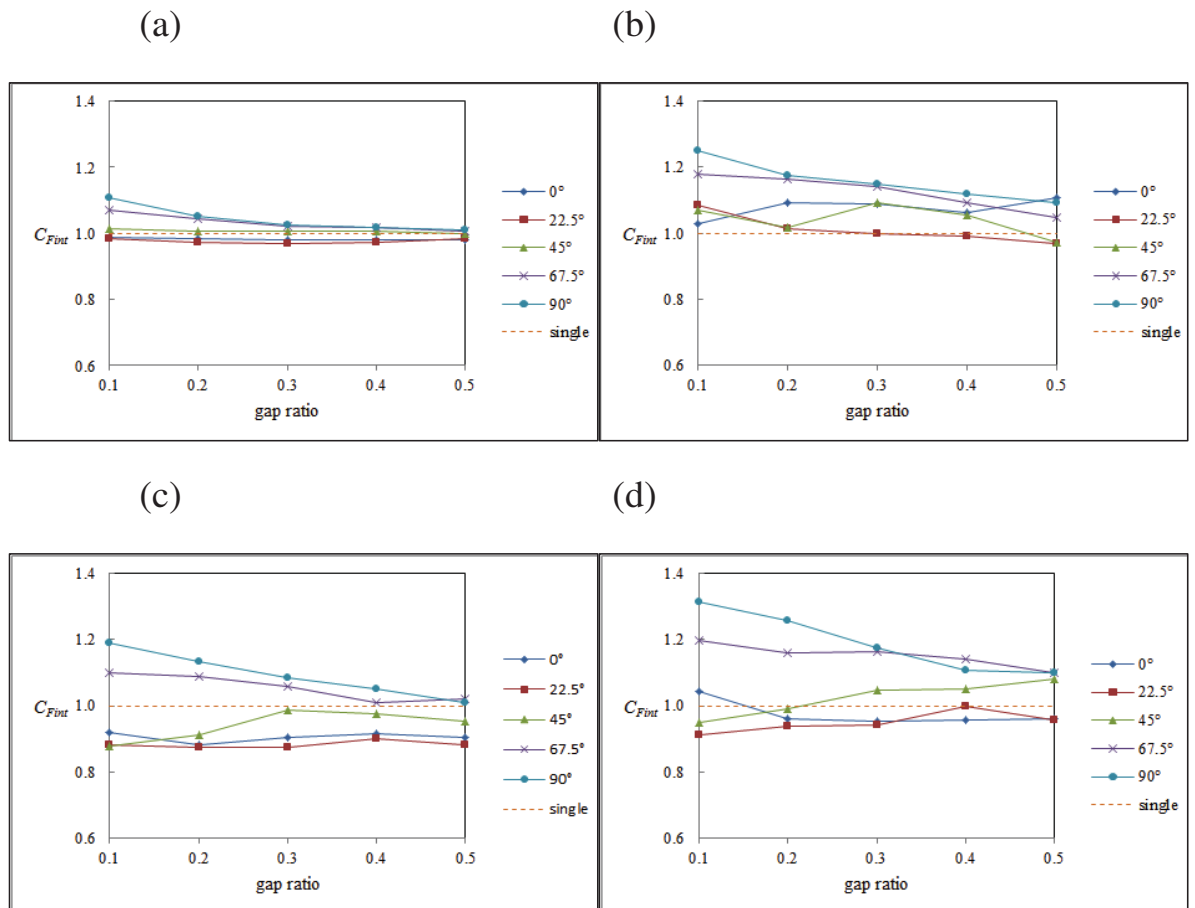
Figure 6.11 In-line interference coefficient C_{Fint} as a function of gap g/D and for various values of KC = (a) 4, (b) 8, (c) 16 and (d) 24.

When the two cylinders are placed in a tandem arrangement (see, for example, Figure 6.12c,d), it is not straightforward to apply the pressure difference method to predict the influence on the in-line force. Under this arrangement, in one half of the period the vortex shedding occurs on the same side as the piggyback and in the next half-period on the opposite. The pressure field generated around the small cylinder causes the pressure field across the primary cylinder to be asymmetric over successive half oscillation

periods. In comparison with the single cylinder case, over the half-period when the main vortex is formed in the half plane containing the small cylinder, the pressure difference between the upwind and lee-wake planes is larger; however, in the next half-period when flow reverses and the main vortex is formed in the opposite half plane, the pressure difference across the primary cylinder is smaller. Nevertheless, the reduction of pressure difference across the primary cylinder in general can be predicted from the fact that the in-line cylinder causes the two-cylinder system to act more like a streamlined body, which explains the decreases of C_F under influences of a small cylinder for most cases studied.
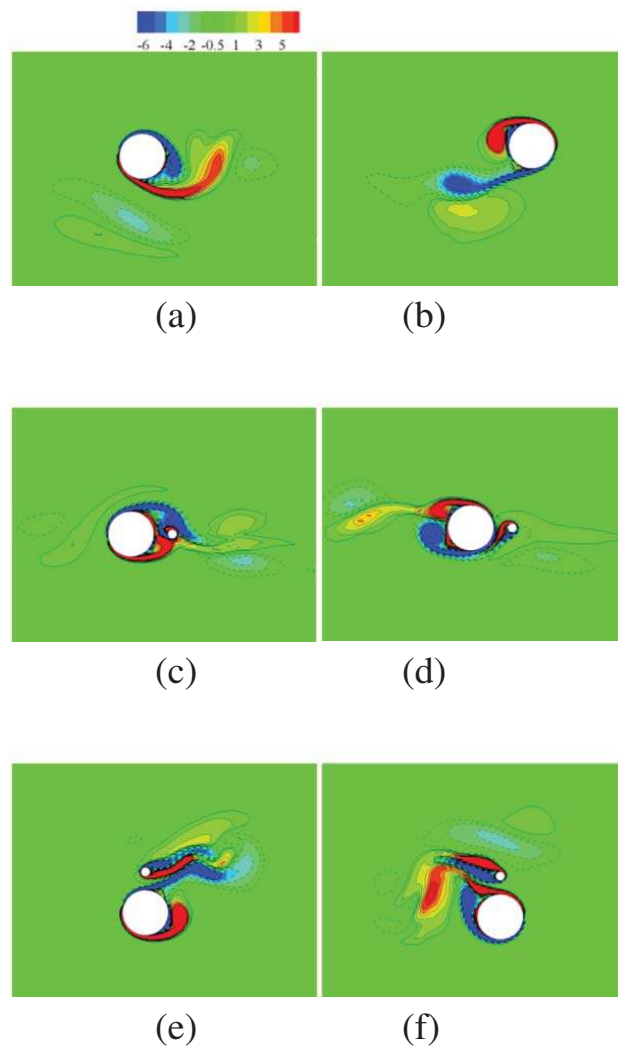
Figure 6.12 Flow structures at phase $3T/8$ and $7T/8$ of two successive half periods with $KC = 8$ and gap $g/D = 0.3$. (a, b) Single cylinder, (c, d) $\alpha = 0°$ and (e, f) $\alpha = 90°$. Plots in the left-hand column correspond to phase $3T/8$ and those on the right $7T/8$.

When α is large (plots for $\alpha = 90°$ are shown in Figure 6.12e,f) the blockage effects of the cylinder system are enhanced, and the piggyback cylinder is located between the upwind and lee-wake in two successive half periods, and hence tends to increase the pressure difference during both the first and second half periods. This in turn induces significant asymmetry in the upwind and the lee-wake of the flow happening across the whole period with the consequence that the in-line force increases.

These flow structures lend credence to the main findings presented in Figure 6.11. However, it is worthwhile to make mention of the specific case when $KC = 16$ and $\alpha <$ 67.5°.The conclusion to be drawn from Figure 6.11c is that at these smaller angles the in-line force seems to be slightly reduced when compared with the single cylinder results. A careful study suggests that this behaviour can be traced to the manner in which the vortex field interacts with the piggyback cylinder although a detailed quantitative explanation remains unknown at this juncture.

6.5   Discussion

The principal concern in this paper has been to demonstrate and understand how the introduction of a piggybacking cylinder into an oscillatory flow affects and drives the structures around and the hydrodynamic forces on a main cylinder. It is seen that the piggyback cylinder has two key roles to play and the magnitudes of these are a joint function of the gap between the cylinders and the orientation of their line of centres to the direction of the far-field flow. The secondary cylinder induces a pressure field of its own and attracts the vortices shed by the main structure. In addition, the flow through the gap between the cylinders appears to be the factor that governs whether vortex shedding occurs. If the gap is too narrow the flow through it is weak compared to the suppression effect of the piggyback cylinder and this is enough to prevent the vortex spawned from the main cylinder and nearer the secondary to be shed. The upshot then is that the vortex on the side away from the gap is the one that is thrown off. In contrast, when the gap is sufficiently wide, the gap flow is stronger and the influence of the piggyback smaller. Then the vortices (including the part of both the main vortex and the piggyback vortex) in the gap region are shed. It should be remarked that as $g/D \rightarrow \infty$ so

C_{Lint}, $C_{\text{Fint}} \to 1$ because then the piggyback cylinder in the far-field has no influence on the main cylinder at all.

For the lift force, the resultant fluid field is determined by the original vortex shedding regime of the main cylinder under different KC numbers plus the influence of the small cylinder. Larger asymmetry in the upper and lower half fluid field as a result of the interaction of the vortices induced by the two cylinders leads to larger lift. The most notable effect of the piggyback cylinder is observed when $KC = 4$. At this stage the existence of the small cylinder distorts the original symmetry of the attached vortices formed around the main cylinder. The resulting asymmetric flow field is characterised by a vortex shedding flow around the main cylinder which results in a remarkably dramatic change in the lift force. The effect is rather less marked for other values of KC, presumably due to a less severe pressure gradient being induced by the asymmetry of vortex field in the near wake. The asymmetry of the main vortex field is already very strong for $KC = 8$, 16 and 24. The lift is mainly decreased for $KC = 8$ and $KC = 16$ owing to the asymmetry decreasing under the influence of the small cylinder. Further increase of the KC number to 24 gives slightly increasing lift for all cases, which is attributable to the stronger vortex field caused by the addition of the pressure field due to the small cylinder.

Turning next to the in-line force, the simply normalized in-line coefficient C_F is adopted here instead of the Morison coefficients because the latter is found to be inappropriate on evaluating aperiodic regimes. It has been seen that in the presence of the piggyback cylinder the in-line force on the main cylinder is more likely to be increased. The influence on the in-line force is more pronounced for a closer neighbouring piggyback cylinder. The trend is that a relatively large α value (67.5° and 90°) tends to increase the in-line force at small gap ratios. The enhanced asymmetry of the upwind and lee-wake of the main cylinder within the two half periods is responsible for the increasing of in-line force.

In theory, this paper provides a possibility for developing an intuitive approach for predicting the trend of change of hydrodynamic forces acting on a primary body by examining the trend of asymmetry of the nearby flow structure.

Acknowledgements

CHAPTER 7

CONCLUSIONS AND FUTURE WORK

7.1 Aim of chapter

This chapter provides a summary of the key outcomes of the research presented in the present dissertation, based on which suggestions for future research are also discussed.

7.2 Summary of the present study

This thesis describes a fundamental investigation on oscillatory flow around cylindrical structures under low governing parameters (KC, β) through a numerical approach. Both 2-D and 3-D calculations have been conducted with the latter as the major focus of the present dissertation. A comprehensive study has been given on the situations when an isolated cylinder of infinite length is immersed in a sinusoidal oscillatory flow at the flow regime where the 2-D to 3-D flow transition occurs under the effects of hydrodynamic instability, in particular, the Honji instability. Under the scenarios concerned, flow behaviours have been evaluated thoroughly regarding both the time-varying flow development and instantaneous flow behaviours.

The research has been conducted through direct numerical simulations on the numerical model generated to represent the physical problem. The calculations of the flow field have been realised by a streamline upwind Petrov-Galerkin's finite element method. Details of this method including the algorithm and setting-up of the numerical model (e.g. the mesh dependence study) have been covered in Chapter 2. In addition, Chapter 3 has introduced a new perturbation method for tackling problems of hydrodynamic instability, such as the Honji instability. After a careful definition of the perturbation as provided in Chapter 3, this method was then applied to several cases discussed in Chapter 4 and Chapter 5, for the purpose of accelerating the flow development as well

as examining the intrinsic stability of the flow field by checking against the possibility of convective instability.

Results obtained through the method described in Chapter 2 and Chapter 3 have been reported in Chapter 4, Chapter 5 and Chapter 6. Calculations were conducted both in 2-D and 3-D numerical simulations. For the 2-D and 3-D flow, we look at different aspects of the flow behaviours. Most of the present dissertation has been devoted to discussions of the hydrodynamic instability which causes the flow to evolve from 2-D to 3-D, for which two scenarios have been evaluated under the chosen values of the governing parameters, as reported in Chapter 4 and Chapter 5. In addition, Chapter 6 presents a 2-D simulation on oscillatory flow near a two-cylinder system at low governing parameters similar to those used in the 3-D calculations.

Calculations in Chapter 4 have been performed to examine the flow behaviours for a slightly oblique inflow around a circular cylinder under the Honji instability regime. This is the first time that the oblique flow effects on the Honji instability have been investigated. A summary of the key outcomes from this investigation reported in Chapter 4 can be listed in four aspects given as follows:

1) Flow development:

- By comparing the flow development processes at different angles of attack (α), it is found that the axial flow component has a stabilising effect on the near-cylinder flow, and that this effect is stronger with a larger α. Increasing the axial flow component by enlarging α may eventually result in a 2-D stable flow field, where the Honji instability is completely suppressed.

- Based on our current numerical results, effects of α at different β values on the resultant flow fields have been summarised in a β-α plane for a constant $KC = 2$, as given in Figure 4.12. With the variation of β and α at a constant KC value, the flow may fall into one of the three possible regimes, namely, an unstable Honji regime marked by strong interactions between the formed vortices, a stable Honji regime with regular and distinct vortical structures, and a featureless purely 2-D regime.

- The flow is intrinsically more active at a larger β, while being more stable at a larger α. Therefore, under the combined effects of these two parameters, the unstable Honji regime was found at $(\alpha, \beta) = (0°, 300)$, $(10°, 300)$, $(0°, 400)$, $(10°, 400)$ and $(20°, 400)$, the stable Honji vortices are observed at $(\alpha, \beta) = (0°, 200)$, $(10°, 200)$, $(20°, 300)$ and $(30°, 400)$, and the 2-D flow field results when $(\alpha, \beta) = (20°, 200)$, $(30°, 300)$ and $(40°, 400)$.

2) The instantaneous Honji structures:

- The Honji vortical structures generated under the oblique inflow are visualized in detail for the very first time. The shape and size of the structures are modified by the existence of the axial flow component compared with the typical Honji structures generated for the perpendicular inflow case. The two-layer vortical structures for the oblique cases are biased, with the rotation of half of the pair apparently stronger than the other. When α is large enough, only the dominant vorticity remains in the top layer, while the opposite-rotating weak vorticity is completely ingested by the axial flow component. In addition, the bottom layer only appears as sheet flow attached to the cylinder for such cases.

- For the oblique inflow cases, the vorticity pairs in the two arrays along the cylinder orient obliquely to the cylinder, however the inclination angle is roughly 5° smaller than that of the free stream. This is because the oblique flow always tends to redirect to be more perpendicular to the cylinder, as it passes the cylinder surface.

- In addition, the dimensions of the oblique vortical structures are different from those of the perpendicular inflow cases. The oblique vortices generally appear to be shorter in the circumferential extent and slender with reduced radial as well as axial extents, due to the weakness of the flow field resulting from the effects of the axial flow component.

- Evolution of the instantaneous vortical structures within one oscillation period for the oblique inflow cases has also been compared with that of the perpendicular inflow cases. Due to the flow reversal every half period, the two

counter-rotating vorticities in the top layer (as observed for the perpendicular case) take turns to dominate and the sheet flow in the bottom layer reversals consistently with the axial flow component. Therefore, for these cases, the flow evolution becomes mirror-imaged every half period.

3) The 2-D flow resulting from large α:

- The near-cylinder flow remains 2-D when the instability is suppressed by the axial flow component. These cases include $(\alpha, \beta) = (20°, 200)$, $(30°, 300)$ and $(40°, 400)$. The instantaneous flow structures also show a two-layer structure, however this structure is axially invariant along the cylinder and consists of two columnar sheet vorticities caused by the no-slip boundary condition.

4) Mechanism of the stabilising effects of α:

- Mechanisms for causing the suppression of the instability have been explained by considering the energy and momentum transfer of the fluid particles as the latter are conveyed around the cylinder following the ambient flow. The biased vortical structures formed under the effects of the oblique inflow are in an unfavourable form for the equal distribution of the energy and momentum between the vortices. As a result, the structures become more unbalanced with more energy and momentum injected into the dominant vorticity; while at the same time, the two-layer structures become flatter under the effects of the axial flow that confines the flow particles closer to the cylinder.

Geometrically, oblique flow around a circular cylinder is similar to a perpendicular flow around an elliptic cylinder. Hence, Chapter 5 arose naturally to consider the shape effects of the cylinder's cross section on the resultant flow field under the same governing parameters. The principle outcomes from the work reported in Chapter 5 are organised in the following four themes:

1) Flow development and instantaneous flow structures:

- Referring to a previous theoretical study by Hall [17], Chapter 5 provides visualizations of the flow structures to study the effects of the cross-sectional

shape on the instability that causes the 2-D to 3-D flow transition. This is the first time that details of the flow field around an elliptic cylinder are described to validate Hall's theory. A full description of the resultant vortical structures formed under different values of the shape ratio K are gained through presenting the flow development as well as the instantaneous flow characteristics.

- It is found that a cylinder with a more streamlined elliptic cross section tends to stabilise the nearby flow field, while at the same time modify the characteristics of the instability-induced vorticies.

- For the case of K = 1 where Honji instability occurs near the top of the cross section of the cylinder, decreasing K causes a delay in the development of the instability. In addition, although the two-layer symmetric vortex pairs appear to be similar between different K values, these vortices become attenuated due to stretching around the circumferential curvature. At the same time, a large portion of the vorticity is likely to accumulate close to the sharpened shoulders.

- Further reducing K may result in a 'Side instability' in the form of axially varying vorticities at the near-shoulder region. Unlike the two-layer mushroom-shaped Honji vortices found at the top of the cross section, the Side instability takes a form of flat alternating vortex patches, which distribute along the cylinder distanced at a value similar to their individual axial span.

- When K is below a certain value, i.e. the cylinder reaches a critical flatness, the 3-D instability is suppressed and the near-cylinder flow field remains 2-D. The columnar 2-D flow wrapping around the cylinder evolves in a similar fashion to that reported by Williamson [56].

2) Mechanisms for the stabilising effects of K:

- The mechanisms for the alteration of the resultant flow field caused by variation of the shape factor are explained from two aspects. Firstly, considering the change of the pressure gradient around the circumference of the cylinder, a flatter cylinder is in a less favourable shape for the Honji instability to occur,

while is more favourable to cause a Side instability. This is attributed to the pressure gradient experiencing a reduction near the Honji region and an increment near the cylinder shoulders.

- Secondly, an elongated curvature causes the fluid particles to lose more energy and momentum before they travel to the top region to form the Honji vortical structures. In addition, for our cases with small KC and β, the period of the oscillation is short and the viscosity of the flow is large, both of which inhibit the flow particles from climbing over the circumference. This explains the accumulation of the vorticity at locations lower than the top of the cross section. As a result, as the cylinder becomes flatter, the instability drops to locations closer to the cylinder shoulders, before K is small enough to result in a 2-D stable flow.

3) Evaluation of Hall's [17] theory:

- Evaluation of Hall's [17] linear stability theory with first order accuracy is discussed associated with the present calculations. Numerical results obtained in this study have proved the general trend predicted by Hall, i.e. the Honji instability is weakened by reducing K. Nevertheless, our calculations have shown a more stable flow field than that predicted by the theory for the cases concerned.

- Possible reasons for the inconsistency are proposed as the following. Firstly, the present study has been conducted at relatively small governing parameters of $(KC, \beta) = (2, 200)$ and $(2, 400)$, while Hall's theory is limited at high β and low KC. Although a relatively good comparison of Hall's theory with Honji's experimental results has been shown for the case concerning a circular cylinder, it is possible that, with an additional influencing parameter, namely the shape ratio K, the theory may not work well beyond the limiting range of large β and small KC. Secondly, the discrepancy is attributed to the neglecting of higher order terms, which play a more important role at smaller governing parameters. It has been shown that the inclusion of a second order term leads to a higher critical curve for the onset of the instability, which stands for a more stable flow

than that predicted with first order accuracy. Finally, the non-linear effects, especially the higher order non-linear effects may also serve to stabilise the flow field, as mentioned by Hall [17].

Chapter 6 concerns a 2-D numerical simulation for the aim of assessing the possible influences of a near-by small cylinder on the flow patterns as well as fluid forces of the main cylinder. The calculations have been carried out on an oscillatory flow around a piggybacking-cylinder system under the subcritical flow regime at low values of (KC, β). The main contribution of the study described in Chapter 6 is that it provides a very straightforward method to predict the trend of the change of the fluid forces on a cylindrical structure by evaluating the symmetry of the nearby flow field. This method is of potential significance to practical applications. The major findings arose from the work presented in Chapter 6 are mentioned below.

- The original vortex shedding of the main cylinder is disturbed by the additional pressure field induced by the nearby piggyback cylinder. The ultimate flow field under the different governing parameters, which determines the resultant hydrodynamic forces on the main cylinder, is largely affected by the gap flow generated between the two cylinders.

- Considering the effects of the governing parameters as well as the influences of the small cylinder, the hydrodynamic forces exerted on the main cylinder are found to be closely associated with the symmetry of the flow field close to the cylinder. The lift force is related to the symmetry of the upper and lower halves of the cross section of the cylinder, while the in-line force is influenced by the symmetry of the upwind and lee-wake of the cylinder. As a rough guide, a large asymmetric flow field leads to an increase of the forces.

7.3 Recommendations for future research

Although this thesis has presented an elaborate study on different aspects considering the near-cylinder flow behaviours under low values of KC and β, there still exist some limitations which need to be addressed in future studies. Based on the results obtained

so far, the following recommendations are made to advance the findings reported in this thesis:

Recommendations for future studies of 3-D hydrodynamic instability:

1. The present study has shown a stabilising trend of the flow behaviours by increasing the axial flow component or streamlining the cylinder's cross section, which may completely suppress the hydrodynamic instability that causes a 2-D to 3-D transition. However, this study is limited to certain values of angle of attack (α) and shape ratio (K) at selected (KC, β) groups. Calculations at other values of governing parameters should be considered in order to gain a more comprehensive understanding of these influencing factors. In particular, special attention is raised for the limiting cases such as a pure-axial flow with $\alpha = 90°$ and the flat plate with K = 0.

2. In addition, determination of the exact critical values of the governing parameters that maintains the 2-D stable flow was not covered in this thesis, because it requires countless test runs that are impossible to be completely covered using the present numerical method. However, a more accurate dependency curve for the onset of instability definitely provides a useful guideline for future studies. It is possible that the perturbation method described in Chapter 3 will be extended with some further effort to facilitate calculations for determining precise critical values.

3. This study of the hydrodynamic instability topic only focuses on descriptions of the flow development and the detailed flow structures. From the practical point of view, in future work it would be necessary to study the hydrodynamic forces subject to possible influences of angle of attack (α) and shape ratio (K), when the flow is under 2-D to 3-D transition caused by hydrodynamic instability, and the possible influences of angle of attack and the shape ratio.

4. It would be very useful if the numerical results can be verified and validated against results obtained through physical experiments. Difficulties in conducting

such experiments might include obtaining the desired governing parameters under laboratory conditions, ensuring that the hydrodynamic instability observed in experiments is an intrinsic flow property and not caused by other disturbances, and detecting the onset of small 3-D features efficiently.

Recommendations for future study of 2-D unequal cylinders:

1. In a follow-up study for the 2-D piggyback system, the dimensions of the two cylinders should be varied to reveal possible alterations to the flow field. In addition, more relative locations of the piggyback cylinder should be examined.

2. It is also worthwhile extending the current 2-D simulations to 3-D simulations, which then allows us to consider the possible 3-D effects on the resultant flow structures and the hydrodynamic forces.

3. 3-D calculations can also be performed for the purpose of studying the Honji instability under the effects of a piggyback cylinder in the proximity of the main cylinder. Similar to the 2-D study, the main influencing factors to be examined may include the relative size and location of the piggyback cylinder.

4. Again, laboratory experiments on the same topic are highly recommended for verifying and validating the results obtained through the numerical method discussed in this thesis.

REFERENCES

1.   Tubb, R., *2013 Worldwide Pipeline Construction Report*, 2013. **240**(1).

2.   Farell, C., *Flow around fixed circular cylinders: fluctuating loads.* Journal of the Engineering Mechanics Division, 1981. **107**(3): p. 565-588.

3.   Karniadakis, G.E. and Triantafyllou, G.S., *Three-dimensional dynamics and transition to turbulence in the wake of bluff objects.* Journal of Fluid Mechanics, 1992. **238**(1).

4.   Beaudan, P. and Moin, P., *Numerical experiments on the flow past a circular cylinder at sub-critical Reynolds number*, 1994. No. TF-62. STANFORD UNIV CA THERMOSCIENCES DIV, 1994.

5.   Williamson, C., *Three-dimensional wake transition*. In *Advances in Turbulence VI*, Springer Netherlands, 1996: p. 399-402.

6.   Williamson, C.H.K., *Vortex dynamics in the cylinder wake.* Annual Review of Fluid Mechanics, 1996. **28**(1): p. 477-539.

7.   Sumer, B.M. and Fredsøe, J., *Hydrodynamics around cylindrical structures*. Advanced Series on Ocean Engineering, World Scientific, 1997. **Vol 12**.

8.   Persillon, H. and Braza, M., *Physical analysis of the transition to turbulence in the wake of a circular cylinder by three-dimensional Navier–Stokes simulation.* Journal of Fluid Mechanics, 1998. **365**(1): p. 23-88.

9.   Lei, C., *Experimental and Numerical Studies of Vortex Shedding Flow over a Circular Cylinder near a Wall*. PhD thesis in The University of Western Australia, 2000.

10.   Schlichting, H., *Berechnung ebener periodischer Grenzschichtströmungen.* Physikalische Zeitschrift, 1932. **33**: p. 327-335.

11.   Keulegan, G.H. and Carpenter, L.H., *Forces on Cylinders and Plates in an Oscillating Fluid.* US Department of Commerce, National Bureau of Standards, 1956.

12.   Sarpkaya, T., *Vortex shedding and resistance in harmonic flow about smooth and rough circular cylinders at high Reynolds numbers.* No. NPS-59SL76021. Naval Postgraduate School Monterey CA, 1976.

13.   Sarpkaya, T., *On the parameter $\beta = Re/KC = D^2/vT$.* Journal of Fluids and Structures, 2005. **21**(4): p. 435-440.

14.   Honji, H., *Streaked flow around an oscillating circular cylinder.* Journal of Fluid Mechanics, 1981. **107**: p. 509-520.

15.   Sarpkaya, T., *Force on a circular cylinder in viscous oscillatory flow at low Keulegan - Carpenter numbers.* Journal of Fluid Mechanics, 1986. **165**: p. 61-71.

16.   Tatsuno, M. and Bearman, P.W., *A visual study of the flow around an oscillating circular cylinder at low Keulegan-Carpenter numbers and low Stokes numbers.* Journal of Fluid Mechanics, 1990. **211**: p. 157-182.

17.   Hall, P., *On the stability of the unsteady boundary layer on a cylinder oscillating transversely in a viscous fluid.* Journal of Fluid Mechanics, 1984. **146**: p. 347-367.

18.   Sarpkaya, T., *Experiments on the stability of sinusoidal flow over a circular cylinder.* Journal of Fluid Mechanics, 2002. **457**: p. 157-180.

19.   Zhang, J. and Dalton, C., *The onset of three-dimensionality in an oscillating flow past a fixed circular cylinder.* International Journal for Numerical Methods in Fluids, 1999. **30**(1): p. 19-42.

20.   Elston, J.R., Blackburn, H.M., and Sheridan, J., *The primary and secondary instabilities of flow generated by an oscillating circular cylinder.* Journal of Fluid Mechanics, 2006. **550**: p. 359-389.

21.   An, H., Cheng, L. and Zhao, M., *Direct numerical simulation of oscillatory flow around a circular cylinder at low Keulegan-Carpenter number.* Journal of Fluid Mechanics, 2011. **666**: p. 77-103.

22.   Suthon, P. and Dalton, C., *Streakline Visualization of the Structures in the Near Wake of a Circular Cylinder in Sinusoidally Oscillating Flow.* Journal of Fluid Mechanics, 2011. **27**(7): p. 885-902.

23.   Suthon, P. and Dalton, C., *Observations on the Honji instability.* Journal of Fluids and Structures, 2012. **32**: p. 27-36.

24.   Sarpkaya, T., *Structures of separation on a circular cylinder in periodic flow.* Journal of Fluid Mechanics, 2006. **567**: p. 281-297.

25.   Sarpkaya, T., *Wave Forces on Offshore Structures*, Cambridge University Press, 2010.

26.   Chorin, A.J., *Numerical solution of the Navier-Stokes equations.* Mathematics of Computation, 1968. **22**(104): p. 745-762.

27.   Temam, R., *Sur l'approximation de la solution des équations de Navier-Stokes par la méthode des pas fractionnaires (II).* Archive for Rational Mechanics and Analysis, 1969. **33**(5): p. 377-385.

28. Lu, X.Y. and Ling, G.C., *Three-dimensional instability of an oscillating viscous flow past a circular cylinder.* Applied Mathematics and Mechanics, 2003. **24**(7): p. 791-800.

29. O'Brien, M. P., and Morison, J. R., *The forces exerted by waves on objects.* Transactions, American Geophysical Union, 1952. **33**: p. 32-38.

30. Rayleigh, L., *On the dynamics of revolving fluids.* Proceedings of the Royal Society of London. Series A, 1917. **93**(648): p. 148-154.

31. Taylor, G.I., *Stability of a viscous liquid contained between two rotating cylinders.* Philosophical Transactions of the Royal Society of London. Series A, 1923. **223**: p. 289-343.

32. Dean, W., *Fluid motion in a curved channel.* Proceedings of the Royal Society of London. Series A, 1928. **121**(787): p. 402-420.

33. Görtler, H., *Über eine dreidimensionale Instabilität laminarer grenzschichten an konkaven Wänden.* Zeitschrift für Angewandte Mathematik und Mechanik, 1940. **21**: p. 250-252.

34. Hoerner, S.F., *Fluid-dynamic drag: practical information on aerodynamic drag and hydrodynamic resistance.* Hoerner Fluid Dynamics, 1965.

35. Fornberg, B., *Steady viscous flow past a circular cylinder up to Reynolds number 600.* Journal of Computational Physics, **61**(2): p. 297-320.

36. Thakur, A., Liu, X., and Marshall, J.S., *Wake flow of single and multiple yawed cylinders.* Journal of Fluids Engineering, 2004. **126**(5): p. 861-870.

37. Hayashi, T. and Kawamura, T., *Non-uniformity in a flow around a yawed circular cylinder.* Flow Measurement and Instrumentation, 1995. **6**(1): p. 33-39.

38. Snarski, S.R., *Flow over yawed circular cylinders: Wall pressure spectra and flow regimes.* Physics of Fluids, 2004. **16**: p. 344.

39. Lucor, D. and Karniadakis, G.E., *Effects of oblique inflow in vortex-induced vibrations.* Flow, Turbulence and Combustion, 2003. **71**(1): p. 375-389.

40. Zhao, M., Cheng, L., and Zhou, T., *Direct numerical simulation of three-dimensional flow past a yawed circular cylinder of infinite length.* Journal of Fluids and Structures, 2009. **25**(5): p. 831-847.

41. Zhao, M., Cheng, L., and Zhou, T., *Three-dimensional numerical simulation of oscillatory flow around a circular cylinder at right and oblique attacks.* Ocean Engineering, 2011. **38**(17): p. 2056-2069.

42.   Vakil, A. and Green, S.I., *Drag and lift coefficients of inclined finite circular cylinders at moderate Reynolds numbers.* Computers & Fluids, 2009. **38**(9): p. 1771-1781.

43.   Shintani, K., Umemura, A., and Takano, A., *Low-Reynolds-number flow past an elliptic cylinder.* Journal of Fluid Mechanics, 1983. **136**: p. 277-289.

44.   Umemura, A., *Matched-asymptotic analysis of low-Reynolds-number flow past two equal circular cylinders.* Journal of Fluid Mechanics, 1982. **121**(1): p. 345-363.

45.   Taneda, S., *Visual study of unsteady separated flows around bodies.* Progress in Aerospace Sciences, 1976. **17**: p. 287-348.

46.   Badr, H.M., *Oscillating viscous flow over an inclined elliptic cylinder.* Ocean Engineering, 1994. **21**(4): p. 401-426.

47.   Nair, M.T. and Sengupta, T.K., *Onset of asymmetry: flow past circular and elliptic cylinders.* International Journal for Numerical Methods in Fluids, 1996. **23**(12): p. 1327-1345.

48.   Nair, M.T. and Sengupta, T.K., *Unsteady flow past elliptic cylinders.* Journal of Fluids and Structures, 1997. **11**(6): p. 555-595.

49.   Sheard, G.J. *Cylinders with elliptic cross-section: wake stability with variation in angle of incidence*. Journal of Fluid Mechanics, 2009. **630**(1): p. 43-69.

50.   Flynn, M.R. and Eisner, A.D., *Verification and validation studies of the time-averaged velocity field in the very near-wake of a finite elliptical cylinder.* Fluid Dynamics Research, 2004. **34**(4): p. 273-288.

51.   Baranyi, L., *Numerical simulation of flow around an orbiting cylinder at different ellipticity values.* Journal of Fluids and Structures, 2008. **24**(6): p. 883-906.

52.   Kim, M.S. and Sengupta, A., *Unsteady viscous flow over elliptic cylinders at various thickness with different reynolds numbers.* Journal of Mechanical Science and Technology, 2005. **19**(3): p. 877-886.

53.   Modi, V. J., and Wiland, E., *Unsteady aerodynamics of stationary elliptic cylinders in subcritical flow*. AIAA Journal, 1970. **8**(10): p. 1814-1821.

54.   Sarpkaya, T. *In-Line and Transverse Forces, On Cylinders in Oscillatory Flow at High Reynolds Numbers*. In Offshore Technology Conference, 1976.

55.   Maull, D.J. and Milliner, M.G., *Sinusoidal flow past a circular cylinder.* Coastal Engineering, 1978. **2**: p. 149-168.

56.   Williamson, C.H.K., *Sinusoidal flow relative to circular cylinders.* Journal of Fluid Mechanics, 1985. **155**(1): p. 141-174.

57.   Justesen, P., *Hydrodynamic forces on large cylinders in oscillatory flow.* Journal of Waterway, Port, Coastal and Ocean Engineering, 1989. **115**(4): p. 497-514.

58.   Wang, X. and Dalton, C., *Numerical solutions for impulsively started and decelerated viscous flow past a circular cylinder.* International Journal for Numerical Methods in Fluids, 1991. **12**(4): p. 383-400.

59.   Zhang, H.L. and Zhang, X., *Flow structure analysis around an oscillating circular cylinder at low KC number: a numerical study.* Computers & Fluids, 1997. **26**(1): p. 83-106.

60.   Dütsch, H., Durst, F., Becker, S., and Lienhart, H., *Low-Reynolds-number flow around an oscillating circular cylinder at low Keulegan-Carpenter numbers.* Journal of Fluid Mechanics, 1998. **360**: p. 249-271.

61.   An, H., Cheng, L., and Zhao, M., *Steady streaming around a circular cylinder in an oscillatory flow*. Ocean Engineering, 2009. **36**(14): p. 1089-1097.

62.   Zhao, M., Cheng, L., and An, H., *Three-dimensional numerical simulation of flow around a circular cylinder under combined steady and oscillatory flow. Journal of Hydrodynamics*, Ser. B, 2010. **22**(5): p. 144-149.

63.   Zdravkovich, M.M., *Flow around Circular Cylinders: Volume 2: Applications*. Oxford University Press. 2003.

64.   Zdravkovich, M.M. and Namork, J.E., *Formation and Reversal of Vortices around Circular Cylinders Subjected to Water Waves.* Journal of the Waterway Port Coastal and Ocean Division, 1977. **103**(3): p. 378-383.

65.   Carstens, B. and Sayer, P.G., *Hydrodynamic interactions between two vertical circular cylinders in linear oscillatory flow.* Ocean Engineering, 1997. **24**(4): p. 351-380.

66.   Zhao, M., Cheng, L., Teng, B., and Liang, D., *Numerical simulation of viscous flow past two circular cylinders of different diameters.* Applied Ocean Research, 2005. **27**(1): p. 39-55.

67.   Zhao, M., Cheng, L., Teng, B., and Dong, G., *Hydrodynamic forces on dual cylinders of different diameters in steady currents.* Journal of Fluids and Structures, 2007. **23**(1): p. 59-83.

68.   McIver, P. and Evans, D.V., *Approximation of wave forces on cylinder arrays.* Applied Ocean Research, 1984. **6**(2): p. 101-107.

69.   Williamson, C.H.K., *Fluid forces on a small cylinder in the presence of a large cylinder in relative oscillatory flow.* Applied Ocean Research, 1985. **7**(3): p. 124-127.

70.   Zienkiewicz, O.C. and Cheung, Y.K., *Finite Elements in the Solution of Field Problems.* The Engineer, 1965: p. 507-510.

71.   Hughes, T.J.R. and Brooks, A.N., *Streamline upwind/Petrov-Galerkin formulations for convection dominated flows with particular emphasis on the incompressible Navier-Stokes equations.* Computer Methods in Applied Mechanics and Engineering, 1982. **32**(1): p. 199-259.

72.   Heinrich, J.C., Huyakorn, P.S., Zienkiewicz, O. C., and Mitchell, A. R., *An 'upwind' finite element scheme for two‐dimensional convective transport equation.* International Journal for Numerical Methods in Engineering, 1977. **11**(1): p. 131-143.

73.   Donea, J., *A Taylor–Galerkin method for convective transport problems.* International Journal for Numerical Methods in Engineering, 1984. **20**(1): p. 101-119.

74.   Patera, A.T., *A spectral element method for fluid dynamics: laminar flow in a channel expansion.* Journal of Computational Physics, 1984. **54**(3): p. 468-488.

75.   Carey, G. and Jiang, B., *Least‐squares finite element method and preconditioned conjugate gradient solution.* International Journal for Numerical Methods in Engineering, 1987. **24**(7): p. 1283-1296.

76.   Monaghan, J.J., *An introduction to SPH.* Computer Physics Communications, 1988. **48**(1): p. 89-96.

77.   Zhao, M., Cheng, L., and An, H., *A finite element solution of wave forces on a horizontal circular cylinder close to the sea-bed.* Journal of Hydrodynamics, Ser. B, 2006. **18**(3): p. 139-145.

78.   Zhao, M., Cheng, L. and Teng, B., *Numerical simulation of solitary wave scattering by a circular cylinder array.* Ocean Engineering, 2007. **34**(3-4): p. 489-499.

79.   Zhao, M., Cheng, L., and Teng, B., *Numerical modeling of flow and hydrodynamic forces around a piggyback pipeline near the seabed.* Journal of Waterway, Port, Coastal, and Ocean Engineering, 2007. **133**(4): p. 286-295.

80.   Yang, K., Cheng, L., An, H., Bassom, A. P., and Zhao, M. *The effect of a piggyback cylinder on the flow characteristics in oscillatory flow.* Ocean Engineering, 2013. **62**: p. 45-55.

81.   Yang, K., Cheng, L., An, H., Bassom, A., and Zhao, M., *Effects of flow oblique angle on three-dimensional steady streaming at low Keulegan-Carpenter number.* In the 18th Australasian Fluid Mechanics Conference, 2012.

82.   Yang, K., Cheng, L., An, H., and Zhao, M. *Direct Numerical Simulation of Effects of Small Angle of Incidence on Honji Instability.* ASME, 2011.

83.   Yang, K., An, H., Cheng, L., and Zhao, M., *Oscillatory flow around a pair of cylinders of different diameters.* In The Sixth International Conference on Asian and Pacific Coasts: APAC, 2011.

84.   Chung, T.J., *Computational Fluid* Dinamics. Cambridge University Press, 2002.

85.   Raymond, W.H. and Garder, A., *Selective damping in a Galerkin method for solving wave problems with variable grids.* Monthly Weather Review, 1976. **104**: p. 1583-1590.

86.   Donea, J., Giuliani, S., Laval, H., and Quartapelle, L., *Finite element solution of the unsteady Navier-Stokes equations by a fractional step method.* Computer Methods in Applied Mechanics and Engineering, 1982. **30**(1): p. 53-73.

87.   Ramaswamy, B., *Finite element solution for advection and natural convection flows.* Computers & Fluids, 1988. **16**(4): p. 349-388.

88.   Ramaswamy, B. and Jue, T., *Some recent trends and developments in finite element analysis for incompressible thermal flows.* International Journal for Numerical Methods in Engineering, 1992. **35**(4): p. 671-707.

89.   Zhao, M., Cheng, L. and Zhou, T., *Three-dimensional numerical simulation of oscillatory flow around a circular cylinder at right and oblique attacks.* Ocean Engineering, 2011. **38**(17–18): p. 2056-2069.

90.   Janssen, R. and Henkes, R., *Influence of Prandtl number on instability mechanisms and transition in a differentially heated square cavity.* Journal of Fluid Mechanics, 1995. **290**: p. 319-344.

91.   Armfield, S. and Janssen, R., *A direct boundary-layer stability analysis of steady-state cavity convection flow.* International Journal of Heat and Fluid Flow, 1996. **17**(6): p. 539-546.

92.   Janssen, R. and Armfield, S., *Stability properties of the vertical boundary layers in differentially heated cavities.* International Journal of Heat and Fluid Flow, 1996. **17**(6): p. 547-556.

93.   Brooker, A.M.H., Patterson, J.C., Graham, T., and Schöpf, W., *Convective instability in a time-dependent buoyancy driven boundary layer.* International Journal of Heat and Mass Transfer, 2000. **43**(2): p. 297-310.

94.   Lei, C. and Patterson, J.C., *A direct stability analysis of a radiation-induced natural convection boundary layer in a shallow wedge.* Journal of Fluid Mechanics, 2003. **480**: p. 161-184.

95.   Aberra, T., Armfield, S.W., Behnia, M., and McBain, G.D., *Stability of natural convection boundary layer flow on an evenly heated vertical plate*. In AIP Conference Proceedings, 2006. **Vol 832**: p 456.

96.   Paul, M.C., Andrew, D., and Rees, S., *Numerical investigation of the linear stability of a free convection boundary layer flow using a thermal disturbance with a slowly increasing frequency.* Journal of heat transfer, 2008. **130**(12).

97.   Williamson, N., Armfield, S. and Kirkpatrick, M., *Transition to oscillatory flow in a differentially heated cavity with a conducting partition.* Journal of Fluid Mechanics, 2012. **1**(1): p. 1-22.

98.   Zhao, Y., Lei, C. and Patterson, J.C., *Resonance of the thermal boundary layer adjacent to an isothermally heated vertical surface.* Journal of Fluid Mechanics, 2013. **724**: p. 305-336.

99.   Zhou, T., Razali, S.M., Zhou, Y., Chua, L.P., and Cheng, L., *Dependence of the wake on inclination of a stationary cylinder.* Experiments in fluids, 2009. **46**(6): p. 1125-1138.

100.   Bearman, P.W., Downie, M.J., Graham, J.M.R., and Obasaju, E.D., *Forces on cylinders in viscous oscillatory flow at low Keulegan-Carpenter numbers.* Journal of Fluid Mechanics, 1985. **154**: p. 337-356.

101.   Obasaju, E.D., Bearman, P.W. and Graham, J.M.R., *A study of forces, circulation and vortex patterns around a circular cylinder in oscillating flow.* Journal of Fluid Mechanics, 1988. **196**: p. 467-494.